HYDRODYNAMIC INTERACTION OF WAVE DRIVEN ICEBERGS IN CLOSE PROXIMITY WITH A FIXED OFFSHORE STRUCTURE

by

© Tanvir Mehedi Sayeed, M.Eng., P.Eng.

A dissertation submitted to the School of Graduate Studies

in partial fulfillment of the requirements for the degree of

Doctor of Philosophy

Faculty of Engineering and Applied Science

Memorial University of Newfoundland,

St. John's, NL, Canada

October 2017

Abstract

Fixed or floating offshore structures and supply vessels in ice prone regions are subject to environmental loading from various forms of glacial ice fragments. Iceberg/bergy bit impact load with offshore structures is an important design consideration but a research gap exists in the study of the viscosity dominated, very near field region, where phenomena such as negative wave drift force (against the direction of propagation of the waves), shadowing, change in added mass, hydrodynamic damping, eccentric impact etc. have been observed in previous studies.

In order to better understand and quantify the hydrodynamic effects on small ice masses, a two phase, experimental and numerical, study has been conducted. Physical model experiments were conducted in the Ocean Engineering Research Center (OERC) at Memorial University of Newfoundland (MUN). In the first phase, experiments were conducted to investigate changes in wave loads on ice masses at different separation distances from the structure. The experimental results show that the distance to wavelength ratio dictates the corresponding wave loads in horizontal and vertical directions. The mean drift force in the horizontal direction becomes negative (against the direction of wave propagation) for most cases, when the body is close to the structure. As the body is positioned closer to the structure, the non-dimensional RMS forces in the horizontal direction decrease, and the non-dimensional RMS forces in the vertical direction increase.

In the second phase, experiments were conducted to investigate the change in wave induced motions for different sizes of free floating ice masses approaching a fixed structure. The experimental results of motion data show excellent correlation with the force data gathered in the first phase. Similar to previous studies, the separation distance to wavelength ratio is shown to

dictate the corresponding wave induced motions. As the body gets close to the structure, the surge motion slows and at the same time the heave motion is increased. Some experiments are also conducted to understand the motion behaviour in irregular waves. The significant wave heights showed a standing wave pattern generated by the superposition of incident and reflected peak frequency wave. Further analysis showed that the significant heave forces and motions will increase and significant surge forces and motions will decrease as the body gets close to the structure.

Numerical simulations were conducted using RANS based commercial CFD code Flow3D. Flow3D showed promising results when compared against the force measurements demonstrating the highest and lowest forces at different locations from the structure. For the motion simulations, the velocity changes at node and antinode locations in front of the structure are well captured by the numerical simulations. The challenges lie in the proper modeling of geometry and mass properties of the physical model considering the limitations of computational resources. The simulation results for irregular waves show the capability to simulate random waves and force and motion results in irregular waves are also reasonable showing the expected trends.

Acknowledgements

I would like to express my deepest gratitude and indebtedness to my supervisory committee members Dr. Bruce Colbourne, Dr. David Molyneux, Dr. Michael Hinchey and Dr. Jungyong Wang for their careful supervision, restless encouragement, untiring assistance and unremitting guidance and support. Dr. Colbourne has always given me valuable advice and suggestions throughout my PhD program and always kindly assisted to overcome my difficulties.

I am grateful for the technical assistance from Trevor Clark, Mathew Curtis and Craig Mitchell at Ocean Engineering Research Center (OERC) at Memorial University of Newfoundland. Their unlimited support and expertise during physical model experiments is highly appreciated.

I also appreciate the supports from all my colleagues at Ocean, Coastal and River Engineering (OCRE) of National Research Council of Canada (NRC). Experienced technical discussions with Michael Sullivan, Rob Pallard, Ayhan Akinturk, Wayne Raman-Nair and others at NRC always assisted me to overcome technical difficulties.

Sincere thanks and gratitude are extended to my fellow graduate students for their friendship and pleasant memories we shared during the program. Finally I am profoundly grateful to my parents, my wife, my daughter and other family members for their continuous love, support and encouragement.

Table of Contents

List of Figures

List of Tables

List of Symbols and Abbreviations

RAO	Response Amplitude Operator
a	Sphere radius
D	Separation distance from structure
D_i	Ice mass diameter
D_s	Fixed structure diameter
FX	Force in x-direction
FZ	Force in z-direction
g	Acceleration due to gravity
H	Wave height
H_{m0}	Significant wave height
K	Wave number
$S(\omega)$	Wave energy in m^2/Hz
T	Wave period
T_p	Peak period
u	Horizontal wave particle velocity
VX	Surge velocity in m/s
VZ	Surge velocity in m/s
Vol	Submerged volume
w	Vertical wave particle velocity
ω	Wave frequency in Hz
λ	Wave length

ρ	Water density
λ_p	Peak wavelength
CFD	Computational Fluid Dynamics
DOF	Degree Of Freedom
FPSO	Floating Production Storage and Offloading
GBS	Gravity Based Structure
NS	No structure case
RANS	Reynolds Averaged Navier Stokes
RMS	Root Mean Square

Declarations of Authorship

This thesis is based on works previously published / submitted in three journal papers with first author Tanvir M. Sayeed and co-authored by others including the supervisory committee members. The lists of corresponding papers are as follows:

1. Sayeed,T., Colbourne, D.B., B. Quinton Peng, H., Spencer, D. (2017). "A Review of Iceberg and Bergy Bit Hydrodynamic Interaction with Offshore Structures", *Cold Regions Science and Technology*, Vol. 135, pp. 34–50.

2. Sayeed, T. M., Colbourne, B., Molyneux, D., Akinturk, A. (2017). "Experimental and Numerical Investigation of Wave Forces on Partially Submerged Bodies in close Proximity to a Fixed Structure", *Ocean Engineering*, Vol. 132, pp. 70-91.

3. Sayeed, T. M., Colbourne, B., Molyneux, D., Akinturk, A., Zaman, H. (2017). "Experimental and Numerical Investigation of Wave Induced Motions of Partially Submerged Bodies Approaching a Fixed Structure", submitted to *Ocean Engineering*.

The work contained in the three papers was conducted by Tanvir M. Sayeed including the bulk of the literature review, development of experimental test plans and procedures, the conduct of the experiments and the analysis of data and outcomes. Similarly the numerical models described in the papers were entirely developed by Tanvir M. Sayeed and run using commercial software Flow-3D, licensed to Memorial University for educational purposes. Specific sections of the review paper (Chapter 2), prepared by one or more co-authors are not included in this thesis.

The published and submitted manuscripts were prepared as drafts by Tanvir M. Sayeed and editorial and technical commentary was provided by the members of the supervisory committee and other authors.

In this thesis, the text has been combined and edited for reader convenience and to eliminate duplications in common elements of the submitted and published papers.

Chapter 1
Introduction

1.1 Introduction

Fixed or floating offshore structures and supply vessels in ice prone regions are subject to a unique environmental loading by various forms of glacial ice fragments identified as iceberg, bergy bit or growler, depending on the fragment size. Estimation of iceberg impact load is an important design consideration which is not fully understood, with uncertainties due to the size and shape of the ice, ice material properties, and environmental effects on iceberg trajectory. Iceberg design load also depends on the type of offshore structure to be considered. Fixed structures need to be designed to withstand large iceberg impacts whereas floating structures can avoid interaction by moving off location. In addition, a significant number of ship-ice collisions have been reported and continue to occur. Small glacial ice masses are harder to detect in sea ice, in bad weather, at night, or in heavy seas.

For structures transparent to waves, like semi-submersibles, iceberg impact velocities predicted by open water test data are reported to be reasonable (Lever et. al (1988b, 1990b)), but for less transparent fixed or floating offshore structures like GBS or FPSO, the proximity effects are thought to be significant. Generally iceberg- structure collisions are anticipated to occur at velocities that place the ice in the brittle failure region, but lower impact velocities might cause the ice to fail in the ductile or transition regions (Cammaert et. al (1983), Johnson and Benoit (1987)), Sodhi and Haehnel (2003)).

There is evidence that the near field hydrodynamic influences do affect impact velocity and trajectory. It has been reported that if the ice mass diameter is less than half of the structure diameter, the ice mass will not hit the structure because of negative wave drift forces (Salvalaggio and Rojansky (1986), Isaacson and McTaggart (1990a, 1990b)). Even in cases

where impacts do occur, the impact velocity can be substantially reduced and several phenomenon like fluid cushioning, shadowing, eccentric impact etc. have been reported because of reflected and standing waves (Bolen (1987), Colbourne et. al (1998), Colbourne (2000), Gagnon (2004)).

The load transmitted to the structure is also heavily influenced by the orientation of the collision with eccentric, off axis and rotational effects, all acting to reduce the load. This was observed in most of the free drift experiments (e.g., Isaacson and McTaggart (1990c), Salvalaggio and Rojansky (1986)). A significant reduction in maximum ice load will occur with eccentric impact compared to head-on collisions because of the transfer of energy to rotation rather than crushing. Eccentric impacts occur more frequently, resulting in significant contribution to statistical design ice load (Matskevitch (1997a, 1997b), Fuglem et. al (1999)). The evidence from the studies reviewed here shows clearly that these parameters are strongly affected by the near field hydrodynamic properties and thus these properties have an indirect but important influence on the impact loads.

With regards to ice-structure interaction, the International Standard ISO 19906 (ISO 19906:2010) states: “Hydrodynamic effects associated with ice feature motions in the vicinity of the structure can be considerable, especially in conditions where the ice concentration is low and relatively small ice features are impacting wide structures. Due to hydrodynamic effects, smaller ice features can slow down as they approach and tend to move around the structure. Consideration should be given to added mass of the impacting ice feature, with due account for the presence of the seabed and the structure. When the structure moves sufficiently during the course of the interaction, its added mass should also be considered.”

It is evident that the prediction of ice impact forces could be substantially improved through a better understanding of the influence of hydrodynamic properties in the very near field interaction phase. Wave driven iceberg and bergy bit interaction and impact with offshore structures is complex and there is still a lack of knowledge on this topic (Tsarau et al. (2015). Reflected waves and viscosity effects in terms of hydrodynamic damping leading to reduced impact velocity, tangential force leading to iceberg rotation and eccentric impact should be considered in iceberg-structure impact analysis. Change in impact velocity also changes the failure mode of ice (ductile, transition or brittle) thus changing the effective pressure. Ignoring these effects may result in an overestimation in impact load which will ultimately affect the design and cost of the structure.

1.2 Research Objectives

The main objective of the present study is to investigate the close proximity hydrodynamic interaction and its effect on the velocity profile of approaching ice masses towards a fixed structure. The following objectives have been identified for this research based on the initial review of the literature.

I. Conduct a more comprehensive review of the literature to identify the significance of hydrodynamic interaction of ice masses with arctic offshore structure in close proximity just prior to impact. This review will seek to identify the important hydrodynamic phenomena (or components) such as changes in added mass, changes in wave induced motions or increases in viscous drag pressures as small floating bodies approach larger fixed structures. Also identify the related research gap(s) in available literature on this topic.

II. Investigate the phenomenon described above with a well-designed yet simplified controlled model experiments that focus on the parameters identified as important in the detailed literature review. It is proposed to divide the experimental program into two phases, one looking at forces and the other looking at motions. Each phase is described below:

   a. Investigate the change in wave loads for different sizes of ice masses at different proximity to a fixed structure through model tests and determine a relationship between ice piece size, driving wave characteristics, and separation distance.

   b. Investigate the change in wave induced motions of free floating ice masses of different sizes approaching towards a fixed structure through model tests and determine a relationship between ice piece size, driving wave characteristics, separation distance and velocity envelope. The motion experiments will be conducted both in regular and irregular waves.

III. Investigate available CFD software and select the package that offers the best modeling of the phenomena of interest, including consideration of the ease of developing the models. Develop numerical models of the experimental cases and compare results to determine if the available numerical/CFD tools capture the phenomenon accurately? It is proposed that the numerical work will be divided into two phases that correspond to the phases of the experimental program, wave forces on the approaching body and wave-induced motions of the approaching body.

1.3 Thesis Outline

The present thesis is divided into five chapters. Chapter 1 presents a preliminary introduction of the problem and the objectives of the present study. In Chapter 2, a comprehensive state of the

art literature review is presented in the subject of iceberg and bergy bit hydrodynamic interaction with offshore structures. Chapter 3 describes the findings of the physical model experiments conducted at the Ocean Engineering Research Center (OERC) of Memorial University of Newfoundland. This chapter is divided into three main sections: experimental investigation of wave forces, experimental investigation on wave induced motions, and experimental investigation in irregular waves. Chapter 4 presents the results of numerical investigations conducted using commercial CFD software Flow3D. Similar to chapter 3, chapter 4 is also divided into three corresponding sections. Finally summary and conclusions as well as recommendations for future work are presented in Chapter 6.

Chapter 2

Literature Review

2.1 Introduction

Estimation of iceberg impact load is an important structural design consideration for structures in iceberg prone waters. Iceberg design load depends on the type of offshore structure. Fixed structures are designed to withstand large iceberg impacts, whereas floating structures can avoid interaction with large bergs by moving off location but may be subject to impacts from smaller ice pieces due to non-detection. Tankers and supply vessels should also be designed to withstand impacts with undetectable ice masses (K.R. Croasdale & Associates Ltd. (2001)). A significant number of ship-ice collisions continue to be reported because small ice masses are harder to detect in bad weather, at night, or in heavy seas. Moreover, the hazard is increased by their short impact duration implied by higher impact velocity for small ice pieces (Lever et al. (1988b)).

Impact forces are heavily dependent on the collision energy and collision energy is largely dependent on the closing velocity between the ice mass and the ship or structure. In the case of fixed structures, impact velocity is entirely dependent on the iceberg instantaneous velocity at the time of impact with the structure. Traditionally, ice mass impact velocity is estimated based on the mean drift velocity plus the wave driven oscillatory velocity (Lever et al. (1988b), Fuglem et al. (1999)). This provides a conservative estimate of impact velocity. However other studies have indicated that the assumption may not be correct. The purpose of this study is to establish current practice in estimating impact velocities for ice mass impacts and to identify the evidence, or lack of, supporting the theory that iceberg impact velocities are substantially reduced as the bergs approach fixed or floating structures.

It is already shown in various previous studies that smaller ice masses tend to drift away from large structures due to wave drift forces against the direction of wave propagation. Even for

scenarios where ice masses hit a structure, the calculation of impact velocity without accurate inclusion of hydrodynamic interaction would lead to over prediction. This will result in an over prediction of impact loads and consequent over design of the structure.

For the purposes of this exercise, the problem of iceberg trajectory and impact with structures can be categorized into three phases or regions, namely far field, near field and contact phases. The near field can be further divided into two regions – an inertia dominated region and a viscous dominated very near-field region (Hay and Company Consultants Inc. (1986)). Figure 2.1 shows a methodology flowchart to determine design iceberg impact load. This indicates that the encounter dynamics are heavily dependent on the impact velocity (termed drift velocity in this case). The use of the term drift velocity implies that no account is taken of reductions of velocity in the near field.

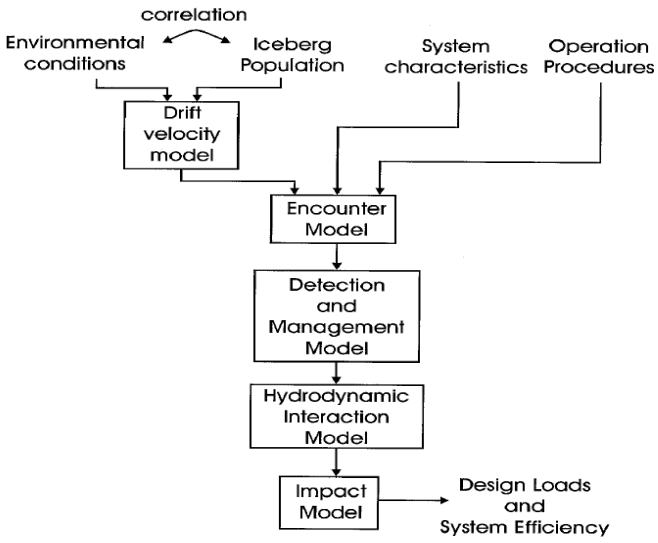

Figure 2.1: Methodology for determining design iceberg impact loads (after Fuglem et al. (1999))

2.2 Iceberg Drift Model in Open Water

In the simplest case, impact velocity can be equated to open water drift velocity. Iceberg drift in open water has been studied by several authors and three models have been utilized for predicting drift motion, namely kinematic, dynamic and statistical models. Kinematic models correlate iceberg velocity with known wind and current velocities while dynamic models estimate the forces on an iceberg of known mass to estimate velocity and position. Statistical models rely on the past drift trajectory of icebergs (Hay and Company Consultants Inc. (1986)) to estimate future drift. Most of these models neglect wave forces or only implicitly include them and have been shown to have little success in forecasting drift for extended periods of time (Carrieres et al. (2001)).

Mountain (1980) developed a dynamic model to predict iceberg drift trajectory considering wind, current, Coriolis force and a sea surface slope term but excluding wave forces. The current drag was calculated using the submerged depth of the berg divided into four layers of current flow. The author established seven classes of icebergs with various mass and cross sectional area based on compiled historical data. The main source of drift errors was indicated to be inaccurate wind and current data as inputs to the model. Sodhi and El-Tahan (1980) presented a numerical model to predict iceberg drift during a storm. The model included wind, current, Coriolis force, pressure gradient force and water acceleration but neglected wave and swell forces. It was claimed that the model provides good results if detailed wind and current field data are available and the size and shape of the iceberg is known. Icebergs in the field were observed to move back and forth, which was attributed to the direct action of wind direction changes.

Hsiung and Aboul-Azm (1982) included second-order wave drift forces in their iceberg drift model along with other conventional forces. The authors only considered translatory motions in the horizontal plane using wave diffraction theory and ignored oscillatory motions. The inclusion of wave forces significantly improved drift trajectory, in particular for small and medium sized icebergs.

Garrett (1985) proposed a statistical model which utilizes previous trajectories to estimate a probability distribution of velocity and position. In this model, the future velocity of an iceberg was considered as a weighted sum of previous velocities where the weights are related to a Lagrangian autocorrelation function. The model can be used to predict the probability of an iceberg coming within a certain radius of an offshore structure.

Gaskill and Rochester (1984) demonstrated a hybrid model combining dynamic and statistical models. A dynamic equilibrium model was used considering wind, current and coriolis terms. The currents were derived from the past drift of icebergs and used those data for predicting future drift of other icebergs in that local region.

Smith (1993) presented a dynamic model to hind-cast iceberg drift. He did not model wave forces explicitly but radiation wave forces were estimated to have an influential contribution. The method of optimizing air and water drag coefficients was helpful to improve the hind-casts but not effective for forecasting. The sensitivity tests showed that the model was relatively insensitive to iceberg size and shape, the pressure gradient term and added mass.

Carrieres et al. (2001) described the iceberg drift model implemented at Canadian Ice Service (CIS). The model included wind and current drag, water pressure gradient, wave radiation stress and added mass effect. The model was validated against a dataset of 17 observed iceberg drift

trajectories and was found to produce 35% RMS drift error at 96 hour forecast periods compared to other models of that time. The improvement was attributed to using improved forecasts of current and iceberg profile. The authors also investigated the effect of wave radiation stress by using a tuning coefficient. The impact of wave radiation stress was estimated at up to 10% of the iceberg drift.

Kubat et al. (2005) described an operational numerical model which predicts iceberg drift, deterioration and calving. This drift model included the vertical distribution of water current and the force due to wave radiation stress with other environmental forces. The most influential factors are found to be water current, waterline length of the iceberg and waves. The vertical profile of water current or mean current over the iceberg's keel depth is recommended for better prediction. A value in between the mean dimensions (of length and width) and the larger dimension (length) produced the best fit with observations. Waves are demonstrated to have impact on drift prediction and suggested for further investigation.

Dmitriev and Nesterov (2007) compared a numerical simulation of iceberg drift with full scale drift data collected in Barents Sea. The drift model was based on Sodhi and El-Tahan (1980) and did not include any wave forces. Uncertainty in iceberg size and shape and lack of accurate wind and tidal information were considered the main reasons for the observed discrepancy.

Pavec and Coche (2007) proposed a stochastic model for iceberg drift including the effect of waves. The wave force was calculated by approximating the iceberg as a truncated cone and a characteristic radius of the iceberg was chosen such that the corresponding cone has the same

waterline length and mass. The inclusion of wave induced forces significantly improved the drift estimation. Figure 2.2 shows such an improvement in predicting iceberg drift trajectory.

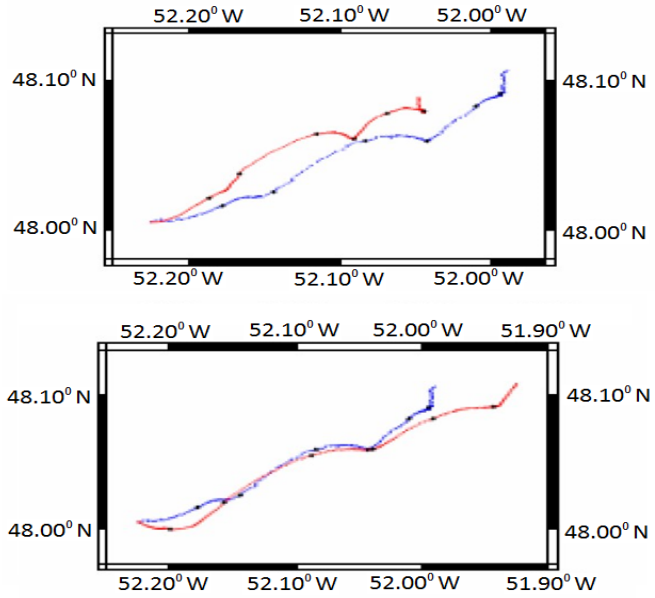

Figure 2.2: Improvement in iceberg drift including wave forces (bottom); red line is computed drift and blue line is observed drift (after Pavec and Coche (2007)).

Eik (2009) applied an iceberg drift model to the Barents and Kara Seas utilizing met ocean data to generate inputs for the model. In his model, Eik (2009) included an extra term to for sea ice drag forces up to 40% ice concentration. Results showed that good quality data for wind and wave but poor current data were applied to the model. Although current is the most important factor for iceberg drift prediction, the author mentioned that wave drift force may become most important in open water.

Turnbull et al. (2015) presented an operational iceberg drift forecast model used during scientific coring operation in northwest Greenland in 2012. The drift model was integrated with ice management strategy to identify possible threats and for safe operations. The forecast model was

optimized by tuning air and water form drag coefficients obtained from hindcast simulations. The authors also performed a sensitivity analysis and identified iceberg keel depth as a major source of uncertainty. The importance of near real time in-situ adequately measured wind and current data was also highlighted by the authors.

In summary, predictions of iceberg drift in open water have been improving steadily in the period since 1980. Significant uncertainties still exist concerning iceberg shape and environmental effects and it is apparent that the explicit inclusion of wave forces provides a better prediction of iceberg drift trajectory. There has been relatively little work reported on open water drift velocities for smaller bergy bits. Drift trajectories for smaller bergs would be less influenced by deep currents and more influenced by wave action, surface currents and wind. Moreover, all these above mentioned drift models consider added mass to be constant which in fact is not valid when ice masses get close to large offshore structure (Tsarau et al. 2015).

2.3. Wave Induced Iceberg Motion – Far Field

It is expected that wave induced motions become more significant as iceberg size decreases. A number of studies specifically related to wave induced motions with emphasis on smaller ice fragments have been conducted. Arunachalam et al. (1987) presented a theoretical and experimental study to compute first order wave induced motions in surge and heave of an iceberg in linear waves. The authors described the importance of motion analysis in terms of its impact on velocity estimation, drift trajectory estimation and stability determination while towing. A potential flow theory, using the three-dimensional source distribution technique, was employed to calculate the surge and heave motions of a free floating iceberg. Viscosity was included empirically using thin vortex sheets and flow outside the boundary layer was only

required to satisfy potential flow conditions. The numerical results were validated against published analytical results and then used to verify experimental results. Two models of cylindrical and cubic shapes were tested and the results were in good agreement with numerical results. The authors also investigated the effect of model draft/water depth ratio on motions.

Lever and Sen (1987) highlighted the importance of wave- induced iceberg motion in risk analyses of iceberg collisions. The authors utilized linear potential flow computer code developed by Sen (1983) to compute wave-induced surge and heave motions of five different size cubic icebergs. Small icebergs showed fluid particle type behavior for wave length/iceberg size ratios greater than 10-15 which matches with experimental results of Lever et al. (1988b) where the ratio was found as 13. Iceberg impact risk analyses, considering only mean drift speed, and collected at an hourly rate, produced underestimated velocity results, which were more pronounced for smaller icebergs. The significant wave induced velocity was included with the drift velocity and their scalar sum was taken as the total velocity to compute probability densities. This scalar sum neglected directional effects and the influence of structure on the flow field was not considered.

Upon finding considerable effects of iceberg model shape on wave induced motions, Lever et al. (1990a) extended their impact velocity probability statistics to include randomly varying iceberg shape. The inclusion of iceberg shape showed important variations on significant velocity exceedance levels which in turn resulted in higher total surge velocities (including drift) for almost all cases. There was no provision for hydrodynamic interaction effects between the iceberg and the structure and kinetic energies were calculated excluding added mass effects. The authors suggested these inclusions for future work in order to apply their risk analyses to fixed large production platforms.

Lever et al. (1988a), and Attwood (1986) conducted wave tank experiments of wave-induced iceberg motions to validate results from linear potential theory. Three different sized cubic models were used to check model scale factor validity and implementation of Froude scaling was found to be reasonable for wave induced iceberg motion tests. The effect of shape was examined by additionally considering cubic, cylindrical, trapezoidal and spherical shaped icebergs and the shape of the iceberg was found to be an influential factor on motions. Figure 2.3 shows measured RAOs for different iceberg shapes. The x-axis shows the wavelength over the characteristic length of specific iceberg which was taken as waterline length.

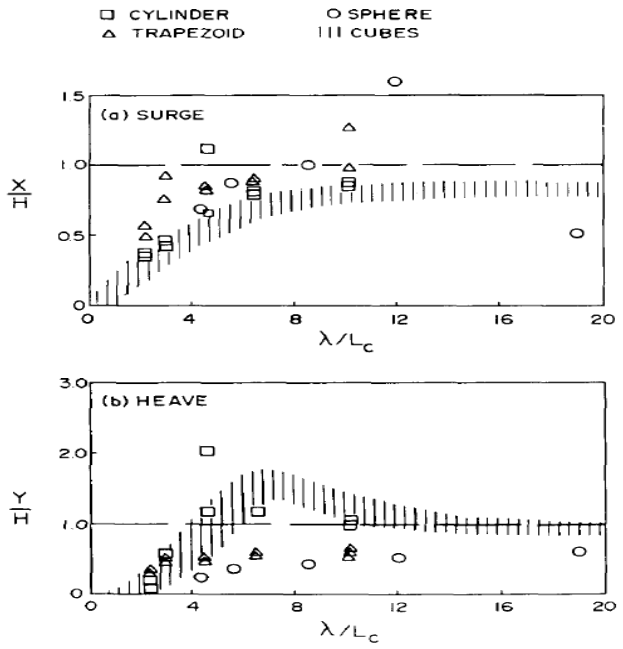

Figure 2.3: Measured RAOs for different shape iceberg models (after Lever et al. (1988a)).

Using linear superposition theory to predict motion response in irregular waves was found to yield good matching with experimental data. Linear diffraction theory predicted reasonable results with slightly underestimated surge and overestimated heave response. The probable reasons for the discrepancies were identified as ignoring viscous damping and the large change

in wetted surface in heave motion. Attwood (1987) also mentioned second order wave effects in surge and viscosity effects at heave resonance as additional causes of discrepancy. Heave resonance predicted by Arunachalam et al. (1987) was better than Lever et al. (1988a) because of the inclusion of a viscous damping term. Hinchey et al. (1991) also conducted analytical and experimental studies for heave resonance chaotic motions of spherical bergy bit.

Lever et al. (1991) presented wave induced motions from a field study of full-scale icebergs collected in the Labrador Sea and on the Grand Banks. The normalized significant surge and heave velocities showed that the motions of four regular shaped icebergs, tested in a wave tank, showed variations attributable to random shape. These velocities should be treated as random quantity for a given iceberg size and sea state and the authors suggested that a gamma probability density function could be fitted to the wave tank data.

This series of studies indicate that wave induced motions become increasingly important in predicting ice piece velocity as the size of the ice mass decreases. This importance was generally recognized and resulted in the inclusion of wave oscillatory velocities in the calculations of small iceberg drift and velocity models. This leads to relatively conservative estimates of velocity when the impact velocity is equated to the mean or extreme drift velocity.

2.4. Iceberg Motion in the Vicinity of Large Structures – Near Field

As analysis of iceberg trajectories and velocities continued with the aim of improving drift models and providing more certainty in impact and risk models, work turned towards the effects of the presence of a large fixed structure. Much of this work was focused on considerations of the Hibernia offshore structure, the first fixed offshore platform designed for iceberg impact. Arunachalam et al. (1985) summarized design and operational aspects of iceberg interaction with offshore

structures. A smaller iceberg in storm waves can have significant kinetic energy compared to a larger slower berg influenced primarily by current. One of the findings from model studies is that surge velocity was found to be considerably reduced while heave velocity was amplified for a few cases during iceberg interaction with a fixed gravity based structure.

Hay and Company Consultants Inc. (1986) studied the inertia dominated region where both the ice mass and structure are in close proximity where the flow field around the ice mass is influenced by the presence of the structure. A numerical model developed by Isaacson (Isaacson and Dello Stritto (1986)) was utilized to predict motions of different size icebergs in close proximity to a large fixed structure. The model superposes wave drift forces, calculated by diffraction theory, and current drag forces with the further inclusion of zero frequency added mass. An empirical viscous damping coefficient was also included. The most influential factor affecting the drift trajectory for smaller ice masses was found to be the wave drift force. The zero frequency added mass showed an increasing trend prior to impact but the numerical results in this region were deemed unreliable due to the exclusion of the complete viscosity effect. The model was also unable to predict behavior for very small gaps between the structure and the approaching berg because of the coarse mesh discretization.

Foschi et al. (1996) studied the wave plus iceberg load combination factor utilized for offshore structure design load calculation. The results from numerical analysis, which calculated loads in waves alone, then from an iceberg alone and then the combination of waves and an iceberg, were used to develop simplified expressions for wave and iceberg loads. These expressions were then used to analyze first order reliability and to identify probability of failure for the three load cases to derive the combined load combination factor. The authors performed a case study for a structure similar to the Hibernia platform with a vertical circular cylinder as the fixed structure

and an iceberg circular in plan and ellipsoidal in elevation. In the contact phase, ice crushing pressure was found to be the most influential factor and the constantly changing contact area makes it difficult to predict maximum load. The wave forces during the contact phase were analyzed by treating the two contacting structures as a single body. Iceberg impact and waves were considered stochastically dependent whereas the opposite was suggested by the Canadian Standards Association (1992). The value of the combination factor 0.8 recommended by CSA code was found to be reasonably safe for the range of parameters studied. Among the parameters taken into account, it is stated that impact velocity, eccentric collisions and iceberg added mass should be subject to strong hydrodynamic interaction effects which would benefit from further investigation.

Foschi and Isaacson (1996) conducted a second similar study with some changes in analysis. The changes included omitting sliding and structural damage, including wave height with an Extreme Type I distribution, and adding a minimum ice crushing pressure with a normal distribution. This yielded the same conclusion that the behavior of an iceberg collision with a structure is influenced by waves and the combination factor of 0.8 should be used.

As a successive study, Foschi et al. (1997, 1998) investigated the sensitivity of the combined load factor to various iceberg and wave parameters typical of three sites off the East Coast of Newfoundland. In this study they considered the incident wave direction and wave parameters during the iceberg season rather than year round annual data. The inclusion of wave angle relative to iceberg trajectory and site dependency resulted in a much smaller value of 0.2 as a load combination factor. This factor value can be modified for different wave direction as presented in the paper. This study dictates the importance of wave direction which needs to be accounted for as an input parameter for future studies. Foschi et al. (2004) again suggested that

iceberg impact and waves should be considered stochastically dependent and a load combination factor of 0.4 was recommended to be conservatively used for a range of conditions. Recently, Fuglem et al. (2015) demonstrated a probabilistic method to determine iceberg-wave companion loads for extreme (10^{-2}) and abnormal (10^{-4}) level conditions. The results which are conservative because of simplified assumptions of the wave load model are yet found to be significantly lower than those based on ISO 19906 combined load factors. Furthermore the Iceberg Load Software (ILS) used by the authors is a probabilistic tool to identify distribution of global iceberg impact forces and does not account for the influence of the structure on the approaching iceberg motion.

Isaacson and Dello Stritto (1986) emphasized near field ice motion with a fixed offshore structure. A diffraction theory model was utilized, with oscillatory and drift motions, to investigate the two body interaction problem. Three flow regimes were classified based on ice mass sizes relative to wavelength. Smaller ice masses (ice diameter/wavelength less than 0.2) in close proximity showed negative wave drift and decaying oscillation. For intermediate masses (ice diameter/wavelength 0.2 to 2) no decay in oscillation was found but a sharp drop in drift resulting from negative wave drift was observed. A 10% increase in added mass was noticed for large masses (ice diameter/wavelength greater than 2) in close proximity. A numerical limitation of facet size prevented reliable results for very small separation distances.

Isaacson and Cheung (1988a) developed a numerical model to study hydrodynamic interaction between two arbitrary shaped cylinders in close proximity under the action of current only. The model was formulated using potential flow theory and solved using the boundary integral method. Results for added mass and damping coefficients, for a case of two circular cylinders were developed and significant variation was found at a proximity distance less than twice the

diameter of the drifting cylinder. These results cannot be applied where flow separation is significant because of the inherent limitation of potential flow theory.

Cheung (1987) and Isaacson and Cheung (1988b) observed an increase in added mass as separation distance decreased, based on predictions utilizing their potential flow code. The added mass coefficient at contact was calculated as 1.6 while the far-field value was 1.0 when the structure (a circular cylinder) diameter is twice the iceberg (another circular cylinder) diameter. Figure 2.4 shows the change in added mass coefficient with separation distance for two circular cylinders. This effect was found to be more pronounced as the ice mass gets smaller than the structure and the ice mass draft gets closer to water depth. The authors developed a kinetic energy impact model where the input energy of the fluid and ice mass was dissipated through ice crushing and foundation deformation. Using the contact point added mass instead of the far-field value provided deeper ice indentation, longer impact duration and higher impact force. Numerical results became unstable when the separation distance reached less than 2% of the ice mass radius and the added masses were estimated through extrapolation and multiplied by a correction factor to include three dimensional effects. Through a sensitivity analysis, the impact velocity was found to be the most influential factor in the predicted load. The authors suggested inclusion of hydrodynamic damping and variation of free surface during impact for further studies.

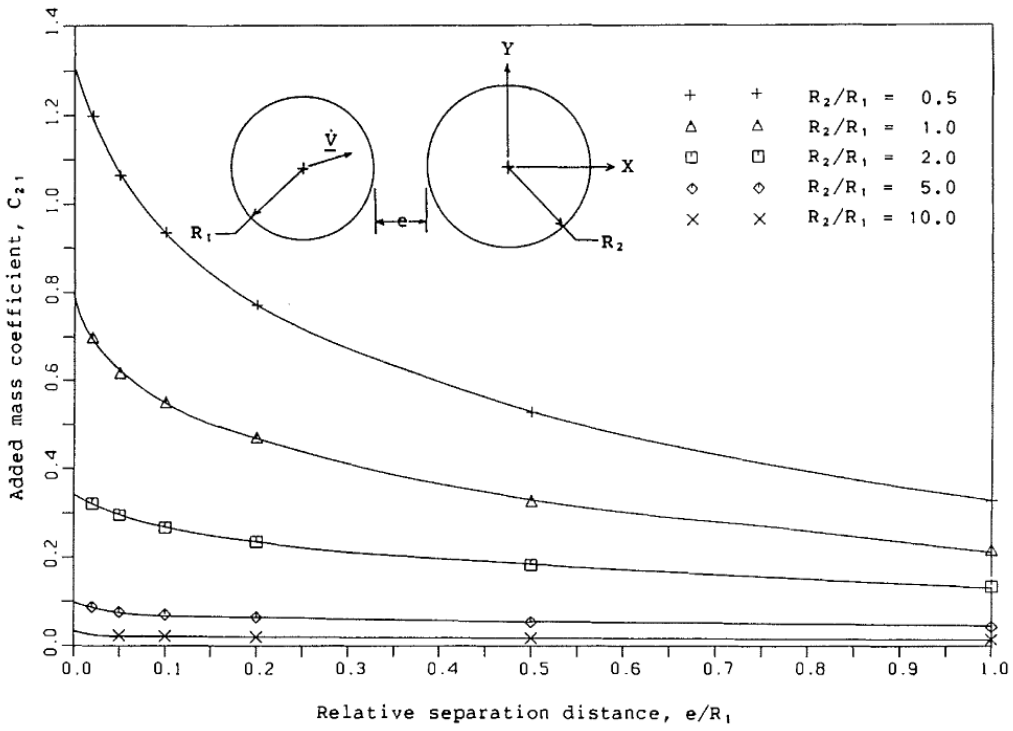

Figure 2.4: Change in added mass coefficient with separation distance (after Isaacson and Cheung (1988b)).

McTaggart (1989) investigated various hydrodynamic aspects such as added mass, wave induced oscillatory motion, and modification of iceberg motion due to the presence of a structure during iceberg impact with the structure. Figures 2.5 and 2.6 show variation in wave drift coefficient and surge RAO for a test case. A potential theory based numerical model predicted significantly lower impact velocities than observed during physical model tests. An investigation of convective forces on iceberg approach eccentricities was suggested for further studies. Two probabilistic models were also developed, one based on kinetic energy and another based on impact force incorporating different hydrodynamic effects.

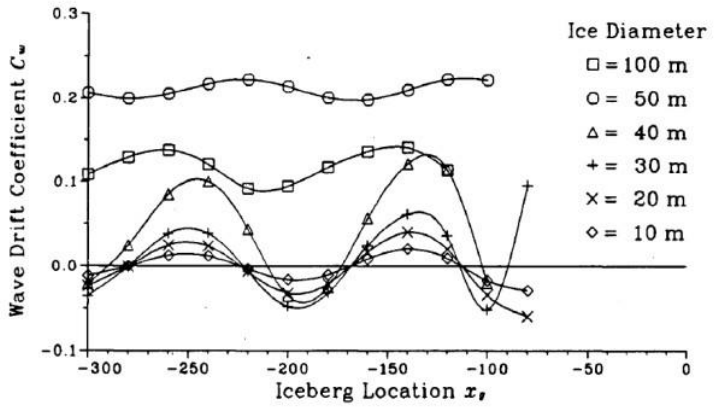

Figure 2.5: Variation of wave drift coefficient with proximity to structure for a wave period of 12s, structure diameter 100 m (after McTaggart (1989)).

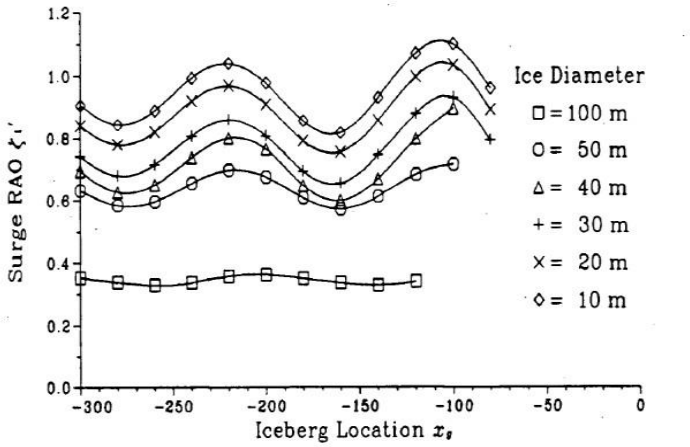

Figure 2.6: Variation of oscillatory surge motion with proximity to structure for a wave period of 12s, structure diameter 100 m (after McTaggart (1989)).

Isaacson and McTaggart (1990c) summarized various hydrodynamic effects during iceberg impact. The effective added mass was found to vary with impact duration. Infinite frequency added mass was suggested as an appropriate value for short duration and zero frequency added mass for longer duration. Both the wave and current field are shown to be modified by the presence of the structure which can result in 10% or more velocity reduction for smaller icebergs

(iceberg-structure diameter ratio less than 0.2) approaching the structure. Wave induced oscillatory motions are important for smaller icebergs but are not affected significantly by the structure's presence. For icebergs with iceberg-structure diameter ratio less than 0.5, negative wave drift forces result in significant reduction in impact velocity or in some cases no impact.

Chernetsov et al. (2008) proposed two types of spar substructure (SPAR-Classic and SPAR-Ring) equipped with mooring system which can resist ice floe and iceberg impact. Both static and dynamic analyses were performed to assess global iceberg impact load for different mooring configurations. Diffraction theory used in dynamic simulation showed considerable reduction in iceberg approach velocity before contact and impact was reduced because of hydrodynamic interaction during contact. In a similar study, Karlinsky and Chernetsov (2010) assessed the resistance of a turret moored FPU to iceberg impact considering three different locations of impact along the hull. The severity of the impact can be reduced because of the turret rotation capacity of the FPU which results in an eccentric impact. They also concluded that there was reduction in iceberg approach velocity due to hydrodynamic influence.

Lee et al. (2010) investigated the effects of the geometry of the iceberg striking face and the water layer entrapped between an iceberg and a LNGC during the collision process through a sensitivity analysis. The geometrical parameters (curvature radius and inclination angle) showed that global and local responses become much less severe if the striking face is irregular instead of perfectly flat. The effect of sea water was investigated using numerical simulation with LS-DYNA including fluid-structure coupling. The fluid problem was solved using a RANSE computer code without a turbulence model and no viscosity was considered. As the iceberg approaches the hull, the pressure increases drastically because of the confined water layer entrapped between the two objects. Icebergs slowly approaching the hull will not have such an

effect as the water between the two bodies will have enough time to flow away without resistance. When the iceberg velocity was kept constant until impact, the hydrodynamic pressure increase due to the confinement effects showed a longer rise time, which eventually modifies the dynamics of the impact. Thus the squeezing pressure of the water eliminates any fast dynamic initial impact and no shock wave is generated due to the lack of a strong discontinuity.

Lee and Nguyen (2011) simulated bow shoulder and side collision responses between a LNGC and a cubic iceberg considering wave making of the LNGC and relative drift velocity, taking the hydrodynamic water pressure into account. Figure 2.7 shows a snapshot of a collision behavior between the LNGC and an iceberg. The iceberg is deflected in the sway direction from the LNGC and the collision velocity is reduced due to the squeezing pressure of the entrapped water layer. The iceberg collided at different locations of the side structure than would be expected if in the collision had occurred in void space instead of water. The flow interaction between the iceberg and the LNGC side structure in close proximity termed as bank effect was considered as a possible reason.

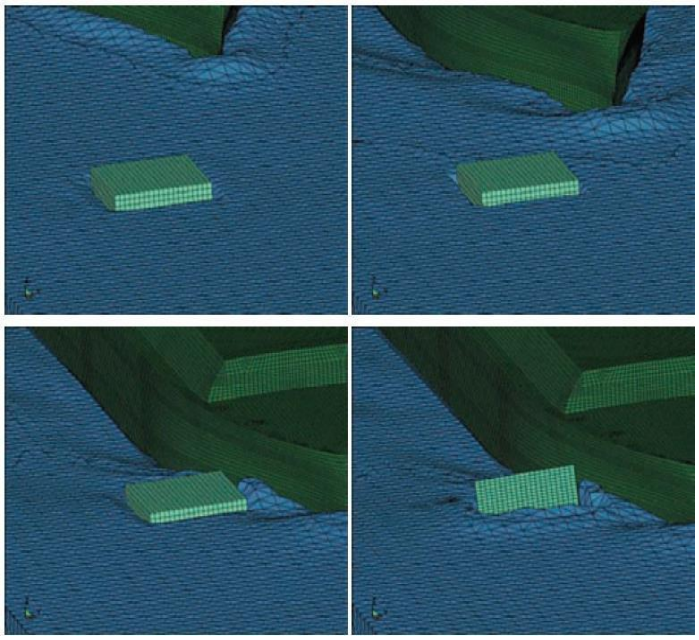

Figure 2.7: Collision behavior of LNGC and iceberg (after Lee and Nguyen (2011))

2.5. Near Field Studies with Physical Model Tests

Salvalaggio and Rojansky (1986) conducted experimental and numerical studies of iceberg-structure interaction, for a range of iceberg sizes, under the influence of waves. It was observed that no impact occurred if the iceberg diameter was less than approximately half the structure diameter. These smaller icebergs approached the structure slowly and shifted to one side and passed by with no impact. The medium sized icebergs tended to produce eccentric impacts which were more pronounced with larger wave periods. Repeated impacts were observed for medium sized bergs with slower rotation until the berg had passed by the structure. Larger icebergs impacted in all cases. Reflected wave heights were up to three times the incident waves. Another phenomenon was observed when the smaller icebergs came to a stop just in front of the structure and stayed there until small disturbances caused sideways movement and eventual bypassing of the structure. The authors also developed a numerical model with combined

kinematic- dynamic impact and a probabilistic model based on the results of their numerical model.

Lever et al. (1988b) conducted model tests in regular waves with spherical, cubical and rectangular prismatic ice models. For wavelength/characteristic ice length ratios greater than 13, all models were found to behave similarly to fluid particle motion. For the ratio of 10 to 13, the model shape came into play in determining whether the motion would be particle-like or not. For the ratio of less than 10, no models behaved as fluid particles and the motions were affected by wave diffraction and possibly viscous drag. During heave resonance tests, significant motions were observed such that the models partially or fully submerged on downward vertical motion. Video images indicated a phase difference between ice and wave motions. Some tests were conducted by placing the models upstream of a group of rigid piles and the presence of the structure substantially changed the ice model behavior in close proximity.

Lever et al. (1990b) conducted model tests of wave driven bergy bits impacting with a semi-submersible in irregular waves. Impact locations and velocities were determined by tracking motions with a camera and transferring the data to a CAD facility to redraw the positions of two bodies at each time step. Repeated impacts were observed during the tests and rotational kinetic energy was found to represent only 13% of the total kinetic energy. The authors developed a simplified procedure to estimate translational impact energies using standard deviations of surge and heave velocities in open water. On average, relative motions between the bergy bit and the semi-submersible tended to mitigate collisions slightly at the contact point.

Mak et al. (1990) conducted a similar study in regular and irregular waves with a floating oil production platform with larger physical dimensions than the transparent semi-submersible

tested by Lever et al. (1990b). Wave diffraction effects were observed with fewer impacts in beam seas than head seas, and a substantial reduction in impact rate for the smaller berg. Open water significant velocities were found to be 10-40% higher than significant impact velocities. The wave-induced impact behavior was observed to be non- linear (due to submergence and large excursions) and linear superposition was suggested to be inappropriate for evaluating impact statistics.

Isaacson and McTaggart (1990a) presented summary results of experiments carried out to investigate iceberg drift in proximity with offshore structures. The experiments were conducted in environmental conditions of waves only, currents only and combined waves and currents. For the waves only condition, no impact occurred when the ratio of iceberg diameter and structure diameter is less or equal to 0.2 whereas Salvalaggio and Rojansky (1986) in their experiments found the ratio to be 0.5. Isaacson and McTaggart (1990b) gave a more detailed presentation of results from the same study. Measurements of collision eccentricity and relative impact velocity were compared with a numerical model. Figure 2.8 shows the observed iceberg trajectory in a test condition and Figure 2.9 shows a comparison of numerical and physical model test results for another test condition. For the current-only cases, agreement was reasonable for velocity ratios but the numerical model under predicted impact eccentricities. For the waves-only condition, the numerical results followed the experimental trend except for one condition. For combined wave-current with larger waves, the numerical results significantly under-predicted. In general, poor agreement resulted especially from the prediction of negative wave drift force in the vicinity of the structure. The authors recommended further numerical and experimental studies to improve the predictions.

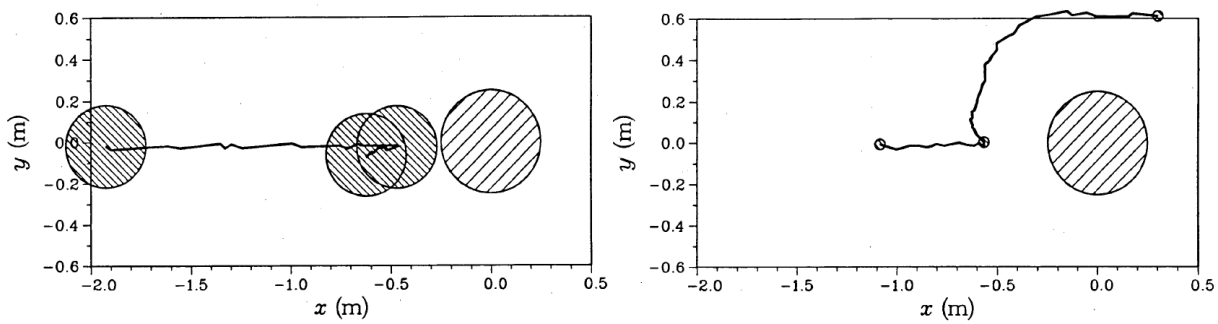

Figure 2.8: Observed iceberg trajectory – current only, Di/Ds = 0.8 (left); 21 mm wave, Di/Ds = 0.1 (right) (after McTaggart (1989), Isaacson and McTaggart (1990b)).

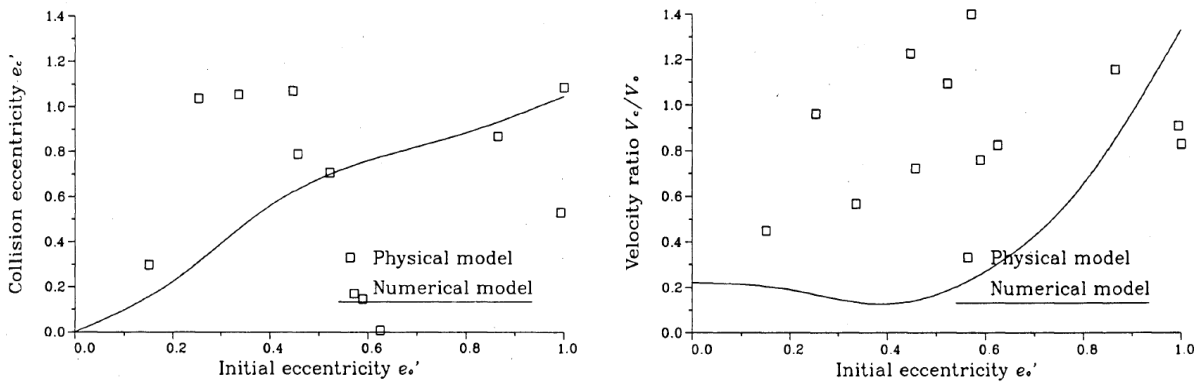

Figure 2.9: Comparison of Isaacson's numerical model with physical model test data – wave-current condition 2, Di/Ds = 0.5 (after McTaggart (1989), Isaacson and McTaggart (1990b)).

Kazi et al. (1998) conducted experiments to investigate hydrodynamic interaction between a fixed cylinder and free floating cylinders of various shapes and sizes. The motions of the floating cylinder centrally approaching towards the fixed one and the forces acting on the fixed cylinder were the main areas of interest. A repulsive interaction force was observed between two bodies. Results were compared with a potential flow model which predicted the velocity of the floating

body reasonably well but over predicted the force acting on the fixed cylinder especially in very near field. Discrepancies were attributed to not accounting for viscous effects.

Colbourne et al. (1998) conducted physical model tests of the Terra Nova FPSO in collision with an iceberg (100,000 t) and a bergy bit (3,600t) at different headings and driving environments. A guide wire was utilized to keep the course of the collision event on track. The iceberg was driven by current only, except in one test where both waves and current were used. The wave-current driven iceberg test showed significant increase in impact force. Wave action on the smaller bergy bit resulted in confused collision trends. In the head on case, the bergy bit was sometimes accelerated towards the vessel and sometimes away from the vessel at the time of collision. For the quartering case, the bergy bit frequently turned as it approached the vessel and passed down the side of the vessel resulting in no impact at all. The action of radiated waves in very near field region was considered as reason of such uncertainty.

Colbourne (2000) indicated that for small ice pieces, increasing input wave energy did not lead to increasing impact energy and postulated that the effect may be due to reflection of waves where the reflected wave energy negated the increased berg energy. This set of experiments differed from previous, in that impacts were forced to occur by a guiding mechanism that did not allow the proximity effects to deflect the ice track. Colbourne (2000) suggested further investigations be performed to analyze wave effect in driving and wave interference during impact of ice masses with stationary structures.

Gagnon (2004a) conducted some growler impact tests with an impact plate representing the ship hull. Two free floating growlers were impacted at speeds ranging from 0.2 to 3 m/s with three different growler orientations and three different impact plate angles. A new type pressure panel

was used to measure contact area and pressure distribution. The maximum impact loads increased linearly with impact velocity and increased with impact angle. The results from the pressure panel at the center of the impact plate showed that contact areas during impact were small resulting high pressures in the range of 20-25 MPa. The impact duration was approximately constant and growlers showed significant resilience to impacts. Some tests were conducted in air to study associated hydrodynamic effects during impact. For a few tests, 1 cm thick foam was also wrapped on most of the impact plate except the center where the impact occurred. The results from subsequent tests demonstrated that the load sensing capability of the impact plate itself was not influenced by putting a foam sheet over most of it to decouple it from the water. The numerical results by Gagnon (2007) produced reasonable load, pressure and collision duration compared to the experimental data. Gagnon (2004b) conducted another comprehensive model tests to investigate hydrodynamic interaction between floating ice mass with a tanker passing at speed. Figure 2.10 shows the small spherical iceberg with transiting tanker (left) and growler impact test (right). This study indicated that the radiation/proximity effect can be significant but this work did not directly consider collisions. Three sizes of three different shaped (sphere, cylinder and pyramid) ice masses were tested at different tanker speed, separation distance and wave conditions. The sizes of ice masses were found to affect the hydrodynamic forces so that they opposed the attraction effects as tanker speed increased. An increase in maximum sway motion was also observed due to the presence of the tanker as a temporary wall boundary thus influencing the wave-induced hydrodynamic forces on the ice mass. The author attributed this to negative added mass and drift force because of standing waves between the tanker and the ice mass. The data showed that surge and sway speeds were low (less than 10% of tanker speed) not enough to significantly reduce impact velocity during collision.

Figure 2.10: small spherical iceberg with transiting tanker (left) and growler impact test (right) (after Gagnon (2004b, 2007)).

Tsarau et al. (2014) presented a numerical model combining discrete element and boundary element methods to predict potential flow with actual movements of bodies in multi-body dynamics. In order to validate the model, they conducted some model tests in calm water. A submerged sphere (ice mass) was fixed and a cylinder (structure) was towed past the sphere at different speeds and separation distances. Figure 2.11 shows the experimental set up for the model test. Surge and sway forces on the sphere were measured and compared with the numerical model. The hydrodynamic forces were found to vary between positive and negative depending on separation distance. The numerical model predicted qualitative results for large separation distance, accurate estimates for moderate distance and overestimates for very small (0.01m) separation distance. Limitations of the experimental set up and viscous effects were considered possible reasons of discrepancy in the very near results.

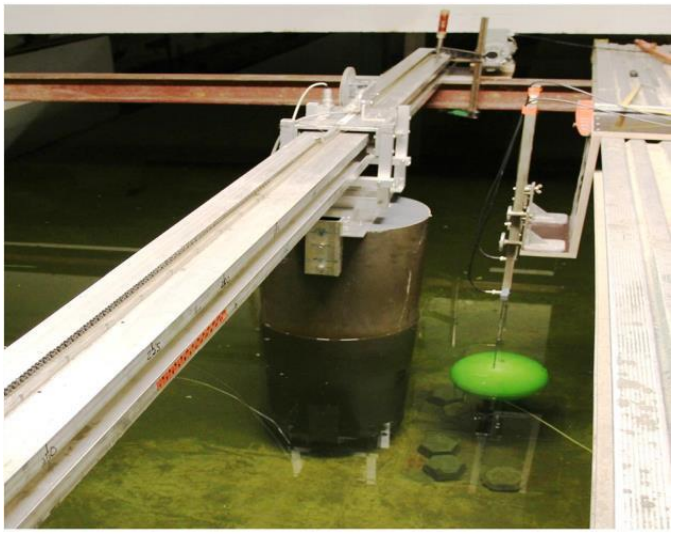

Figure 2.11: Experimental set up – Fixed sphere and towed cylinder (after Tsarau et al. (2014))

Eik et al. (2009) conducted model tests with three cubic and three cylindrical icebergs of different size made of wax in regular and irregular waves to measure iceberg drift speed. Based on the experimental results an empirical equation was developed for wave drift coefficient as a function of wave height and iceberg length. Standard wave drift theory can be applied to larger icebergs but for smaller icebergs and bergy bits, the theory is not applicable because of negligible reflected waves. The tests showed that for smaller bergs, higher waves caused higher wave drift. Exclusion of viscous forces was considered a possible reason for this as viscous wave drift force is proportional to the cube of wave amplitude. Due to the experimental limitations, the authors suggested further tests to derive a relationship between wave drift force and wave period.

Kim (2014) conducted drop tests of laboratory grown ice blocks onto stiffened steel panels in air and impact tests in water with a moored structure and ice blocks towed at 1 and 2 m/s at NTNU and Alto University. The objective was to investigate simultaneous inelastic deformations of ice and steel structure and the drop tests in air helped to separate associated

hydrodynamic aspects. A numerical model developed by Liu et al. (2011) was used for comparison with the experiments and the numerical simulations showed slight overestimation of maximum damage and the difference increased for the tests in water.

McGovern and Bai (2014a) conducted an experiment on isolated ice floes of different sizes and shapes and investigated their surge and heave motions in regular waves. The motions observed for ice floes were found to be different than those of icebergs. The scale factor, surface roughness, floe size and orientation did not influence the surge and heave motions. Floe thickness was found to have considerable effect, causing heave resonance for thicker ice. At wavelength to characteristic length ratio of 3.3 to 5, the floe behaved like a fluid particle. Maximum velocities were greater than 70% and 80% of the fluid particle velocity for surge and heave respectively but did not exceed particle velocity. McGovern and Bai (2014b) also investigated the presence of a circular cylinder on the kinematics of ice floes in regular and irregular waves. At separation distance to cylinder diameter ratio less than 10, increase in heave response and significant reduction in surge response was observed. The mean drift velocities also showed low and negative values as the ice floe approached head-on towards the cylinder.

Model scale testing plays an important role by showing real world phenomenon in a controlled environment. Model scale testing is also feasible and inexpensive compared to full scale testing. Various model testing approaches discussed in this section show different phenomena like negative wave drift force, fluid cushioning, shadowing, reduction in impact velocity, and hydrodynamic damping during iceberg-structure interaction, thus leaving the study of hydrodynamic interaction in close proximity an area of further research and analysis.

2.6. Iceberg Collisions – Full Scale Trials

Duthinh et al. (1990) conducted experiments at Dumont d'Urville, Terre Adelie, Antarctica. A 1700 tonne iceberg was towed into a rock cliff which extended to a depth of 13m under water. The impact velocity was measured as 0.89 m/s and impact duration as 2.25 seconds. The authors estimated the contact area between 1.8 and 3.6 m^2 and the impact force to be between 4.5 and 6.5 MN. In their first attempt, when the berg was pulled within 10-15m of the cliff and then let it drift freely, the berg stopped before the cliff and the authors considered a switch in wind direction as probable reason. During the second attempt when the berg was pulled within 5m, the impact occurred. The contact area measurement was considered as the greatest source of errors. Any wave or current effect was ignored during calculation. The authors used an added mass coefficient of 1.5 and suggested further investigation of added mass of the iceberg during collision especially in immediate vicinity.

Bruneau et al. (1994) reviewed the results of full scale iceberg impact tests conducted at Newmans Cove, Bonavista Bay, Newfoundland in 1992. The iceberg masses ranged from 8430 to 22342 kg and the impact speeds were 0.55 to 1.19 m/s. The ice pieces were towed into a purpose-built steel load panel and global loads were measured with two load cells. Sheets of bubble wrap packaging material were used to measure contact areas and in total eight impacts were obtained. The results showed a significant reduction in measured iceberg load from estimated values.

Crocker et al. (1997), Ralph et al. (2004) reported on a similar full scale iceberg impact experiment conducted on Grappling Island in 1995. An instrumented panel of 6m by 6m was mounted on a nearly vertical cliff face and icebergs were towed into the panel using a tugboat

(Figure 2.12). The panel was divided into 36 triangular sub-panels and a 750 tonne loadcell was used at each corner of the triangle. The iceberg masses ranged from 180 to 1000 tonnes and the impact speeds were 0.36 to 1.9 m/s. Impact velocities and angles were estimated from digitized frames captured with an overhead video camera. Peak forces ranged from 0.09 to 2.09 MN and estimated contact areas ranged from 0.02 to 2.17 m^2. Ralph et al. (2004) also compared Grappling Island pressure/area data to other ship ram tests and medium scale test data. Out of 28 impacts, 22 were stated to be good impacts and best fit pressure/area relationship was derived as $P = 0.73A^{-0.65}$ where area, A in m^2 pressure, P in MN. The constant 0.73 is considerably lower than values from other data (3.22 in Pond Inlet tests, 3.0 in ship ram trials). Repeated impacts suggested that the tested icebergs were warm at the surface and repeated crushing caused increased pressure even though iceberg mass was lost after each impact.

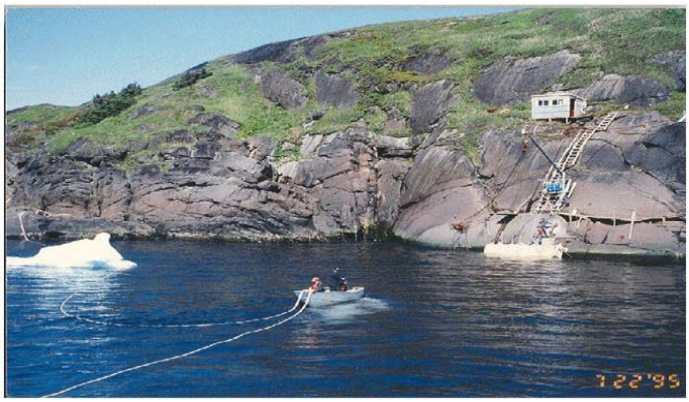

Figure 2.12: Grappling Island iceberg impact test (after Timco (2011)).

Gagnon et al. (2008a, 2008b) and Ritch et al. (2008) gave a detailed description of bergy bit impact field trials conducted with CCGS Terry Fox off the north east coast of Newfoundland in 2001. Ice masses ranging from 100 tonnes to 22000 tonnes were impacted at ship speeds of 5-12 knots and impact forces, contact areas, pressures and ship motions were obtained. A strain

gauge panel, an external impact panel and an inertial measurement instrument called MOTAN were used to measure loads during collision. Johnston et al. (2008) compared the forces measured by different instrumentation during these impact trials. Forces on the impact panel were found lower than forces on strain gauged panel and both these instruments measured lower forces than MOTAN. The reason was the design and limited size of the panels which influenced the amount of ice contact that was captured by the panels. For the tests where contact was entirely captured by the strain gauged panel there was good agreement with the MOTAN results. In general, smaller ice masses produced lower impact pressures and vessel impact speed produced higher pressures for higher velocities (Ritch et al. (2008)).

Although full scale trials are very few in number, the data from these tests consistently shows lower ice loads than would be estimated from the existing knowledge base. The unquantified hydrodynamic interaction in close proximity might be a cause of the apparent reduction of ice loads. Also there is complicated scale effect due to the structural properties of ice which causes reduction in pressure as the contact area is increased.

2.7. Iceberg Collision – Contact Phase

Most studies have treated the structure contact phase of iceberg impact separately from the other phases. In all cases, assumptions about the impact velocity and the hydrodynamic coefficients are shown to influence the impact energy and the ice crushing mechanism and thus the models are somewhat conservative.

Cammaert and Tsinker (1981) developed a simple model to calculate large ice floe and iceberg impact forces on structures. The model was based on kinetic energy dissipation through crushing of the ice feature. For constant impact velocity, ice strength and assuming an added mass

coefficient of 0.5, the model was used to calculate the impact force arising from iceberg collisions with cylindrical and conical gravity platforms. Cammaert et al. (1983) examined the influence of contact face and the effect of variable crushing strength varying with strain rate and penetration depth on the iceberg impact forces on a gravity platform. Depending on the impact velocity, the iceberg ice will fail at different strain rate which will affect the ice crushing strength. Jones et al. (2003) conducted uniaxial compression tests of iceberg ice samples over a wide range of strain rate 10^{-8} to 10^{+1} s^{-1} at -10^{0} C. Figure 2.13 shows the peak stress against strain rate for the measured data. Strength increase followed a power-law when the strain rate is less than 10^{-4} s^{-1}, almost constant at 4 MPa in between 10^{-4} and 10^{-1} and again rises to about 10 MPa at 10^{+1} s-1.

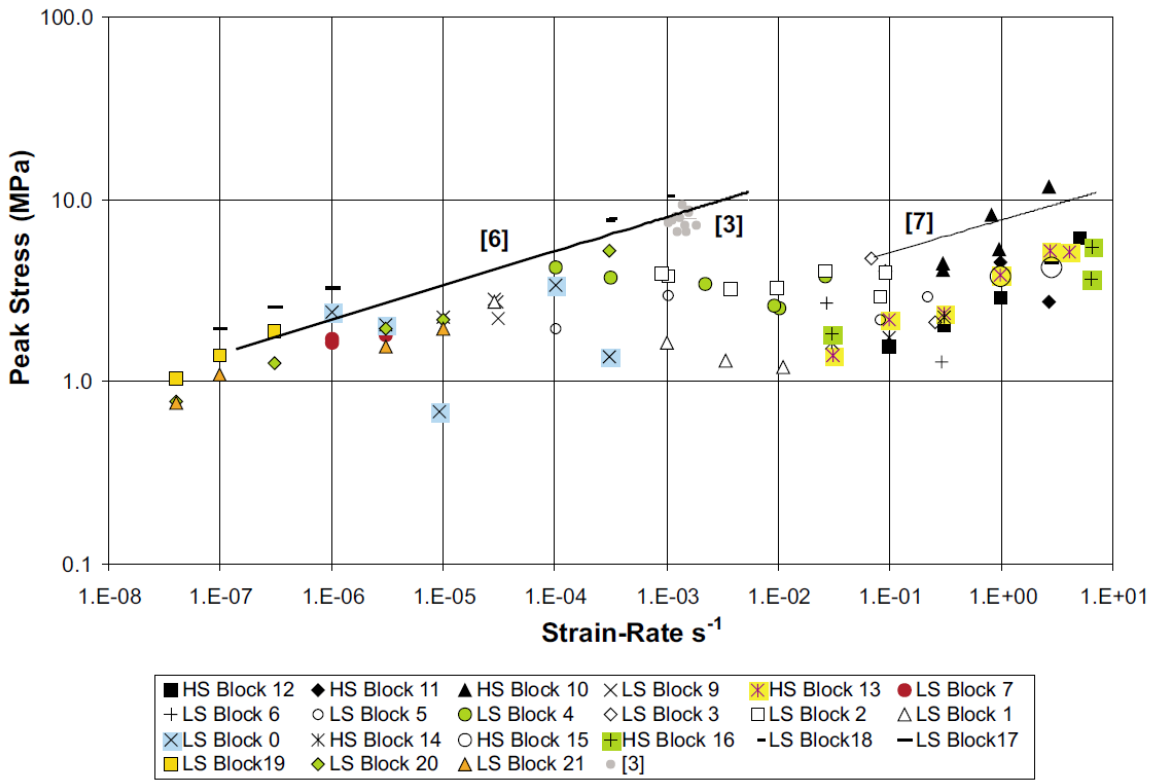

Figure 2.13: Peak stress versus strain rate, HS and LS indicates high speed and low speed machine respectively (after Jones et al. (2003)).

Swamidas and Arockiasamy (1984) developed a numerical model to calculate the forces exerted on a gravity platform from an iceberg impact. Both central (cylindrical crushing interface) and non-central (combination of crushed and rotated interfaces) were considered assuming only surge motion at the impact interface. The constant hydrodynamic coefficients were collected from published data and ice strength was assumed constant. Non- central impacts caused larger forces when both surge and yaw velocities were included at the impact interface. Swamidas et al. (1986) investigated the structural integrity of a semi-submersible and a GBS subjected to iceberg and bergy bit impact through experimental and numerical studies. The added mass coefficient for the bergy bit was assumed as 0.5 and all the analyses ignored effects of wave forces. Besides structural stiffness, the impact force was also found to be almost proportional to impact velocity and to the square root of the ice mass.

Johnson and Nevel (1985) developed an energy based mathematical model to estimate structure design load for ice impact. Assuming constant ice strength, rigid structure and head on impact, the design loads were estimated using a Monte Carlo simulation and statistical input distributions. The added mass coefficient was taken as 0.5 and no force variation during the collision period was obtained.

Bass et al. (1985) developed a horizontal plane three degree of freedom math model for iceberg collisions in calm water. The model included both non- eccentric (kinetic energy absorbed by ice crushing) and oblique (kinetic energy absorbed by ice crushing and induced yaw motion) impacts of icebergs with variation in underwater profile. The effects of various parameters such

as: impact velocity, iceberg vertical profile, offset, and added mass coefficient; on peak force were investigated. A change in added mass coefficient from 0.5 to 2.5 caused a 50% increase in peak force and collision duration for a central impact.

Gershunov (1986) developed analytical equations for ice kinetic energy, ice indentation and global ice load arising from an ice feature collision with a structure, using energy balance criteria. Introducing "limit-momentum", the author defined critical velocity as the velocity required to gain full indentation of the structure into the ice. The author emphasized the uncertainty of estimated added mass coefficients and chose a range of values from 1.2 to 1.8. Bolen (1987) emphasized the wave effects to be considered during iceberg impact analysis. The hydrodynamic effects were categorized as cushioning (reflected waves creating negative wave drift force in the vicinity of the structure, causing reduced iceberg approach speed), shadowing (structure in the shadow of the iceberg causing reduced wave load to the structure) and transmission (iceberg and structure in physical contact causing increased wave load on structure because of the transmitted wave load from iceberg). The author made simplified assumptions to account for these hydrodynamic effects. The inclusion of added wave loads caused a moderate to large increase in iceberg impact loads.

Holthe (1989) developed a time domain dynamic model for iceberg- structure interaction. The added mass of the iceberg was taken as 50% of its mass and the impact velocity as 0.3 m/s. A simple ice force model was used with uniform and radial static ice pressure, no elastic deformation and fixed point of interaction. No hydrodynamic interaction effects were included in the model. Duthinh (1989) utilized an analytical model to identify influential factors for iceberg impact load estimation. Impact velocity and indenter shape were found to be the most significant factors. Ice strength was also important, especially at large contact areas. Most

collisions occurred at rates in the brittle range but maximum impact load during the final stage may be affected by variation of ice strength with reduced strain rate. Load attenuators helped to mitigate impact load by slowing iceberg velocity and thus decreasing its kinetic energy.

Johnson and Prodanovic (1989) presented four different math models to calculate global impact forces during iceberg collision considering different levels of eccentricity. A comparison of results using different methods was presented. The preferred approach (method IV) considered the kinetic energy lost in ice crushing and rotation of the iceberg.

Matskevitch (1997a) emphasized the effect of eccentric impact of an ice feature with a rigid structure. The maximum impact load was reduced by almost 50% for an eccentric impact of an elliptical cylinder with a rigid wall. Matskevitch (1997b) further developed a non-linear numerical and analytical model to incorporate an ice failure pressure-area curve. This resulted in a reduction of the effect of impact eccentricity on the maximum ice load. Constant added mass terms were used in both the linear and non-linear models.

Fuglem et al. (1999) used probabilistic methods to determine iceberg design loads for a GBS and an FPSO considering random variables iceberg population, water depth, iceberg management, impact velocity, iceberg shape and ice failure strength. Open water iceberg velocity was considered as impact velocity. The analytical model developed by Matskevitch (1997b) was modified to include rotation about three principal axes. Hydrodynamic interaction effects were ignored and a constant added mass factor of 0.5 was used for both rotation and translation.

Brown and Daley (1999) developed a collision model in Working Model 2D software to simulate a transverse collision between a stationary ship and a spherical iceberg moving towards a ship with constant velocity. The collision forces were obtained using different pressure-area

relationships in the model. The authors recommended inclusion of wave motions and hydrodynamics with viscous fluid damping in future work.

Timco (2011) analyzed various field trial and laboratory test data for ice floe impact on structures. The impact force was found to be best related to the kinetic energy of a floe during impact and an empirical equation was developed. This equation shows that the impact force is approximately proportional to the square root of ice mass and directly to velocity. Extrapolated data from laboratory tests were found to over predict full scale data.

Jordaan et al. (2014) utilized a probabilistic methodology using Monte Carlo Methods to determine global and local iceberg impact loads on an FPSO following ISO 19906 guidelines. Quasi- static and dynamic iceberg design loads were obtained considering a number of factors including the influence of pack ice, effects of floater inertia, and mooring system compliance. Open water wave induced iceberg velocity was used in the analysis and no hydrodynamic interaction except added mass was taken into consideration in close vicinity of the structure.

Mravak et al. (2009) considered both external and internal mechanics during an iceberg collision with a turret moored FPSO. The external mechanics assumed that the entire kinetic energy of the collision is absorbed by the mooring system. The example problem produced low additional tension forces in mooring lines. Internal dynamics were analyzed using the finite element software Abaqus and considered the iceberg as rigid body without any ice crushing effect. A constant drifting speed was considered for global and local load analysis throughout the collision process.

Gao et al. (2014) conducted a sensitivity analysis to investigate iceberg geometry shape effect in the ship-iceberg collision process. The authors also investigated the effects of impact velocity

and entrapped water effect during interaction. It was suggested to consider damping and hydrodynamic pressure effects for further analysis.

Liu and Amdahl (2010) presented a six degree of freedom model for the external mechanics of a ship collision. This model was applied to assess the energy dissipation during ship-iceberg collision. An oil tanker with a speed of 4.5 m/s collided with a resting simplified cone shaped iceberg and an added mass value of 0.5 was used for the iceberg. The sensitivity analysis of the uncertain added mass factor showed considerable influence in the normal direction of the tangential plane. Liu et al. (2011) presented another numerical model mainly focusing on the internal mechanics of iceberg collision with a foreship structure. The dissipation of energy was determined by iceberg and ship masses and the relative velocity between them. The evolution of contact pressure and corresponding deformation of iceberg and ship were studied without considering hydrodynamic interaction effect prior to impact. Bøhlerengen (2013) included inhomogeneity (stochastic variation of material parameters to produce hard and weak zones) in Liu's (2011) material model. Bøhlerengen's (2013) model gave better results during early stages of impact, especially the local pressure distribution and the location of high pressure zones were better estimated. The new model also produced more structural damage to the panel compared to Liu's (2011) homogeneous material model.

Gagnon and Wang (2012) performed numerical simulations of a tanker collision with a bergy bit using LS-DYNA and its ALE formulation. The numerical model included hydrodynamics (calm water), a crushable foam ice model and a collision model sustaining deformation and damage. The model generated realistic motion of the bergy bit caused by the bow wave generated by the tanker and the damage to the structural grillage resembled the results of laboratory experiments.

Figure 2.14 shows numerical simulation results of grillage damage (left) and interface pressure distribution (right) during iceberg collision.

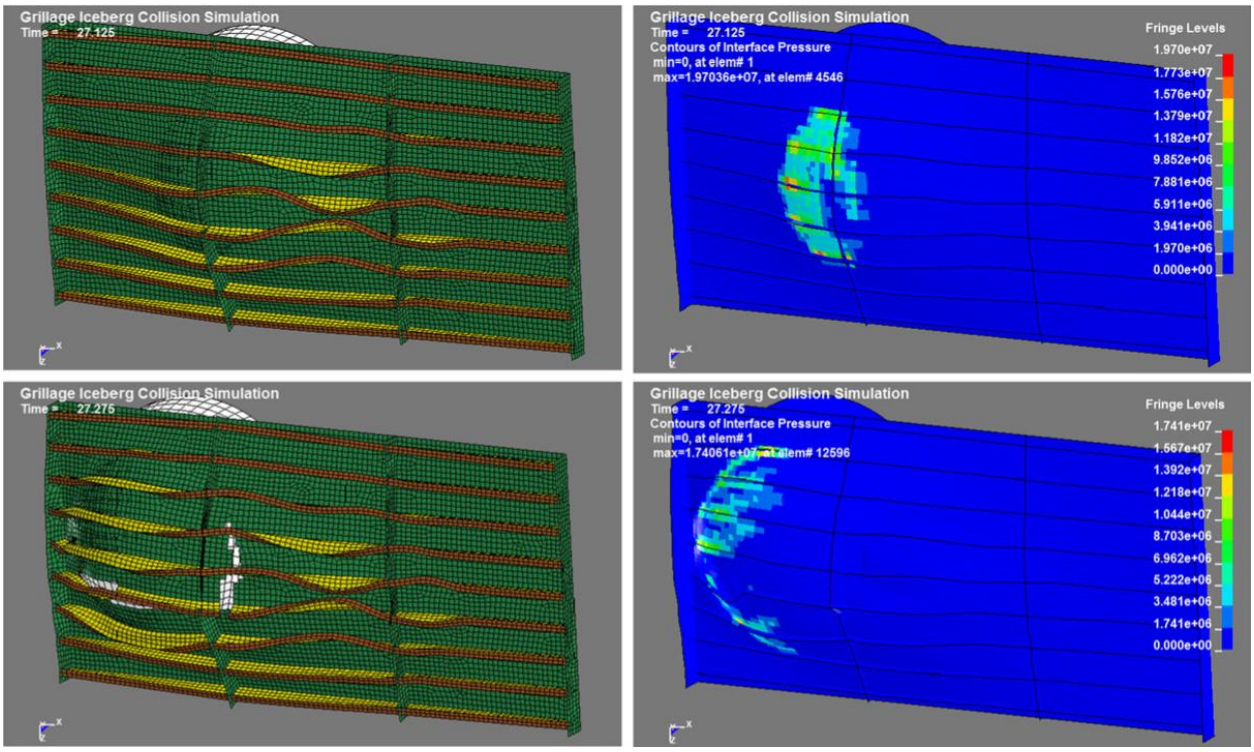

Figure 2.14: Numerical simulation of grillage damage with iceberg collision (after Gagnon and Wang (2012))

2.8. Multi-Body Hydrodynamic Interaction Studies

Hydrodynamic interaction between multi-bodies has been a challenging research topic for decades. It is relevant to various offshore activities such as side by side or tandem offloading, vessel replenishment, multiple vessel operation during installation, multiple wave energy converters etc. Conventional practice is to use potential flow codes to assess multi-body interactions, but this does not account for viscous effects. Typically problems arise in predicting

resonant free surface elevations in gaps between multi-bodies, but there has been some progress made.

Huijsmans (2001) introduced a rigid lid approach in between free surface to reduce unrealistic wave elevations in the gap. Pauw et al. (2007) conducted model tests with one LNGC close to the tank wall assuming symmetry to study interaction between side by side floating bodies. The experimental results were compared with a diffraction code based on the epsilon damping lid method, originally developed by Chen (2005). The results revealed that the tuning of the damping parameter has greater effects on second order drift forces than on first order quantities and a unique value cannot be determined to give results for smaller gaps.

Bunnik et al. (2009) modified the damping lid method by adding damping not only in the free surface between the vessels but also on the bodies. A rigid lid on the bodies require high grid resolution and use of a damping lid instead of the rigid lid improved the results of wave elevation and low frequency forces when compared to model test data.

Zhu et al. (2005) investigated the influence of gap width, gap length and gap depth on resonant wave forces between two three dimensional box shaped floating structures using potential theory. Strong interaction effects were observed and sharp peak forces varied in both magnitude and frequency shift influenced by the gap dimension. The numerical results showed that the peak forces may reach about ten times those on well separated bodies or isolated body wave forces at some frequencies for small yet finite gaps. This indicates important point to be considered during iceberg-structure interaction since icebergs have considerable draught.

Ali and Khalil (2005) also investigated hydrodynamic interaction of several free floating cylinders using potential theory. Strong interaction for surge mode was observed for head sea condition compared to heave and pitch mode.

Kristiansen and Faltinsen (2009) used two dimensional linear and non-linear boundary element methods to study resonant piston-mode behavior of water motion in the gap between a LNG carrier and a terminal in shallow water. The authors compared the results with experimental data and found that both linear and non-linear potential theories over predict the gap kinematics, although non-linear results are better.

Wang and Wu (2010) used the finite element method to investigate non-linear interactions between incident waves and an array of vertical bottom mounted and truncated cylinders. The method captured the effect of trapped mode for small amplitude waves. The authors also found that the increase of wave amplitude reduces the relative importance of the trapped mode.

Hong et al. (2013) introduced nine node discontinuous higher order boundary element method based on conventional two-body formulation (9dHOBEM) and constant boundary element method based on the boundary matching formulation (BM-CBEM) to study the gap resonance of two floating bodies side-by-side in close proximity. Significant improvement in predicting first order hydrodynamic coefficients and repulsive drift forces was obtained by BM-CBEM method combined with free surface damping and 9dHOBEM combined with the wetted surface damping.

Huang et al. (2014) conducted specifically designed model tests to identify transient hydrodynamic forces on the buoy and complex interaction between the buoy and hull during disconnection for a disconnectable turret-moored FPSO. Three types of heave oscillation (oscillation about mean position at various depths, descending motion with and without

oscillation) were conducted with the buoy itself and with buoy plus FPSO. Good results were obtained using the diffraction analysis code WAMIT, except for the cases of very close proximity (vertical offset of 0.167m, model scale of 1:30) between the buoy and the hull. For those cases CFD simulations using Flow3D were performed and good agreement was obtained. The authors suggested estimating the range of added mass variation through experimental and CFD studies for close proximity hydrodynamic force calculations.

Recently Zhou et al. (2015) conducted experiments with two box-shaped floating bodies with various gaps and wave environments and compared data with two potential flow codes – the panel method based code WAMIT and the panel free method based code MAPS0. The numerical motion RAOs showed good agreement with experiment but over predicted wave elevations in the gap.

With regards to ice-structure interaction, the International Standard ISO 19906 states: "Hydrodynamic effects associated with ice feature motions in the vicinity of the structure can be considerable, especially in conditions where the ice concentration is low and relatively small ice features are impacting wide structures. Due to hydrodynamic effects, smaller ice features can slow down as they approach and tend to move around the structure. Consideration should be given to added mass of the impacting ice feature, with due account for the presence of the seabed and the structure. When the structure moves sufficiently during the course of the interaction, its added mass should also be considered."

Current normal practice is to use a constant added mass coefficient of 0.5 for the impacting ice feature. Several researchers identified changes in added mass as the separation distance gets closer. There also exists the concept of negative added mass which occurs when the water

motion is produced by the oscillating body and the associated potential energy is larger than the kinetic energy (Falnes (1983)).

Mciver and Evans (1984) investigated negative added mass for the heave oscillation of bottom mounted submerged vertical cylinder. The authors mentioned that the added mass becomes negative if the depth of submergence is small and free surface effects are significant.

Chwang (2003) reviewed hydrodynamic interaction between two bodies for central, oblique and rotational impacts. The author claimed that the added mass coefficient should be a function of the relative position of the two bodies. Additional added mass terms associated with two body interaction were included for the potential flow model. Results of a test case where a rectangular cylinder centrally approaches a fixed circular cylinder showed that the added mass coefficients and force on the fixed cylinder increases drastically when the separation distance becomes smaller.

Zhou et al. (2005) investigated shallow and narrow water effect on two-dimensional cylinders of semi-circular, rectangular and triangular cross-section. Significant increase in added mass was obtained because of the stronger flow patterns induced by bottom and side walls. The shallow water effect on sway added mass was stronger than on heave whereas the narrow water effect on sway was weaker than on heave. Both effects were stronger for the rectangular section and weakest for the triangular section because of difference in area.

Lewandowski (2008) examined hydrodynamic interaction of two side-by-side rectangular barges using two and three-dimensional potential flow theory. The author mentioned that the standing waves in between the hulls (sloshing mode) causes significant changes in hydrodynamic forces with damping behaving like a delta function and added mass having a high maximum and a low

(usually negative) minimum. The linear potential theory was able to predict maximum wave amplitude at pumping mode (water surface moves vertically with horizontal surface) but failed to predict free surface in sloshing mode because of the inherent inviscid theory.

Lu et al. (2010) developed a two-dimensional viscous flow model based on the finite element solution of Navier-Stokes equations and free surface is captured using CLEAR-Volume of Fluid method. The numerical results of viscous model agreed well with experimental data. The authors found that both potential flow and viscous flow models can predict the resonant frequency at narrow gaps but the wave height at frequencies near the resonant frequency is significantly over-predicted by potential flow model. However, the potential flow model with a properly tuned damping coefficient can provide satisfactory predictions of resonant wave height and horizontal wave forces.

Lu et al. (2011) investigated the effects of body geometric dimensions and gap width on the artificial damping coefficient used in potential flow model. The authors found that the damping coefficient is not sensitive to the variation of gap width, body draft, body number and body breadth ratio and a value in the range of 0.4 to 0.5 can predict the resonant wave height close to experimental data.

Kristiansen and Faltinsen (2012) developed a two-dimensional numerical hybrid method by coupling Navier-Stokes solver with potential theory. The full domain is decomposed (Figure 2.15) and the CFD domain is fully submerged while free-surface is captured by potential theory. The authors validated the code against two-dimensional moonpool experiments. Kristiansen et al. (2013) applied the three-dimensional potential viscous code (PVC3D) to study the gap resonance inside the moonpool and validated against experimental data. The numerical results

showed good agreements with model tests. This method allows parametric studies due to low computational time.

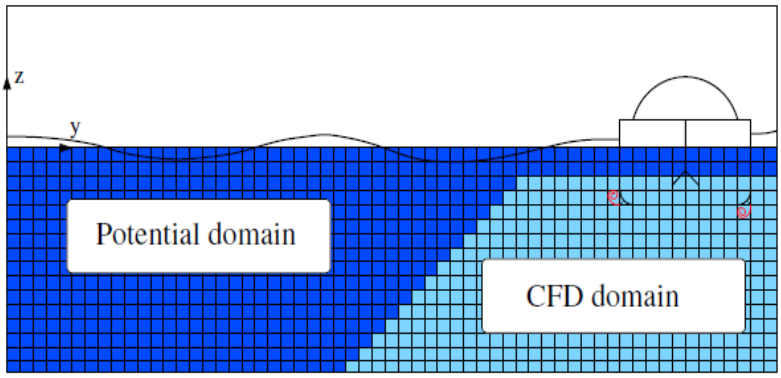

Figure 2.15: Full computational domain using Hybrid method (after Kristiansen et al. (2013))

Subodh et al. (2015) conducted experimental and numerical studies to investigate the kinematics of submerged ice collisions. The ice model was released from different depths and moved solely due to buoyancy and collided with a plate on the free surface. The model initially travelled in a straight line but small lateral motions were observed as the model approached the plate. The authors calculated added mass from experimental velocity and acceleration of the ice model and found a sudden increase of added mass prior to impact reaching maximum at the time of impact. The commercial CFD model Flow3D provided excellent results when compared with experimental data.

Bai et al. (2017) compared the experimental results of McGovern and Bai (2014a) with linear potential flow model HydroSTAR© and viscous flow CFD model OpenFOAM©. The comparison showed that the surge and heave RAOs are overestimated by linear flow model whereas the CFD results showed reasonably accurate comparison with experimental data.

Besides mass of the iceberg, impact velocity and added mass are the two parameters which will govern iceberg impact load based on kinetic energy or momentum methods. As discussed in this section, the added mass of the approaching iceberg clearly undergoes significant changes but needs further investigation to determine the effect on ice-structure collisions.

2.9. Numerical Simulation Using Commercial Software

To date, there has been at least one successful study of the ship-iceberg collision using commercial simulation software where hydrodynamic interactions between the ship and ice were modeled; and both the ship and ice were modeled as deformable bodies (Gagnon and Wang (2012)). This study employed the arbitrary-Lagrangian-Eulerian (ALE) formulation in LS-Dyna (LSTC). Similar to this study and earlier work by Gagnon and Derradji-Aouat (2006), Song et al. (2015) have used the ALE formulation in LS-Dyna to model a towed bergy bit (deformable body) impact with a target structural panel (rigid body). Their goal is to extend this work to include deformation of the structure as well.

All of these works were conducted in calm water. For the work of Gagnon et al. (2006, 2012), the ship was accelerated from rest at a sufficient distance from the bergy bit such that the impact event occurred under steady-state hydrodynamic conditions (e.g. the ship's bow-wave was fully developed). Similarly, Song et al. (2015) accelerated the ice from rest from a sufficient distance, but ceased prescribing its velocity just prior to impact (as fitted this impact scenario).

Both works were benchmarked in various ways. Gagnon et al. (2006, 2012) benchmarked their "crushable foam" material model against field and laboratory experiments; and benchmarked the bergy bit sway simulation results against full-scale sea trials data. Song et al. (2015) also benchmarked their simulation results with experimental data, but also by comparing the added

mass predicted by the ALE model with those predicted by WADAM (a code based on potential theory). Both works concluded that reasonable results were achieved.

The work of Gagnon et al. (2006, 2012) and Song et al. (2015) show that fluid structure interaction (FSI) by the ALE method is a viable solution for simulating the deformable ship-ice interactions involving hydrodynamic effects.

2.10. Conclusions

Iceberg/bergy bit impact load with fixed and floating offshore structures is an important design consideration for structures in ice- prone regions. A considerable volume of work has been directed towards the problem. It is clear that prediction of ice impact loads depend strongly on the velocity at impact and that this velocity depends on the hydrodynamic forces at play just before impact. It is evident from the literature that the complex hydrodynamic interaction between the iceberg and structure, just before impact has effects on impact force estimation by changing added mass, impact velocity, or impact trajectory. Some of these effects, such as wave reflection, increasing pressure, trajectory changes and viscosity, may act to decrease, or mitigate the load, while other effects such as incident wave forces or added mass may act to increase the load. These effects have been touched on by many studies but have not been comprehensively brought together. Several studies have noted that impact velocity can be substantially reduced and several phenomena like fluid cushioning, shadowing, eccentric impact etc. have been reported because of reflected and standing waves (Bolen (1987), Colbourne et al. (1998), Colbourne (2000), Gagnon (2004b)) In all these cases the effects of the hydrodynamic interaction have been identified in a qualitative sense but there is a dearth of quantitative information on either magnitudes or even the relative importance of the identified effects. The

consequence of this is an inability to estimate the effects of near-field hydrodynamic interactions on the approach velocity for small ice masses.

It is somewhat surprising that there is only one study (Bai et al. (2017) was found in the literature where RANS based CFD codes were used to study ice floe drift in regular waves. CFD is one method where wind, wave and current forces could be combined in a single numerical domain. The limitations in the application of this method may be in the number of cells required to model all the effects and the lack of accurate geometry data for the icebergs. Both of these may make the method impractical with the current state of the art.

Collisions do not occur in an instant, they occur over a time period. And in water they occur within a hydrodynamic environment that developed prior to contact and that continues to evolve during the collision. Moreover, incoming and reflected waves from structure make this interaction more complicated. Impact velocity can be considered as one of the key factors since it will govern how much energy is involved during collision and then dissipated throughout the collision period. The far field velocity of ice masses has been well studied using a number of different approaches from statistical through to potential flow models. Near field cases have been less well studied.

For structures transparent to waves like semi-submersibles, iceberg impact velocities predicted by open water test data are reported to be reasonable (Lever et al. (1988b, 1990b)), but for less transparent fixed or floating offshore structures like GBS or FPSO, the proximity effect has been noted to be significant but no work has been reported regarding hydrodynamic interaction in the very near field region for either type of structure.

Because the collision force is so dependent on impact energy and the energy is largely dependent on final velocity, knowledge of effects that influence the final velocity is important to improved load predictions. Another factor is the rate dependence of ice failure. Generally iceberg- structure collisions are anticipated to occur at velocities that place the ice in the brittle failure region, but lower impact velocities might cause the ice to fail in the ductile or transition regions (Cammaert et al. (1983), Johnson and Benoit (1987), Habib et al. (2014)). Sodhi and Haehnel (2003) also emphasized that effective pressure will depend on the indentation speed and compliance of the structure and an increase in indentation speed will cause the ice failure mode to transition from ductile to brittle causing a decrease in effective pressure. The nature of ice material properties indicates that the impact velocity and the progression of velocity during the impact will influence the magnitude of the load; thus, it is important to be able to predict both the initial velocity and the changes in velocity as a collision proceeds.

The load transmitted to the structure is influenced by the orientation of the collision, with eccentric, off axis and rotational effects, all acting to reduce the load. This was observed in most of the free drift experiments (e.g., Isaacson and McTaggart (1990c), Salvalaggio and Rojansky (1986)). A significant reduction in maximum ice load will occur with eccentric impact compared to head- on collisions because of the transfer of energy to rotation rather than crushing. Eccentric impacts occur more frequently, resulting in significant contribution to design ice load (Matskevitch (1997a, 1997b), Fuglem et al. (1999)). The evidence from the studies reviewed here shows clearly that these parameters are strongly affected by the near field hydrodynamic properties and thus these properties have an indirect but important influence on the impact loads.

It is evident that most current studies have not been able to fully consider the hydrodynamic interaction just prior to collision. The hydrodynamic effect most often considered was added mass through the use of constant coefficients. There is not a good estimate of the effective added mass of an ice berg during an impact, with estimates for the added mass coefficient ranging between 0.5 and 1.8. There is however strong evidence that as the iceberg approaches the structure, the added mass changes to accommodate the surrounding fluid acceleration (Cheung (1987) and Isaacson and Cheung (1988b), Chwang (2003)). The value of the added mass is shown to have a large influence on the estimation of impact load (Bass et al. (1985)).

It is clear that the ratio of iceberg size to structure size is also an influential factor. It has been noted that if the ice mass diameter is less than half of the structure diameter, the ice mass will not hit the structure because of negative wave drift forces (Salvalaggio and Rojansky (1986), Isaacson and McTaggart (1990a, 1990b)).

In conclusion the prediction of ice impact forces is currently limited by lack of knowledge of the near field hydrodynamic effects and could be improved through a better understanding of the influence of hydrodynamic properties in the very near field interaction. It is likely that reflected waves and hydrodynamic damping leading to reduced impact velocity, and off axis forces leading to iceberg rotation and eccentric impact should be considered in iceberg-structure impact analysis. An inability to quantify these effects results in uncertain predictions of impact load which will ultimately affect the design and cost of the structure. It is expected that improvements could come through modeling and inclusion of the effects of: changes in added mass effects (or hydrodynamic pressure) as the gap closes, changes in wave drift force, possibly from positive to negative as the influence of the structure is felt, changes in linear wave forces as the gap reduces to sub wavelength distances and inclusion of viscous effects which may act independently or

influence the nature of the previously identified parameters. The authors of this study are currently developing a numerical and experimental program to model and assess the influence of hydrodynamic interaction of ice mass and offshore structure in very near field region.

Some recent numerical studies show good validation results of hydrodynamic behavior of floating bergy-bit subjected to collision (Gagnon et al. (2006, 2012), Song et al. (2015)), but all of these works were conducted in calm water. Wave driven iceberg and bergy bit interaction and impact with offshore structure is far more complex and there is still a lack of knowledge in this topic area (Tsarau et al. (2015).

Based on this review of the literature, the following gaps in the understanding of near field hydrodynamics were identified and form the basis of the present study. These are as follows:

1. Further information on wave forces and the change in wave forces as a structure is approached based on experiments.

2. Further information on the motions and the changes in motions as a structure is approached based on experiments.

3. Development of a non-dimensional expression to allow the proximity effects of wave forces and motions to be quantified for various relative sizes and scales of interacting ice masses and structures.

4. Assessment of viscous flow solvers ability to capture the proximity effects.

Chapter 3

Experimental Investigations

3.1 Experimental Investigation of Wave Forces at Different Proximity to a Fixed Structure in Regular Waves

Previous studies in the literature investigated the motions of free floating ice masses in open water or near a fixed / floating structure (Salvalaggio and Rojansky (1986), Attwood (1987), Lever et al. (1988a, 1990a, 1990b), Mak et al. (1990), Isaacson and McTaggart (1990a, 1990b, 1990c), Colbourne et al. (1998), McGovern and Bai (2014a, 2014b)). Various complex phenomena have been reported due to the near field hydrodynamic interaction between the ice mass and the structure. These experiments have often shown very little repeatability in the results and thus very little quantifiable information can be obtained. In this study an alternative approach has been taken where the ice mass was fixed at different proximity from the structure and the forces on the ice mass were measured. The objective is to investigate how the wave load on the ice mass is changed at different separation distances from the structure. This will help to understand the fundamental physics of the problem and obtain quantifiable data products as one of the key factors for the motions of free floating ice masses is the hydrodynamic loading acting on them.

3.1.1 Experimental Program

The current set of experiments involved measurements of wave forces on a fixed smaller body held at different distances from the fixed structure. In this case, we have directly measured wave forces on a stationary body with the emphasis on surge and heave forces as the body approached the structure. It is recognized that the motions and loads are not independent of each other. However it is challenging to measure forces and motions at the same time without having the measurements influence the results. These measurements were intended to provide a more direct indication of how the wave forces changed with separation distance and to provide further insights into how numerical models of the scenario might be developed and validated.

3.1.1.1 Facility

The experiments were conducted in the Towing Tank of the Ocean Engineering Research Center (OERC) at Memorial University of Newfoundland (MUN) in St. John's, NL Canada. The Towing tank is 58 m long and 4.5 m wide with maximum still water depth of 2.2 m. The tank is equipped with a hydraulically actuated wave board on one side and a wave absorbing beach on the other side.

3.1.1.2 Models and Instrumentation

A hexagonal aluminium cylinder of 0.5 m diameter was used as the fixed offshore structure. The scale ratio is nominally 1:50. Thus the full scale structure diameter is 25 m. Three spheres with diameters of 0.152 m, 0.203 m and 0.305 m were used to represent different size ice masses. The ratios of ice mass diameters to the fixed structure diameter are 0.3, 0.4 and 0.6 respectively.

A six component global force balance, referred to as the NSERC Global Dynamometer (McNeil (2011)) was used. The dynamometer consists of six load cells of 4447 N (1 in X-direction, 2 in Y-direction and 3 in Z-direction). Each individual load cell of the dynamometer was calibrated and reported by Mohammadafzali (2016). The predicted load by each load cell had less than 1% error. This dynamometer has been reliably used by several graduate students, for example Islam (2009), McNeil (2011), and Mohammadafzali (2016). A rigid adapter was fabricated to attach the sphere to the dynamometer without introducing vibration. Capacitance type wave probes were used to measure the wave profile of the incoming and reflected stationary waves. As part of a data quality check, before conducting experiments, both the dynamometer and the required waves were calibrated. Figure 3.1 shows the layout of the experimental set up in the towing tank with dimensions and coordinate system. The forces are considered positive in the direction of

wave propagation in the x-direction and positive downward in the z-direction. Figure 3.2 shows the experimental set up including the dynamometer, the fixed structure, and the large sphere attached by the adapter and the wave probe for reflected waves. In addition videos were recorded during experiments and digital still photographs were taken.

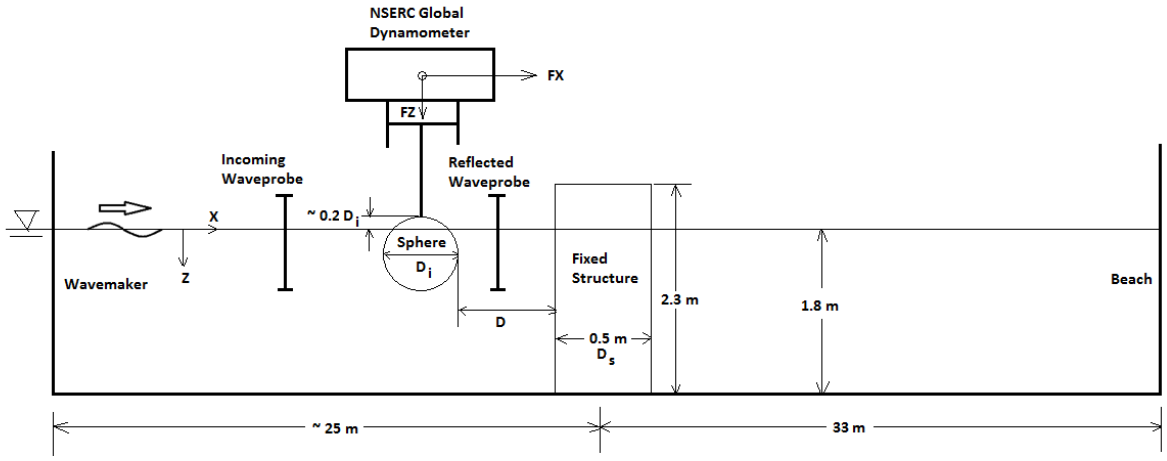

Figure 3.1: Schematic layout of the experimental set up in towing tank

Figure 3.2: Experimental Set up – Dynamometer, fixed structure and sphere $D_i/D_s = 0.6$

3.1.1.3 Environment

The towing tank water depth was 1.8 m. Six regular waves with two different wave steepness were selected with wave lengths as multiples of the fixed structure diameter and also to cover full scale wave periods of 7~10 seconds. The stroke limitation of the wave generator did not allow for waves with frequency greater than 1 Hz to be created. The wave particulars are given in Table 3.1.

Table 3.1: Regular wave particulars

	Wave Height, H (m)	Wave Period, T (sec)	Wavelength / Structure diameter (λ/D_s)	Wave Frequency, f (Hz)	Wave Steepness (H/λ)	Wave Period (sec), Full Scale
Wave -1	0.05	0.98	3	1.02	1/30	6.93
Wave -2	0.067	1.13	4	0.88	1/30	7.99
Wave -3	0.083	1.26	5	0.79	1/30	8.91
Wave -4	0.1	1.39	6	0.72	1/30	9.83
Wave -5	0.0875	1.06	3.5	0.94	1/20	7.49
Wave -6	0.1125	1.2	4.5	0.83	1/20	8.49

3.1.1.4 Methodology

The fixed structure model was placed in the tank and filled with water ballast. The structure was also clamped against a fixed cross-tank platform to avoid any movement. The sphere was mounted with the rigid adapter to the dynamometer and the draft adjusted to the required level of submersion to represent a nominal iceberg floating position. The spheres were ballasted with paraffin wax of density 870 $kg/m^3$to provide neutral buoyancy at the correct draft. When filled with wax, there was little gap on top inside the sphere and there was a small socket on top of the sphere which was used to attach the rod. Since these are captive tests, exact mass properties were not matched except that all models were ballasted so that the displacement is equivalent to a

similar sized piece of fresh water (glacial) ice. The submersion depth was approximately 0.2 times the diameter of the sphere from top of the sphere. Experiments were carried out for the spheres alone, and for each sphere at different separation distances from the fixed structure. Separation distance was based on multiples of the sphere diameter. Twenty steady state wave cycles were selected to analyze the data. Besides experiments in waves, several calm water cases were tested to measure the static load on the sphere and also the load of the adapter only. Several repeat experiments were conducted for data validation.

Froude scaling was used as this is the most suitable scaling law where surface waves are the dominant mechanism. All of the studies related to free floating ice masses and ice floes used the same scaling law (Isaacson and McTaggart (1990a), Lever et al. (1990a, 1990b), Mak et al. (1990), Colbourne et al. (1998), McGovern and Bai (2014a, 2014b) etc.). Also since three identical shapes of sphere of different sizes are tested, it is expected that Reynolds dissimilitude does not likely have an effect (Attwood (1987), Lever et al. (1988a), McGovern and Bai (2014a)).

The number of separation distances covered for large, medium and small spheres are six, five and four respectively. The closest distance to the structure for each sphere was determined by moving the carriage as close to the structure as possible, without the live end beam of the dynamometer touching the structure. This physical limitation restricted the ability to test spheres located very close to the structure. The details of distances tested along with the test matrix are shown in Table 3.2.

Table 3.2: Test matrix for force experiments

	No Structure			With Structure																
Separation (m), D D/D_i	∞	∞	∞	0.15 1	0.13 0.6	0.12 0.4	0.22 1.4	0.23 1.1	0.18 0.6	0.36 2.4	0.33 1.6	0.35 1.1	0.66 4.4	0.63 3.1	0.64 2.1	NA	1.04 5.1	1.25 4.1	NA	NA	2.04 6.7
Sphere (D_i/D_s)	0.3	0.4	0.6	0.3	0.4	0.6	0.3	0.4	0.6	0.3	0.4	0.6	0.3	0.4	0.6	0.3	0.4	0.6	0.3	0.4	0.6
Wave (λ/D_s)																					
3	x	x	x	x	xx	x	x	x	x	x	x	x	x	x	x	0	x	x	0	0	x
4	x	xx	x	x	x	x	x	x	x	x	xx	x	xx	x	x	0	xx	x	0	0	x
5	x	x	xx	x	x	x	xx	xx	x	x	x	x	x	x	x	0	x	x	0	0	x
6	xx	x	x	x	xx	x	x	x	xx	xx	xx	xx	x	xx	x	0	x	x	0	0	x
3.5	x	x	x	x	x	x	x	x	x	x	x	x	x	xx	xx	0	x	xx	0	0	x
4.5	x	x	x	x	x	x	x	x	x	x	x	x	x	x	x	0	x	x	0	0	xx

(D – Separation distance measured from sphere face to structure face, D_i – Sphere diameter, D_s – Structure diameter, λ – Wavelength, x – one test, xx – repeat tests, 0 – No test)

3.1.2 Results and Discussion

The data measured included time series of forces in x, y and z-directions from the dynamometer and the wave profiles from the wave probes. In analyzing the data time series of raw data of FX and FZ forces were selected after initial transient values had passed. Each data series contained at least 20 cycles of responses. Any static offset was removed to yield wave loads only. A Butterworth low-pass filter was applied to the raw data to filter out high frequency noise. Figure 3.3 shows two typical wave cases during the experiment.

Figure 3.3: Sphere ($D_i/D_s = 0.6$) during wave testing, wave direction is from left to right

3.1.2.1 Large Sphere ($D_i/D_s = 0.6$)

The time series of raw data of FX and FZ force for sphere $D_i/D_s = 0.6$ located at $D/D_i = 1.1$ tested in wave $\lambda/D_s = 5$ is shown in Figure 3.4. These results are typical in form for all the raw data collected during the experiments. Figure 3.5 shows the time series of FY force raw data for sphere $D_i/D_s = 0.6$ tested in calm water, wave $\lambda/D_s = 5$ at $D/D_i = 1.1$ and wave $\lambda/D_s = 3.5$ at $D/D_i = 2.1$. These results show mostly noise from the two load cells in y-direction each of which has 4447 N load range capacity. Since the waves were symmetrical about the centreline of the tank, the forces in y- direction were negligible and not analysed as part of the study.

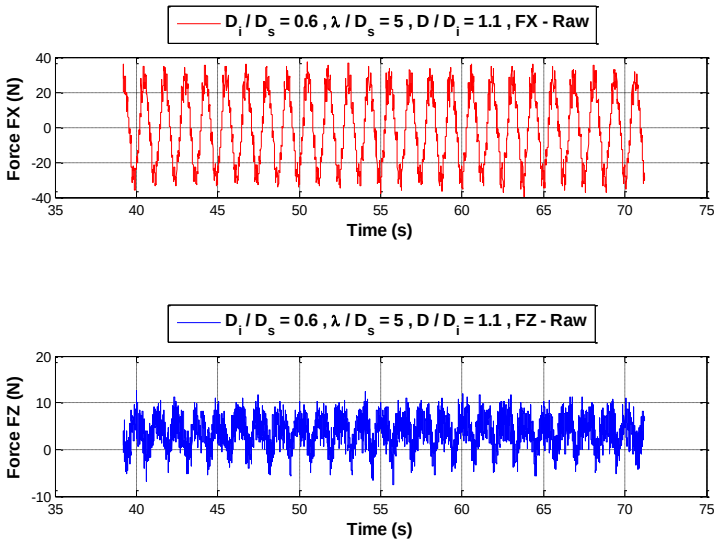

Figure 3.4: Time series of FX and FZ force raw data for sphere $D_i/D_s = 0.6$ located at $D/D_i = 1.1$ tested in wave $\lambda/D_s = 5$

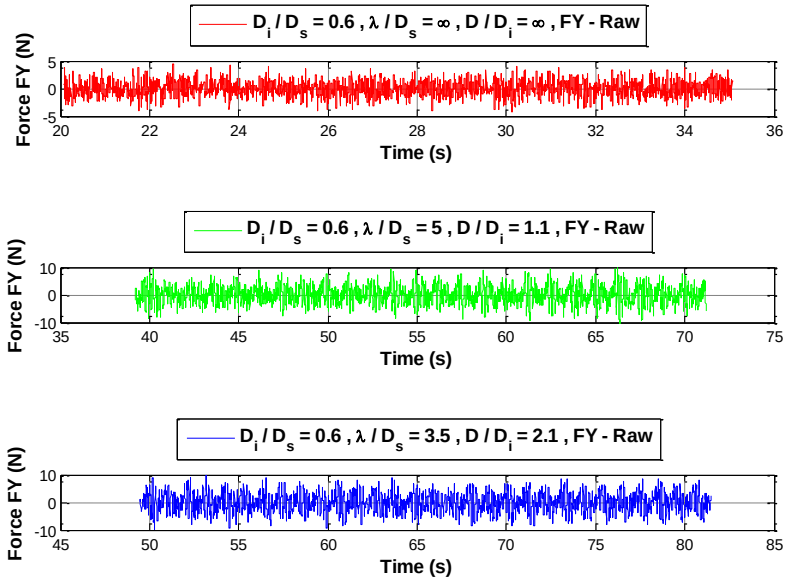

Figure 3.5: Time series of FY force raw data for sphere $D_i/D_s = 0.6$ tested in calm water, wave $\lambda/D_s = 5$ at $D/D_i = 1.1$ and wave $\lambda/D_s = 3.5$ at $D/D_i = 2.1$

Figures 3.6 and 3.7 show the steady state time series of filtered data of FX and FZ forces for sphere $D_i/D_s = 0.6$ for the no-structure case and the with structure case, for the sphere located at $D/D_i = 0.6$ respectively, both tested in wave $\lambda/D_s = 6$. It is observed that both force magnitude and profile changes with reduced proximity of the sphere to the structure.

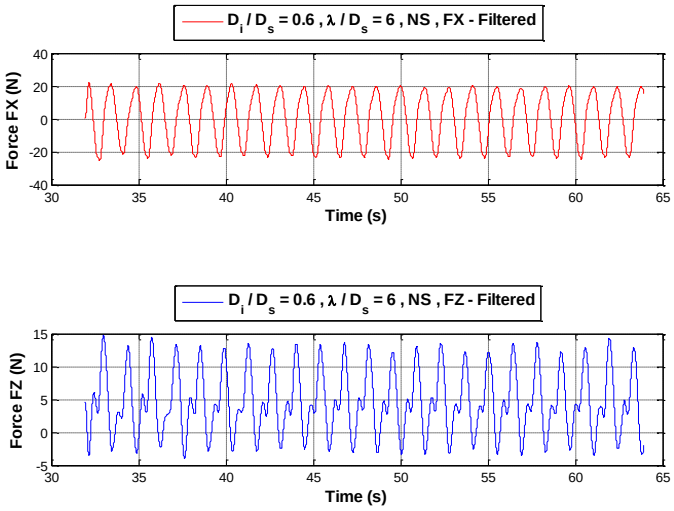

Figure 3.6: Time series of filtered force data for sphere $D_i/D_s = 0.6$ tested in wave $\lambda/D_s = 6$ at no-structure case

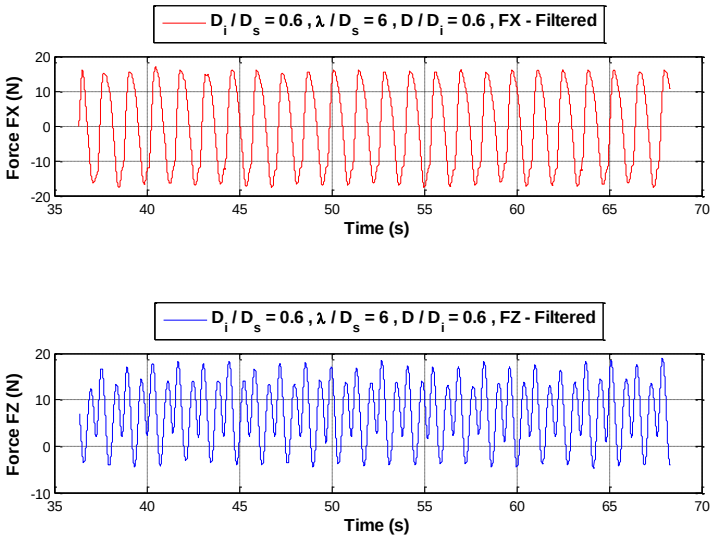

Figure 3.7: Time series of filtered force data for sphere $D_i/D_s = 0.6$ tested in wave $\lambda/D_s = 6$ at $D/D_i = 0.6$

Table 3.3 shows the RMS values of FX and FZ for the same cases. The RMS FX force has its lowest value at $D/D_i = 0.4$ which is the closest distance tested from the structure and has its highest value at $D/D_i = 2.1$. Also RMS values of FZ show their highest and lowest values at the same locations where RMS FX values are lowest and highest respectively. These results can be explained due to the standing wave formed by the superposition of incident and reflected waves. The corresponding D/λ values are also given in Table 3.3. The distance where RMS FX is lowest and RMS FZ is highest is at $D/\lambda = 0.04$ (close to $D/\lambda \approx 0$) where the standing wave profile will have maximum values of both the vertical velocity and the hydrodynamic pressure component. Also the distance where RMS FX is highest and RMS FZ is lowest is at $D/\lambda = 0.21$ (close to $D/\lambda \approx 0.25$) where the vertical velocity and hydrodynamic pressure component of the standing wave profile are zero.

Table 3.3: RMS forces for sphere $D_i/D_s = 0.6$ tested in wave $\lambda/D_s = 6$

D/D_i	D/λ	RMS FX (N)	RMS FZ (N)
∞	∞	15.48	6.72
0.4	0.04	10.67	10.01
0.6	0.06	11.85	9.78
1.1	0.12	15.46	7.89
2.1	0.21	19.93	5.02
4.1	0.42	14.64	7.5
6.7	0.68	16.61	6.31

This form of analysis and use of the RMS values were used for all the cases measured and the results are further reduced in the following graphical presentations.

Figure 3.8 shows the mean drift force FX for the sphere $D_i/D_s = 0.6$ at different separation distances and for different waves. It can be seen that when the structure was not present, the mean drift FX forces are all positive. The wave drift forces are generally lower than no-structure case. All these forces become negative at $D/D_i = 0.4$ and also at $D/D_i = 0.6$ except for wave $\lambda/D_s = 3$. This implies that as the body gets close to the structure, negative drift forces, against the direction of the waves, will be acting on the body. It is also noted that this mean value is very small compared to the first order wave loads of RMS FX forces acting on the body. Though small in magnitude, this mean drift force is important as it dictates the drift speed and direction of the iceberg and its potential to impact a structure. During impact, first order wave forces will dominate because the velocity of the small body is the sum of the first order and drift induced velocities. The first order forces and velocities tend to be an order of magnitude higher than the drift forces and velocities. Thus the proximity effects on the first order wave forces are of greater significance to the actual impact velocity for most cases.

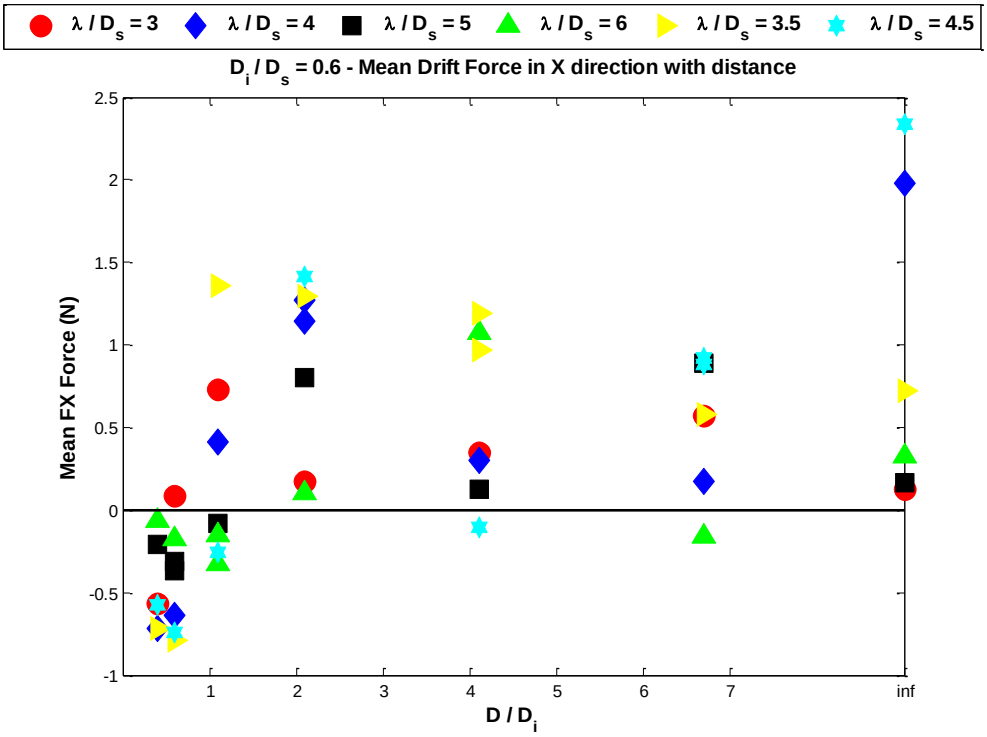

Figure 3.8: Mean drift FX force for sphere $D_i/D_s = 0.6$

Figure 3.9 shows the mean vertical force, FZ, for the same sphere at different locations and for different waves. It can be seen that the mean FZ forces are all positive for all waves and at all separation distances. The mean FZ forces act downwards for all cases with or without the presence of the structure. Thus the mean FZ forces will be acting downwards for all cases since the majority portion of the sphere is submerged. Also the mean FZ force tends to increase in magnitude as the sphere gets close to the structure.

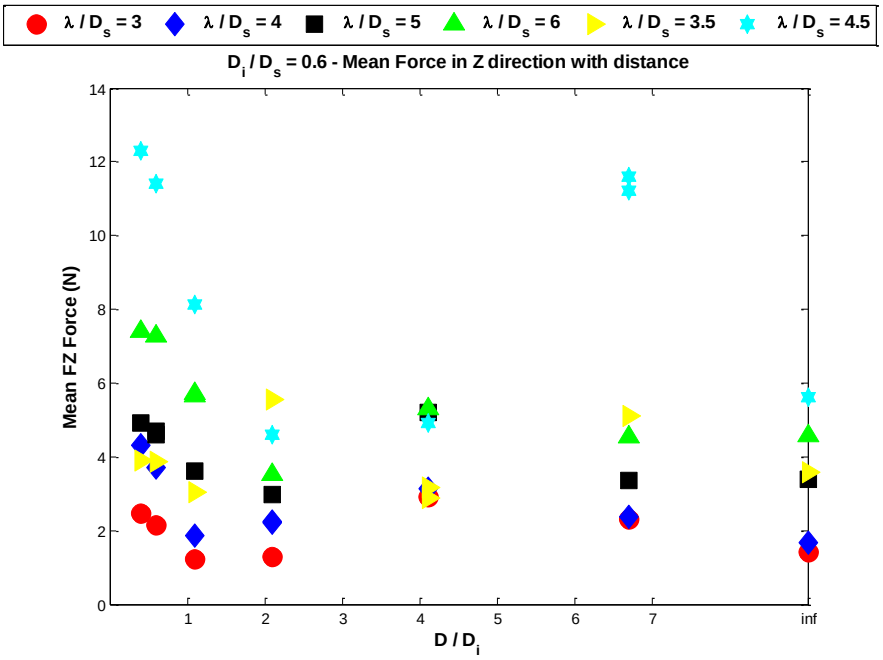

Figure 3.9: Mean drift FZ force for sphere $D_i/D_s = 0.6$

Figures 3.10 and 3.11 show the traditional non dimensional Force RAOs plotted against the diffraction parameter, Ka, where K is the wave number and a is the sphere radius. The forces are non-dimensionalized by $\rho g H a^2$, where H is the wave height, ρ is the water density and g is the acceleration due to gravity. The cases with no-structure are shown as red circles with dotted lines and the other distances are plotted with different colored symbols. As seen from these figures, the loads will vary depending on the separation distance from the structure, but there are no definite trends that can be derived from these plots. It is also noted that at the same location, the wave loads can be higher or lower for different waves compared to the no-structure cases.

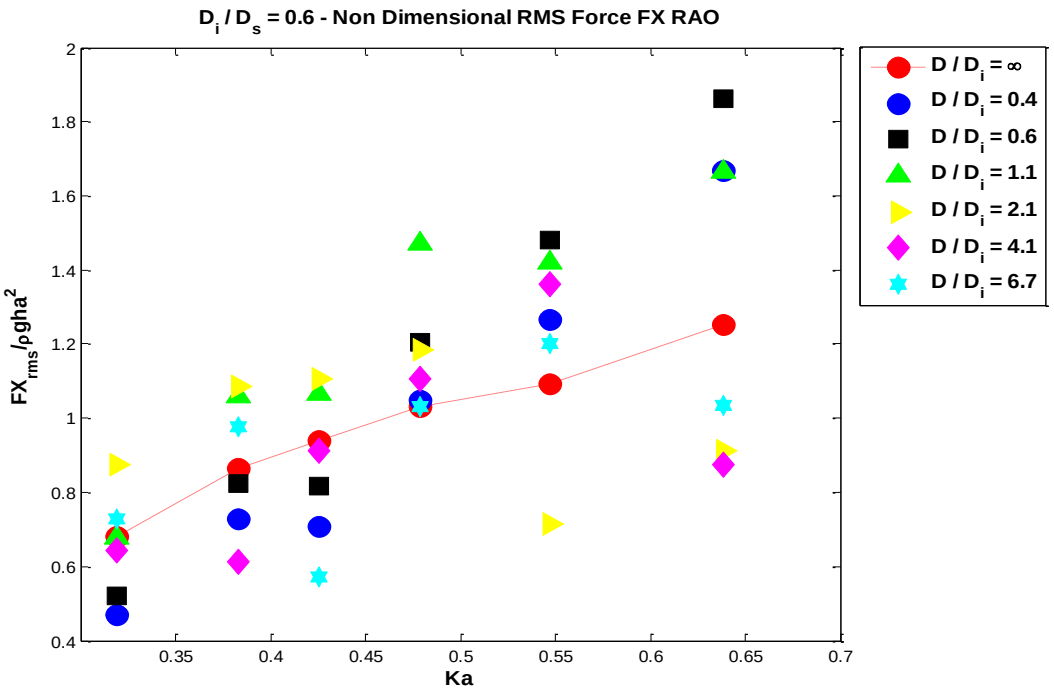

Figure 3.10: RAO for horizontal FX force for sphere $D_i/D_s = 0.6$

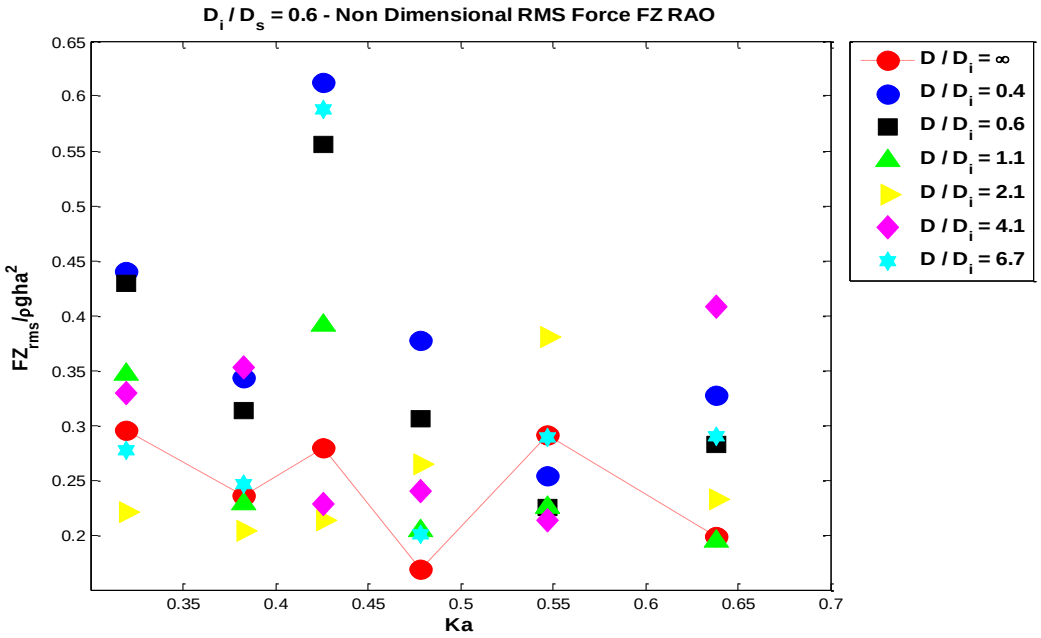

Figure 3.11: RAO for vertical FZ force for sphere $D_i/D_s = 0.6$

The initial approach to normalize the results was to consider separation distance as a fraction of the incident wavelength and to normalize the measured forces with respect to the forces measured with no structure present. These are plotted in Figures 3.12 and 3.13 for the sphere $D_i/D_s = 0.6$ for individual waves.

It is apparent from these plots that the relative wave loads depend on the parameter, D/λ , and the non-dimensional RMS forces against D/λ show an envelope type profile which is expected because of the superposition of incident and reflected waves. This indicates the importance of the separation distance on changing the forces acting on the approaching body. It also shows that separation distance must be considered in terms of incident wavelength. These plots also show that the force seems to be magnified for certain D/λ ratios although there is a general trend of reducing normalized force as the relative distance increases.

Another interesting point is that as the FX force decreases, the FZ force increases, which implies that although the approaching body will oscillate with lower amplitude in the surge direction, the energy will be transferred to Z direction, resulting higher heave oscillations. This may have implications for bergy bits approaching structures with overhangs just above the waterline resulting in increased risk of impact.

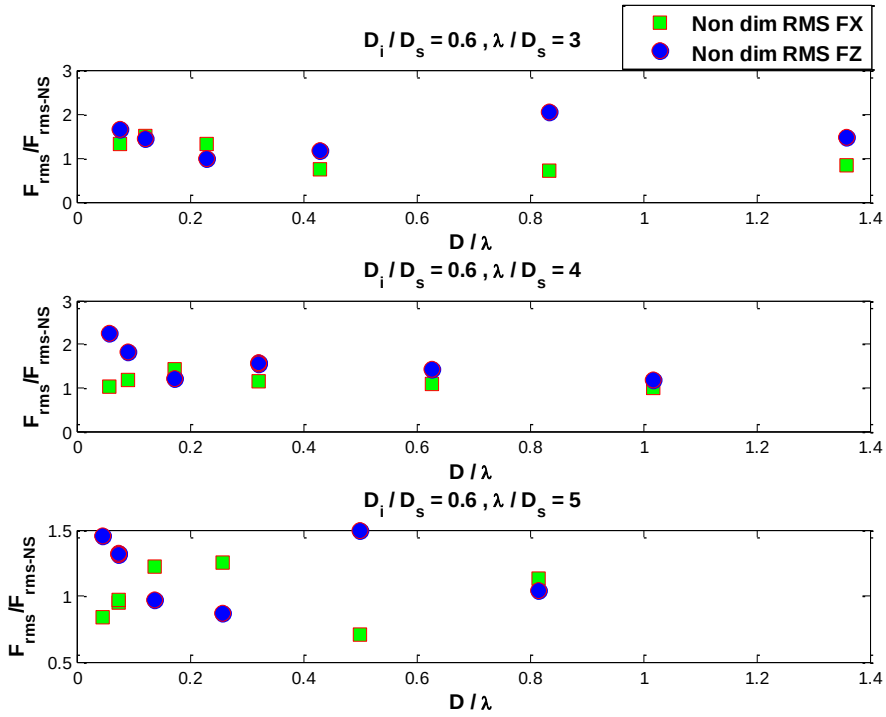

Figure 3.12: Non-dimensional RMS forces with non-dimensional separation distance (sphere $D_i/D_s = 0.6$, waves $\lambda/D_s = 3, 4, 5$)

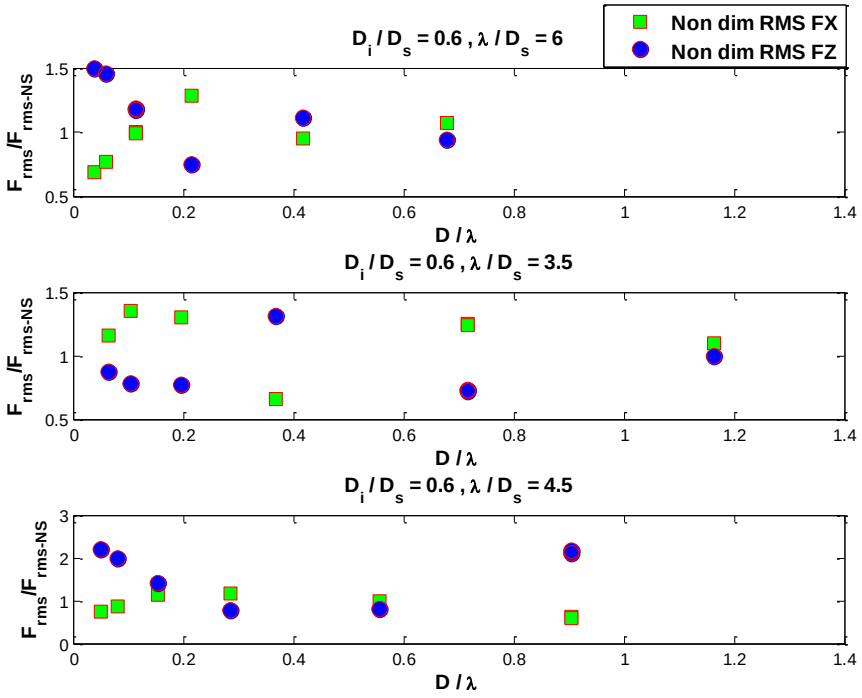

Figure 3.13: Non-dimensional RMS forces with non-dimensional separation distance (sphere $D_i/D_s = 0.6$, waves $\lambda/D_s = 6, 3.5, 4.5$)

A further collapse of the data can be achieved when the normalized RMS FX and FZ forces are further normalized by the relative separation distance and divided by D/λ. Figure 3.14 shows the results for the sphere $D_i/D_s = 0.6$ including the effects of wave steepness (H/λ), where H is the wave height. Four waves ($\lambda/D_s = 3,4,5,6$) of steepness 1/30 and two waves ($\lambda/D_s = 3.5,4.5$) of steepness 1/20 were tested and there is no discernible trend can be observed due to the effect of wave steepness.

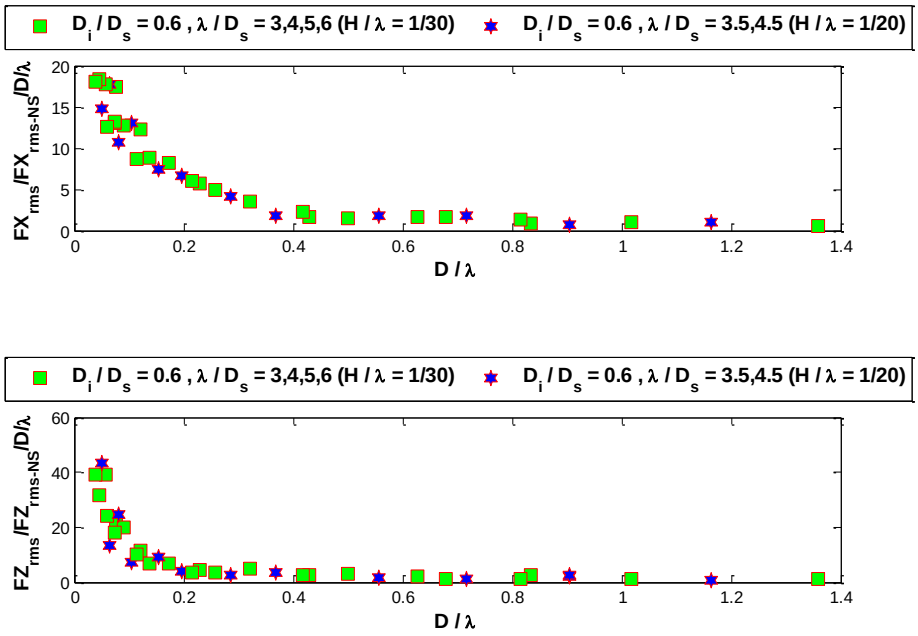

Figure 3.14: Non-dimensional RMS forces normalized by D/λ for FX and FZ for sphere $D_i/D_s = 0.6$

In a similar manner, if we divide the Force RAOs by D/λ for FX and FZ respectively, this distinguishes the effects of separation distances quite well. Figures 3.15 and 3.16 show the Force RAOs against Ka for different sphere locations. As the sphere approaches the structure the increases and decreases in FZ and FX with changes in wavelength become much more pronounced.

Overall as D/λ gets smaller or as the body gets closer to the fixed structure, the wave frequency FX force tends to go down and the FZ force tends to go up. This implies the oscillatory motions in surge direction will be reduced but at the same time the oscillatory motions in heave direction will be increased.

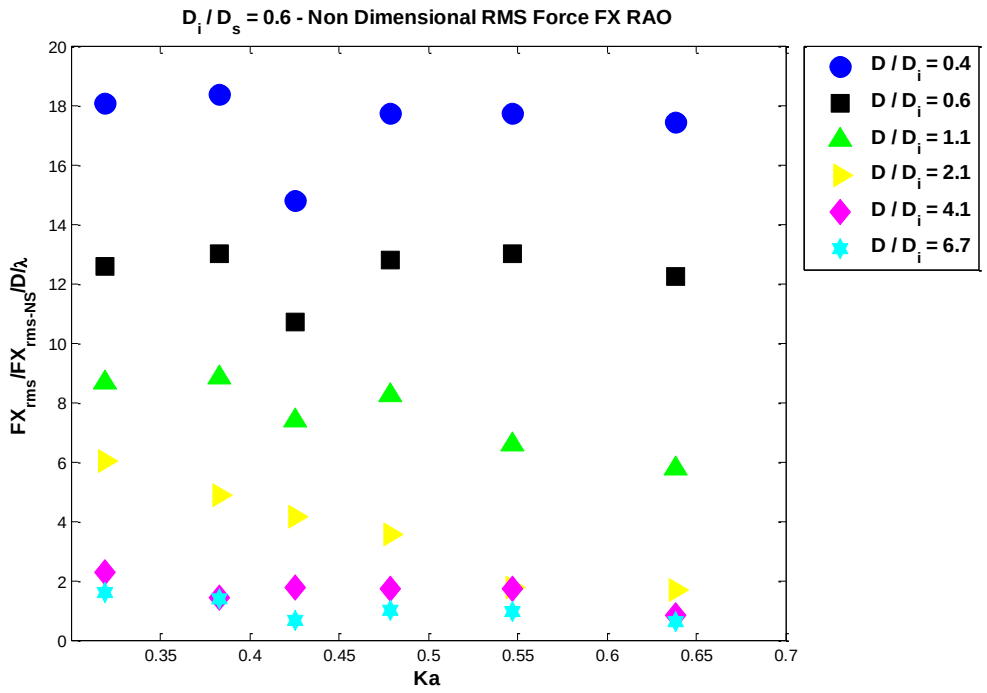

Figure 3.15: RAO for horizontal FX force divided by D/λ for sphere $D_i/D_s = 0.6$

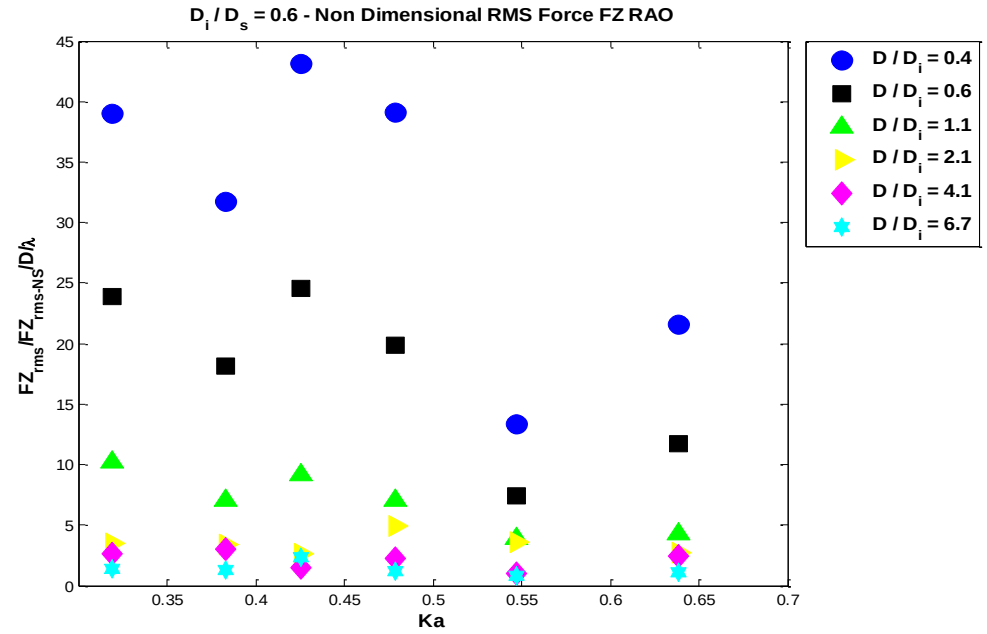

Figure 3.16: RAO for vertical FZ force divided by D/λ for sphere $D_i/D_s = 0.6$

3.1.2.2 Medium $(D_i/D_s = 0.4)$ *and Small* $(D_i/D_s = 0.3)$ *Spheres*

Results for the two smaller spheres show similar results to the larger sphere. The mean drift force FX as shown in Figure 3.17 for the sphere $(D_i/D_s = 0.4)$ at the closest two distances ($D/D_i = 0.6, 1.1$) from the structure show negative mean drift FX force for all wave cases. Also the mean drift FX forces are all positive when the structure was not present. The mean FZ forces for sphere $(D_i/D_s = 0.4)$ as shown in Figure 3.18 are all positive for all waves and all separation distances. Thus the mean FZ forces will be acting downwards for all cases. Also the closer the sphere gets to the structure, the mean FZ force magnitude tends to increase.

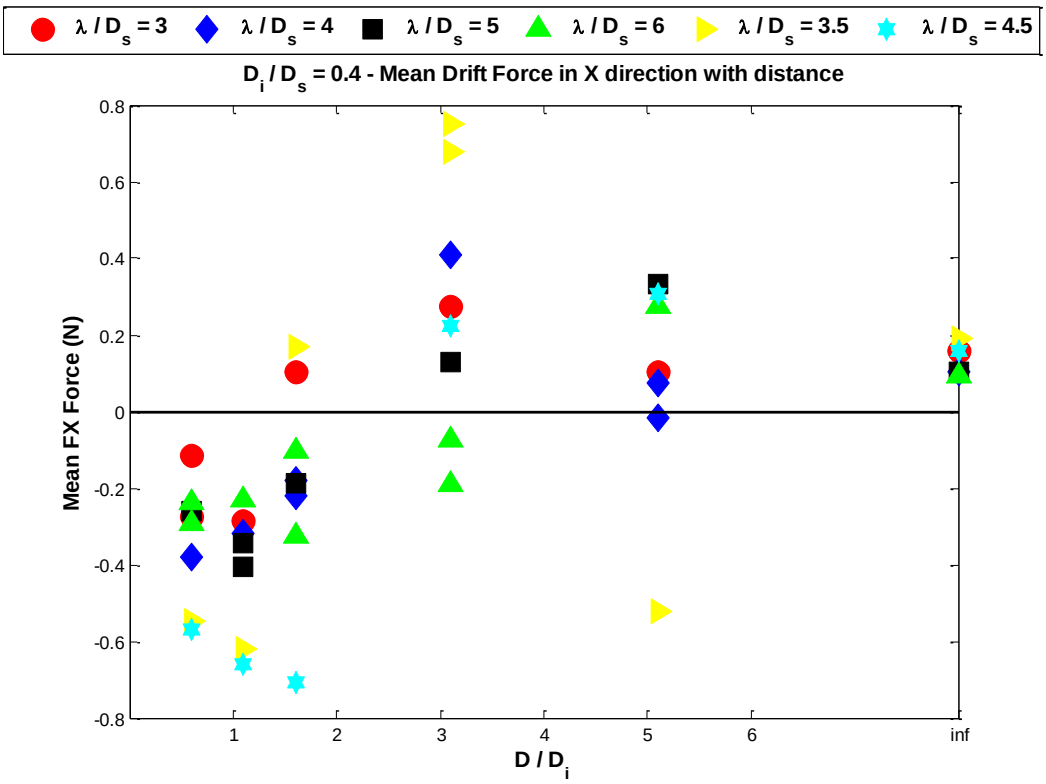

Figure 3.17: Mean drift FX force for sphere $(D_i/D_s = 0.4)$

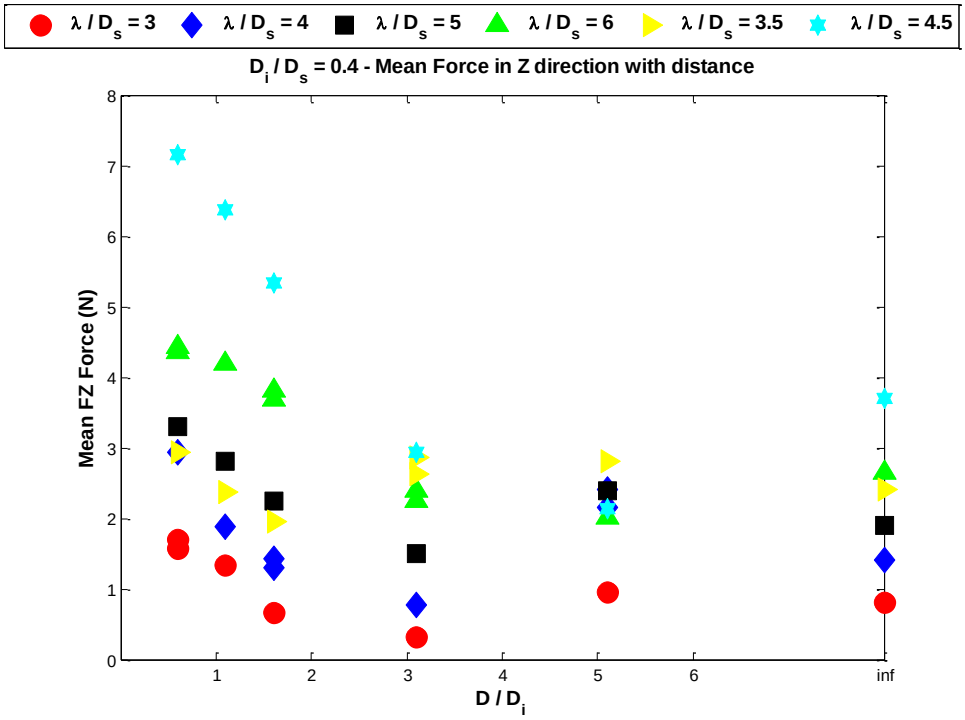

Figure 3.18: Mean FZ force for sphere ($D_i/D_s = 0.4$)

Figure 3.19 shows the mean drift force FX for the small sphere ($D_i/D_s = 0.3$) at different separation distances subject to different waves. For this sphere ($D_i/D_s = 0.3$), the closest three distances ($D/D_i = 1, 1.4, 2.4$) from the structure show negative mean drift FX force except for wave $\lambda/D_s = 6$ at distance $D/D_i = 1$ and wave $\lambda/D_s = 3.5$ at distance $D/D_i = 2.4$. Also the mean drift FX forces are all positive for the cases with no structure.

Figure 3.20 shows the mean vertical force FZ for the sphere ($D_i/D_s = 0.3$) at different locations and for different waves. It can be seen that the mean FZ forces are all positive for all waves and all separation distances. Also the mean FZ force tends to go higher as the sphere gets close to the structure.

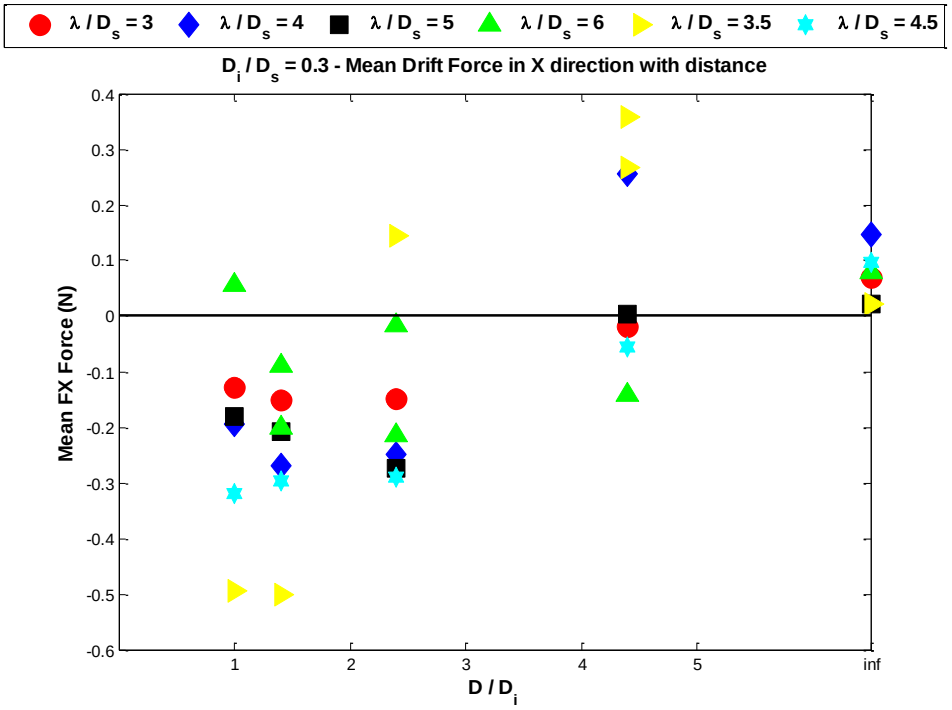

Figure 3.19: Mean drift FX force for sphere ($D_i/D_s = 0.3$)

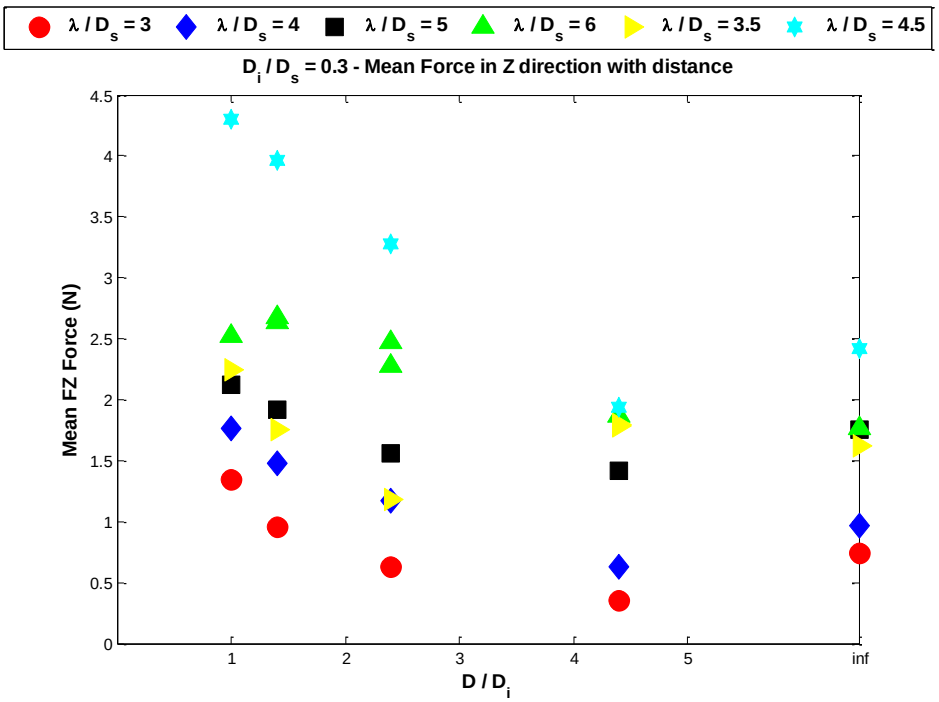

Figure 3.20: Mean FZ force for sphere ($D_i/D_s = 0.3$)

Figure 3.21 shows all the non-dimensional RMS FX and FZ forces divided by D/λ and plotted against D/λ. This non-dimensional quantity actually obscures the change in the force regimes as the body approaches the fixed structure but it does allow the derivation of a single equation that captures the results from all tests. This figure also shows the same trend of non-dimensional forces with little scatter for all the model spheres. Based on these results it appears that Reynolds dissimilitude has little influence on wave forces and the application of Froude scaling seems to be the most appropriate scaling law.

The best-fit equations derived from this data for FX and FZ are as follows:

$$\left(\frac{FX_{rms}}{FX_{rms-NS}}\right)/\left(\frac{D}{\lambda}\right) = 1.07 * \left(\frac{D}{\lambda}\right)^{-0.96}$$

$$==>\left(\frac{FX_{rms}}{FX_{rms-NS}}\right) = 1.07 * \left(\frac{D}{\lambda}\right)^{+0.04} \quad (3.1)$$

$$\left(\frac{FZ_{rms}}{FZ_{rms-NS}}\right)/\left(\frac{D}{\lambda}\right) = 0.98 * \left(\frac{D}{\lambda}\right)^{-1.11}$$

$$==>\left(\frac{FZ_{rms}}{FZ_{rms-NS}}\right) = 0.98 * \left(\frac{D}{\lambda}\right)^{-0.11} \quad (3.2)$$

These fits indicate relatively weaker effect of proximity in FX with a somewhat stronger effect in FZ. At very close proximity the fit predicts an average reduction of about 10% in Surge forces and an average increase of about 60% in Heave force. At one wavelength distance the proximity effect on both forces is negligible. Also the change in x direction force is relatively small and this is evident in Equation 3.1 where both the factor and the exponent give values that provide results close to unity. Other factors such as changes in added mass with proximity may be in play but these would be challenging to verify independently. It is also to be noted that although the results

are presented in a non-dimensional format, the ratio D_i/D_s is not fully validated because the structure size D_s was constant in these experiments.

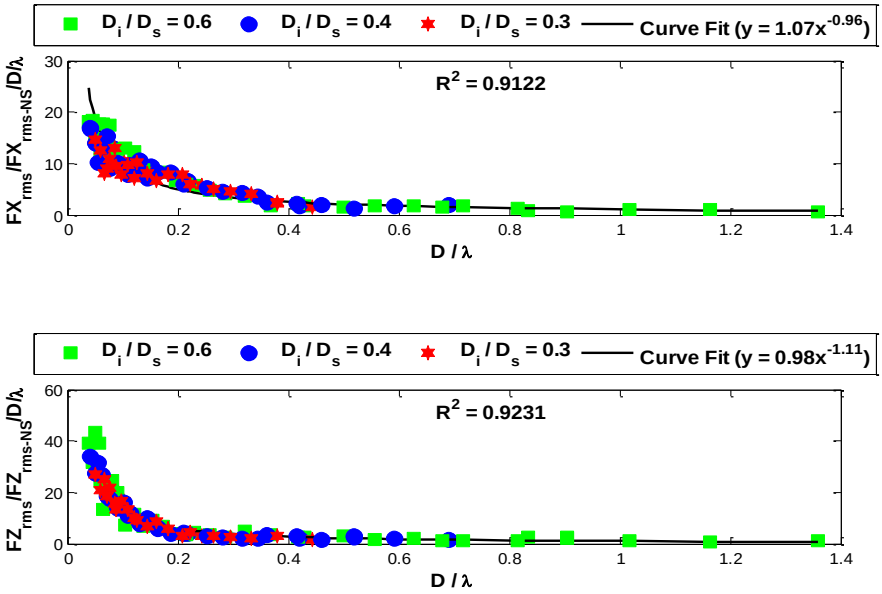

Figure 3.21: Non-dimensional RMS forces normalized by D/λ for FX and FZ for all data

3.1.2.3 Force Correlation with Wave Height

In the force data collected in this study, there is evidence of peaks and nodes in the force data as the relative distance between the body and the fixed structure changes. This effect can be explained in terms of standing waves in front of the fixed structure. When a wave of small amplitude encounters a vertical wall, the waves are reflected in order to satisfy the wall boundary condition. The combined wave form is called standing wave as it does not propagate in any direction. Figure 3.22 shows free surface displacement associated with a standing wave form.

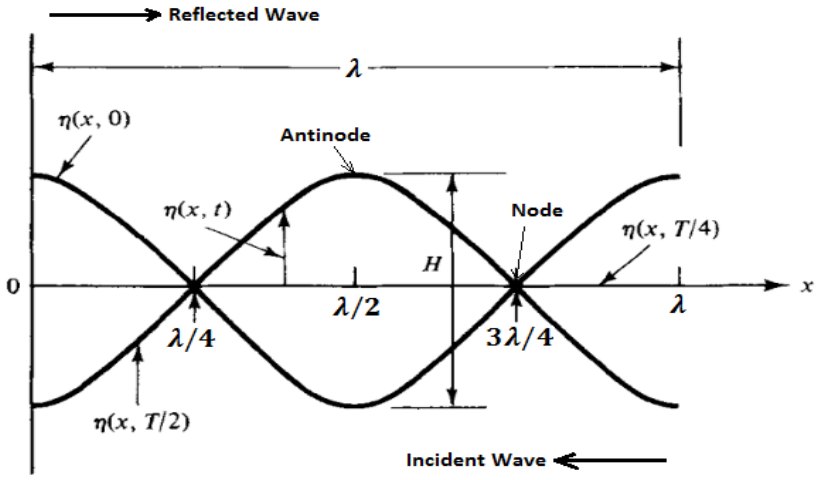

Figure 3.22: Standing Wave profile in front of vertical wall (after Dean and Dalrymple (1991))

At positions $kx = \pi/2, 3\pi/2,$ and so on, nodes exist where free surface elevation, η is zero. At these node locations, the vertical velocity, w and the hydrodynamic pressure component, $(p + \rho gz)$ are also zero. On the other hand at positions $kx = 0, \pi,$ and so on, antinodes exist where free surface elevation, η has maximum variation. At these antinode locations, the horizontal velocity, u is zero, while maximum variations occur in w and $(p + \rho gz)$. The trough to crest height of the standing wave is twice that of incident wave train (Sarpkaya and Isaacson (1981), Dean and Dalrymple (1991)).

In order to investigate the vertical force correlation with standing wave height, two methods were employed. Firstly, wave heights at the force measurement locations were measured using fixed wave probes. The wave heights at different locations are non-dimensionalized by the wave height far removed from the structure. The variation in wave heights at these locations arise from reflected waves in front of the structure. It is found that the measured FZ forces at different locations correlate well with the wave heights at those locations. Figure 3.23 show such correlation for two wave cases of two spheres $(D_i/D_s = 0.6, 0.4)$.

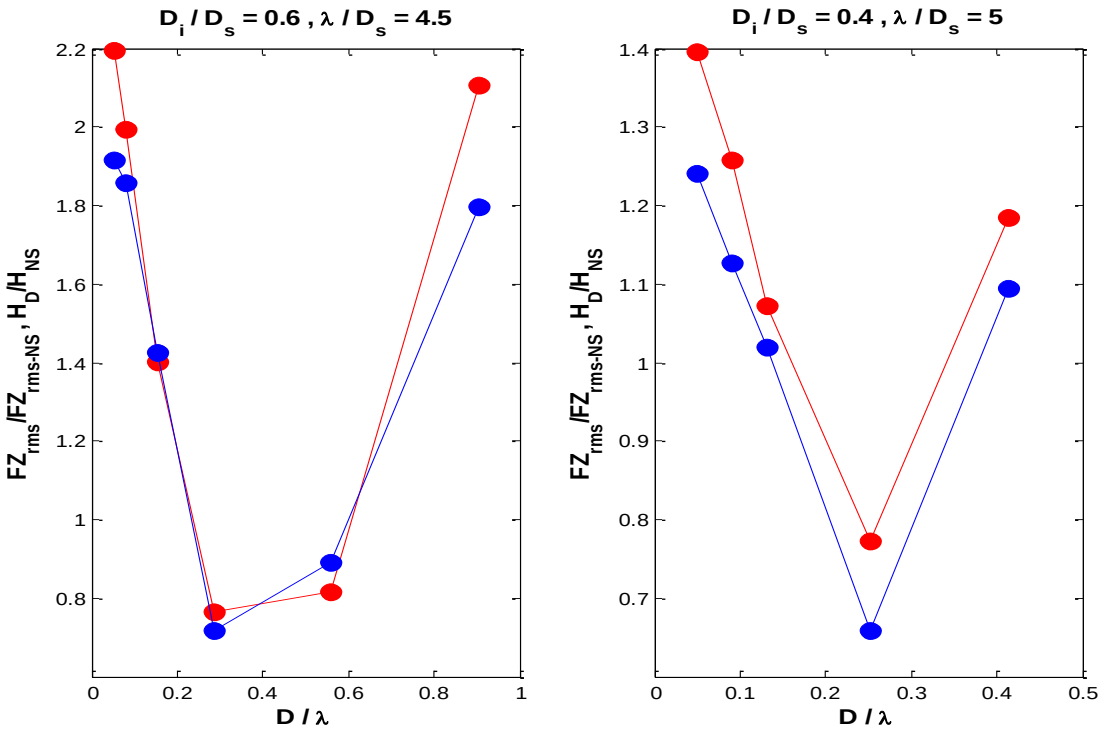

Figure 3.23: Vertical force FZ correlation with wave heights

Secondly, the wave envelope in front of the structure was measured by traversing a wave probe along the direction of wave propagation at slow constant speed using the tow carriage. This is a common method often used to measure the wave envelope of the standing wave profile and reflection coefficients from beach (Nallayarasu et al. (1995), Sarpkaya and Isaacson (1981), Dean and Dalrymple (1991)). The two towing speeds were 5 cm/s and 10 cm/s and the corresponding wave envelope for wave $\lambda/D_s = 6$ is shown in Figure 3.24. Since the incident wave energy is not fully reflected and partially dissipated and transmitted, this figure shows the quasi standing wave in front of the structure.

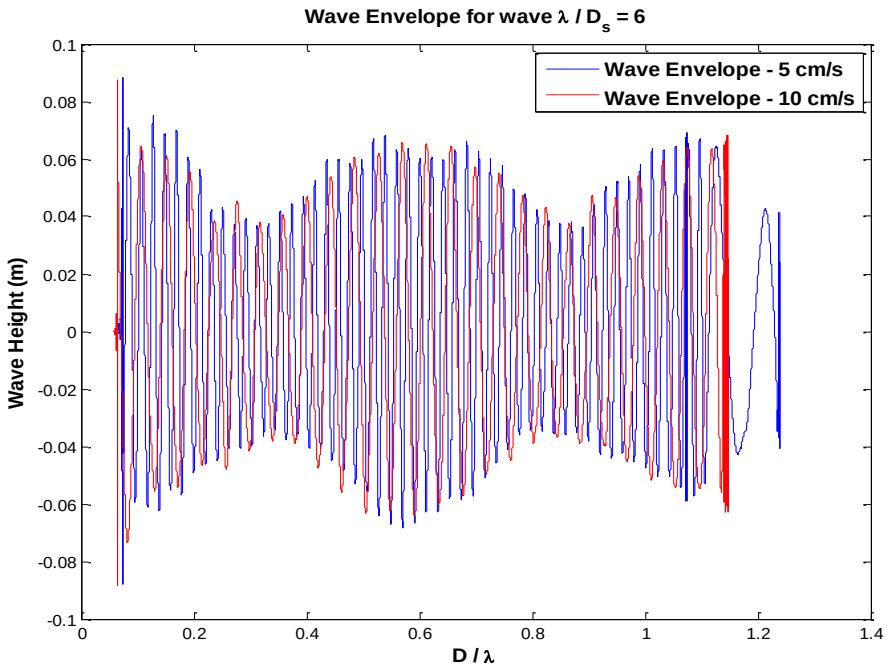

Figure 3.24: Wave envelope in front of structure for wave $\lambda/D_s = 6$ measured at two speeds

It is expected that depending on where the location of force measurement lies on the wave envelope, the FZ force will be proportional to wave height at that location. Figures 3.25 and 3.26 show the measured wave envelope in front of structure for two waves ($\lambda/D_s = 5,4.5$) along with the non-dimensional RMS FZ forces for the three spheres measured at different locations in front of structure. This envelope also demonstrates the FZ force correlation with wave height at different separation distances from the structure.

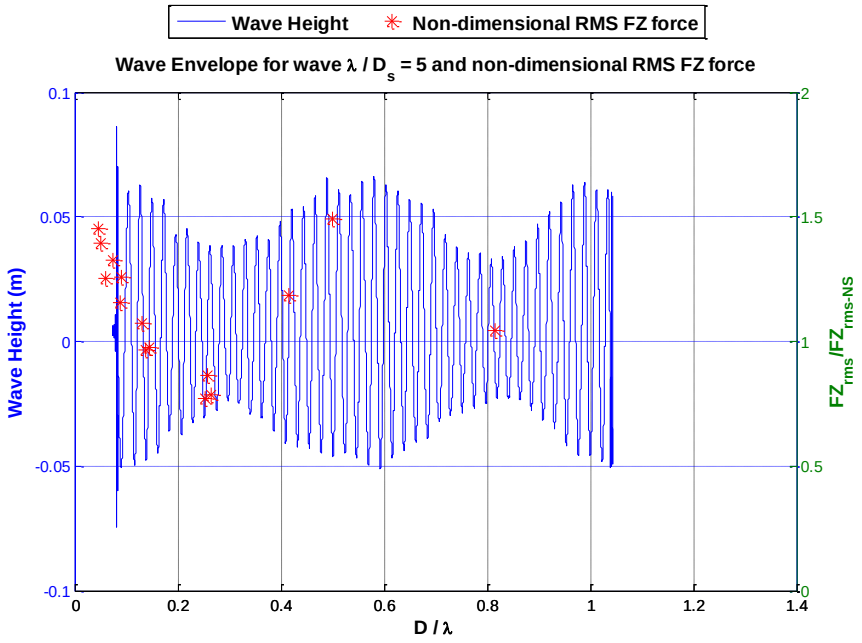

Figure 3.25: Wave envelope for wave $\lambda/D_s = 5$ and non-dimensional RMS FZ force

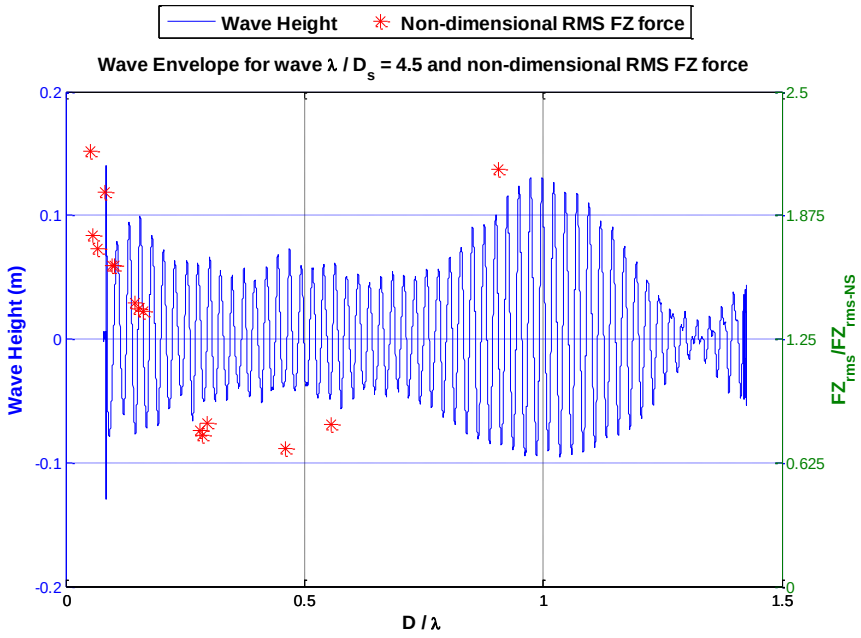

Figure 3.26: Wave envelope for wave $\lambda/D_s = 4.5$ and non-dimensional RMS FZ force

3.1.2.4 Size Effect

3.1.2.4.1 No-Structure Case

This section investigates the sphere size effects on absolute and relative wave loads. Figures 3.27 and 3.28 show the RMS FX and RMS FZ loads on the three spheres for different waves for no-structure cases. As the sphere diameter increases, the absolute magnitudes of both FX and FZ RMS forces are increased because of larger surface area and larger displacement. It is also observed that the size effect is more pronounced for the FX force than for the FZ force. This is expected because the bodies are significantly submerged and thus the FZ forces have a limited range of increase before the body is fully submerged by the wave.

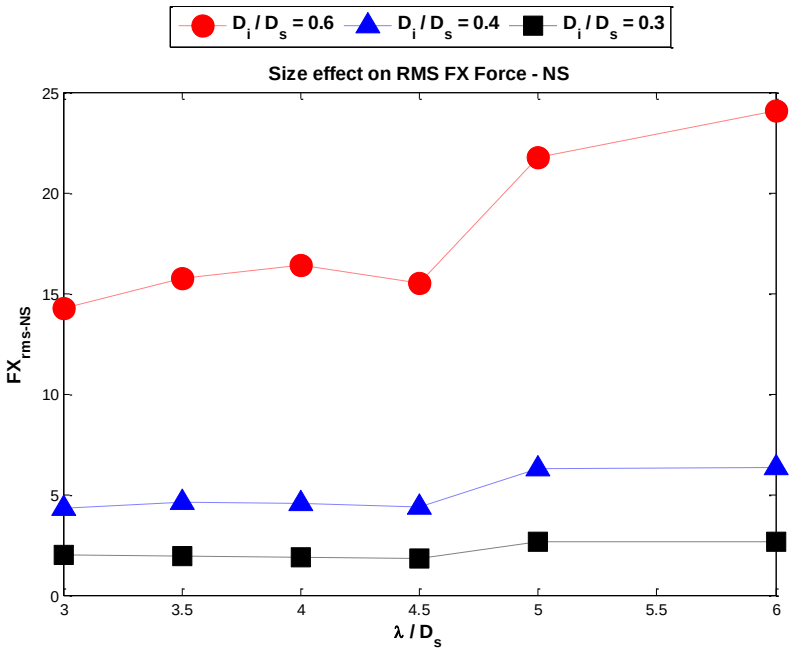

Figure 3.27: Size effect on RMS FX force for no-structure cases

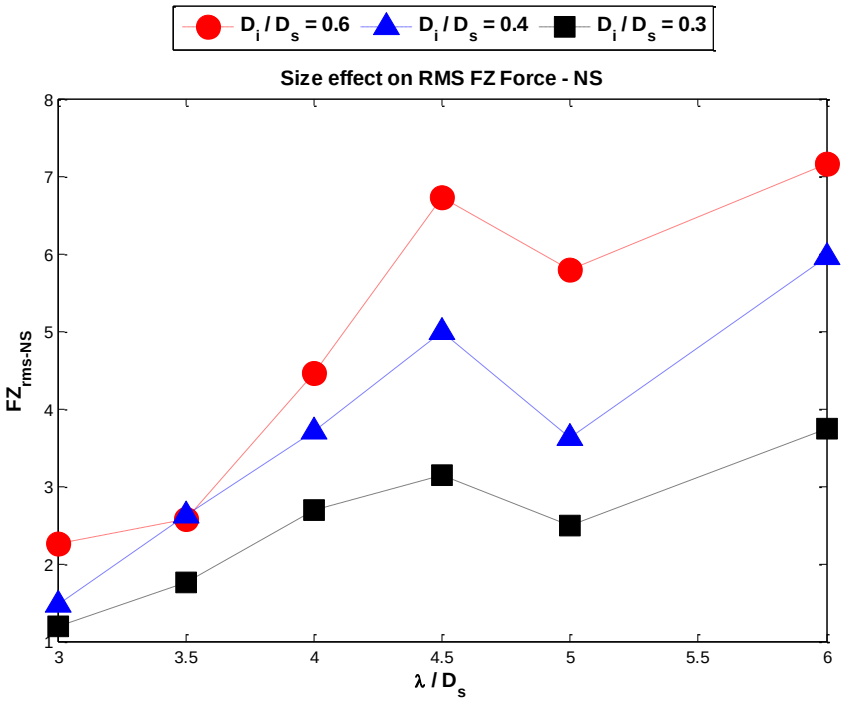

Figure 3.28: Size effect on RMS FZ force for no-structure cases

3.1.2.4.2 One Sphere Diameter Distance

Figures 3.29 and 3.30 show the non-dimensional RMS FX and FZ forces for the three spheres tested at 1 sphere diameter away from the structure. The trend of the force profile is same for all the spheres but the magnitude varies because of the resulting variation in distance/wavelength ratio. In this case there is an expected result that the reduction in relative forces show a size effect and that the smaller body shows a more significant reduction in FX force and a more significant increase in FZ force when normalized to the no-structure wave forces. This is consistent with the observation that smaller bodies are more affected by the proximity effect.

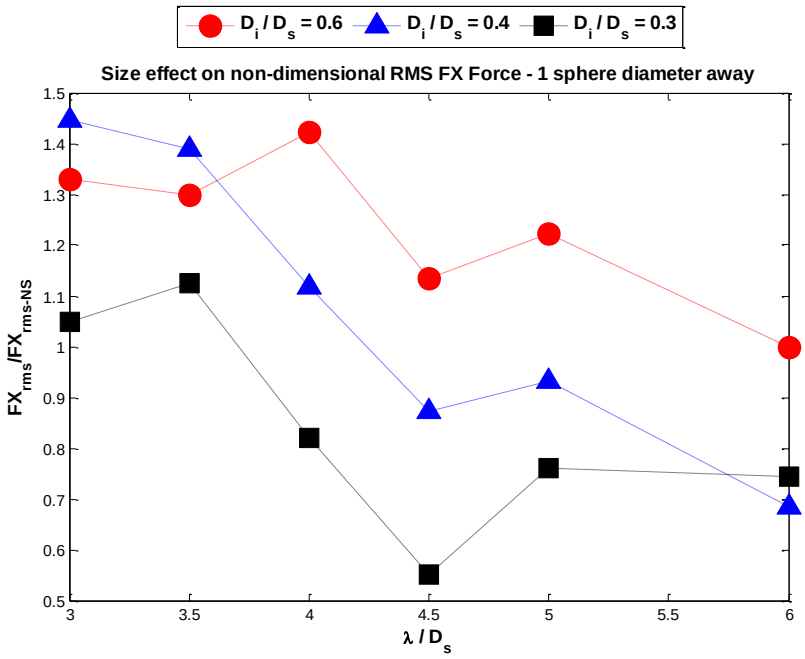

Figure 3.29: Size effect on non-dimensional RMS FX force at 1 sphere diameter away

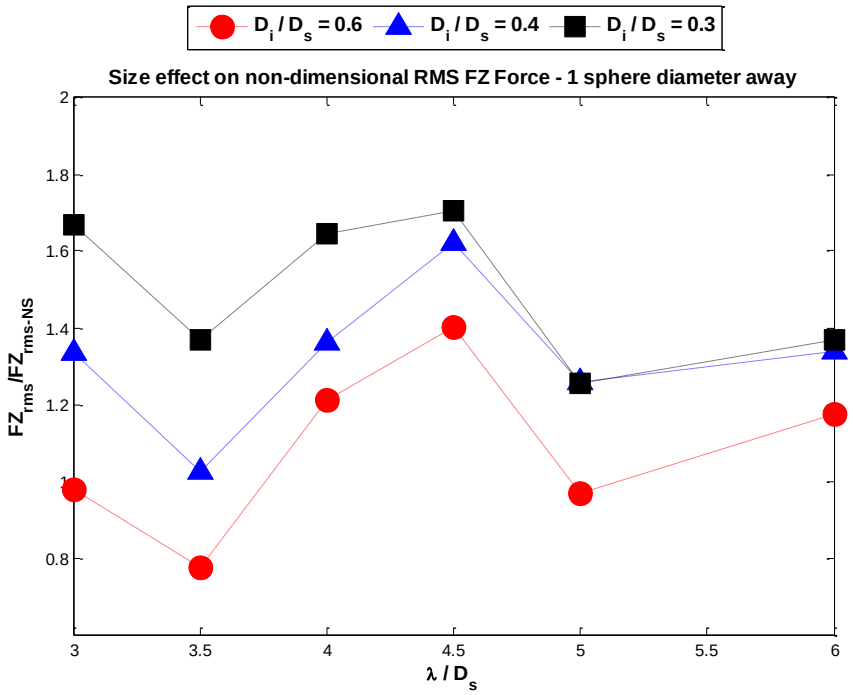

Figure 3.30: Size effect on non-dimensional RMS FZ force at 1 sphere diameter away

3.2 Experimental Investigation of Wave Induced Motions Approaching to a Fixed Structure in Regular Waves

This section describes the results of the second phase study where the change in wave induced motions of free floating ice masses, approaching a fixed structure, is investigated through physical experiments. This phase of the investigation was conducted to determine if the motions measured in proximity to the fixed structure will correlate with the forces measured in the previous experiment (section 3.1). Also the high and low frequency wave induced motions will reveal the velocity profiles of approaching ice masses and how that changes prior to impact. Some experiments have also been conducted to understand the effect of initial starting location on the resulting drift velocity.

3.2.1 Experimental Program

The current set of experiments involved the measurement of the motions of the free floating ice masses with and without the presence of the fixed structure. The objective of these experiments is to identify the change in velocity profiles due to the presence of the structure. This should also help to identify the potential velocity just prior to impact.

3.2.1.1 Facility

The experiments were conducted in the Towing Tank of the Ocean Engineering Research Center (OERC) at Memorial University of Newfoundland (MUN) in St. John's, NL Canada. The Towing tank particulars are given in previous section (3.1.1.1).

3.2.1.2 Models and Instrumentation

A hexagonal aluminium cylinder of 0.5 m diameter was used as the fixed offshore structure. The scale ratio is nominally 1:50. Thus the full scale structure diameter is 25m. Three spheres with diameters of 0.152m, 0.203m and 0.305m were used to represent different size ice masses. The ratios of ice mass diameters to the fixed structure diameter are 0.3, 0.4 and 0.6 respectively. In

addition, a cylindrical model of the same diameter as the medium sphere and 0.098m high was tested to investigate possible shape effect. The centre of gravity for each model was experimentally measured and theoretically calculated. Table 3.4 shows the vertical center of gravity for each model from the top of the model being considered. To measure the motions, a Qualisys Optical Tracking System was used. Qualisys is an optical tracking system that utilizes infrared cameras to track target markers and measure the 6 degrees of freedom motions of the model. Three infrared cameras were mounted and calibrated to cover the desired field of view. Three capacitance type wave probes were used to measure the wave profile of the incoming and reflected waves. One wave probe was placed far upstream to measure the incoming wave profile and two probes were used on two sides in front of the structure so that the models do not touch the probes during the experiment. Before conducting experiments, both the Qualisys cameras and the required waves were calibrated. Figure 3.31 shows the layout of the experimental set up in the towing tank with dimensions and coordinate system. The distances are considered positive in the direction of wave propagation in x-direction and positive upward in z-direction. In addition videos were recorded during experiments and digital still photographs were taken.

Table 3.4: Vertical center of gravity of models

Sphere, $D_i/D_s = 0.6$	Sphere, $D_i/D_s = 0.4$	Sphere, $D_i/D_s = 0.3$	Cylinder, $D_i/D_s = 0.4$
190 mm	125 mm	105 mm	46 mm

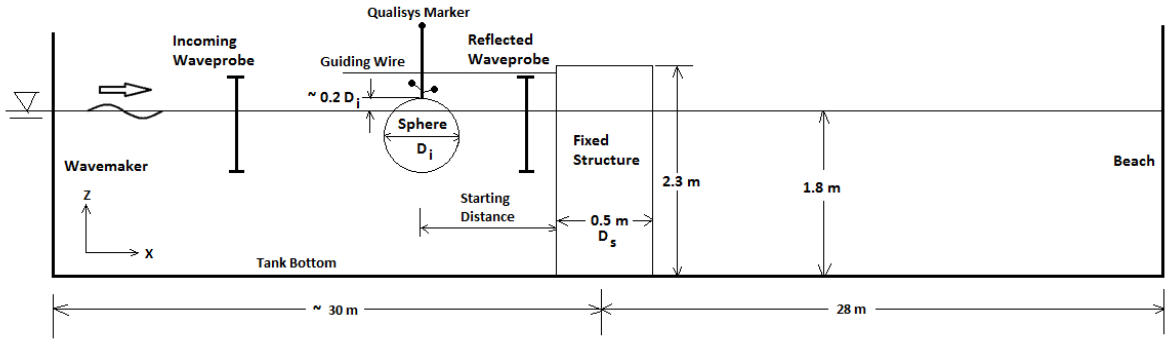

Figure 3.31: Schematic layout of the experimental set up

3.2.1.3 Environment

The towing tank water depth was 1.8 m. The same six regular waves with two different wave steepness were used in this case and wave particulars are given in previous section (3.1) and in Table 3.1.

3.2.1.4 Methodology

The fixed structure model was placed in the tank and filled with water ballast. The structure was also clamped against a fixed cross-tank platform to avoid any movement. The spheres are ballasted with paraffin wax to float with the nominal draft of the iceberg. The sphere motions are restrained to the vertical plane motions only (surge, heave and pitch) by two guide wires and a light weight carbon-fibre rod on top of the sphere. Moreover, the spheres were further ballasted by inserting a rod at the bottom of the spheres with small weights at the end to reduce pitch motions and better extract heave and surge motions. The optical tracking system, Qualysis® was used to track the motions in six degrees of freedom. Four light weight reflective marker balls were installed on the rod attached to the sphere. The marker balls were arranged in such a manner that there is no shadowing of multiple markers when the model rotates and the markers

can be seen distinctively by the cameras. Figure 3.32 shows the experimental set up including the fixed structure, the medium sphere with Qualisys markers arranged on top and the wave probes for reflected waves. The sphere model was held at the release distance from the structure and then was let go after few seconds. The release distances were 2m for the cylinder, medium and large spheres and 1.6m for the small sphere since this sphere takes a longer time to travel than the other two spheres. The large sphere was also tested at different release distances of 2.5m, 2m, 1.6m, 1m and 0.6m to investigate the effect of different starting location on the corresponding kinematics of the sphere. Each test duration was about 2 minutes to avoid possible contamination of the incident wave field due to reflections coming from the tank beach. The waiting time in between tests was about 15 minutes to let the tank settle. Once the tests with the structure were finished, the structure was taken out of the tank and the sphere models were tested in a similar fashion without the presence of the structure. The release locations for no structure cases were maintained same as the test cases with the structure. Table 3.5 shows the test matrix along with different release locations. A number of repeat tests were conducted to validate and to identify reliability on motion results. Specially, most tests with the structure in place were repeated at least twice to improve reliability of the data.

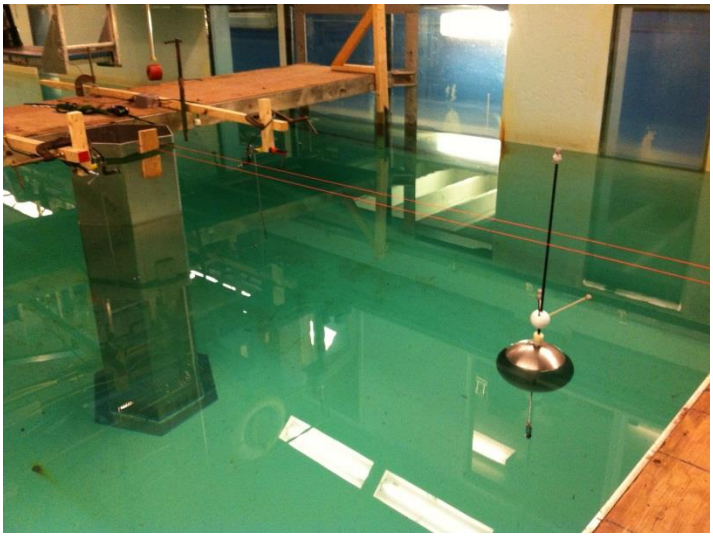

Figure 3.32: Experimental set up for motion experiments

Table 3.5: Test matrix for motion experiments

		No Structure				With Structure			
Wave (λ/D_s)	Ice model	Sphere, $D_i/D_s = 0.6$ ($D = 2m$)	Sphere, $D_i/D_s = 0.4$ ($D = 2m$)	Sphere, $D_i/D_s = 0.3$ ($D = 1.6m$)	Cylinder, $D_i/D_s = 0.4$ ($D = 2m$)	Sphere, $D_i/D_s = 0.6$ ($D = 2m$)	Sphere, $D_i/D_s = 0.4$ ($D = 2m$)	Sphere, $D_i/D_s = 0.3$ ($D = 1.6m$)	Cylinder, $D_i/D_s = 0.4$ ($D = 2m$)
3		x	x	x	x	xx	xx	xx	x
4		xx	x	x	x	xx	xx	xx	x
5		x	xx	xx	x	xx	xxx	xx	xx
6		xx	x	xx	x	xx	xx	xx	x
3.5		xx	x	x	x	xx	xx	xx	xx
4.5		x	x	x	x	xx	xx	xx	x

(D – Initial release distance measured from ice model center to structure face, D_i – Sphere diameter, D_s – Structure diameter, λ – Wavelength, x – one test, xx – repeat twice, xxx – repeat thrice)

3.2.2 Results and Discussion

The same spheres are used in this case as in the previous force measurement experiments and the wave particulars are also kept the same as those previously used. The data measured included time series of full 6 DOF motions and the wave profiles from the wave probes. Among the 6 DOF motions, surge and heave motions are the most important motions concerning structure impacts (McGovern and Bai (2014a)). Moreover previous experiments measured the forces in x- and z-directions. Since the models are restrained to vertical plane motions only (surge, heave and pitch) by two guide wires and also further ballasted to minimize pitch motions, only surge and heave motion data are considered for this analysis. The distance in the surge direction is considered positive in the direction of wave travel and the heave displacement is positive upward. In analyzing the data time series of raw data of surge and heave displacements were selected after initial transient values had passed. Several calm runs were conducted and the static offset was removed to yield wave induced heave motions only. A Butterworth low-pass filter was applied to the raw data to filter out high frequency noise. Figure 3.33 shows two typical wave cases during the experiment.

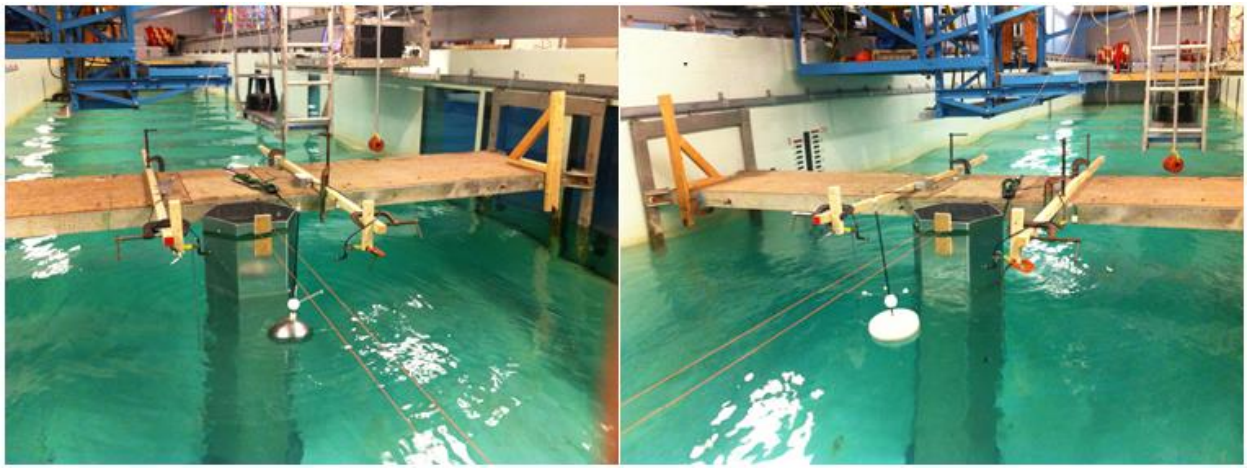

Figure 3.33: Spherical and cylindrical models in waves

3.2.2.1 No-Structure Cases

The 6 DOF motion data are resolved to the center of gravity for each model. The structure face location in x-direction is considered as the origin. The time series of raw data for surge, and heave motions for sphere $D_i/D_s = 0.6$ tested without the structure in wave $\lambda/D_s = 3.5$ is shown in Figure 3.34.

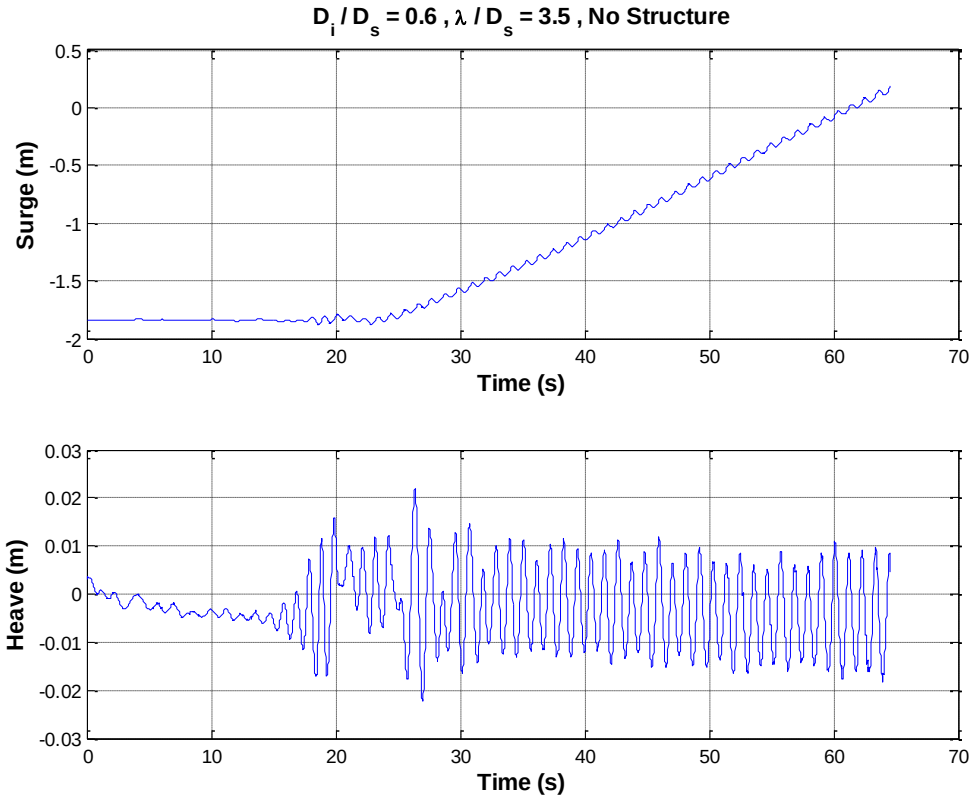

Figure 3.34: Time series of raw data of surge, and heave motions for sphere $D_i/D_s = 0.6$ tested without structure in wave $\lambda/D_s = 3.5$

The x-displacement data contains both low and high frequency motions. The high frequency motions are the oscillatory motions due to the wave frequency and low frequency motions are due to the second order wave drift forces. Huang et al. (2011) showed two methods of

determining the drift velocity. The first method is to calculate the period-average mean drift velocity as a function of time by dividing the horizontal displacement between two neighboring peaks by the wave period. The second method is to calculate the slope of a best fitting linear trend line from the x trajectory. The drift motion in the present analysis is calculated from the signal by determining the slope of the best fitting linear trend line once steady state is reached (Bai et al. (2017), Huang et al. (2011), McGovern and Bai (2014a)). Figure 3.35 shows the x trajectory and the corresponding linear curve fit for sphere $D_i/D_s = 0.4$ for 10 wave cycles tested without the structure in wave $\lambda/D_s = 4$. The slope of the curve determines the drift velocity as 0.039 m/s. Surge and heave velocities are calculated from the corresponding displacement time series.

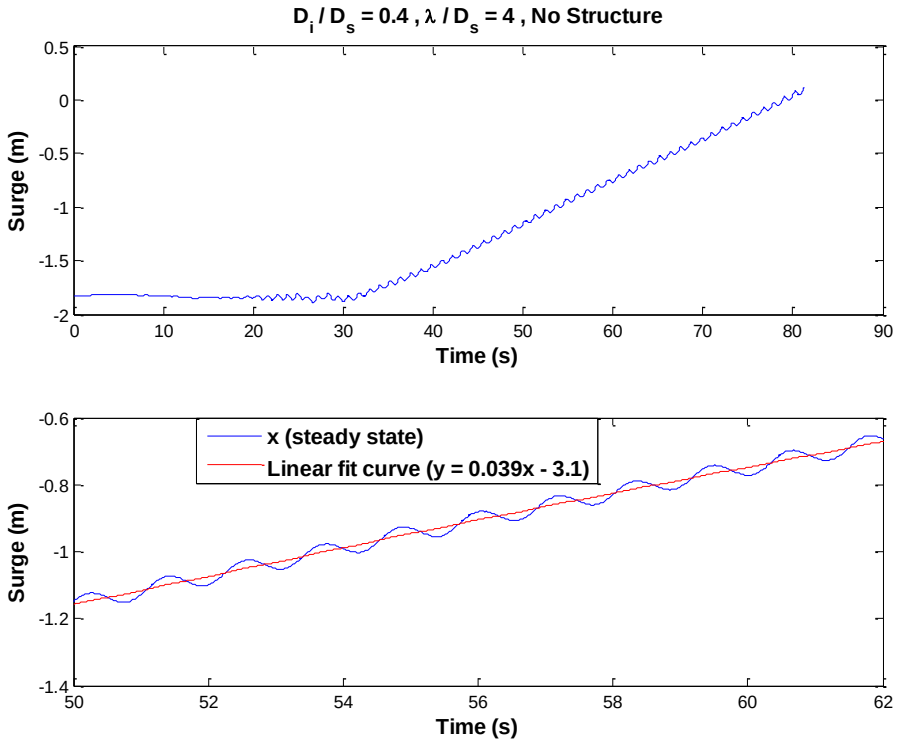

Figure 3.35: x trajectory and the corresponding linear curve fit for sphere $D_i/D_s = 0.4$ tested without structure in wave $\lambda/D_s = 4$

In previous experiments the x- and z- forces were measured on the same spherical models at different proximity to the same fixed structure. The forces in the z-direction showed non-linear behaviour for most of the wave cases. Wishahy et al. (1987) and Hinchey et al. (1991) also discussed non-linear heave motions of spherical bergy bit models. In general, the non-linearity arises from the very small freeboard of floating ice or models ballasted to represent floating ice, waves quickly wash over the top surface, completely submerging the berg (or model). Figure 3.36 shows the wave forces in the z-direction for sphere $D_i/D_s = 0.6$ tested without structure in wave $\lambda/D_s = 6$ from previous experiments and the heave motions and velocities for the same sphere tested without the structure in the same wave from the present analysis. The results clearly show the non-linear behaviour in the forces and corresponding motions.

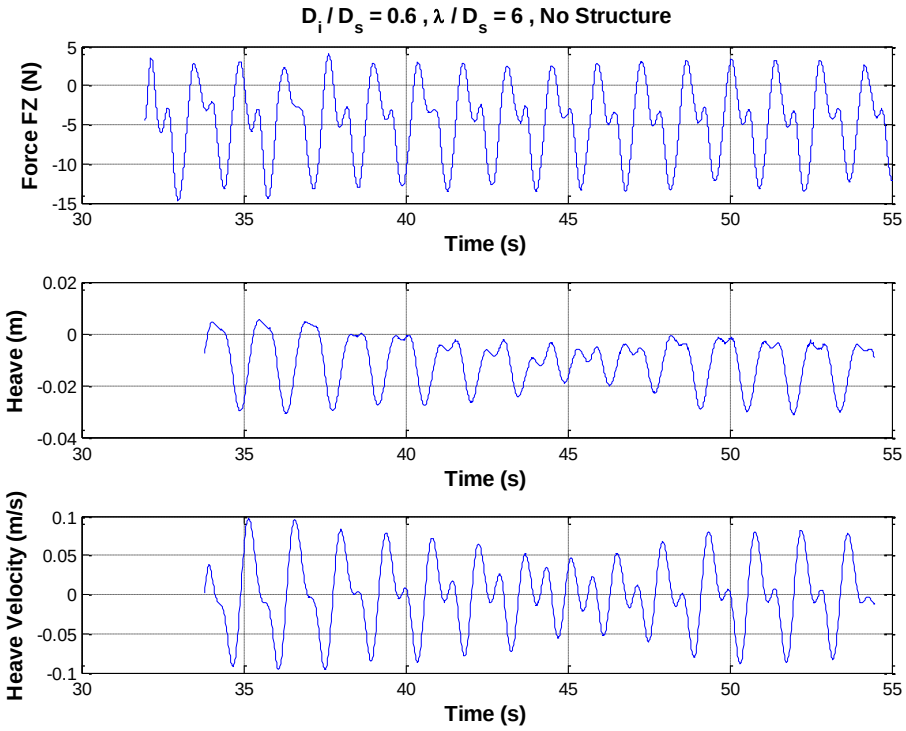

Figure 3.36: Non-linear forces and motions for sphere $D_i/D_s = 0.6$ tested without the structure present in wave $\lambda/D_s = 6$

In order to plot the motion RAOs, the low frequency motions are removed from the x trajectory. Then the RMS motion for surge and heave were calculated over at least 10 steady state cycles and divided by the wave height. Since the heave motions of the spherical models show non-linear motions in some of the wave cases, more than 10 cycles were considered for the analysis of those cases. Figures 3.37 and 3.38 show the surge and heave RAOs respectively for the three spherical and the cylindrical models plotted against the diffraction parameter Ka, where K is the wave number and a is the model radius. The three spherical models show similar trend indicating that Reynolds dissimilitude has little influence on wave induced motions and the application of Froude scaling is reasonable.

The results also show significant difference due to the shape effect on both surge and heave motions. The cylindrical model shows much higher RAO values than the same diameter spherical model for both surge and heave. Lever et al. (1990a) also showed significant difference between different shaped models on wave induced motions, particularly cubical and cylindrical models showed higher RAO values than the sloping side models of trapezoid and sphere.

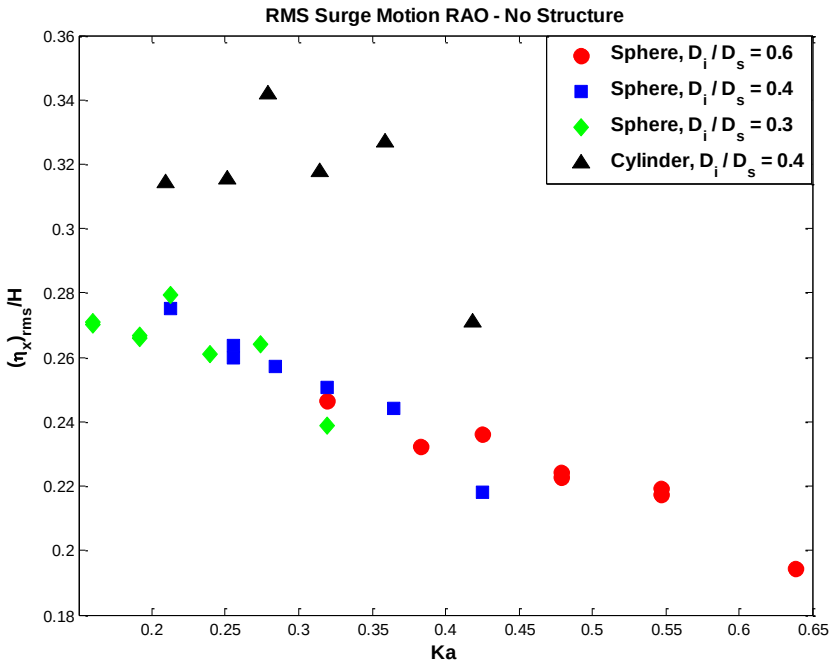

Figure 3.37: RMS surge motion RAO for no structure cases

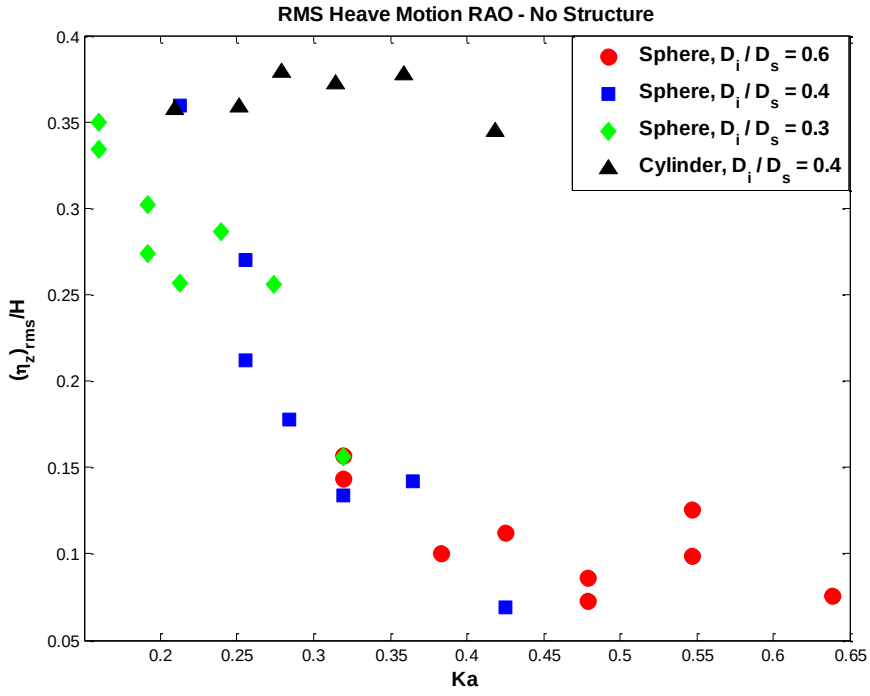

Figure 3.38: RMS heave motion RAO for no structure cases

Figures 3.39 and 3.40 show the sphere size effects on RMS surge and heave velocities for different waves for no-structure cases. Both surge and heave RMS velocities are smaller for the sphere $D_i/D_s = 0.6$ compared to the other two smaller spheres. This can be attributed to larger surface area and larger displacement. The surge and heave RMS velocities for sphere $D_i/D_s = 0.3$ is higher than the sphere $D_i/D_s = 0.4$ except for waves $\lambda/D_s = 5\ and\ 6$. It is also observed that the size effect is more pronounced in the heave direction than in the surge direction contrary to what was found in previous experiments where the size effect was more pronounced for the FX force than the FZ force. This is because the forces are measured by holding the bodies in place and the motions are measured on free floating bodies.

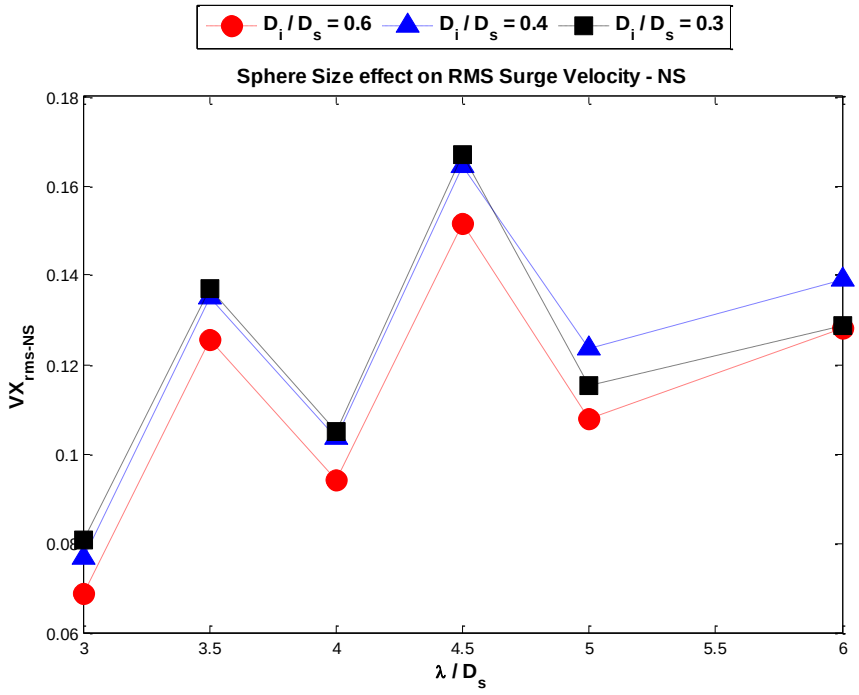

Figure 3.39: Size effect on RMS Surge Velocity for no-structure cases

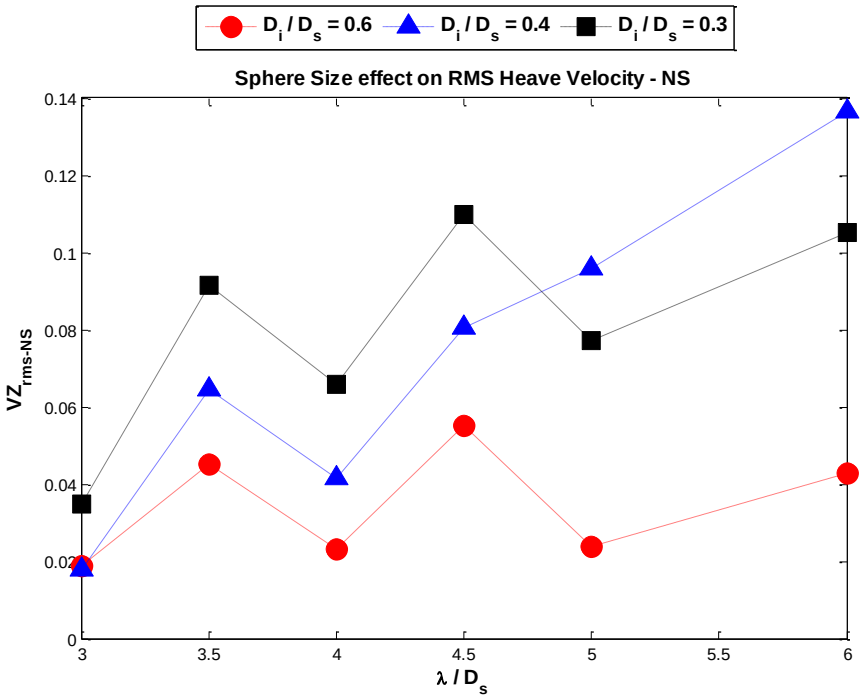

Figure 3.40: Size effect on RMS Heave Velocity for no-structure cases

Figures 3.41 and 3.42 show the RMS surge and heave velocities of the same diameter sphere and cylinder for different waves in the no-structure cases. The velocities are non-dimensionalized by volumetric Froude number, $\sqrt{gVol^{1/3}}$, where g is the acceleration due to gravity and *Vol* is the submerged volume. Although the diameters are the same, the draft of the cylinder is less and the cylinder model is considerably lighter than the spherical model. Both RMS surge and heave velocities, for the cylindrical model, are considerably higher than the spherical model.

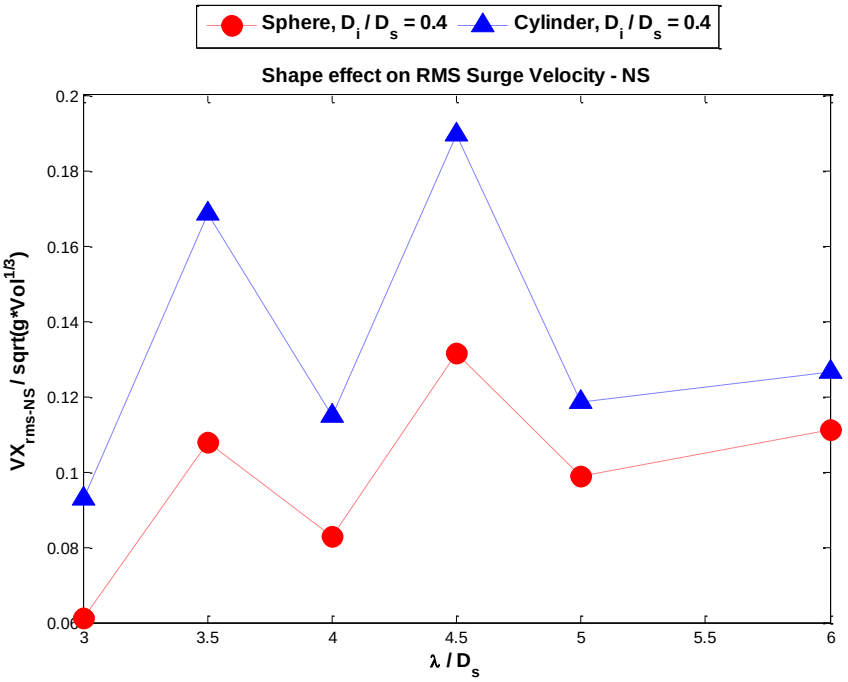

Figure 3.41: Shape effect on RMS Surge Velocity for no-structure cases

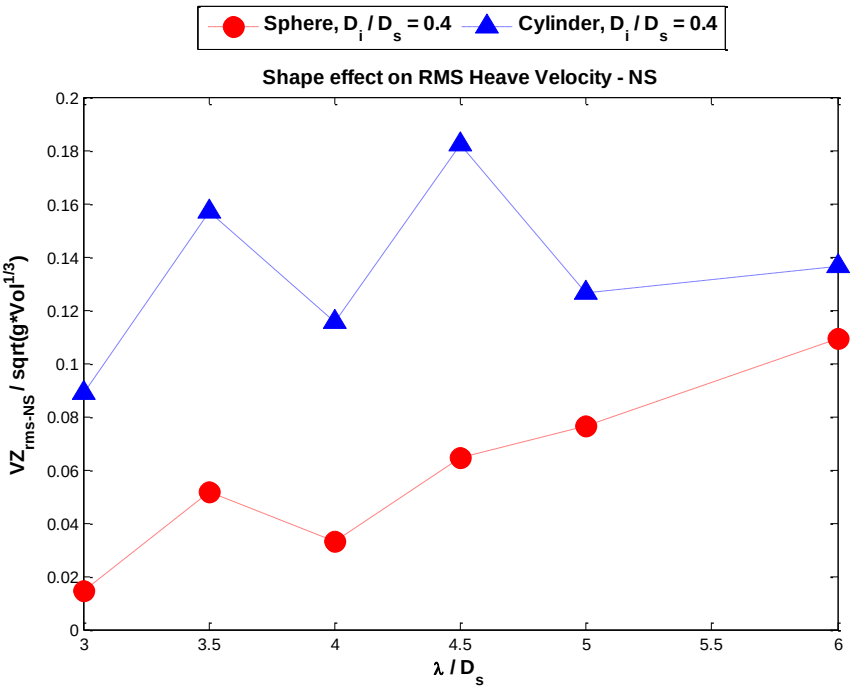

Figure 3.42: Shape effect on RMS Heave Velocity for no-structure cases

3.2.2.2 With-Structure Cases

As part of the experimental procedure, each model was placed in the initial starting position and held for few seconds to let a few wave cycles pass by and insure that steady state reflections are developed from the structure. It was observed that the model was slowed down in some locations on its way towards the structure. In some waves the model went forward and came back and in other occasions the model proceeded to hit the structure. The data has been analyzed only for the forward motion. Figure 3.43 shows the time series of surge and heave displacements for two models in two different wave conditions. The sphere $D_i/D_s = 0.4$ in wave $\lambda/D_s = 5$ went and hit the structure, whereas the sphere $D_i/D_s = 0.3$ in wave $\lambda/D_s = 4$ went close to the structure and came back. These motion profiles also indicate the change in velocity throughout the trajectory. It is to be noted that the purpose of our study is not to analyze the impacts themselves but rather to investigate the change in velocity profile prior to impact due to hydrodynamic interaction with the structure.

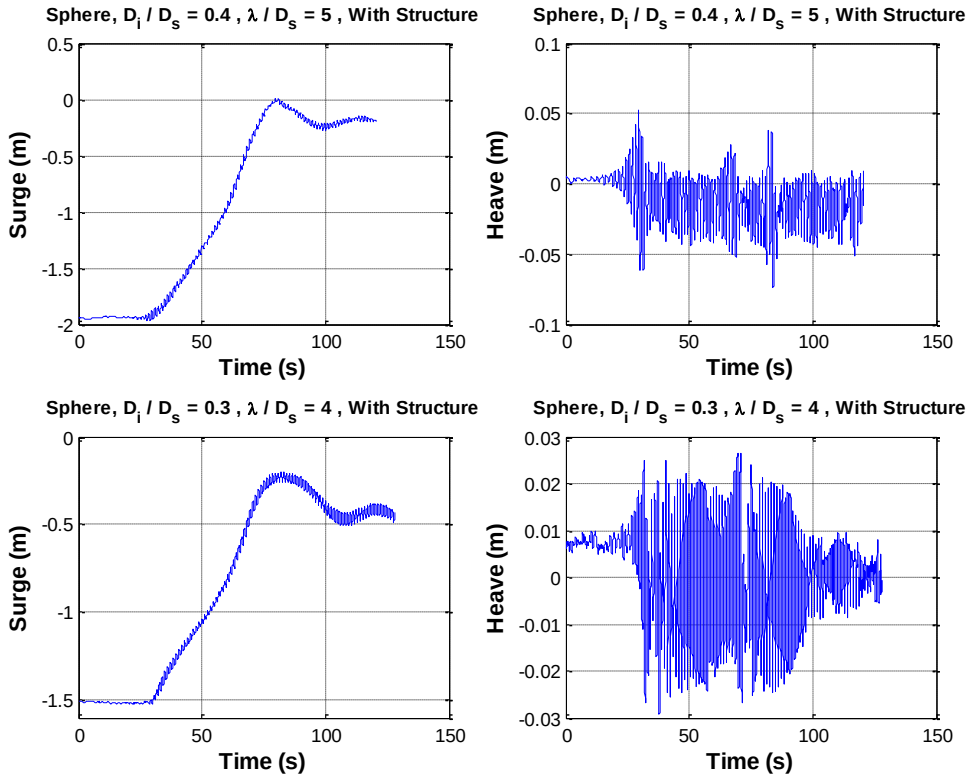

Figure 3.43: Time series of raw data of surge and heave motions for sphere $D_i/D_s = 0.4$ tested in wave $\lambda/D_s = 5$ and for sphere $D_i/D_s = 0.3$ tested in wave $\lambda/D_s = 4$ with structure

For each test the surge and heave velocities are calculated from the recorded motion data. Figures 3.44 and 3.45 show the calculated time series of surge and heave velocities respectively for sphere $D_i/D_s = 0.6$ tested in wave $\lambda/D_s = 5$, for sphere $D_i/D_s = 0.4$ tested in wave $\lambda/D_s = 3.5$ and for cylinder $D_i/D_s = 0.4$ tested in wave $\lambda/D_s = 4$ with structure. The results clearly show an envelope type profile indicating the change in velocities with time. Surge velocities include the low frequency motion as well, thus showing the mean velocity is greater than zero and the body moved forward.

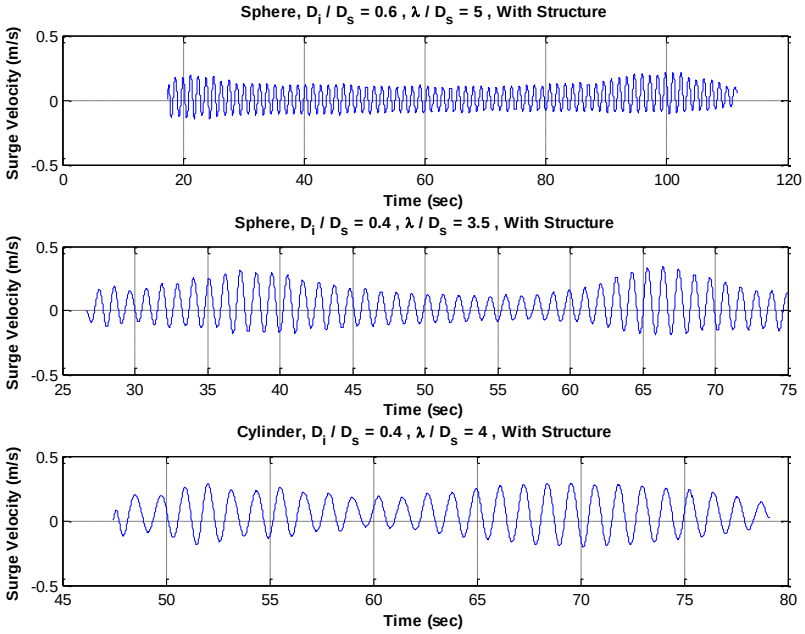

Figure 3.44: Time series of surge velocity for three test cases

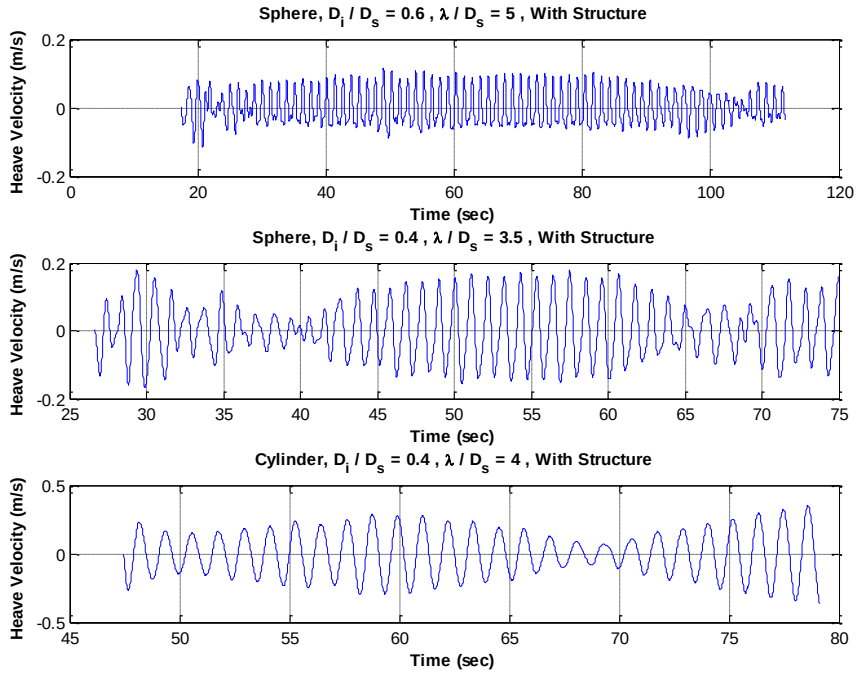

Figure 3.45: Time series of heave velocity for three test cases

In earlier experiments, the wave loads at different proximity to the structure are found to be dictated by the separation distance to wavelength ratio and the non-dimensional RMS forces against D/λ show an envelope type profile because of the standing wave in front of the structure. Also as the forces in the x- direction decreased, the forces in z- direction increased. Figure 3.46 shows the surge and heave velocities for sphere $D_i/D_s = 0.4$ in wave $\lambda/D_s = 3.5$ tested with structure and plotted against D/λ. The distance from the structure, D was evaluated from the low frequency drift motion data.

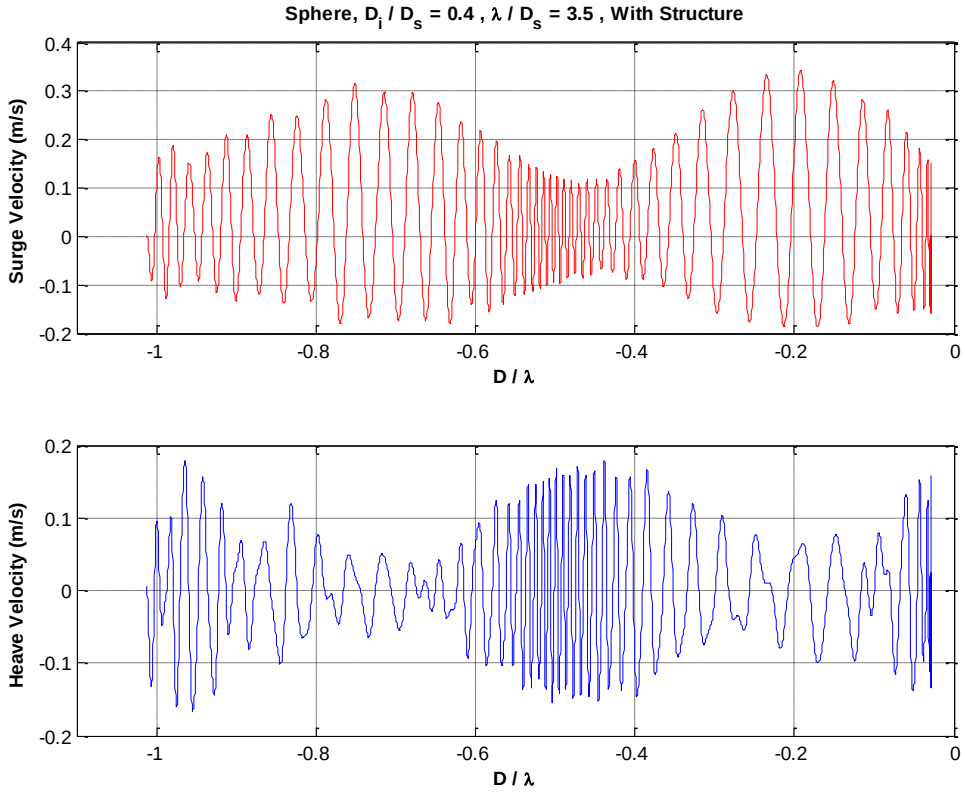

Figure 3.46: Surge and Heave velocity for sphere $D_i/D_s = 0.4$ tested in wave $\lambda/D_s = 3.5$ with structure plotted against D/λ

These results are consistent across tests with strong correlation between forces measured in previous experiments and motions measured in the present analysis. The results indicate the effect of standing wave in front of the structure. The results in Figure 3.46 clearly show the how the motions are amplified at nodes and antinodes. At nodes the surge motions are increased and heave motions are decreased and at antinodes the surge motions are decreased and heave motions are increased.

In order to keep consistency with previous analysis, the RMS velocities were non-dimensionalized using the RMS velocities for no-structure cases and plotted against an average range of D/λ. Figures 3.47 to 3.54 show the non-dimensional surge and heave velocities for spheres $D_i/D_s = 0.6, 0.4, 0.3$ and for cylinder $D_i/D_s = 0.4$ tested in all waves with structure and plotted against D/λ. The results contain all the repeat runs as well. There is more scatter in non-dimensional heave velocities for the spheres because of the non-linear heave motions for most of the wave cases.

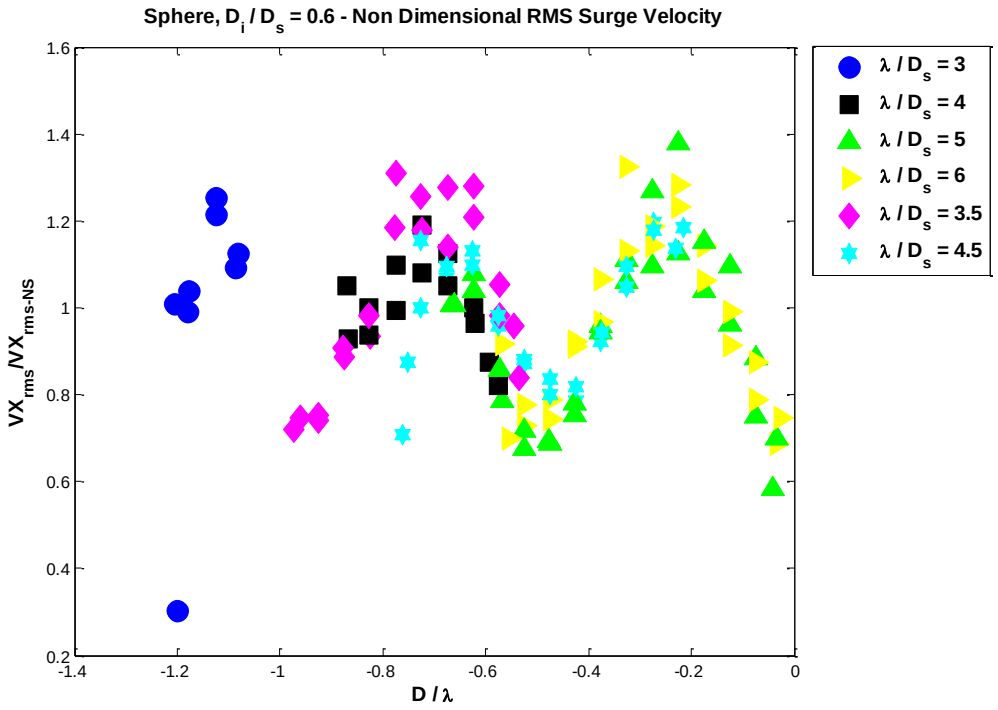

Figure 3.47: Non-dimensional RMS Surge velocity for sphere $D_i/D_s = 0.6$ tested in all waves

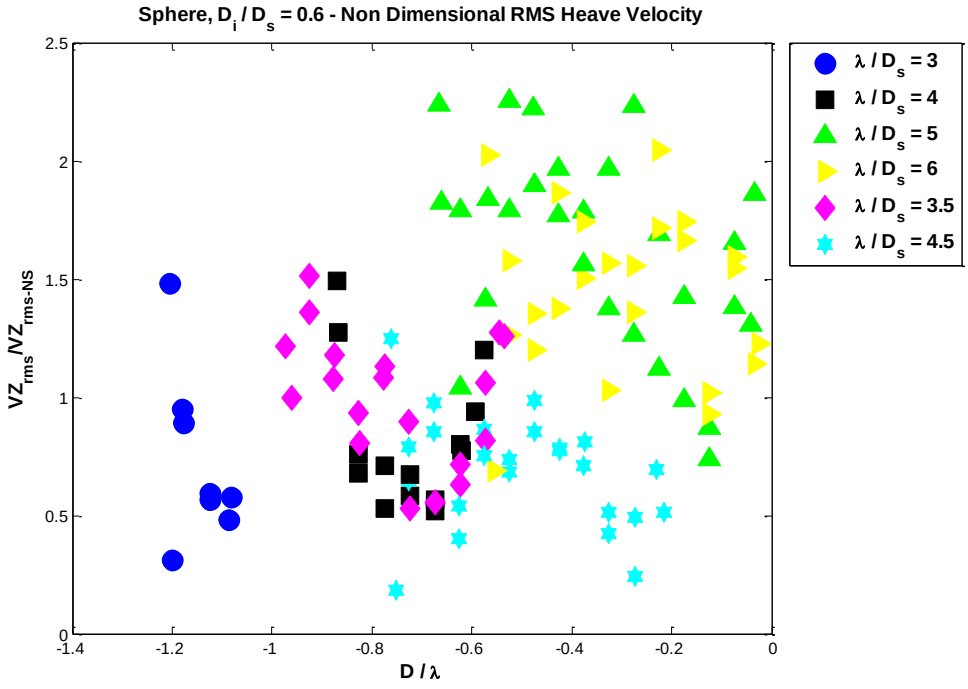

Figure 3.48: Non-dimensional RMS Heave velocity for sphere $D_i/D_s = 0.6$ tested in all waves

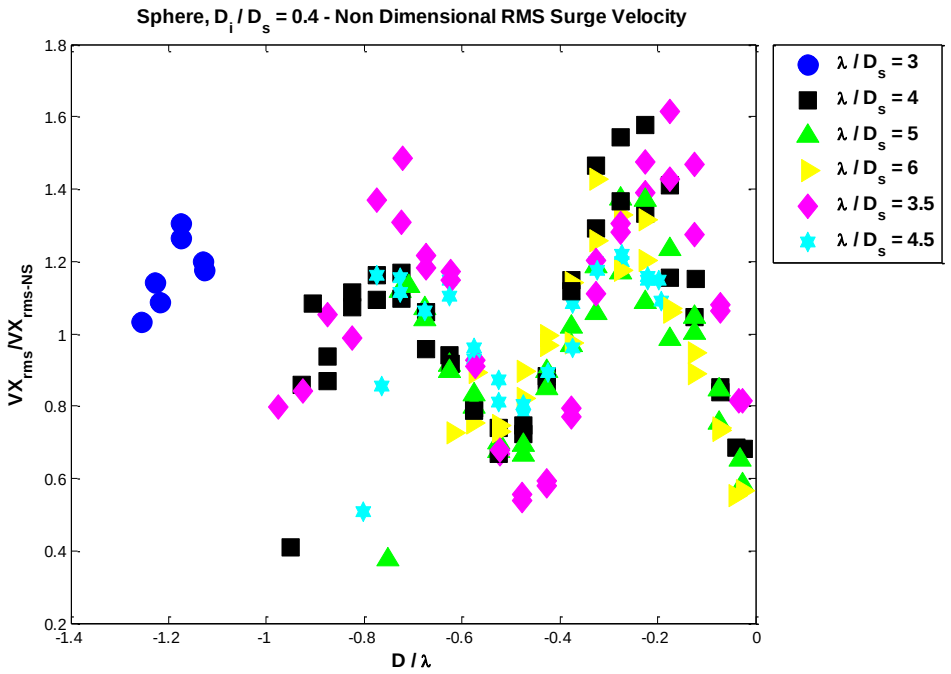

Figure 3.49: Non-dimensional RMS Surge velocity for sphere $D_i/D_s = 0.4$ tested in all waves

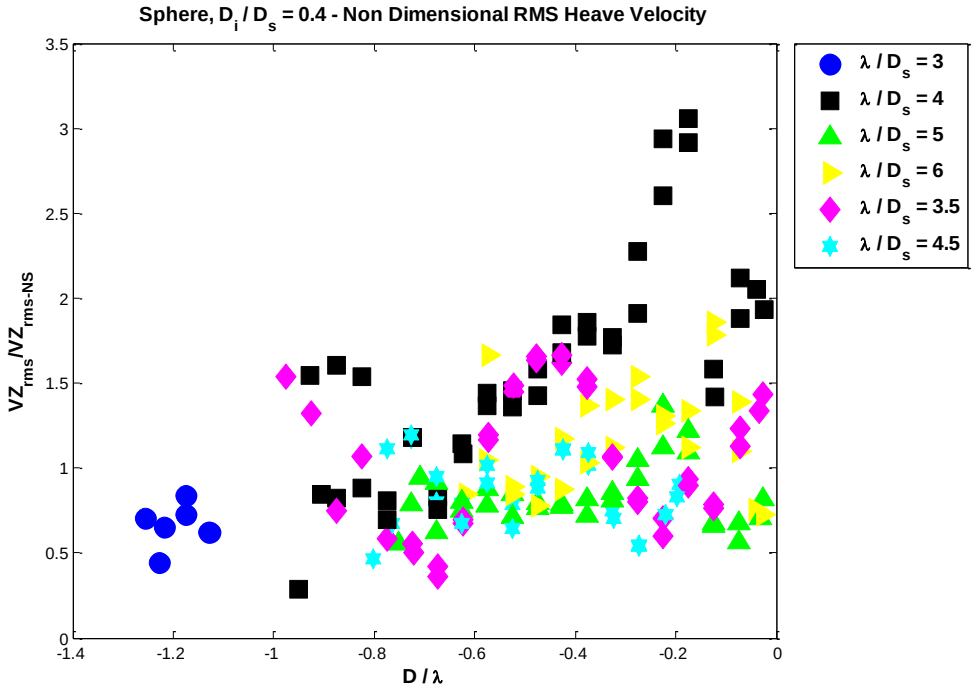

Figure 3.50: Non-dimensional RMS Heave velocity for sphere $D_i/D_s = 0.4$ tested in all waves

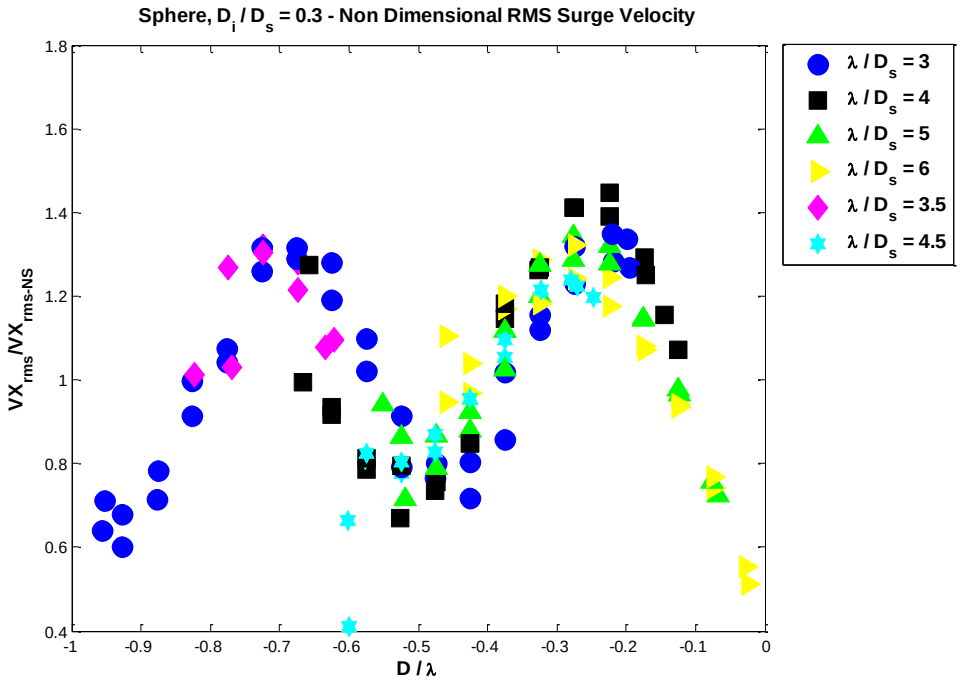

Figure 3.51: Non-dimensional RMS Surge velocity for sphere $D_i/D_s = 0.3$ tested in all waves

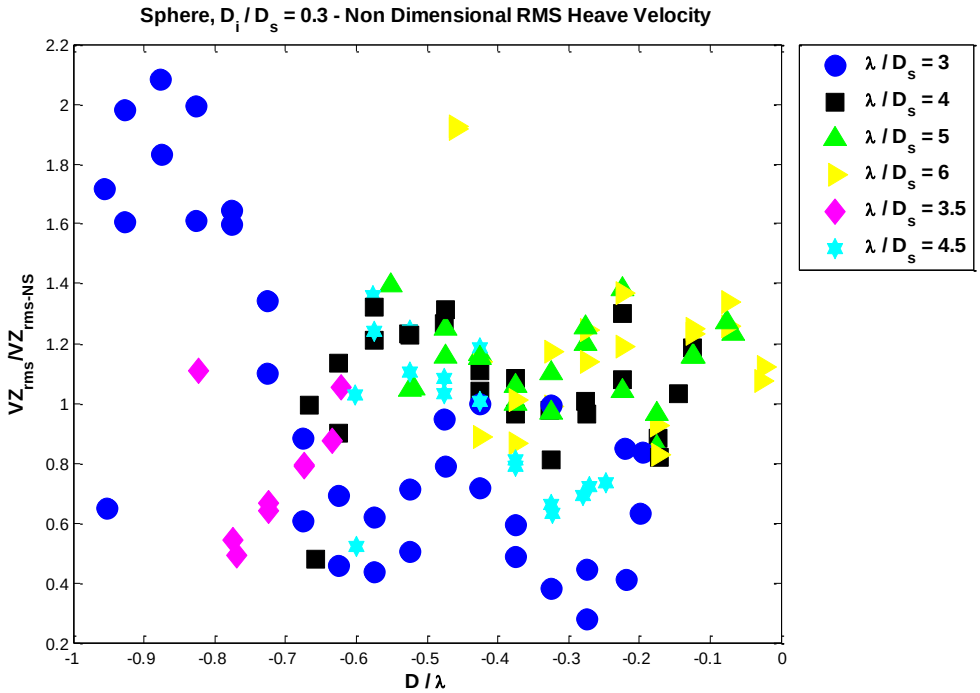

Figure 3.52: Non-dimensional RMS Heave velocity for sphere $D_i/D_s = 0.3$ tested in all waves

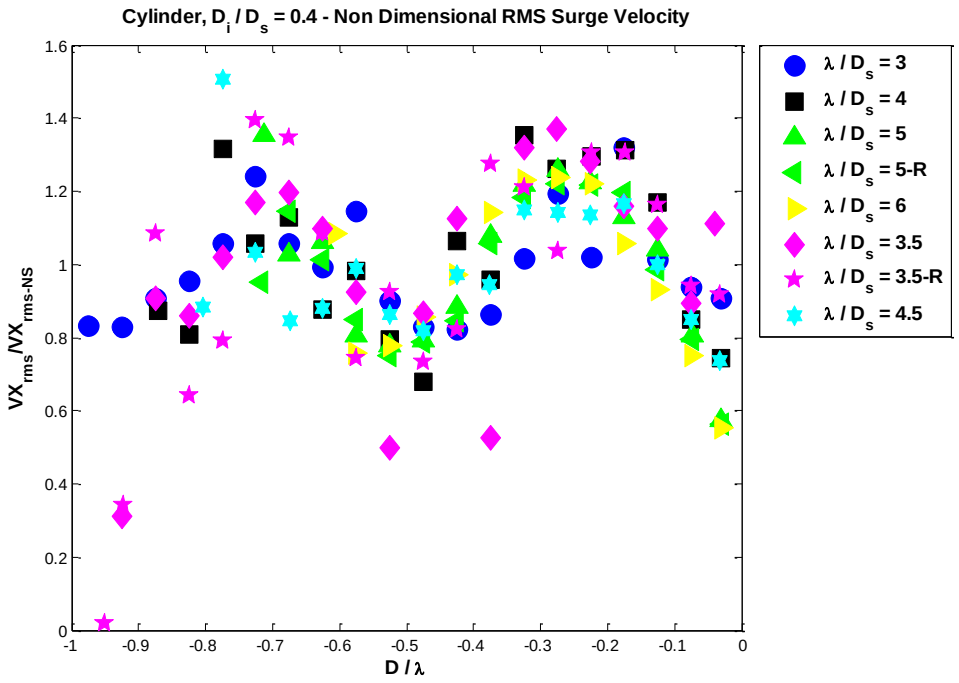

Figure 3.53: Non-dimensional RMS Surge velocity for cylinder $D_i/D_s = 0.4$ tested in all waves

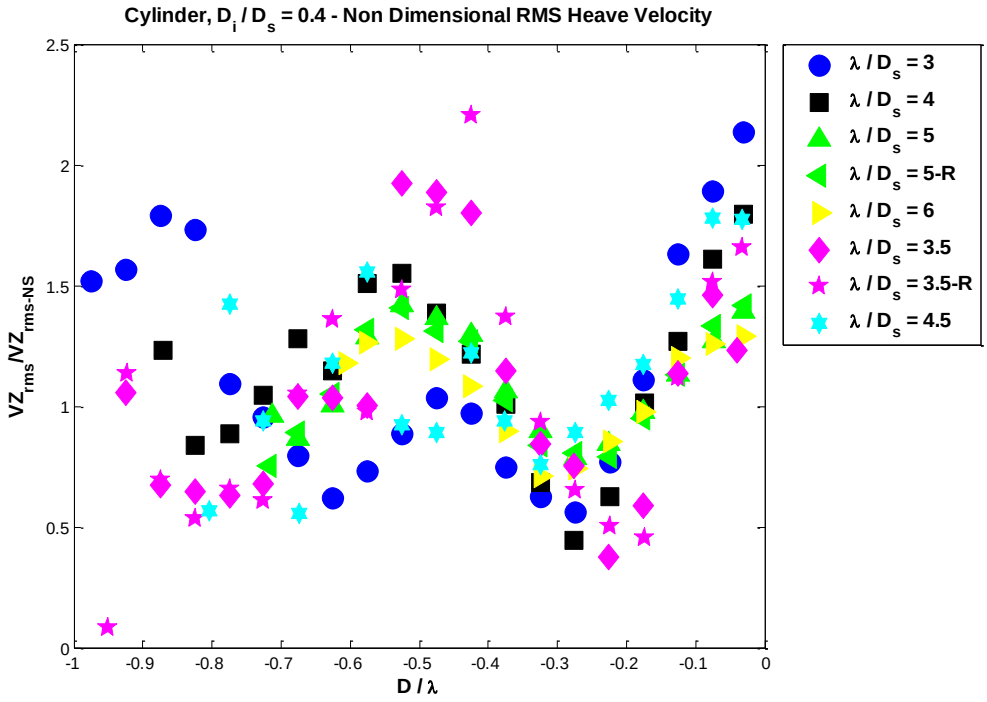

Figure 3.54: Non-dimensional RMS Heave velocity for cylinder $D_i/D_s = 0.4$ tested in all waves

Again similar to previous analysis, a further collapse of the data can be achieved when the normalized RMS velocities are further normalized by the relative separation distance and divided by D/λ. This non-dimensionalization obscures the effect of proximity somewhat as the D/λ term becomes very small as the structure is approached and thus the normalized velocity becomes very large for both surge and heave. It does however demonstrate that all the data can be reduced to a single curve. The data also shows that the relative velocity, normalized by the separation distance is not dependent on the ratio of sphere size to structure size but more dependent on the sphere size to wavelength ratio. Figure 3.55 shows the results for the sphere $D_i/D_s = 0.6$ including the effects of wave steepness (H/λ), where H is the wave height. Four waves ($\lambda/D_s =$ 3,4,5,6) of steepness 1/30 and two waves ($\lambda/D_s = 3.5,4.5$) of steepness 1/20 were tested and there is no discernible trend can be observed due to the effect of wave steepness.

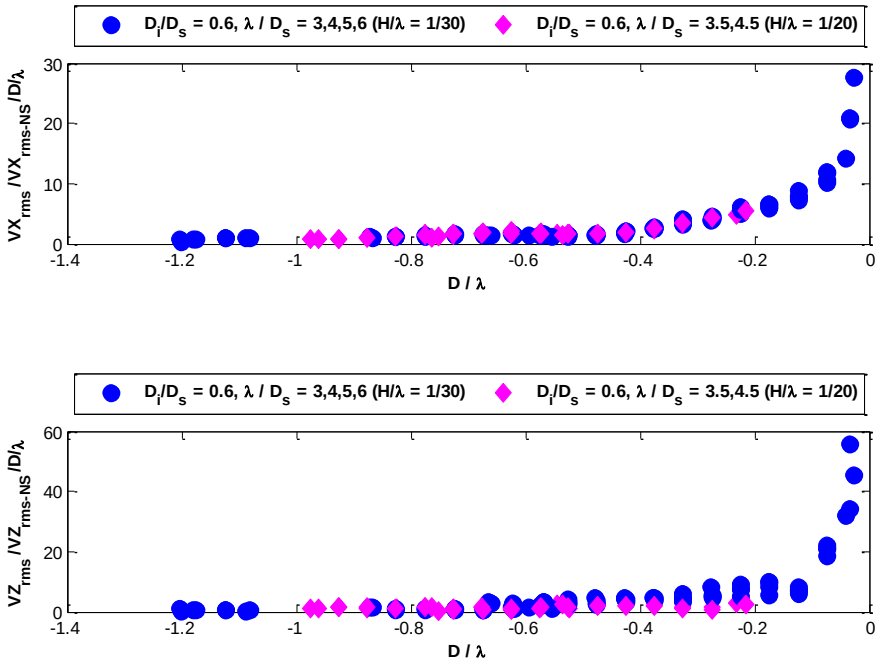

Figure 3.55: Non-dimensional RMS velocities normalized by D/λ for sphere $D_i/D_s = 0.6$

Figure 3.56 shows all non-dimensional RMS surge and heave velocities for the three spheres and the cylinder divided by D/λ and plotted against D/λ. This allows the derivation of a single equation that captures the results from all tests. This figure also shows the same trend of non-dimensional motions with little scatter for all the tested models. Based on these results it appears that Reynolds dissimilitude has little influence on wave induced motions and the application of Froude scaling seems to be the most appropriate scaling law.

The best-fit equations derived from this data for VX and VZ are as follows:

$$\log\left[\left(\frac{VX_{rms}}{VX_{rms-NS}}\right)/\left(\frac{D}{\lambda}\right)\right] = -0.984 * \log\left(\frac{D}{\lambda}\right) - 0.007$$

$$==>\left(\frac{VX_{rms}}{VX_{rms-NS}}\right)/\left(\frac{D}{\lambda}\right) = (10)^{-0.007} * \left(\frac{D}{\lambda}\right)^{-0.984} \quad (3.3)$$

$$\log\left[\left(\frac{VZ_{rms}}{VZ_{rms-NS}}\right)/\left(\frac{D}{\lambda}\right)\right] = -1.1174 * \log\left(\frac{D}{\lambda}\right) - 0.047$$

$$==>\left(\frac{VZ_{rms}}{VZ_{rms-NS}}\right)/\left(\frac{D}{\lambda}\right) = (10)^{-0.047} * \left(\frac{D}{\lambda}\right)^{-1.1174} \quad (3.4)$$

These equations show the same trend, and strength of trend, evident in the similar equations derived for the forces in Section 3.1, and indicate that there is good correlation between the force measurements and the resulting velocity profiles. It is to be noted that the negative values shown on the plots needed to be made positive distances for the curve fit.

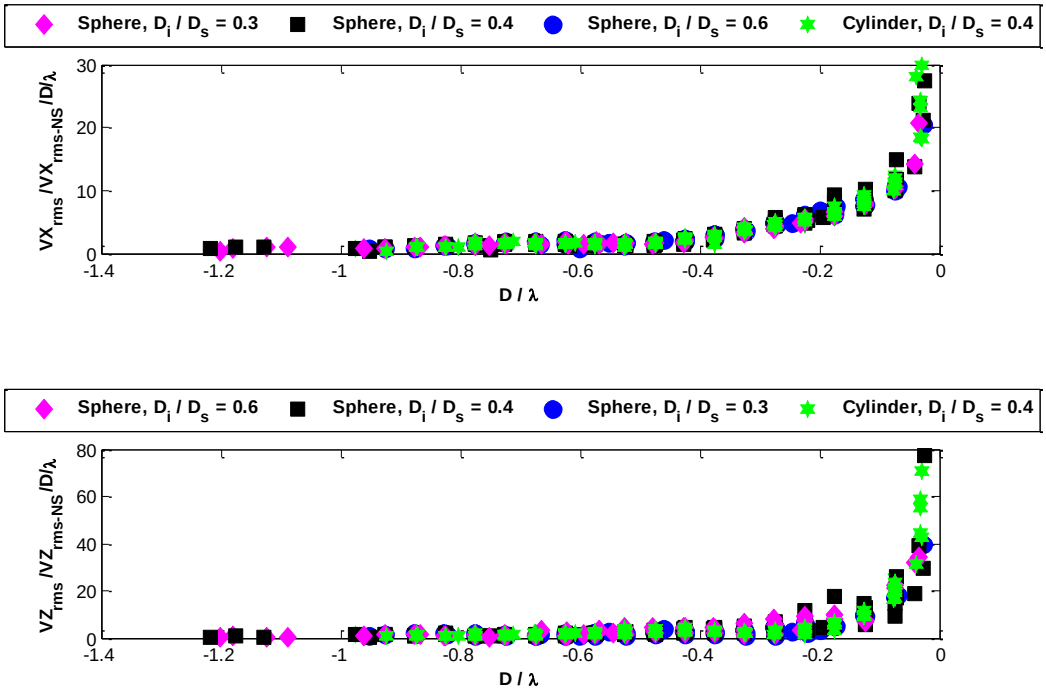

Figure 3.56: Non-dimensional RMS surge and heave velocities normalized by D/λ for all data

3.2.2.3 Correlation with Wave Envelope

In previous experiments, the wave envelope was measured in front of the structure by traversing a wave probe along the direction of wave propagation at slow constant speed using the tow carriage. Figure 3.57 shows the measured wave envelope for wave $\lambda/D_s = 5$ at two speeds and Figure 3.58 shows the surge and heave velocities for cylinder $D_i/D_s = 0.4$ tested with structure in the same wave condition. This shows the strong correlation between the wave envelope in front of the structure and the surge and heave motions of an approaching body towards a fixed structure.

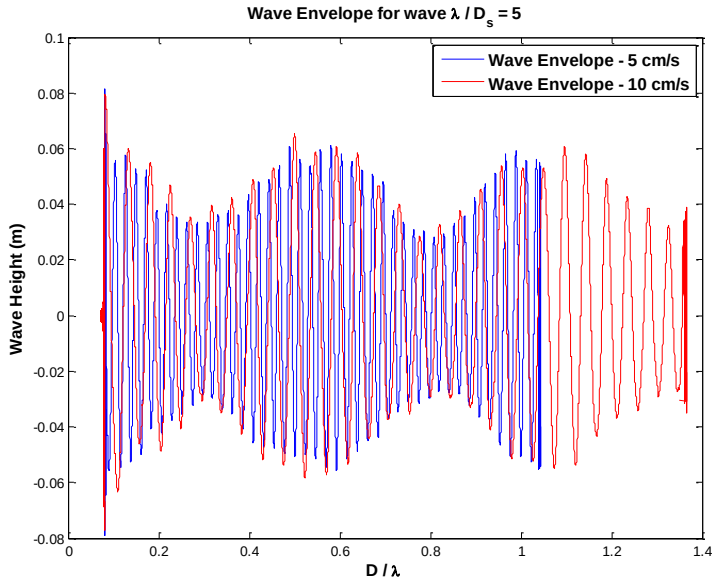

Figure 3.57: Wave envelope in front of structure for wave $\lambda/D_s = 5$ measured at two speeds

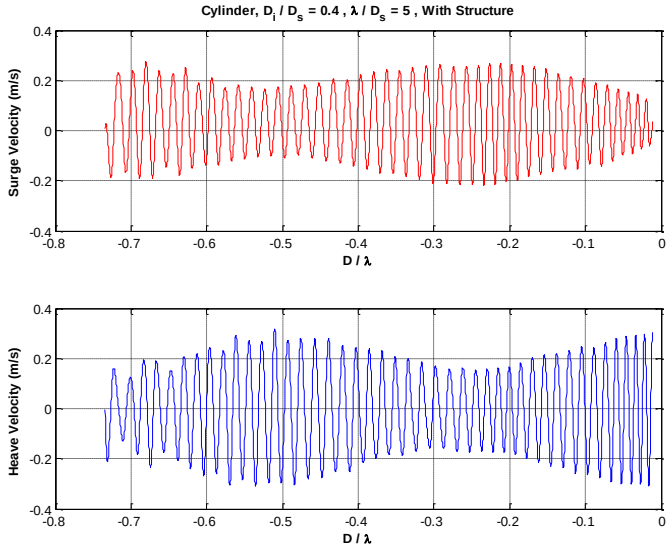

Figure 3.58: Surge and Heave velocity for cylinder $D_i/D_s = 0.4$ tested in wave $\lambda/D_s = 5$ with structure

The surge motions always follow nicely with the corresponding wave envelope, whereas the heave motions are not as well correlated, particularly for the spherical models. Figure 3.59 shows

the heave velocities for the three spheres in the same wave $\lambda/D_s = 5$ tested with structure. This shows the non-linear heave motions of the spherical models due to large submergence and large excursions from equilibrium position during wave excitation similar to that observed by Attwood (1987), and Wishahy et al. (1987).

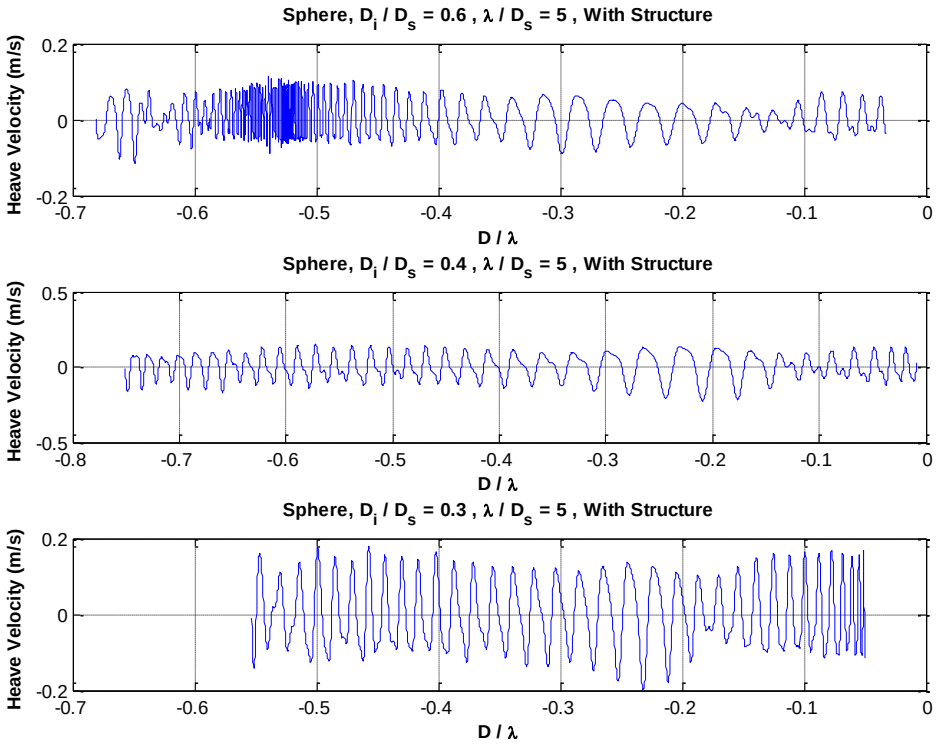

Figure 3.59: Heave velocities for the three spheres in wave $\lambda/D_s = 5$ tested with structure

3.2.2.4 Effect of Initial Starting Location

McGovern and Bai (2014b), Su et al. (2016) reported that small variations in initial starting condition may lead to significant variations in resulting impact location and velocity. During the initial testing phase, similar behavior was noticed when the same sphere moved towards the structure when started from a certain location and moved away from the structure when started

from another location. Hence some experiments were conducted to understand the effect of initial starting location on the resulting drift velocity. It is to be noted that initial starting condition implies both starting location and the wave phase during release. In the experiments only starting location with respect to the structure was varied and not the wave phase. The sphere $D_i/D_s = 0.6$ was tested with structure at five different starting locations and each test was repeated at least twice. The test matrix is given Table 3.6.

Table 3.6: Sphere, $D_i/D_s = 0.6$, with structure cases

Wave (λ/D_s)	2.6m	2m	1.6m	1m	0.6m
3	xx	xx	xx	xx	xx
4	xx	xx	xx	xx	xx
5	xx	xx	xx	xx	xxxxx
6	xx	xx	xx	xx	xx
3.5	xx	xx	xx	xx	xx
4.5	xx	xx	xx	xx	xx

It was observed that for the same wave condition and different starting location, the sphere exhibits different motion behaviour. Figures 3.60 shows the time history of surge motions for the sphere tested in $\lambda/D_s = 4$ starting at five different locations from the structure. The differences in the resulting drift motions are obvious due to different initial starting locations.

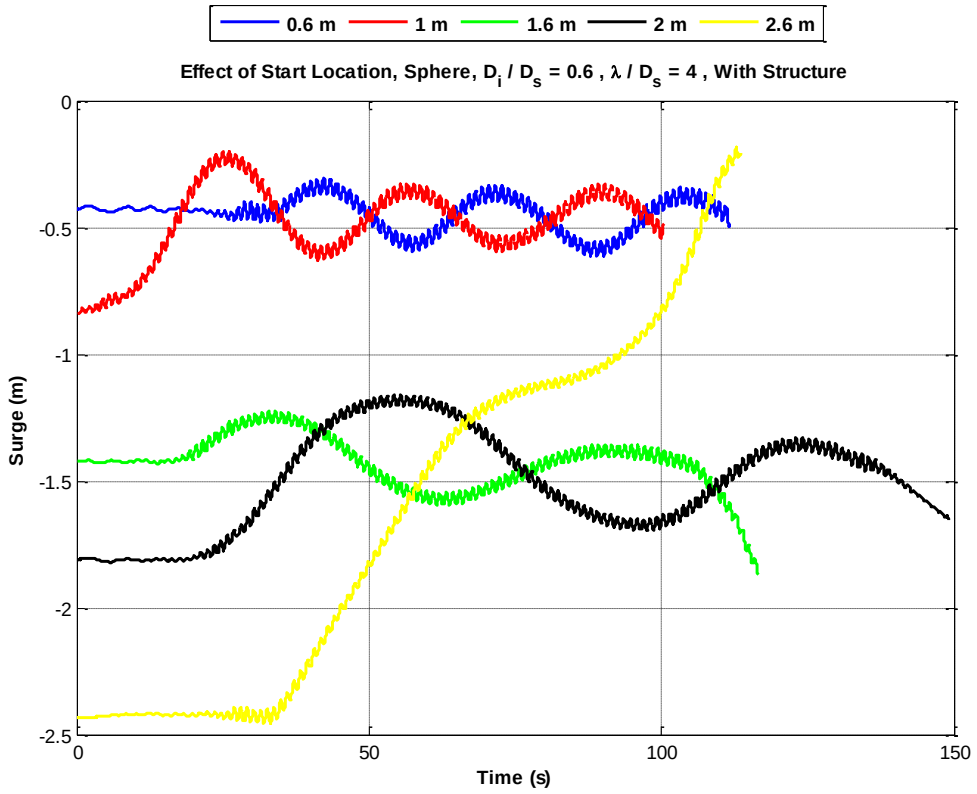

Figure 3.60: Effect of start location on surge drift for sphere $D_i/D_s = 0.6$ tested in wave $\lambda/D_s = 4$

Figure 3.61 shows the surge velocity of the sphere plotted against D/λ for wave $\lambda/D_s = 3.5$ tested in five different release locations. There is an offset of half the diameter in surge displacement since the starting location is measured from the center of the sphere to the face of the structure. The starting locations of 2.6, 2 and 1.6 m are ahead of the point where $D/\lambda = 0.5$ and the sphere gets stuck close to $D/\lambda = 0.5$ and then reverses direction, whereas the starting locations of 1 and 0.6 m are behind the point where $D/\lambda = 0.5$ and the sphere then proceeds to a point very close to the structure and then reverses direction. As discussed before, there are multiple nodes and antinodes in front of the structure due to the standing wave profile. At antinode locations, the body is slowed in surge and experiences increased heave motions.

Depending on the forward momentum of the sphere, the body may be slowed sufficiently in those locations to reduce the forward momentum to zero thus causing it to reverse direction or it may have enough forward momentum to continue to move forward. The initial starting location dictates how many antinodes (obstacles) the body has to overcome to go forward towards the structure. This is why the direction of drift velocity changes depending on the initial release location. It is to be noted that the other factor of wave phase is also important because the initial momentum of the body will vary depending on whether the body is released at wave crest or wave trough.

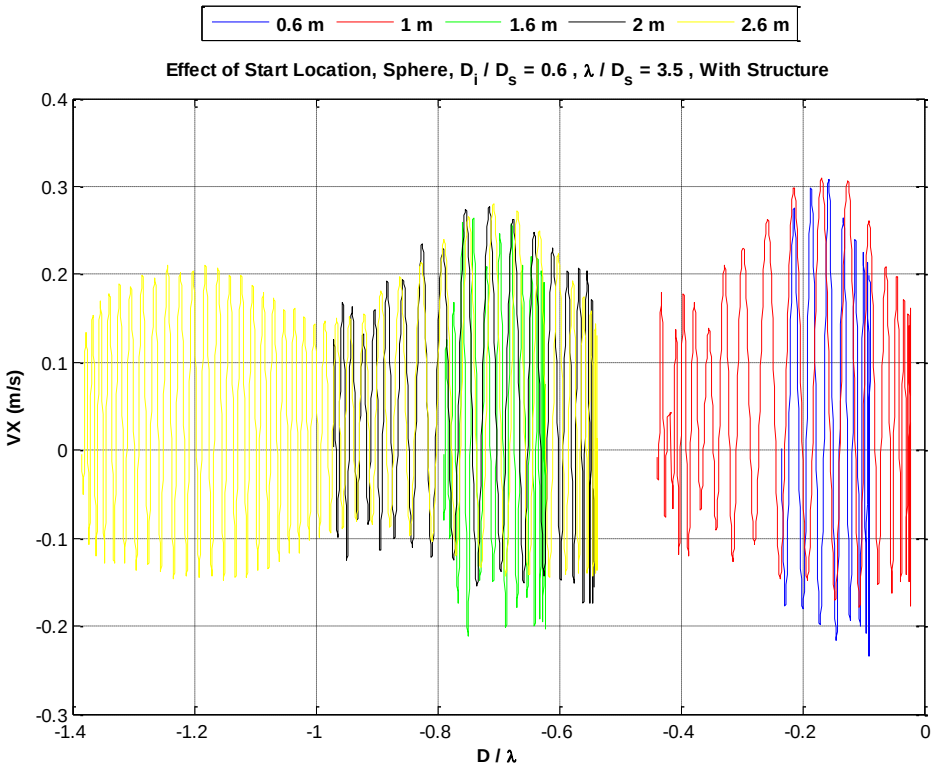

Figure 3.61: Effect of start location on surge velocity for sphere $D_i/D_s = 0.6$ tested in wave $\lambda/D_s = 3.5$

For the same wave condition and same starting location, the repeat runs showed exactly the same behaviour except for two conditions: one for wave $\lambda/D_s = 5$ started from 0.6m ahead of the structure and the other one for wave $\lambda/D_s = 4.5$ started from 2.6m ahead of the structure. Five repeats were conducted for wave $\lambda/D_s = 5$ started from 0.6m, where in two cases the sphere went in and hit the structure and in three cases the sphere did not hit the structure and reversed direction. Similarly for wave $\lambda/D_s = 4.5$ started from 2.6m, in one case the sphere went forward towards the structure and in the other case the sphere reversed direction as it approached the structure after release. These two cases can be attributed to the difference in the initial wave phase being not matched in those repeat runs. The distance of 0.6m is very close to the structure and the initial transient makes the difference in the initial momentum of the sphere. Initial difference in momentum was also felt in the case of 2.6m and the sphere started going forward when slightly pushed by hand.

Thus initial starting conditions of location and wave phase have significant influence on the resulting direction of the drift velocity. It is to be noted that this work is only studying the wave induced motions of the ice masses and there are other environmental forces like current, wind, pack ice etc., in prototype conditions the iceberg may be driven to any offset location from the structure and then the berg can be influenced by wave forces. Thus the main focus is to understand the velocity profile change in front of the structure prior to impact and not concerned with whether the body will hit the structure or not.

3.3 Experimental Investigation in Irregular Waves

The next logical step after investigating the wave forces and wave induced motions in regular waves is to investigate the phenomenon in irregular waves. It is also interesting to know whether the observations found in regular waves will still hold in irregular sea and whether linear superposition theory may be applicable to identify the motion statistics in irregular waves.

3.3.1 Experimental Program

The irregular wave experiments involved the measurement of the motions of the free floating ice masses with and without the presence of the fixed structure in irregular waves in the same way as the previous experiments. The objective of these experiments is to identify the change in velocity profiles due to the presence of the structure. Some tests are also conducted to measure the spatial distribution of significant wave heights up to a distance of 2m in front of the structure at locations 10cm apart.

3.3.1.1 Facility

The experiments were conducted in the Towing Tank of the Ocean Engineering Research Center (OERC) at Memorial University of Newfoundland (MUN) in St. John's, NL Canada. The Towing tank particulars are given in previous section (3.1.1.1).

3.3.1.2 Models and Instrumentation

The same ice mass models and fixed structure is used for the experiments in irregular waves. The motions are measured using Qualisys Optical Tracking System. The details of models and instrumentation are described in section 3.2.1.2.

3.3.1.3 Environment

The towing tank water depth was 1.8 m. Five irregular waves of different significant wave heights and periods were used. JONSWAP spectrum was used to generate the irregular sea as used by several researchers (Mak et al. (1990), Isaacson and McTaggart (1990b), McGovern and Bai (2014b)). The peak enhancement factor, γ of 2.2 was used. The wave spectra were selected to cover the range of dominant wavelengths covered by the regular wave tests but were not otherwise matched to any particular wave condition. The duration of the generated spectra was 2 minutes. The wave particulars are given in Table 3.7. Both the results of spectral and zero crossing analyses are given here. The results of the spectral analysis are considered for the further data analysis. The peak wavelength, λ_p is calculated using the dispersion relationship of linear wave theory.

Table 3.7: Irregular wave particulars

Wave	Measured (Spectral Analysis)		Measured (Zero crossing Analysis)		Peak Wavelength, λ_p (m)	λ_p/D_s
	Significant Wave Height, H_{m0} (m)	Peak Period, T_p (sec)	Significant Wave Height, H_{m0} (m)	Peak Period, , T_p (sec)		
IRR -1	0.048	1.12	0.048	1.06	1.96	3.9
IRR -2	0.069	1.26	0.069	1.17	2.48	4.9
IRR -3	0.083	1.43	0.083	1.31	3.19	6.4
IRR -4	0.099	1.48	0.100	1.44	3.42	6.8
IRR -5	0.107	1.64	0.103	1.54	4.12	8.4

3.3.1.4 Methodology

The procedure of the experimental set up is similar to what described in 3.2.1.4. Table 3.8 shows the test matrix for the experiments in irregular waves.

Table 3.8: Test matrix for experiments in irregular waves

		No Structure				With Structure			
Wave (λ_p/D_s)	Ice model	Sphere, $D_i/D_s = 0.6$ ($D = 2m$)	Sphere, $D_i/D_s = 0.4$ ($D = 2m$)	Sphere, $D_i/D_s = 0.3$ ($D = 1.6m$)	Cylinder, $D_i/D_s = 0.4$ ($D = 2m$)	Sphere, $D_i/D_s = 0.6$ ($D = 2m$)	Sphere, $D_i/D_s = 0.4$ ($D = 2m$)	Sphere, $D_i/D_s = 0.3$ ($D = 1.6m$)	Cylinder, $D_i/D_s = 0.4$ ($D = 2m$)
3.9		X	XX	X	XX	XX	XX	XX	X
4.9		X	X	X	X	XX	XX	XX	X
6.4		XX	X	X	X	XX	XXX	XXX	XX
6.8		XX	X	X	X	XX	XX	XXX	X
8.4		X	X	X	X	XX	XX	XX	X

(D – Initial release distance measured from ice model center to structure face, D_i – Sphere diameter, D_s – Structure diameter, λ – Wavelength, X – one test, XX – repeat twice, XXX – repeat thrice)

3.3.2 Results and Discussion

3.3.2.1 Wave Data

Klopman and van der Meer (1999) investigated the spatial variation of wave spectrum and significant wave height in front of a vertical wall and a rubble mound breakwater in random waves. The significant wave heights show a standing wave pattern extending over two times the peak wavelength for the given JONSWAP spectrum. The findings of nodal and antinodal frequencies follow the patterns of linear wave theory. Figure 3.62 shows the variation of significant wave height in front of two reflective structures and the standing wave pattern from linear wave theory for two wave steepness cases.

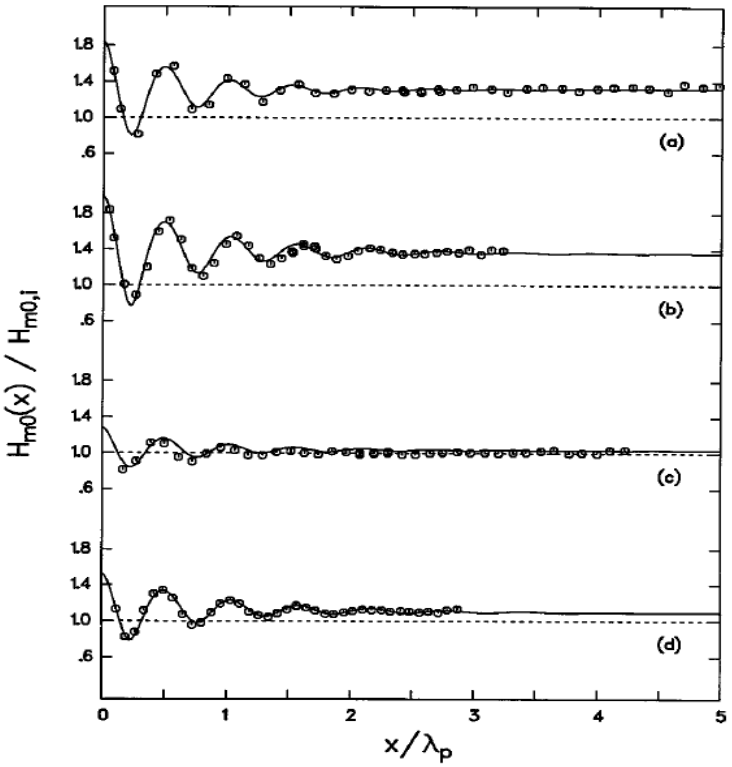

Figure 3.62: Spatial variation of measured and theoretical non-dimensional significant wave height in front of (a) vertical wall and wave steepness 0.04, (b) vertical wall and wave steepness 0.02, (c) breakwater and wave steepness 0.04, and (d) breakwater and wave steepness 0.02; solid line – theory, circle – experiment (from Klopman and van der Meer (1999))

In the present study, an array of four stationary wave probes as shown in Figure 3.63 were used to measure the spatial distribution of wave heights in front of the structure. The closest distance was 4 cm ahead of the structure and the probes were 10 cm apart. Another wave probe was placed far upstream and close to the wave board. The probes were attached to the carriage and the carriage was moved to change the locations of the probes. A total distance of 2 m in front of the structure was covered.

Figure 3.63: Array of wave probes in front of fixed structure

Figure 3.64 shows the spatial variation of non-dimensional significant wave heights in front of the structure. It is obvious the presence of the structure has significant influence on the measured significant wave heights at different locations away from the structure. This influence decays after a distance of $D/\lambda_p = 0.5$. It is to be noted that the significant wave height significantly increases close to the structure. This is due to the standing wave in front of the structure generated by the superposition of the incident and reflected peak-frequency wave. The standing wave pattern is also similar to linear wave theory demonstrating the nodes and antinodes at expected locations.

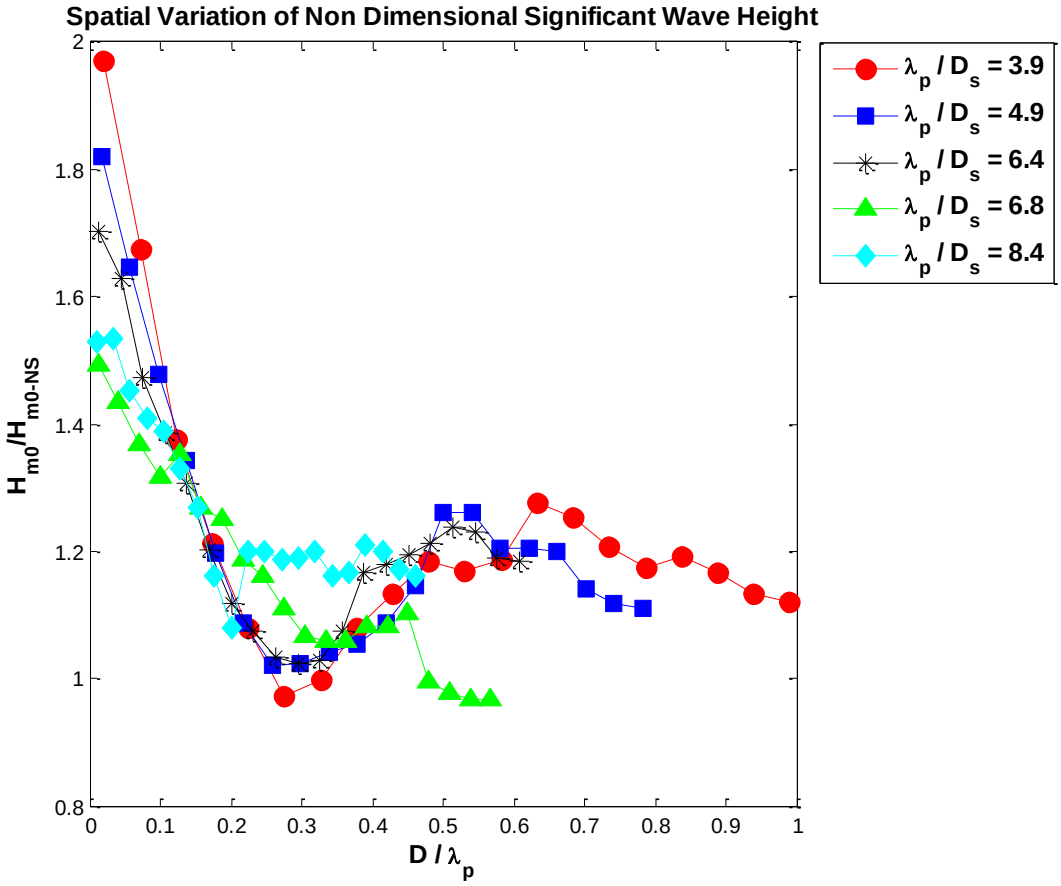

Figure 3.64: Non dimensional significant wave height at different locations in front of structure

Figure 3.65 shows the change in wave spectrum at five different locations away from the structure for wave $\lambda_p/D_s = 6.4$. It also includes the wave spectrum for no structure case ($D/\lambda_p = \infty$). It is evident that there is significant change in wave energy content spatially due to the structure presence. Wave energy is lower at node $D/\lambda_p = 0.26$ and comparatively higher at antinode $D/\lambda_p = 0.51$. Also beyond $D/\lambda_p = 0.26$, the wave energy keeps increasing as the body gets close to the structure.

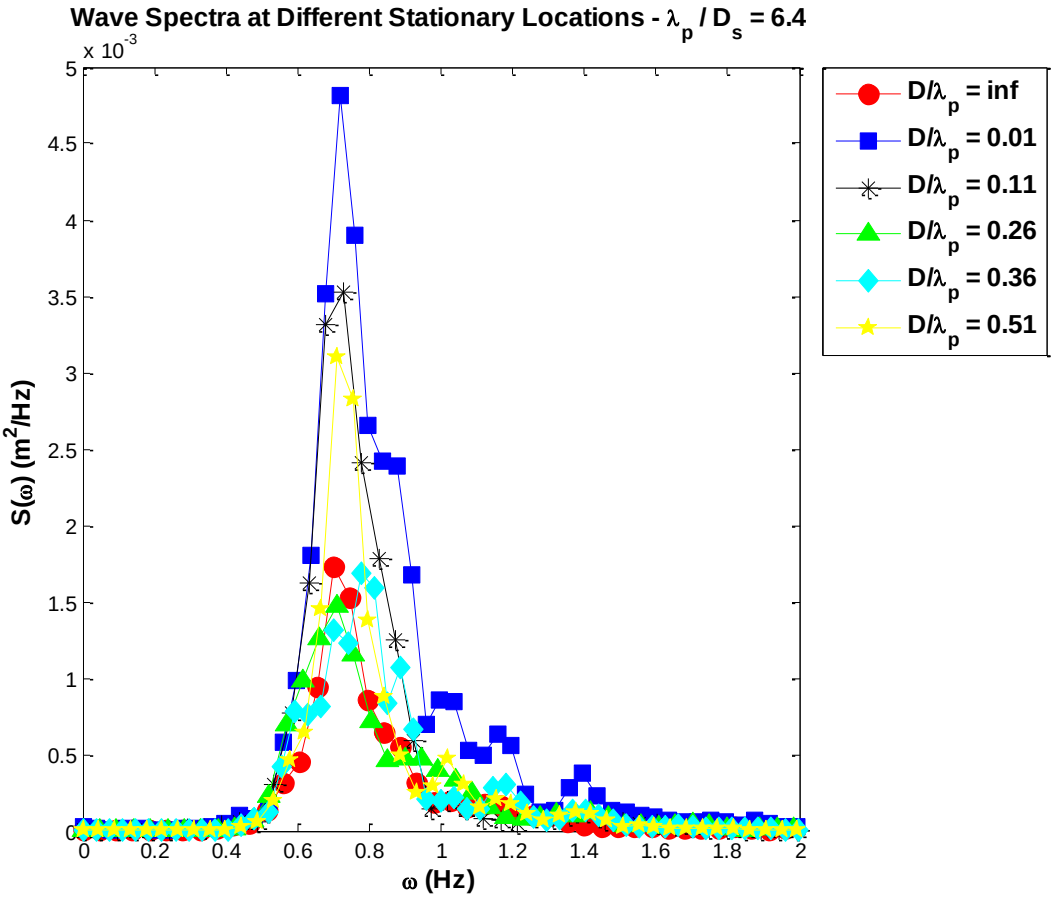

Figure 3.65: Wave spectra without structure and at five different locations in front of structure for wave $\lambda_p/D_s = 6.4$

It may be inferred from the present analysis that at the tested stationary locations in front of the structure, the significant forces and motions for surge and heave will be amplified at the node and antinode locations in front of the structure. Also the significant heave forces and motions will increase and significant surge forces and motions will decrease as the body gets closer to the structure.

3.3.2.2 Free Floating Motion Data

Experiments were conducted with the three spherical and one cylindrical model subjected to five irregular waves. The models were tested with and without the fixed structure and motions are captured using Qualisys. The data measured included time series of full 6 DOF motions and the wave profiles from the wave probes. The models are restrained to vertical plane motions only (surge, heave and pitch) by two guide wires and also further ballasted to minimize pitch motions. Only surge and heave motion data are considered for the present analysis. The distance in the surge direction is considered positive in the direction of wave travel and the heave displacement is positive upward. A Butterworth low-pass filter was applied to the raw data to filter out high frequency noise. Figure 3.66 shows two typical irregular wave cases during the experiment.

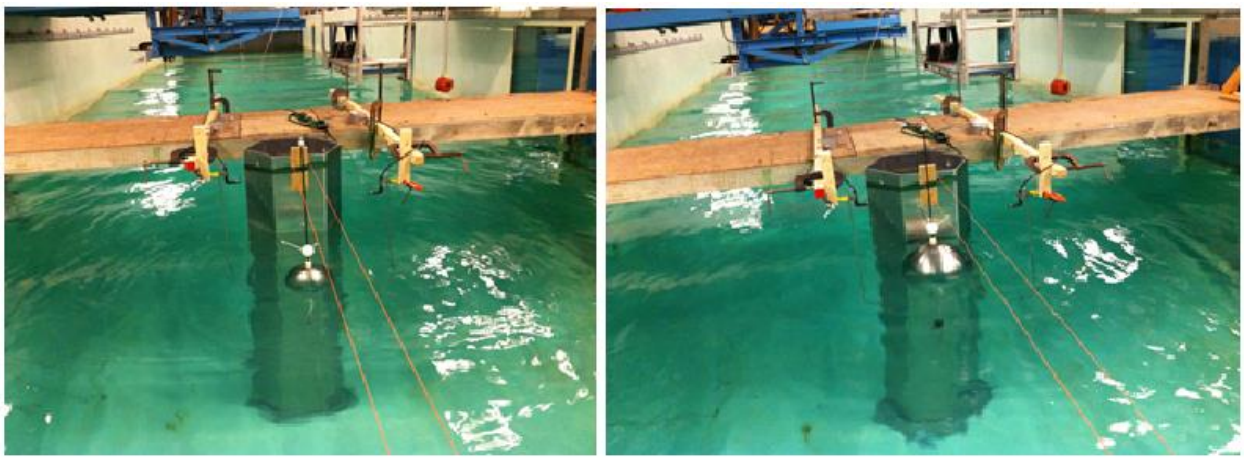

Figure 3.66: Spherical models in irregular waves

The 6 DOF motion data are resolved to the center of gravity for each model. The structure face location in x-direction is considered as the origin. The time series of raw data for surge, and heave motions for sphere $D_i/D_s = 0.4$ tested without the structure in wave $\lambda_p/D_s = 6.8$ is shown in Figure 3.67.

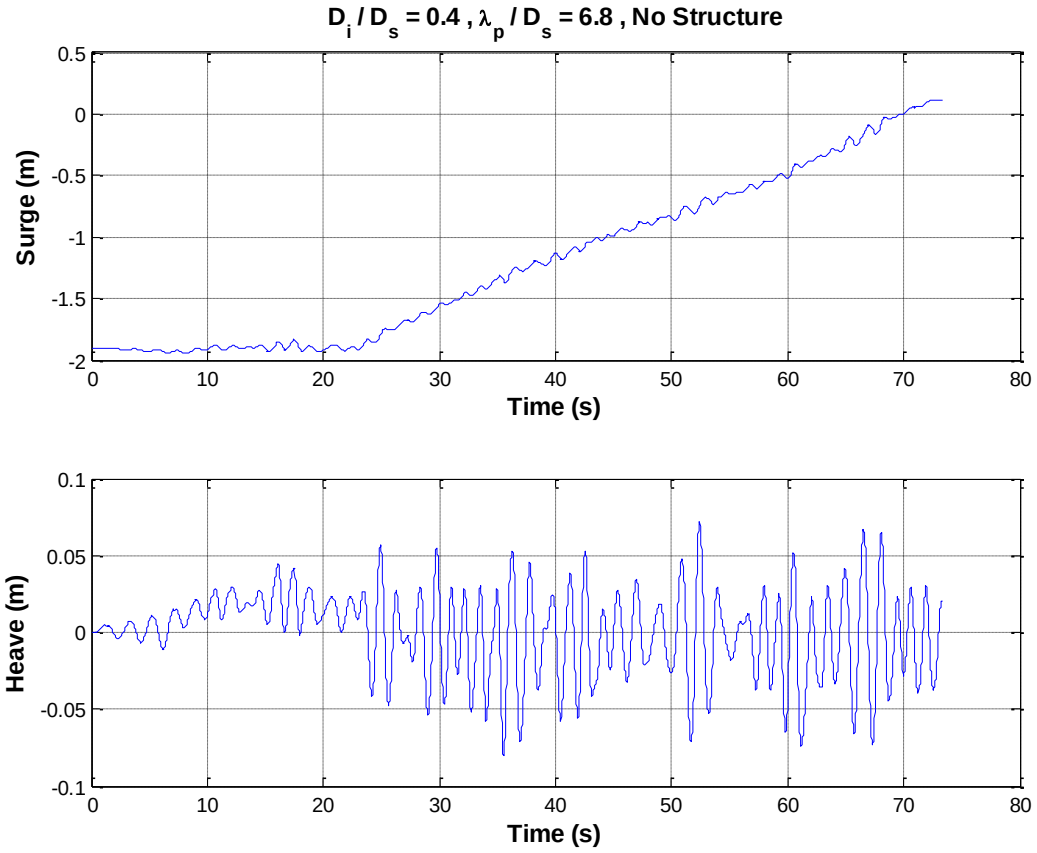

Figure 3.67: Time series of raw data of surge, and heave motions for sphere $D_i/D_s = 0.4$ tested without structure in wave $\lambda_p/D_s = 6.8$

Surge and heave displacements are differentiated to calculate corresponding surge and heave velocity. Figures 3.68 and 3.69 show the time series of surge and heave velocity for sphere $D_i/D_s = 0.6$ tested without structure and with structure respectively in wave $\lambda_p/D_s = 6.4$. Both figures also include results from repeat tests. It is to be noted that during these experiments, the wave phases are not matched while releasing the models.

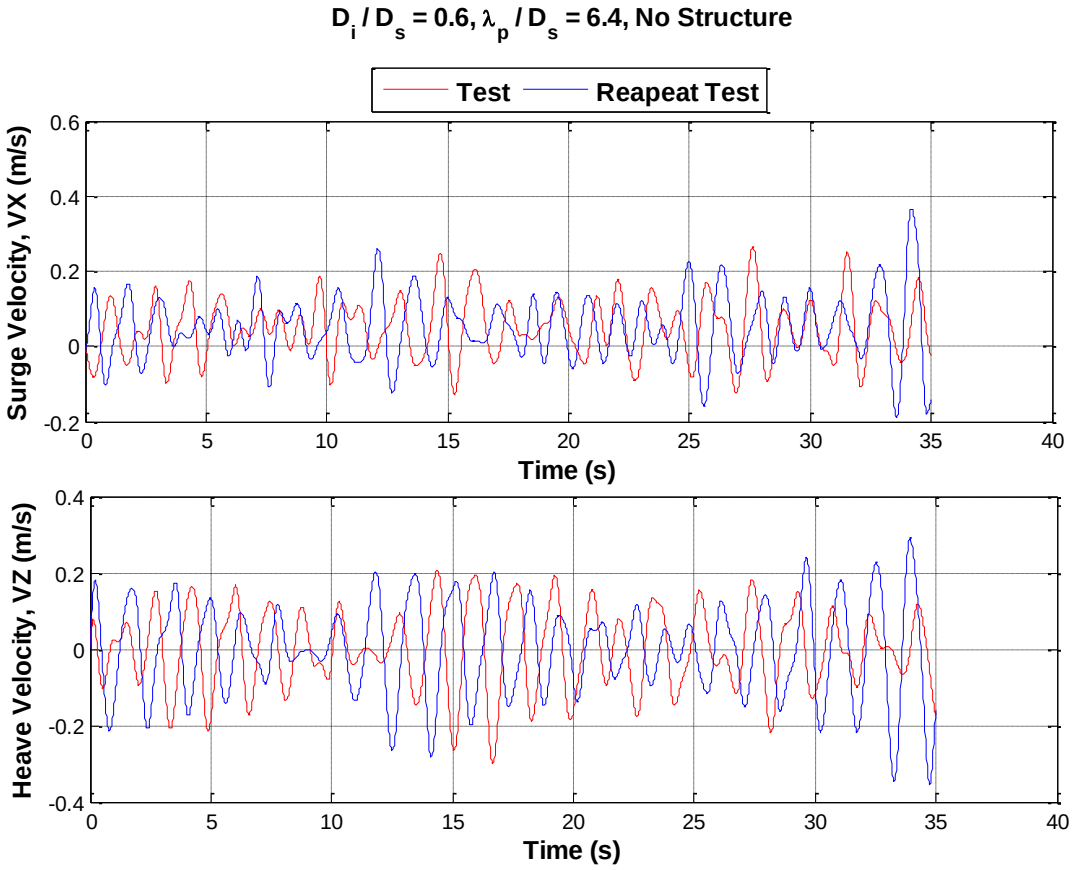

Figure 3.68: Time series of surge, and heave velocity for sphere $D_i/D_s = 0.6$ tested without structure in wave $\lambda_p/D_s = 6.4$

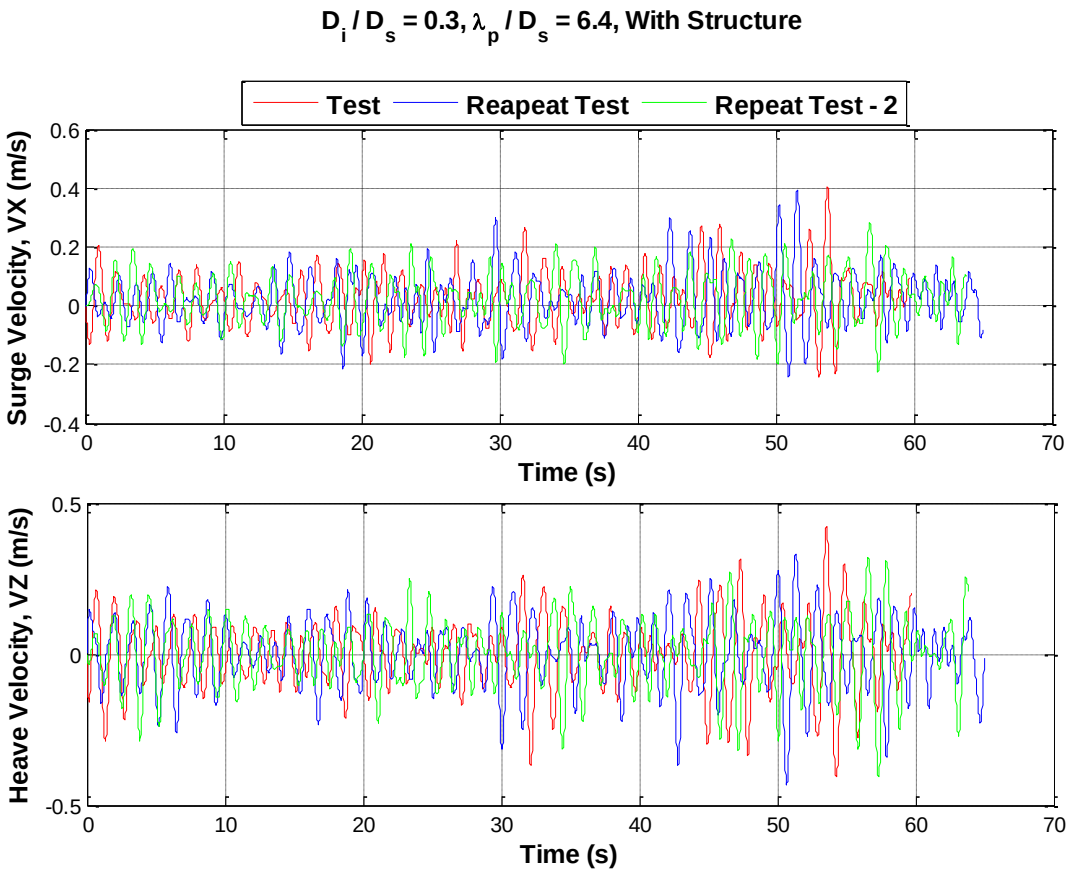

Figure 3.69: Time series of surge, and heave velocity for sphere $D_i/D_s = 0.3$ tested with structure in wave $\lambda_p/D_s = 6.4$

As part of the experimental procedure, each model was placed in the initial starting position and held for few seconds to let a few wave cycles pass by and insure that steady state reflections are developed from the structure. In all test cases in irregular waves, the models eventually go forward and hit the structure. From these free floating tests, there is not enough data at specific fixed locations in front of structure to compare the spatial velocity change due to the presence of the structure. This problem arises because the models continued to drift towards the structure as the experiment proceeded and could not be held at any particular location for a period of time

that would allow motions statistics to accumulate. Figures 3.70 and 3.71 show the comparison of surge and heave velocity plotted against D/D_i for sphere $D_i/D_s = 0.4$ tested with and without structure in wave $\lambda_p/D_s = 3.9$ and for cylinder $D_i/D_s = 0.4$ tested with and without structure in wave $\lambda_p/D_s = 8.4$. Since release conditions were not matched except for the initial starting location, this time series comparison doesn't provide exactly quantifiable information regarding the spatial velocity change because of the structure presence but it does show a slight decrease in surge velocity and a slight increase in heave velocity for the close proximity section.

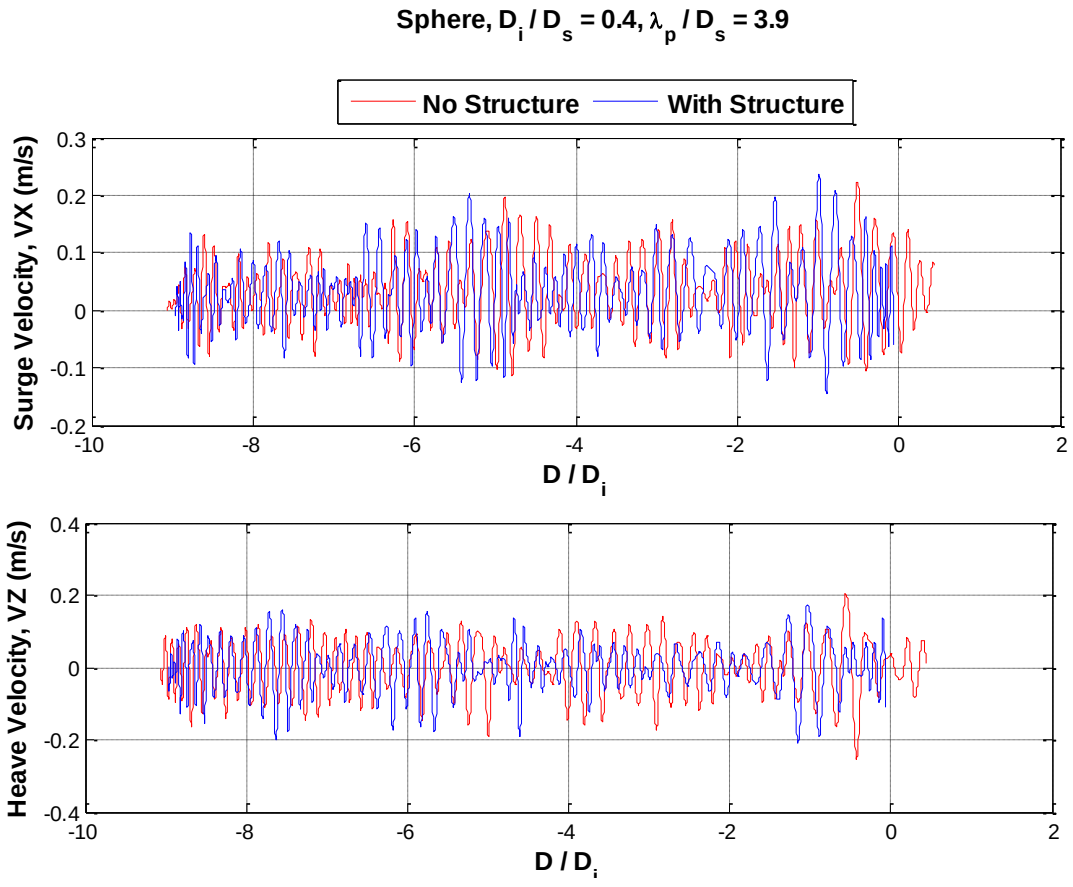

Figure 3.70: Comparison of surge, and heave velocity for sphere $D_i/D_s = 0.4$ tested with and without structure in wave $\lambda_p/D_s = 3.9$

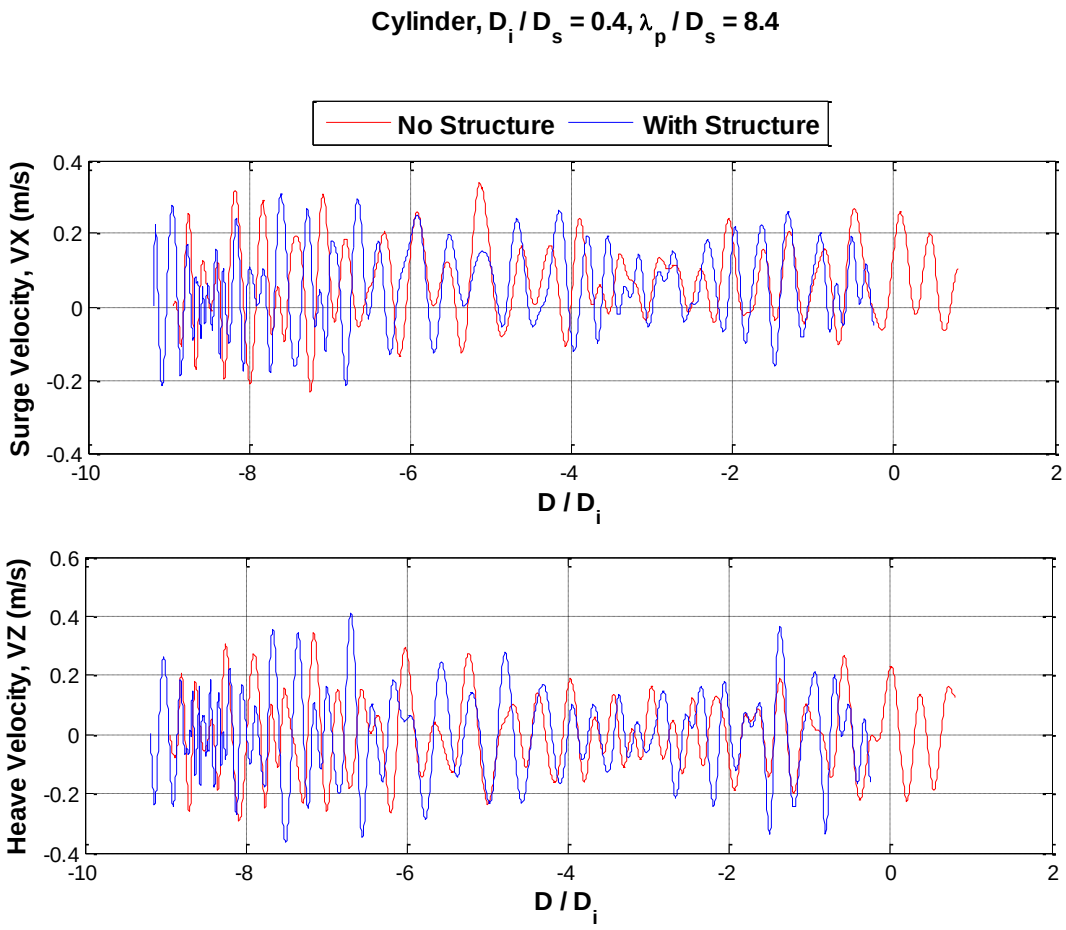

Figure 3.71: Comparison of surge, and heave velocity for cylinder $D_i/D_s = 0.4$ tested with and without structure in wave $\lambda_p/D_s = 8.4$

Next from the whole time series of surge and heave velocity, the velocity spectrums were calculated and the significant surge and heave velocities were compared for with and without structure conditions. Figures 3.72 and 3.73 show the comparison of surge and heave velocity spectrum for sphere $D_i/D_s = 0.6$ tested in wave $\lambda_p/D_s = 6.8$. The corresponding significant velocities, V_H for surge and heave are also given in Table 3.9. It is evident that there is small difference in velocity spectrum due to the presence of the structure.

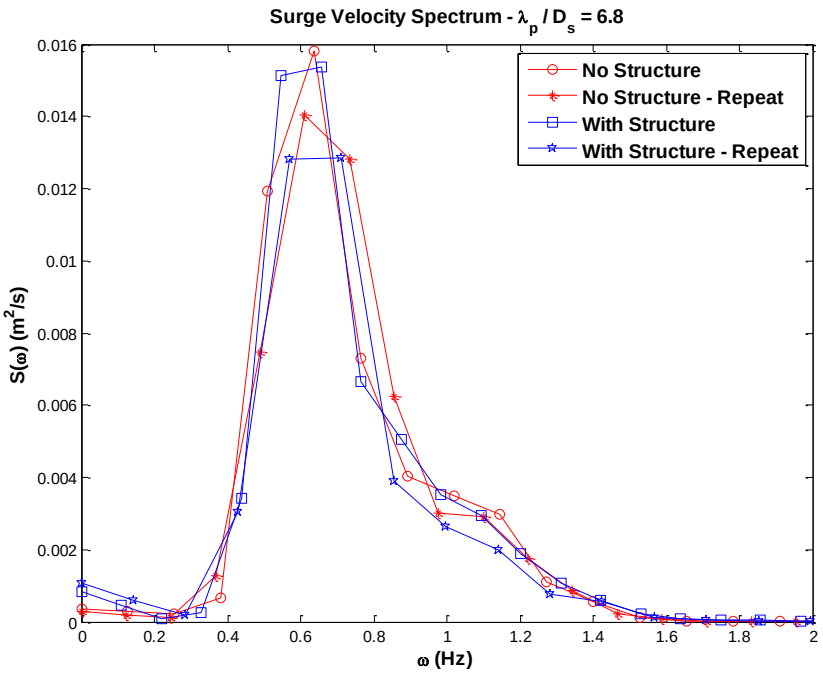

Figure 3.72: Surge velocity spectrum for sphere $D_i/D_s = 0.6$ tested in wave $\lambda_p/D_s = 6.8$

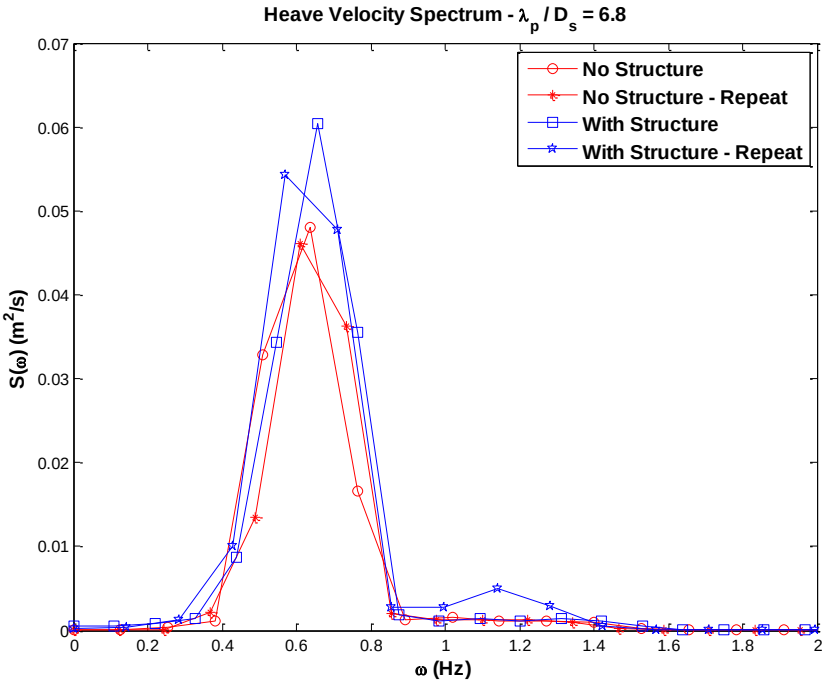

Figure 3.73: Heave velocity spectrum for sphere $D_i/D_s = 0.6$ tested in wave $\lambda_p/D_s = 6.8$

Table 3.9: Significant velocities for sphere $D_i/D_s = 0.6$ tested in wave $\lambda_p/D_s = 6.8$

Significant Velocity	No Structure	No Structure - Repeat	With Structure	With Structure - Repeat
$(V_H)_{Surge}$	0.3153	0.3163	0.3168	0.3027
$(V_H)_{Heave}$	0.4638	0.4546	0.5135	0.5403

Figures 3.74 and 3.75 show the non-dimensional significant velocities for surge and heave respectively for all the tested models in all wave conditions. The significant velocities are non-dimensionalized by the significant velocities of no-structure cases. Although the differences are small, on average the significant surge velocities go down and the significant heave velocities increase due to the structure presence.

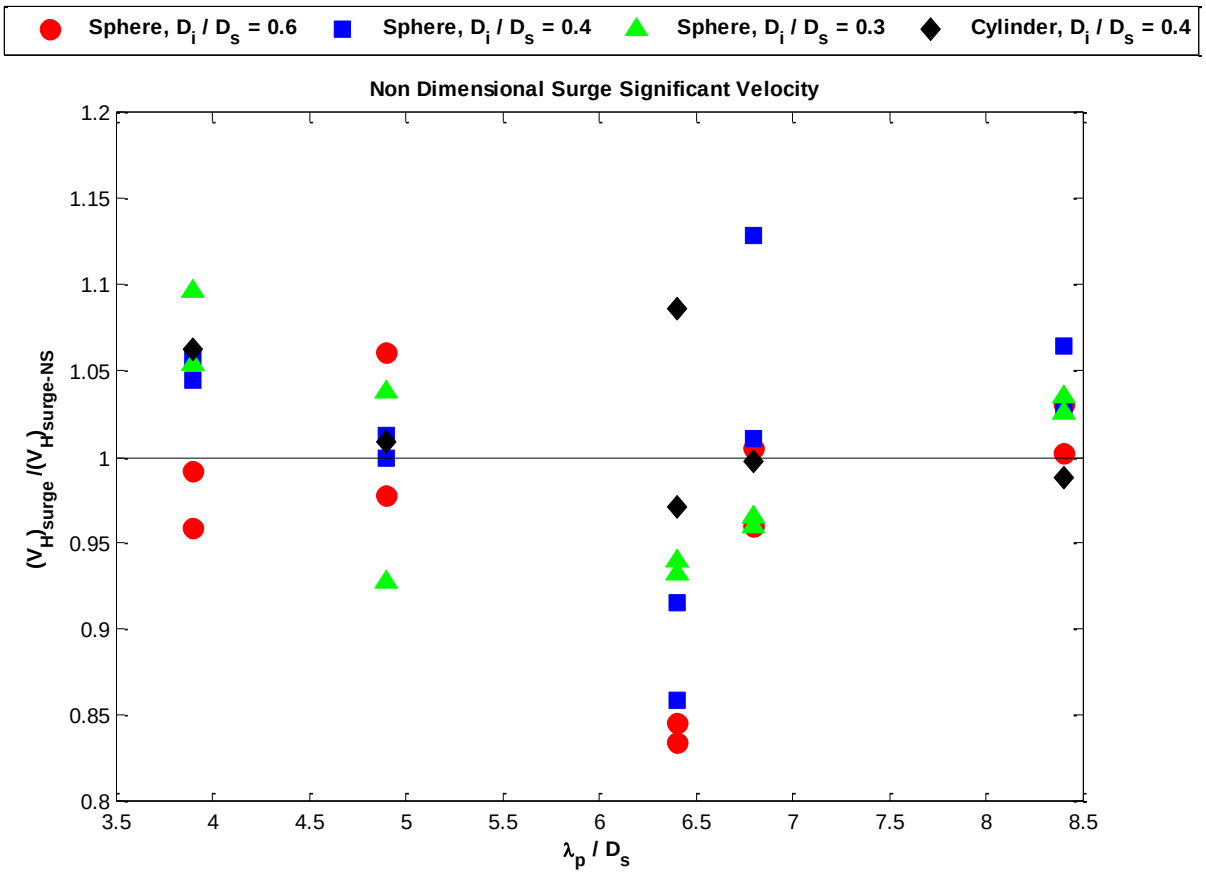

Figure 3.74: Non-dimensional surge significant velocity for all models tested in all waves

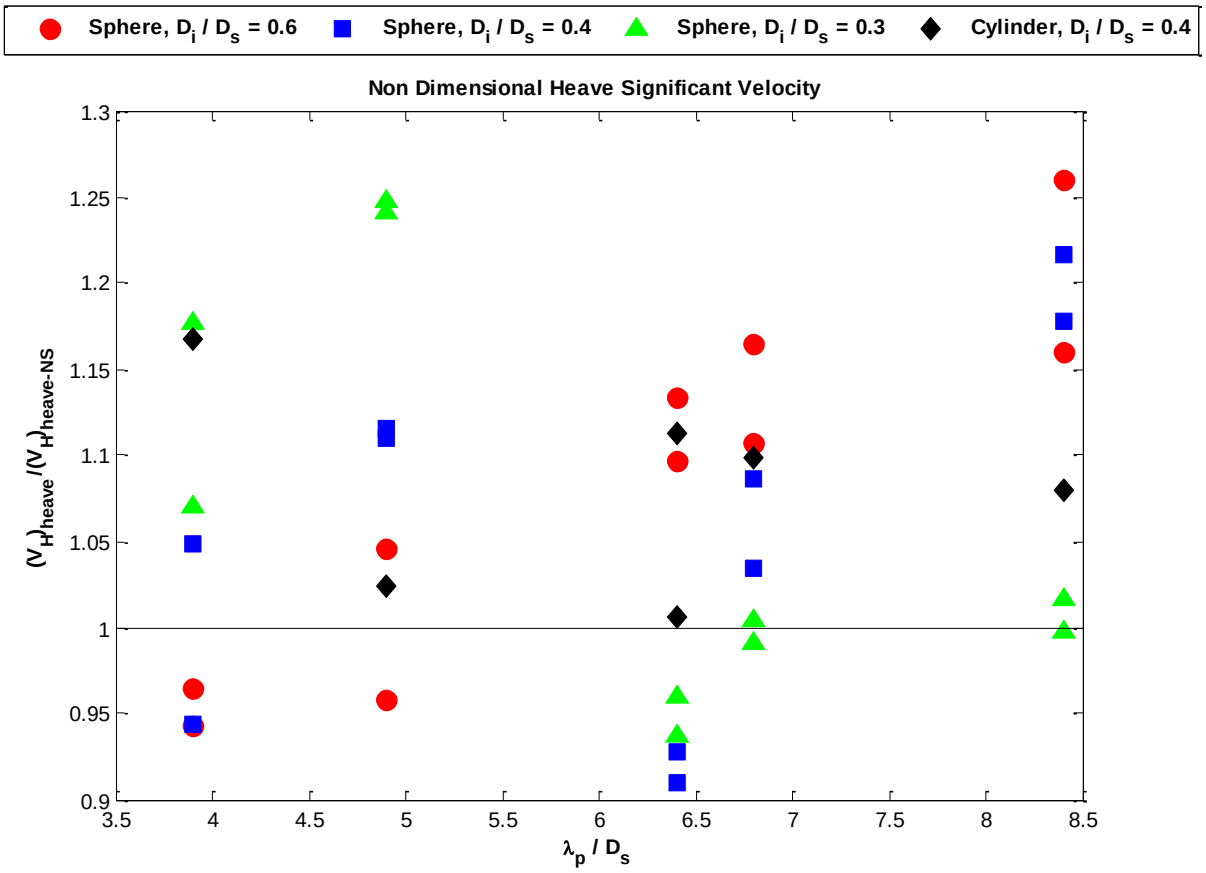

Figure 3.75: Non-dimensional heave significant velocity for all models tested in all waves

3.3.2.3 RAO Analysis

In this section, the force measurements of the sphere $D_i/D_s = 0.6$ tested at six different locations away from the structure in regular waves (described in section 3.1) are utilized along with the wave measurements in irregular waves to derive the corresponding force spectrum in irregular waves. The square of the force RAO of a particular frequency is multiplied by the wave energy at that frequency. Same procedure is followed for all the frequencies and surge and heave force spectrums are obtained. Finally from the surge and heave force spectrum, the significant surge and heave forces are calculated. Figures 3.76 and 3.77 show the variation of significant surge and

heave forces respectively as a function of D/λ_p for the five irregular waves. It is evident that beyond the nodal location at $D/\lambda_p \approx 0.25$, the significant surge force goes down and significant heave force goes up as the body gets close to the structure.

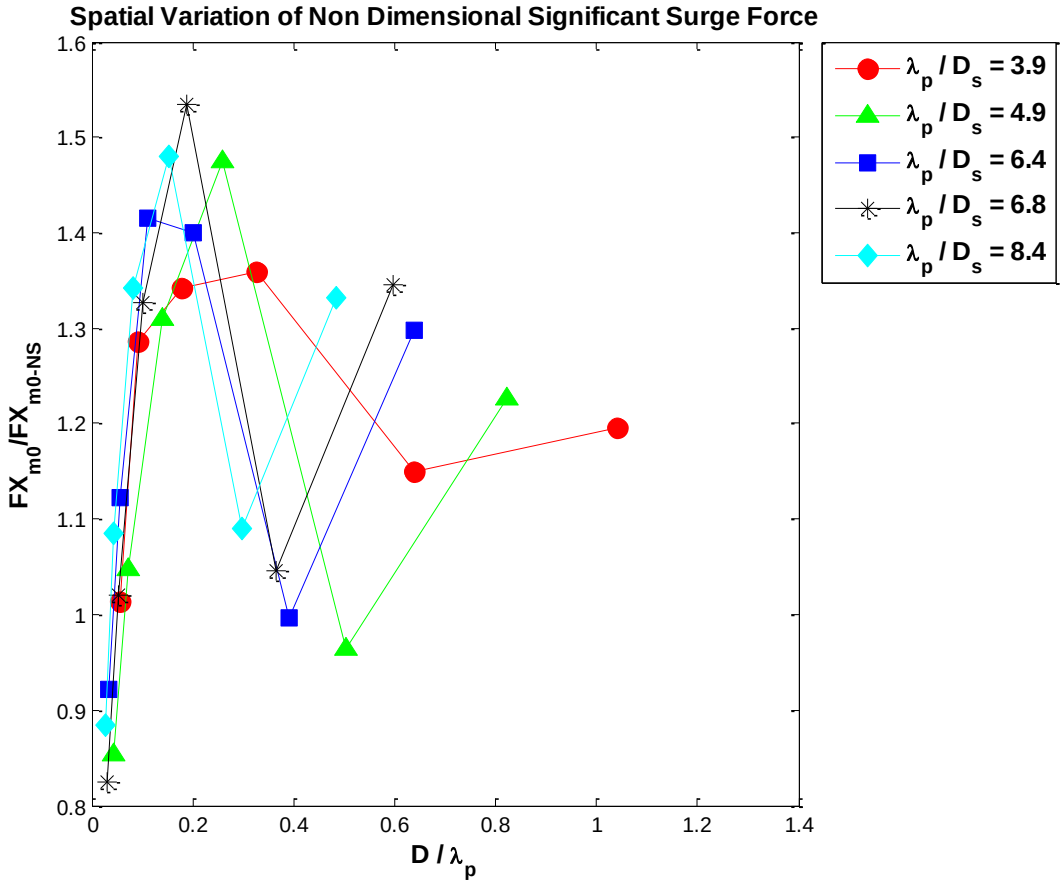

Figure 3.76: Non-dimensional significant surge force derived from linear superposition of regular wave force data

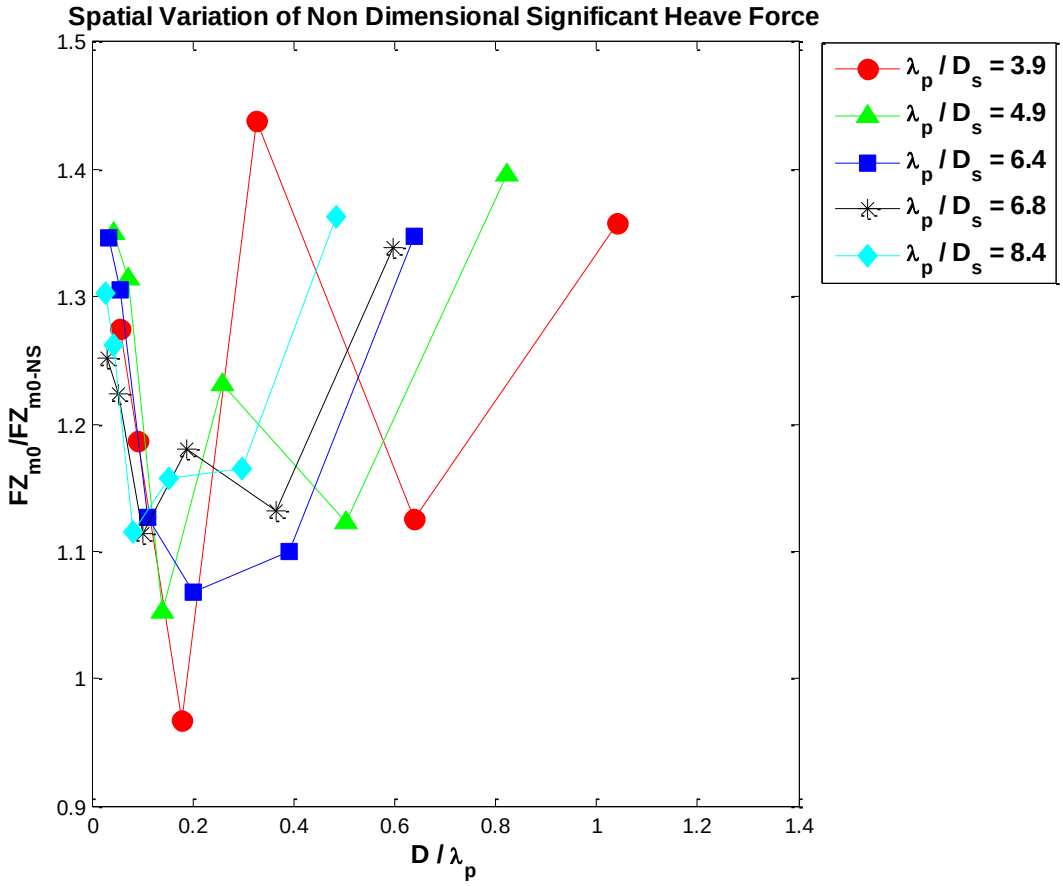

Figure 3.77: Non-dimensional significant heave force derived from linear superposition of regular wave force data

As with the previous cases, the results here show a decreasing trend in surge forces and motions and an increasing trend on heave forces and motions. The effect of irregular waves obscures the trends somewhat due to the mix of wavelengths present in an irregular signal but the trends are still discernable and of similar magnitude for those seen in the regular wave cases.

Chapter 4

Numerical Investigations

4.1 Numerical Investigation of Wave Forces at Different Proximity to a Fixed Structure in Regular Waves

Some numerical simulations have been carried out for a sample of the experimental test cases (section 3.1) using the commercial CFD software Flow3D (Flow Science Inc. version 11.0.3). Flow3D is a general purpose CFD code based on the Reynolds Averaged Navier Stokes (RANS) equations. The computational domain divides the physical space into a number of small volumes called cells which are connected with several nodes. The nodes store the values of unknown variables such as pressure, temperature and velocity. Using a finite difference approach, a structured-type computational mesh block is formed. Non-uniform grid spacing is also allowed in Flow-3D. Solid body geometry is defined by a technique named FAVOR (Fractional Area/Volume Obstacle Representation). Flow3D utilizes volume of fluid method called TruVOF for free surface tracking. The wave boundary condition allows for the generation of linear or stokes waves at the boundary (Flow Science Inc. version 11.0.3). Flow3D has been used by several researchers for different fluid flow and free surface problems (e.g. Bhinder et al. (2009), Thanyamanta et al. (2011), Maguire (2011)). Numerical results from Flow3D are validated against experimental data. These numerical results provide additional support to observations made from the experimental data.

4.1.1 Numerical Test Case Set-up

A three-dimensional mesh block was created and wave heights were calibrated at the centre of the sphere location without sphere or structure. The required number of cells of uniform size to generate a grid with the desired wave heights in the free surface region was determined through sensitivity analysis. Figure 4.1 shows the results of grid sensitivity analysis for generating a wave with $\lambda/D_s = 6$. The width and height of the tank was 4.5 and 2.5m respectively and the initial fluid elevation was 1.8 m. The length of the tank varied with wavelength (usually one wavelength between the inlet and the sphere, two wavelengths between the structure and the end

of the finer mesh plane and then another three wavelengths of coarse mesh plane). This allows sufficient time for the simulation to have generated the required number of wave encounters before the first wave reaches outflow boundary and any change in fluid volume of the tank occurs (Thanyamanta et al. (2011)). The boundary conditions applied are: Xmin – wave, Xmax – outflow, Ymin and Ymax – wall, Zmin – wall and Zmax – specified pressure. The geometry files were imported into Flow3D in .stl format. The rendered output was checked to identify whether the grid size was sufficiently fine to maintain the geometric shapes properly. The top portion of Figure 4.2 shows the tank with the sphere and hexagonal structure along with the boundary conditions and the bottom portion shows the mesh planes with grid lines.

The simulated waves were all deep water waves and fall into the Stoke's 2^{nd} order region. Stokes (Fenton's 5^{th}-order theory) was chosen in Flow3D as an available option. Incompressible fluid flow mode was selected with free surface or sharp interface tracking. The implicit, GMRES pressure solver and explicit viscous stress solver were used. First-order momentum advection was selected and the Split Lagrangian method was used to resolve volume of fluid advection. The two equation $k - \epsilon$ model was used as the turbulence model, with dynamically computed maximum turbulent mixing length. The default automatic time step control option was used which ensures the numerical stability limits for the solver.

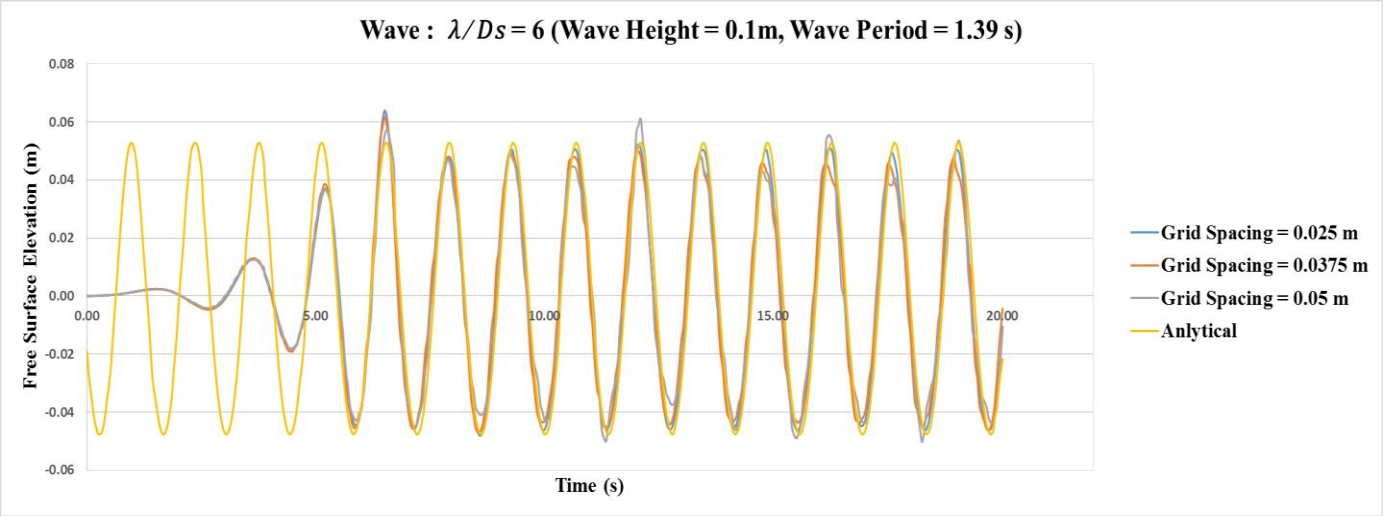

Figure 4.1: Grid sensitivity analysis for generating wave $\lambda/D_s = 6$ in numerical wave tank

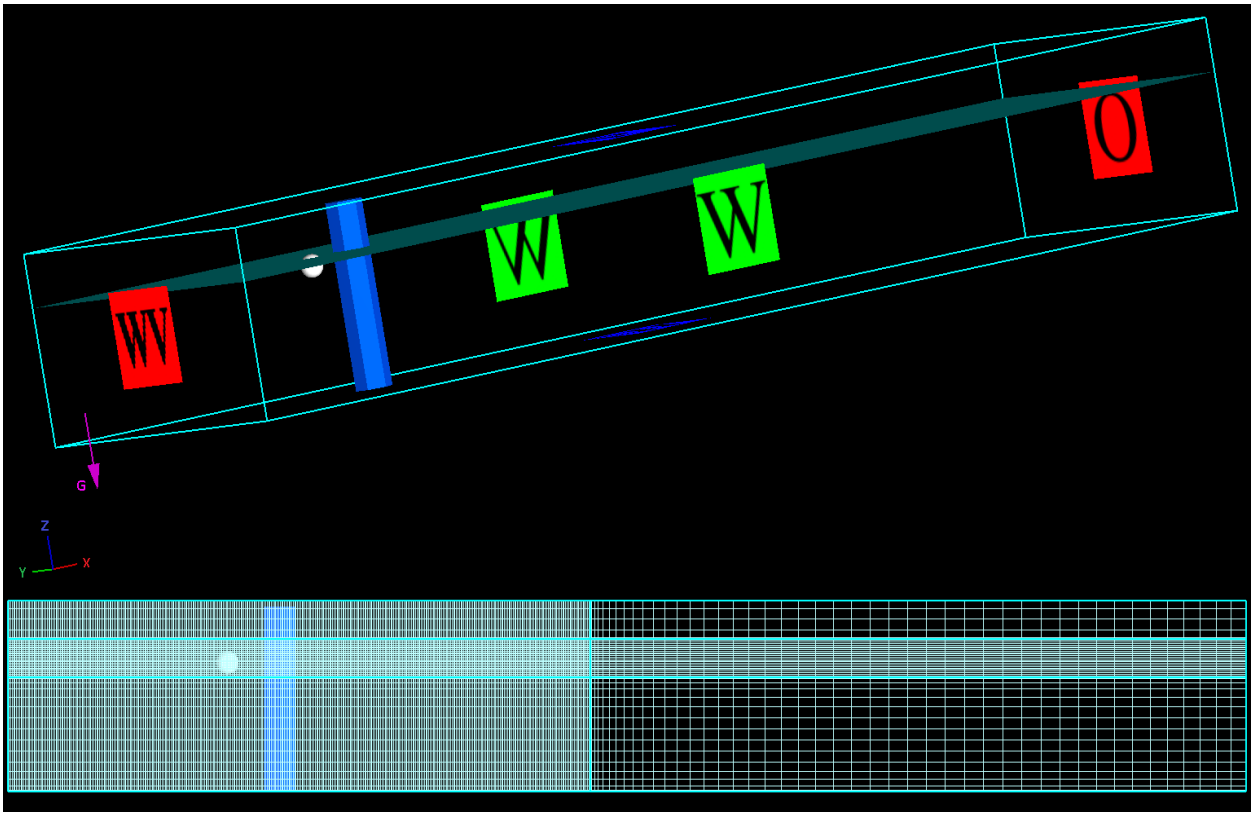

Figure 4.2: Computational domain with boundary conditions and grid structure in different mesh planes

4.1.2 Numerical Results

One sphere ($(D_i/D_s = 0.6)$ and three waves ($\lambda/D_s = 4, 6, 3.5$) were selected for the numerical simulations. The total number of cells depended on the wavelength and varied between 4 and 6 million. The associated simulation time varied between 5 and 11 hours respectively. The numerical simulations were run for 20 seconds and compared with the steady state section of the experimental data. Figures 4.3 and 4.4 show the time series comparison of FX and FZ forces for the sphere ($D_i/D_s = 0.6$) for no-structure case and at distance $D/D_i = 0.4$ respectively in waves with $\lambda/D_s = 6$. It is found that the numerical results agree quite well with experimental data.

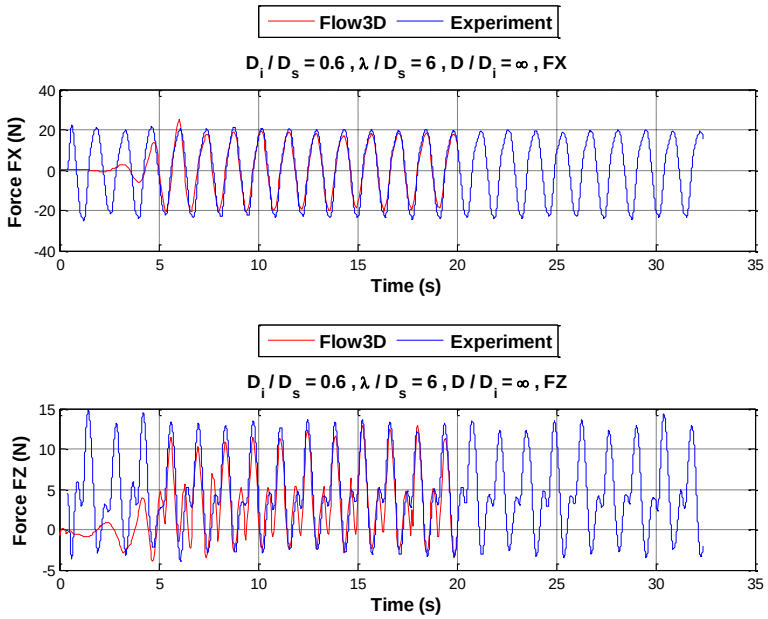

Figure 4.3: Comparison of Flow3D and experimental time history of FX and FZ forces for sphere $D_i/D_s = 0.6$ in wave $\lambda/D_s = 6$ at no-structure case ($D/D_i = \infty$)

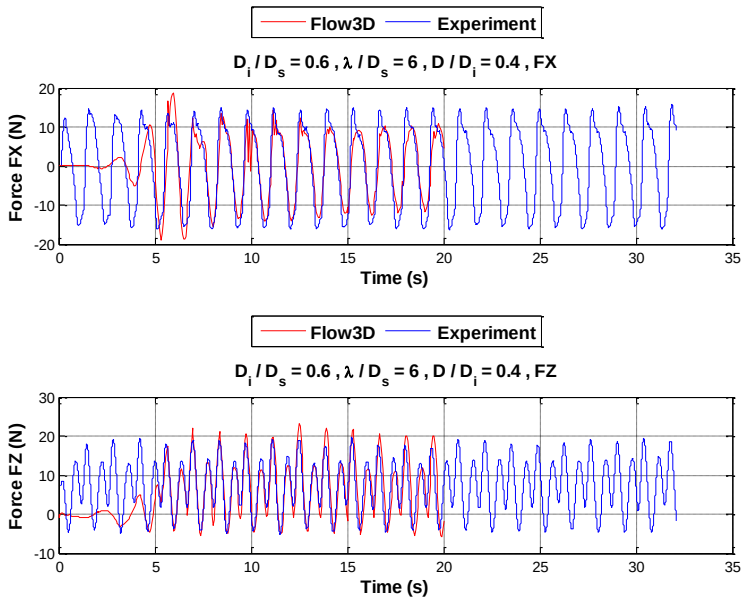

Figure 4.4: Comparison of Flow3D and experimental time history of FX and FZ forces for sphere $D_i/D_s = 0.6$ at distance $D/D_i = 0.4$ in wave $\lambda/D_s = 6$

Figure 4.5 shows the RMS FX and FZ force comparisons for the sphere ($D_i/D_s = 0.6$) in wave $\lambda/D_s = 6$. The results match quite well showing the highest and lowest forces at different locations from the structure. Numerical simulations did not include the attached rod used during experiments. This may explain the small difference in RMS FX force. Another factor may be the small differences in wave heights generated between the experimental facility and the numerical wave tank. The numerical results indicate that the viscous forces are negligible compared to pressure forces for the tested cases.

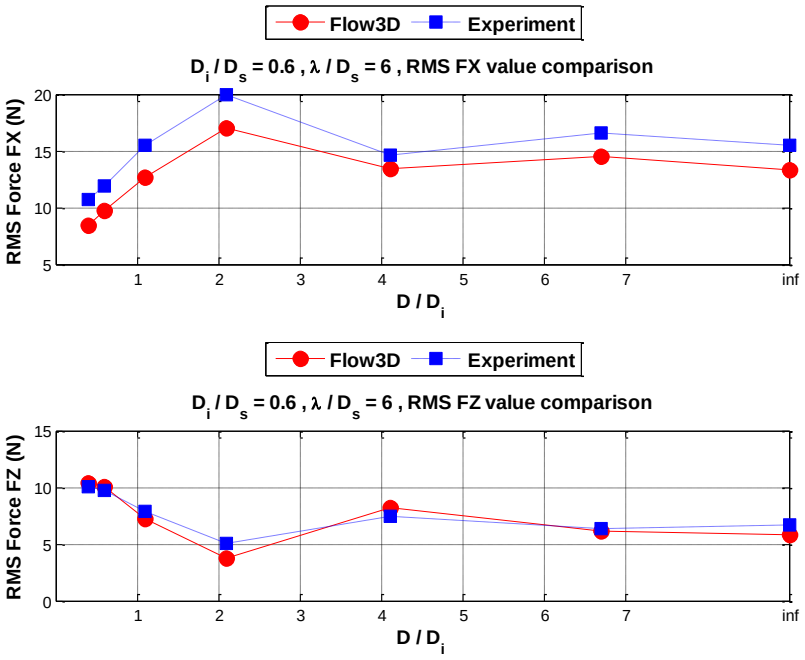

Figure 4.5: Comparison of Flow3D and experimental RMS FX and FZ forces for sphere $D_i/D_s = 0.6$ in wave $\lambda/D_s = 6$

The sphere ($D_i/D_s = 0.6$) was simulated for two more wave cases ($\lambda/D_s = 4, 3.5$). Figures 4.6 and 4.7 show the time series comparison for wave $\lambda/D_s = 4$ at distance $D/D_i = 0.4$ and wave $\lambda/D_s = 3.5$ at distance $D/D_i = 4.1$. Figures 4.8 and 4.9 show the RMS force comparison for waves $\lambda/D_s = 4$ and $\lambda/D_s = 3.5$ respectively. Although there are some noticeable differences between simulated and experimental FZ forces, the overall results compare well.

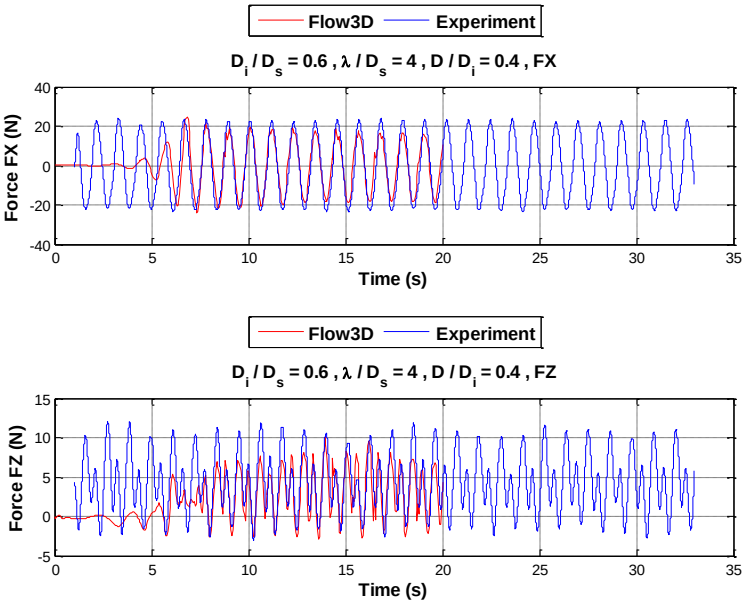

Figure 4.6: Comparison of Flow3D and experimental time history of FX and FZ forces for large sphere at distance $D/D_i = 0.4$ in wave $\lambda/D_s = 4$

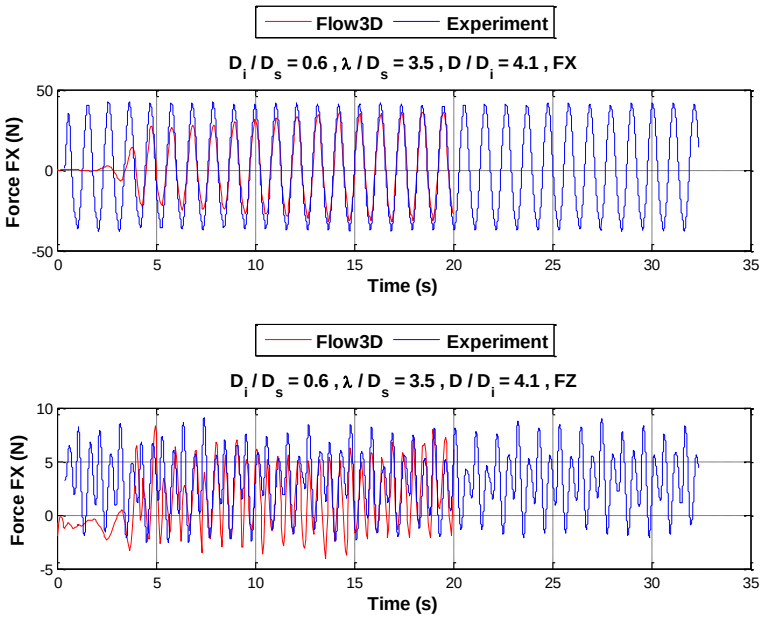

Figure 4.7: Comparison of Flow3D and experimental time history of FX and FZ forces for large sphere at distance $D/D_i = 4.1$ in wave $\lambda/D_s = 3.5$

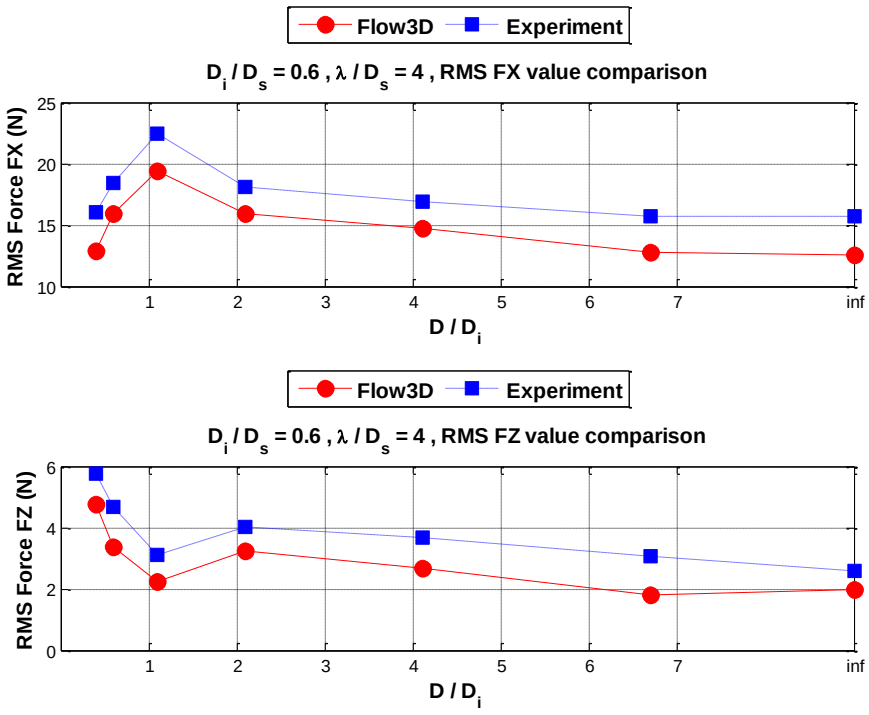

Figure 4.8: Comparison of Flow3D and experimental RMS FX and FZ forces for large sphere in wave $\lambda/D_s = 4$

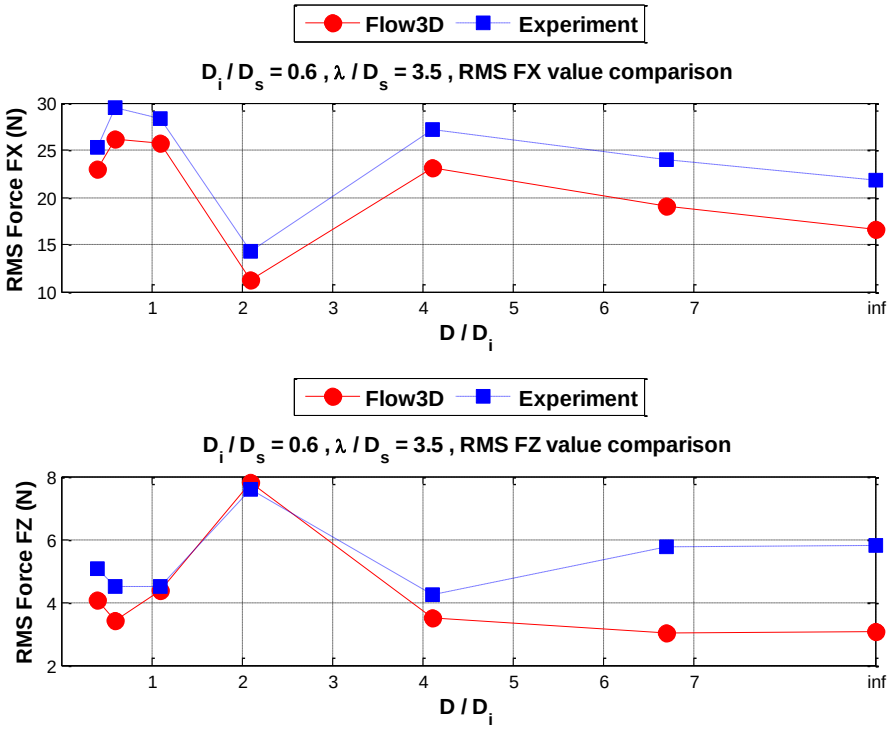

Figure 4.9: Comparison of Flow3D and experimental RMS FX and FZ forces for large sphere in wave $\lambda/D_s = 3.5$

4.2 Numerical Investigation of Wave Induced Motions Approaching to a Fixed Structure in Regular Waves

Some numerical simulations have been conducted for selected experimental test cases (section 3.2) using commercial CFD software Flow3D (Flow Science Inc. version 11.1). The objective is to provide a check on the experimental data and to investigate the capability of a CFD tool to capture the close proximity multi-body hydrodynamic effects. A general description of Flow3D is given in previous section (4.1). A General Moving Object (GMO) modeling option allows rigid body motions in six degrees of freedom which is used in the present study. The wave boundary condition allows simple wave generation of linear or Stokes waves at the boundary. A wave damping region called the sponge layer can be used in the outlet to absorb waves and reduce reflections at the outflow boundary (Flow Science Inc. version 11.1). Numerical results from Flow3D are compared with the current experimental data.

4.2.1 Numerical Test Case Set-up

The sphere $D_i/D_s = 0.6$ and waves $\lambda/D_s = 4, 6\ and\ 3.5$ are selected as test cases, similar to previous numerical studies (section 4.1). The same grid size was used in the free surface region to match the targeted wave heights. The width and height of the numerical tank was 4.5 and 2.5 m respectively and initial fluid elevation was 1.8 m. The length of the tank varied with wavelength. The boundary conditions applied are: Xmin – wave, Xmax – outflow, Ymin and Ymax – wall, Zmin – wall and Zmax – specified pressure. An additional wave absorbing component was added before outflow boundary to reduce wave reflections from the boundary and to maintain fluid volume in the domain. The hexagonal fixed structure was treated as a non-moving object and the sphere was treated as a moving object. The General Moving Object (GMO) modeling option was used to allow coupled motions in x- and z- translation only (surge and heave). The mass properties of the sphere were edited accordingly without modeling the top or bottom rods used in the experiment. Figure 4.10 shows the computational domain with sphere

and hexagonal structure along with boundary conditions. Stokes (Fenton's 5th-order theory) was chosen to simulate the waves in Flow3D. Other numerical options used were similar to previous study described in section 4.1.

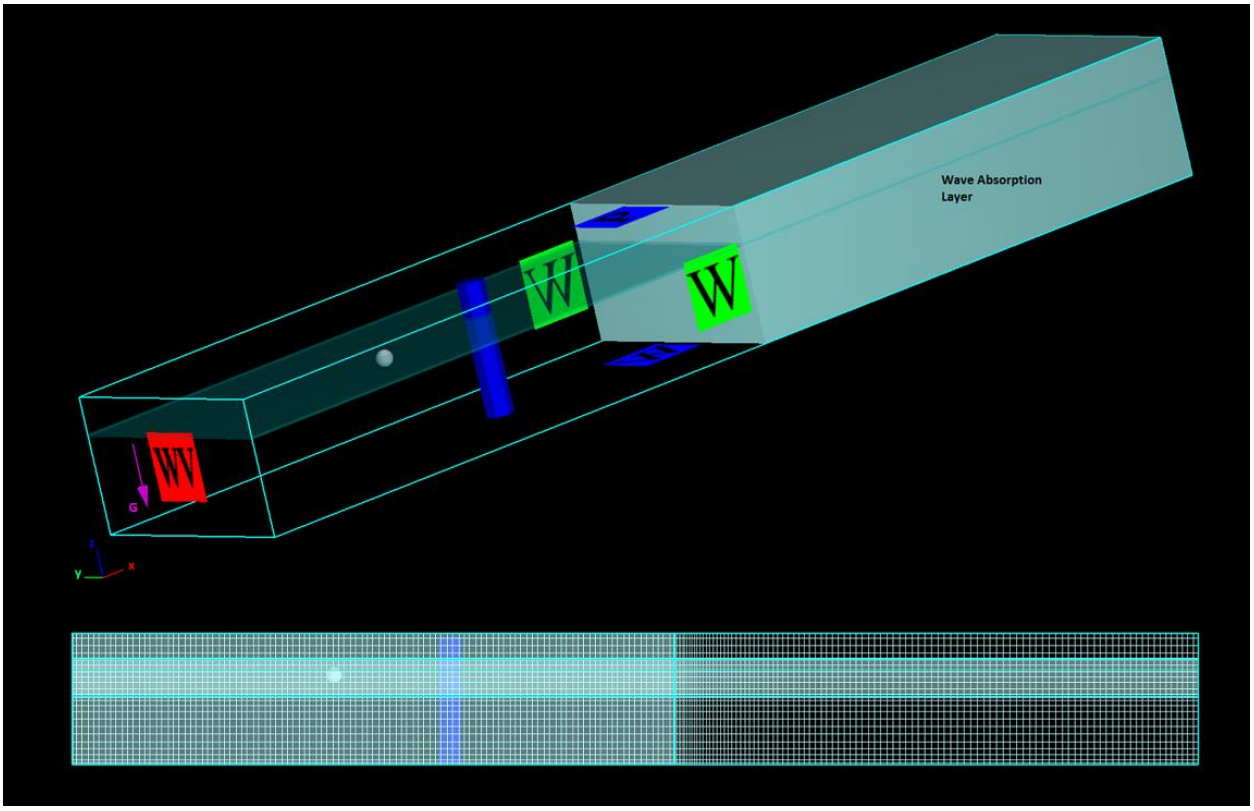

Figure 4.10: Computational domain with boundary conditions and grid structure in different mesh planes

4.2.2 Numerical Results

The total number of cells depend on wavelength and varied between 5 to 7 million and associated simulation time varied between 20 to 30 hours. The numerical simulations were run for at least 40 seconds and compared with steady state sections from the corresponding experimental data. Figure 4.11 shows the time series comparison of surge displacement of the sphere tested without structure in waves $\lambda/D_s = 4{,}6$ and 3.5. This clearly shows the big

difference in average drift velocity between experiment and numerical simulation for all the cases except for $\lambda/D_s = 6$. Table 4.1 shows the magnitudes of the drift velocity, calculated from the steady state cycles for no-structure cases. This difference can be largely attributed to the modeling difference in the numerical simulations. The numerical simulations were conducted for surge and heave only without allowing any pitch motion whereas the physical model experienced pitch motions. Also the physical model has a rod and small mass attached to it at the bottom of the model which is not practical to model numerically due to the requirement of very small grid size. Besides this, there is also a small difference in wave heights generated between the experimental facility and the numerical wave tank.

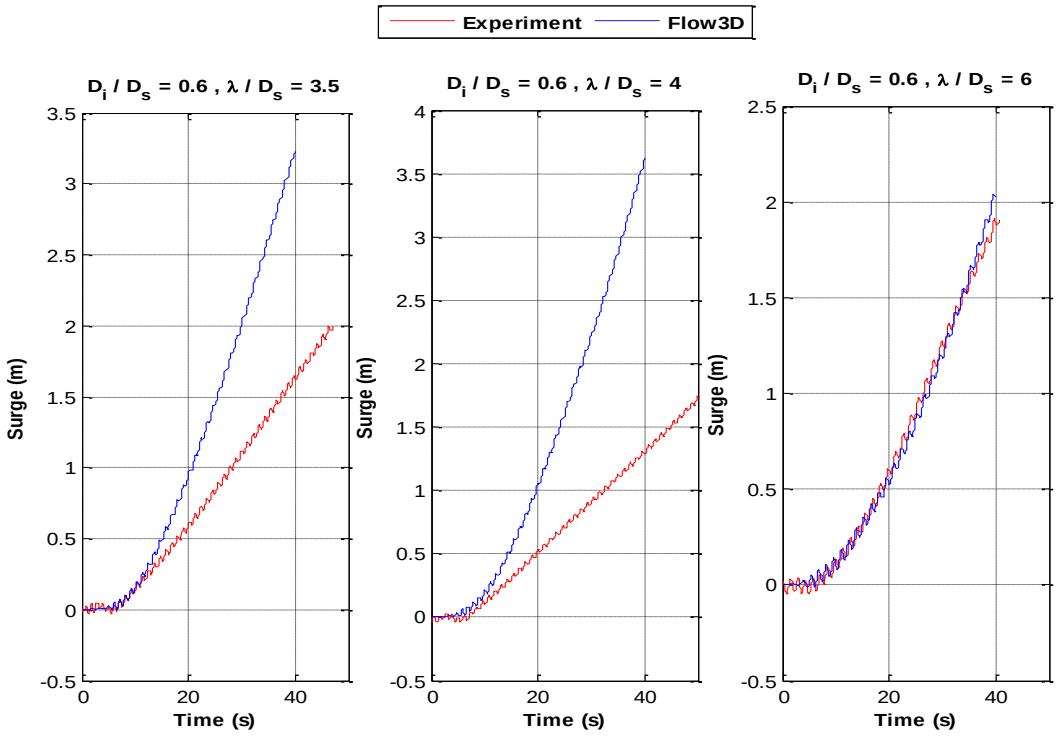

Figure 4.11: Time series comparison of surge displacement of the sphere tested without structure in waves $\lambda/D_s = 4$,6 and 3.5

Table 4.1: Comparison of drift velocity between experiment and numerical simulation for no-structure cases

Wave, λ/D_s	Drift velocity (m/s), Experiment	Drift velocity (m/s), Flow3D
3.5	0.053	0.115
4	0.041	0.142
6	0.066	0.073

The drift speeds in the numerical simulations are higher than experiments because the attached rod and allowable pitch motions in the physical model damped the surge drift motions. Bai et al. (2017) compared their numerical results with experiment for surge and heave oscillatory motions by removing the mean drift motion from the surge displacement signal. Figures 4.12 and 4.13 show the steady state time series of oscillatory surge and heave velocities, similar to those presented in Bai et al. (2017) for the sphere tested without structure in waves $\lambda/D_s = 4$ and 6 respectively. It is found that the oscillatory surge and heave motion results agree reasonably well with experimental data. The numerical results also capture the non-linear heave motions in wave $\lambda/D_s = 6$ quite well.

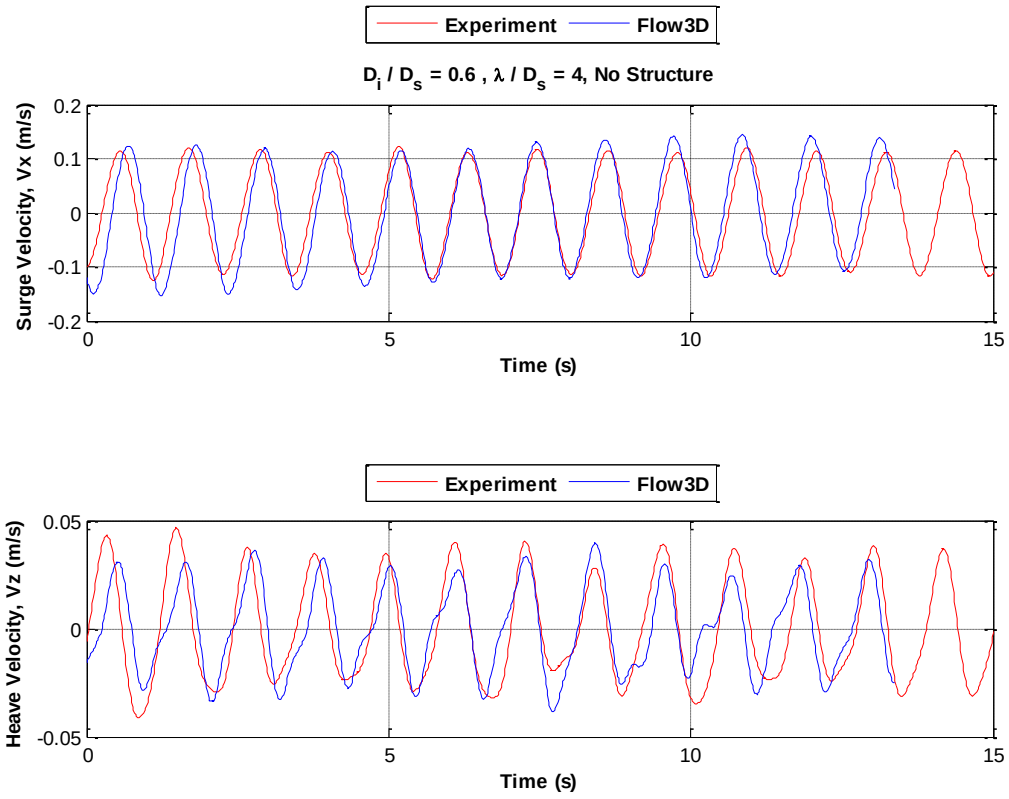

Figure 4.12: Time series of oscillatory surge and heave velocities of the sphere tested without structure in wave $\lambda/D_s = 4$

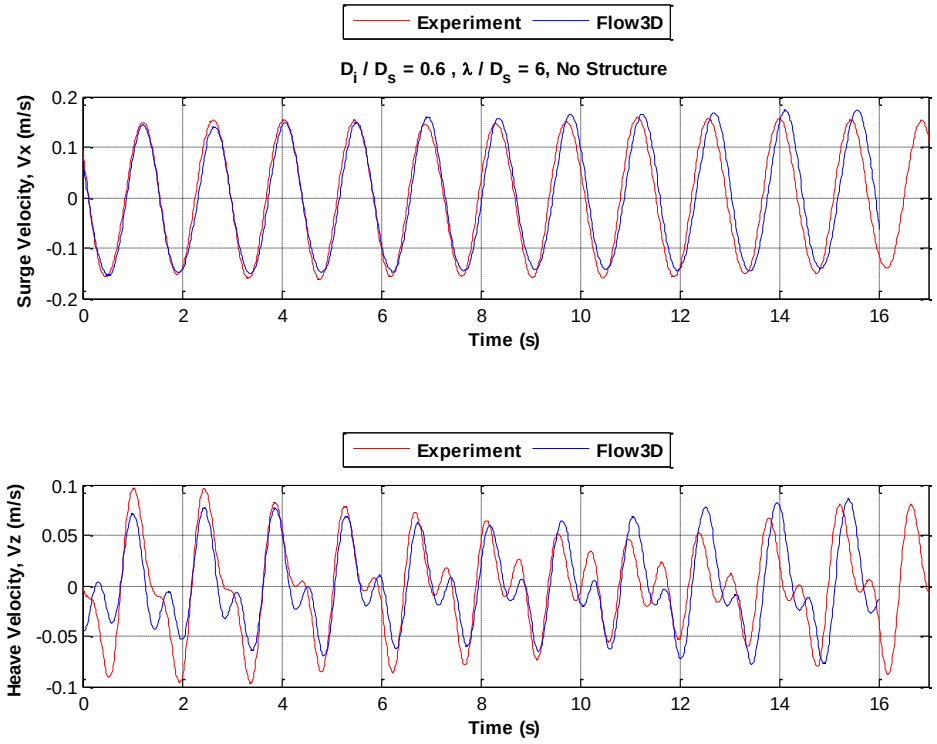

Figure 4.13: Time series of oscillatory surge and heave velocities of the sphere tested without structure in wave $\lambda/D_s = 6$

Figure 4.14 shows the comparison of surge and heave velocities plotted against D/λ for the sphere tested with structure in wave $\lambda/D_s = 6$. The initial starting location of the sphere was 2m. The numerical results match quite well with experimental data. The numerical results show that the sphere goes forward and hits the structure similar to experiment. The velocity changes at node and antinode locations in front of the structure are also well captured by the numerical simulations.

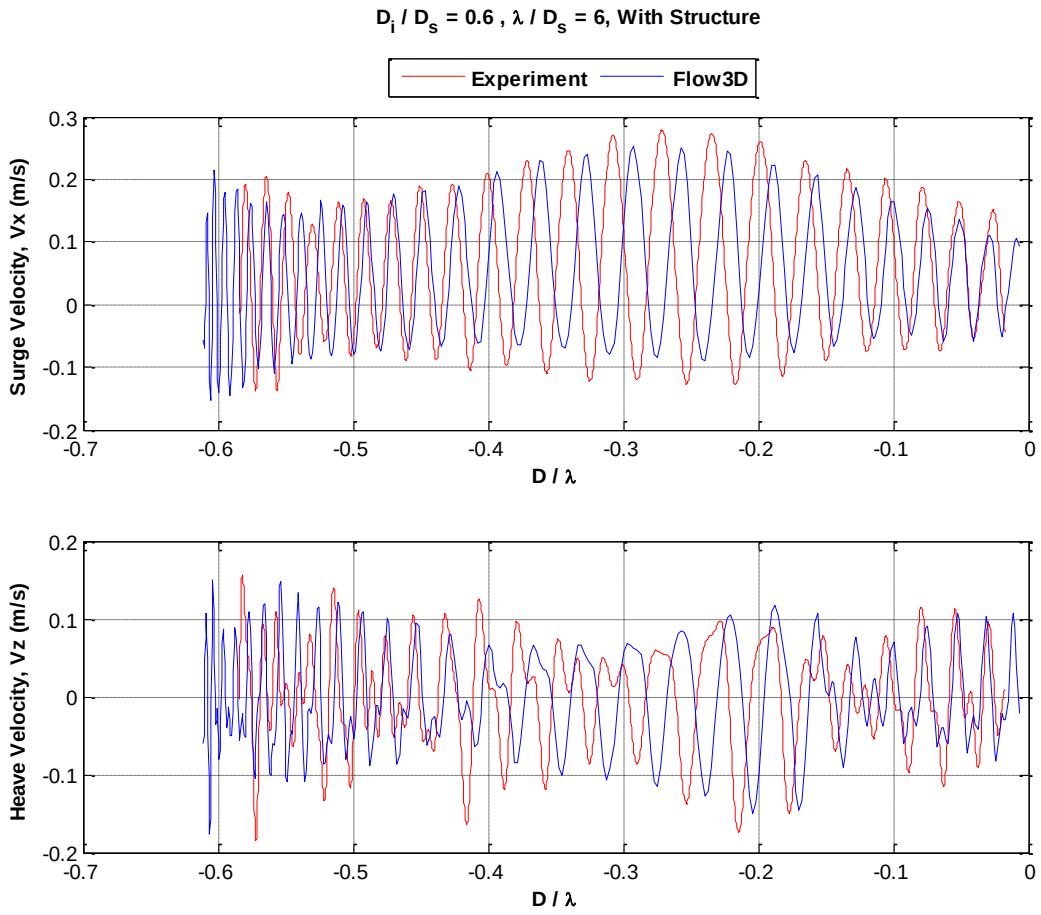

Figure 4.14: Surge and heave velocity comparison plotted against D/λ for the sphere tested with structure in wave $\lambda/D_s = 6$

Figure 4.15 shows the comparison of surge and heave velocities plotted against D/λ for the sphere tested with structure in wave $\lambda/D_s = 4$. The initial starting location of the sphere was 2m. In this case, the sphere went forward up to $D/\lambda = 0.59$, stayed there and then came back during experiment whereas in the numerical simulation, the sphere keeps going forward and hits the structure. As presented in Table 4.1 that for this wave condition, the drift velocity in the numerical simulation was significantly higher than the experimental case for no-structure cases. In spite of this difference in mean velocity, the numerical simulation results show the relative velocity changes at the node and antinode locations similar to those observed in the experiments.

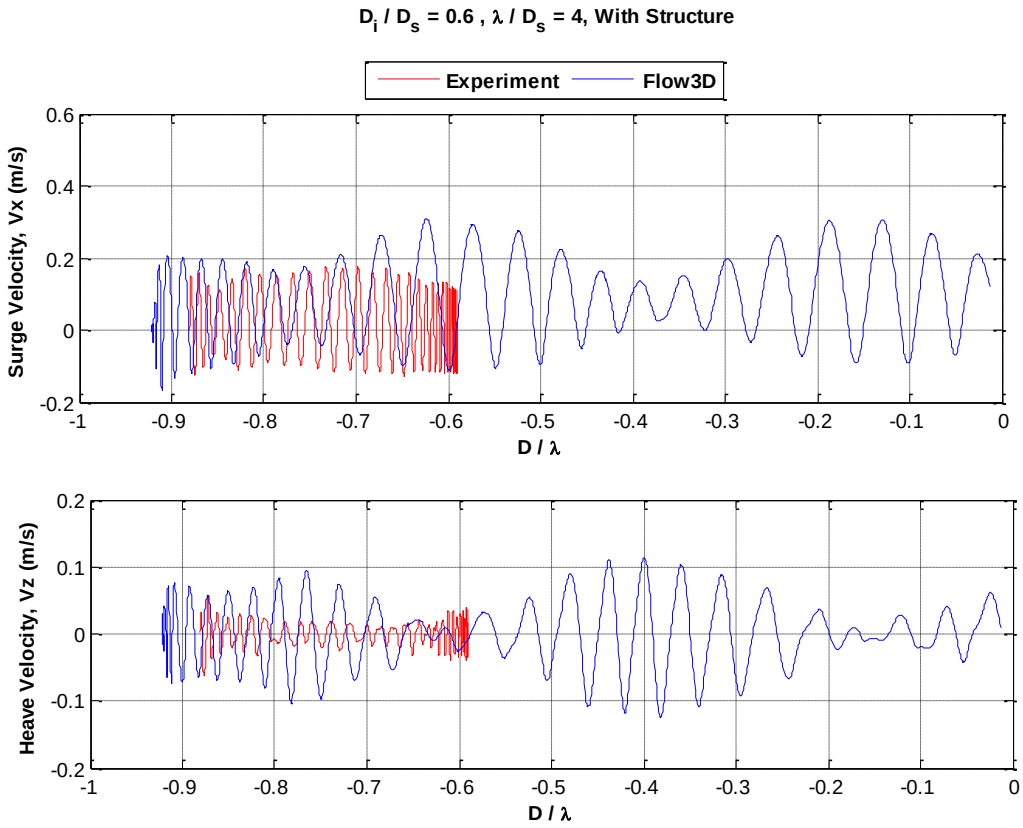

Figure 4.15: Surge and heave velocity comparison plotted against D/λ for the sphere tested with structure in wave $\lambda/D_s = 4$

Figures 4.16 and 4.17 show the comparison of surge and heave velocity of the sphere tested in wave $\lambda/D_s = 3.5$ for two different release locations, 2 m and 1 m. In numerical simulation, the sphere goes forward and hits the structure for both release locations whereas in the experiments, the sphere proceeds up to $D/\lambda = 0.5$ and then reverses direction for the 2 m release location and the sphere goes very close to the structure and then reverses for the 1 m release location. Irrespective of these differences in the mean drift behaviour, the numerical simulation shows good agreement with experiment in terms of the wave induced velocity trends and can predict the change in wave induced velocity profile prior to impact.

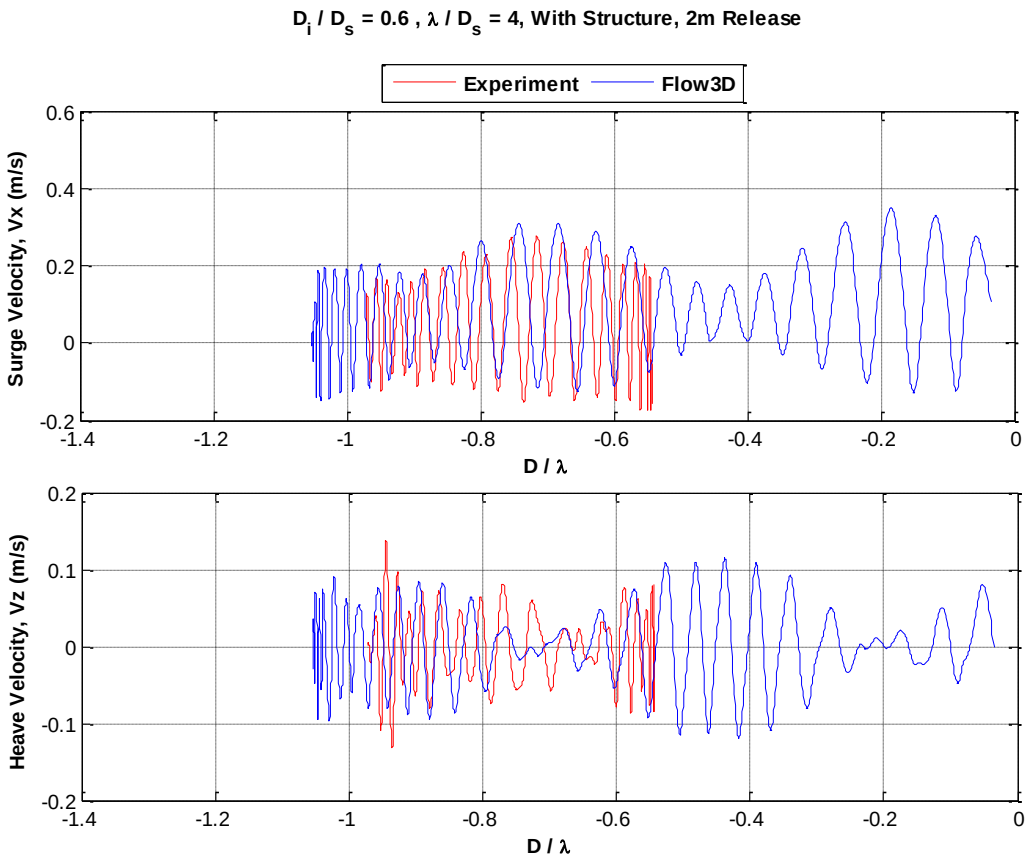

Figure 4.16: Surge and heave velocity comparison plotted against D/λ for the sphere tested with structure in wave $\lambda/D_s = 3.5$ and released from 2 m

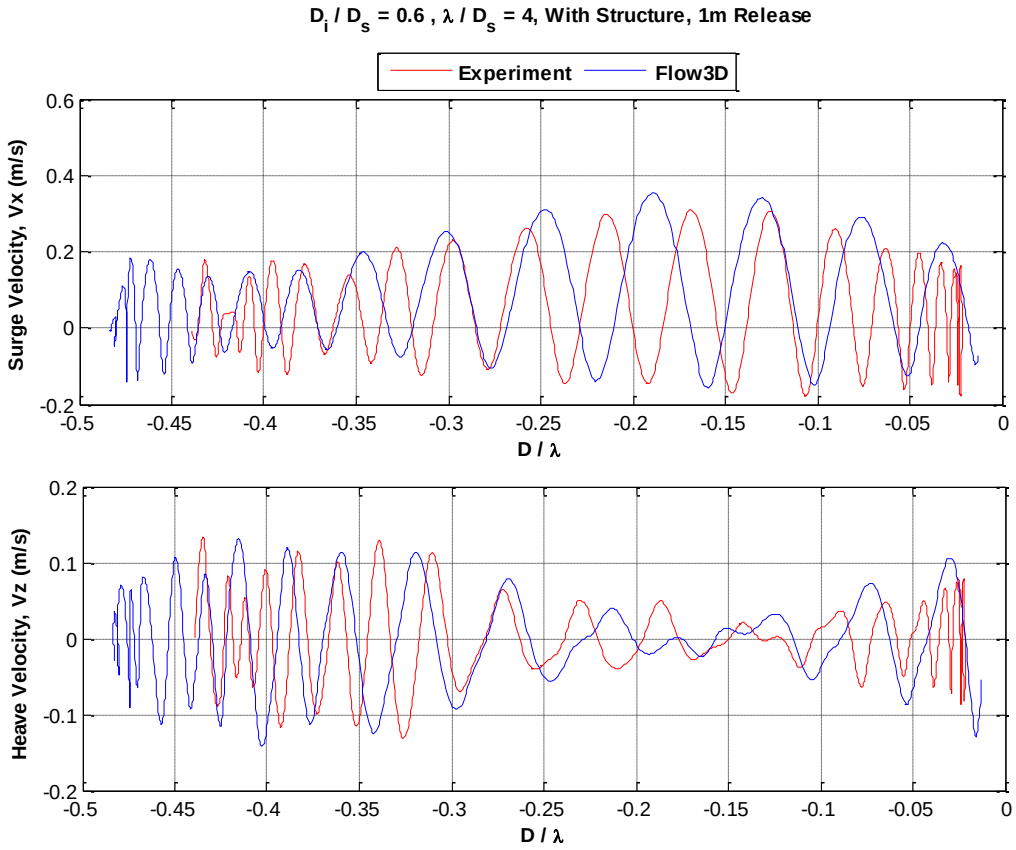

Figure 4.17: Surge and heave velocity comparison plotted against D/λ for the sphere tested with structure in wave $\lambda/D_s = 3.5$ and released from 1 m

4.3 Numerical Investigation in Irregular Waves

Some numerical simulations have been conducted for selected experimental test cases (section 3.3) using commercial CFD software Flow3D (Flow Science Inc. version 11.1). A general description of Flow3D is given in section 4.1. Numerical set up in the present study is similar to section 4.2. Additionally random wave option of Flow3D is used to generate irregular waves.

4.3.1 Numerical Test Case Set-up

The sphere $D_i/D_s = 0.6$ and three irregular waves $\lambda_p/D_s = 4.9, 6.4\ and\ 6.8$ are selected as test cases for the present numerical study. The width and height of the numerical tank was 4.5 and 2.5m respectively and initial fluid elevation was 1.8m. The boundary conditions applied are: Xmin – wave, Xmax – outflow, Ymin and Ymax – wall, Zmin – wall and Zmax – specified pressure. An additional wave absorbing component was added before outflow boundary to reduce wave reflections from the boundary and to maintain fluid volume in the domain. A uniform grid size of 0.025 m was used in the free surface region. First of all a 2D simulation was conducted to match the significant heights and peak periods of irregular waves. Once the desired waves were matched, then 3D simulation was conducted using the hexagonal fixed structure as a non-moving object and the sphere as a moving object. Figure 4.18 shows the mesh grid for 2D simulation (top) and the computational domain with sphere and hexagonal structure along with boundary conditions (bottom). The General Moving Object (GMO) modeling option was used to allow coupled motions in x- and z- translation only (surge and heave). The mass properties of the sphere were edited accordingly without modeling the top or bottom rods used in the experiment. Other numerical options are similar to those described in sections 4.1 and 4.2.

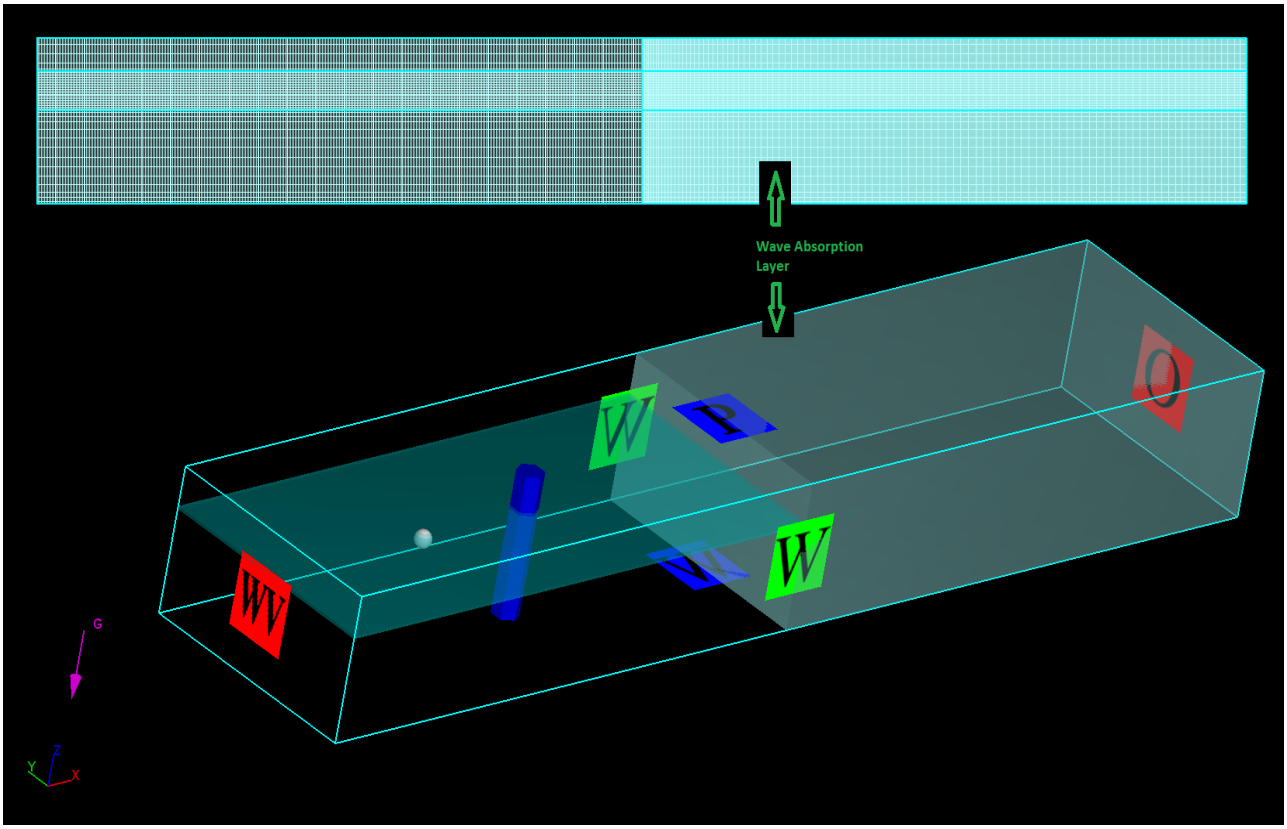

Figure 4.18: Computational domain with boundary conditions and grid structure in different mesh planes

It is not possible in Flow-3D to provide a time series irregular wave input. It is only possible to provide the wave spectral characteristics and the program then generates a time series that matches the specified spectrum. Thus a direct wave by wave comparison is not possible between the experimental and numerical cases. Only the average trends, statistics and extremes can be compared.

4.3.2 Numerical Results

The total number of cells was 4.4 million and associated simulation time varied between 17 to 20 hours. The numerical simulations were run for 60 seconds and compared with steady state

sections from the corresponding experimental data. Figure 4.19 shows the time series comparison of wave height and corresponding spectrum for wave $\lambda_p/D_s = 6.4$ between experiment and 2D simulation of Flow3D. Table 4.2 shows the comparison of significant wave heights and peak periods between experiment and 2D simulation of Flow3D for the three selected irregular wave cases.

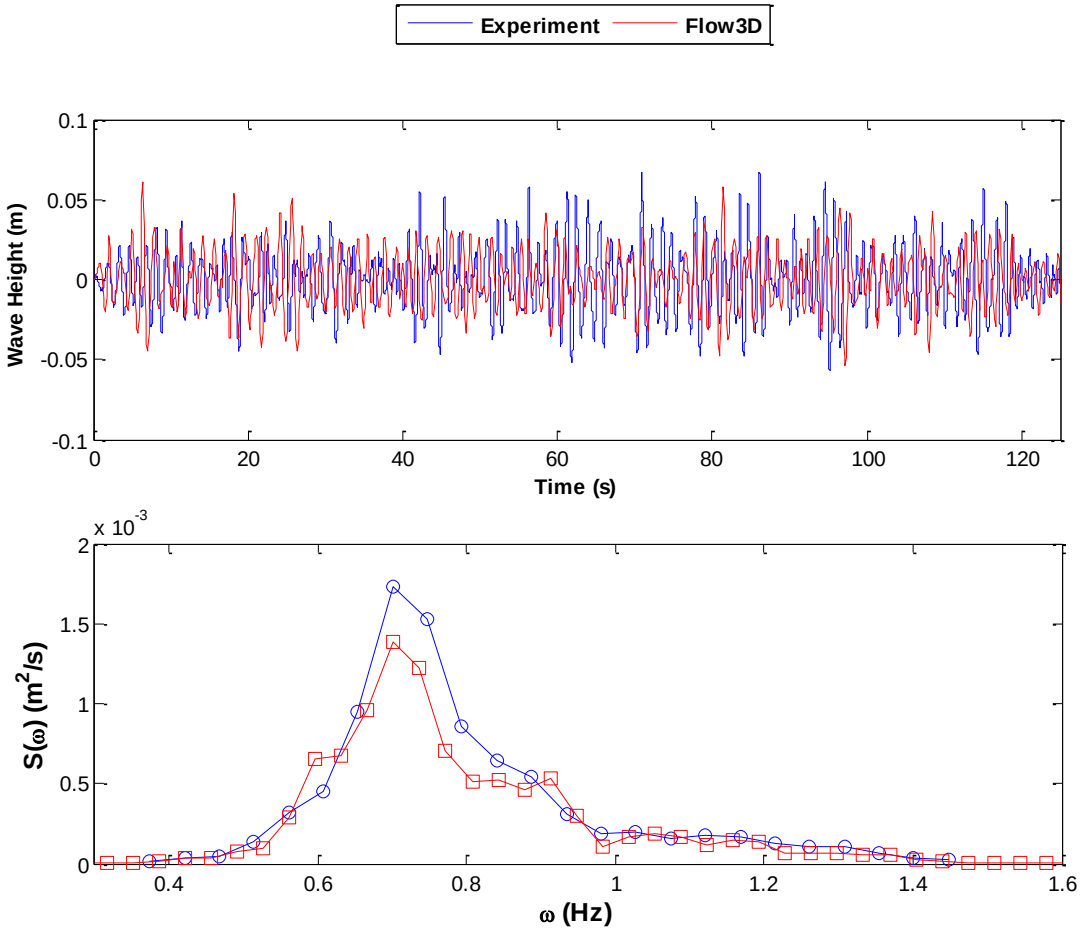

Figure 4.19: Comparison of wave height and corresponding spectrum for wave $\lambda_p/D_s = 6.4$ between experiment and 2D simulation of Flow3D

Table 4.2: Comparison of experimental and numerical irregular wave particulars

Wave (λ_p/D_s)	Experiment		Flow3D	
	Significant Wave Height, H (m)	Peak Period, T_p (sec)	Significant Wave Height, H (m)	Peak Period, , T_p (sec)
4.9	0.069	1.26	0.062	1.23
6.4	0.083	1.43	0.075	1.43
6.8	0.099	1.48	0.091	1.53

Figure 4.20 shows the time series comparison of surge displacement of the sphere tested without structure in waves $\lambda_p/D_s = 4.9, 6.4$ and 6.8. The results show some difference in average drift velocity between experiment and numerical simulation which is expected due to the modeling difference in the numerical simulations. The numerical simulations were conducted for surge and heave only without allowing any pitch motion whereas the physical model experienced pitch motions. Also the physical model has a rod and small mass attached to it at the bottom of the model which is not practical to model numerically due to the requirement of very small grid size. Besides this, there is also a small difference in wave heights generated between the experimental facility and the numerical wave tank.

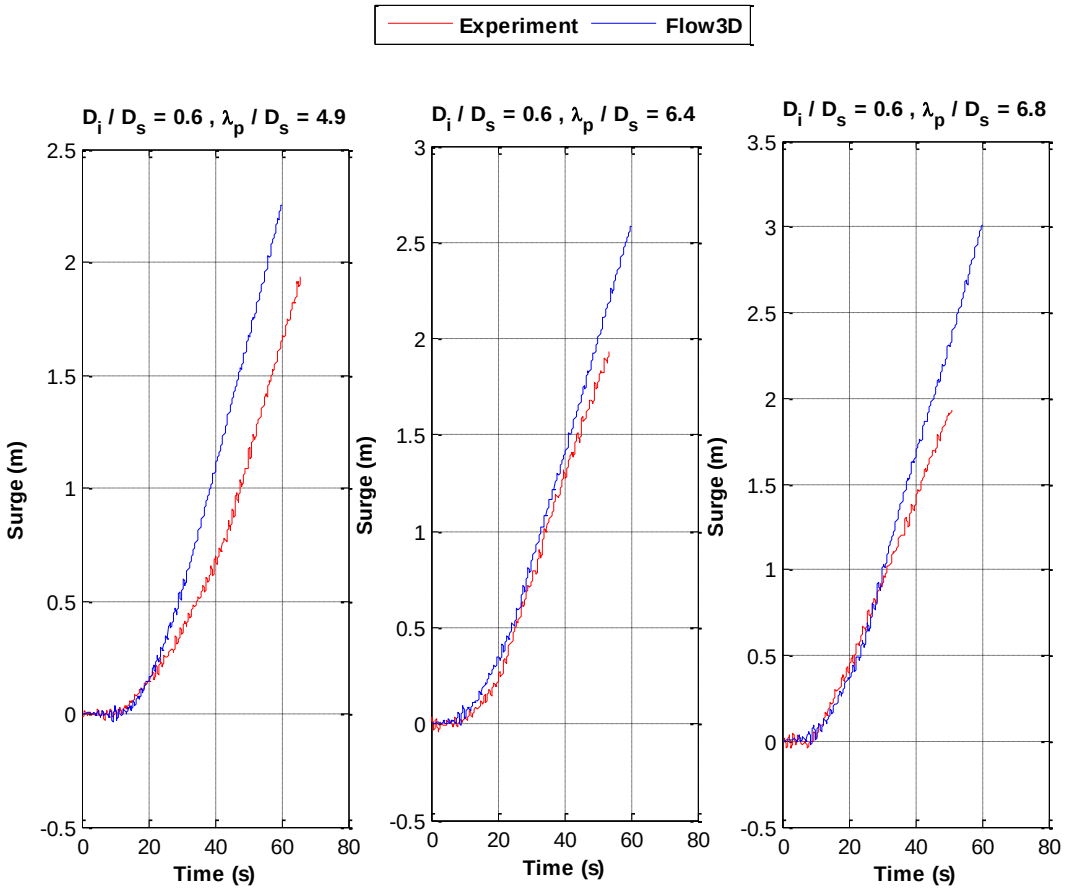

Figure 4.20: Time series comparison of surge displacement of the sphere tested without structure in waves $\lambda_p/D_s = 4.9, 6.4$ and 6.8

Figures 4.21 to 4.23 show the time series comparison of surge and heave velocities between experiment and numerical simulation for the sphere tested without structure in waves $\lambda_p/D_s = 4.9, 6.4$ and 6.8 respectively. The corresponding surge and heave significant velocities are also given in the plots. The numerical results show reasonable agreement with experiment despite the modeling difference. In numerical simulations, the heave velocities are more underestimated than the surge velocities.

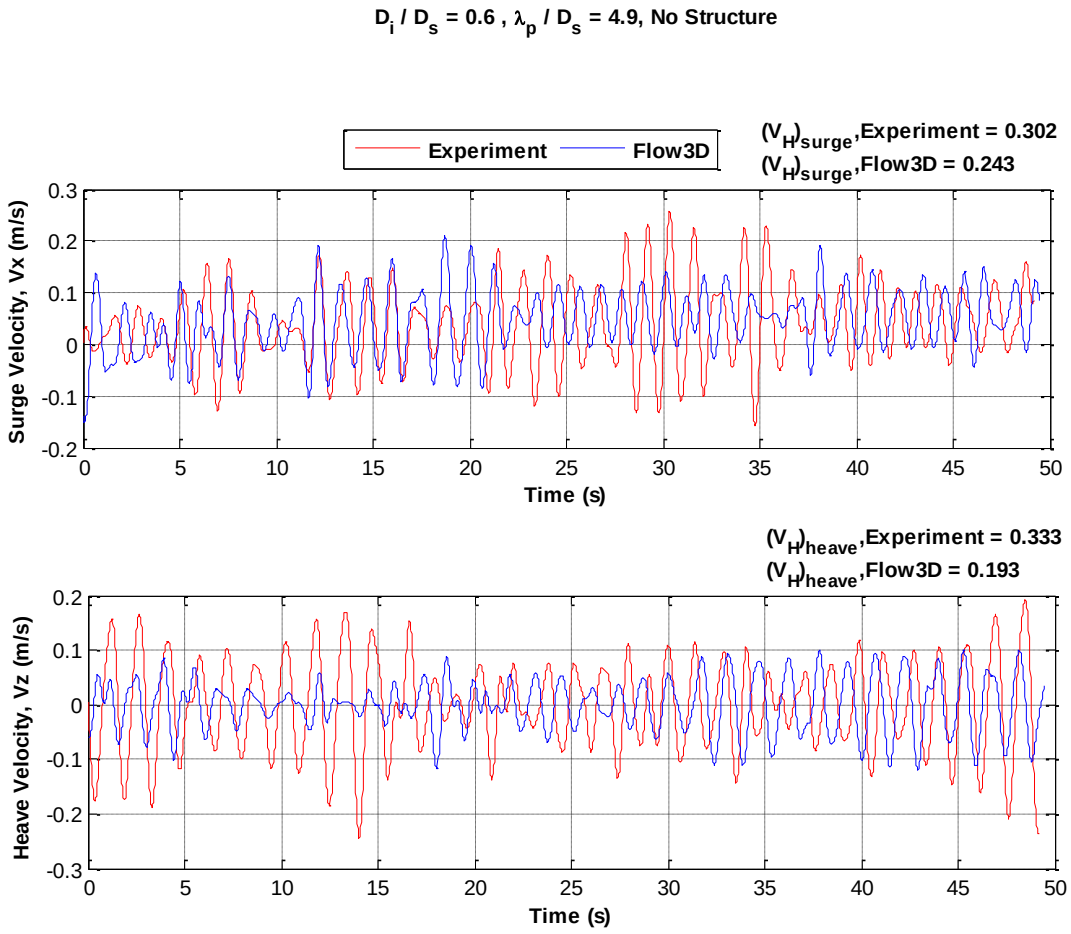

Figure 4.21: Comparison of surge and heave velocity between experiment and Flow3D for sphere $D_i/D_s = 0.6$ tested without structure in wave $\lambda_p/D_s = 4.9$

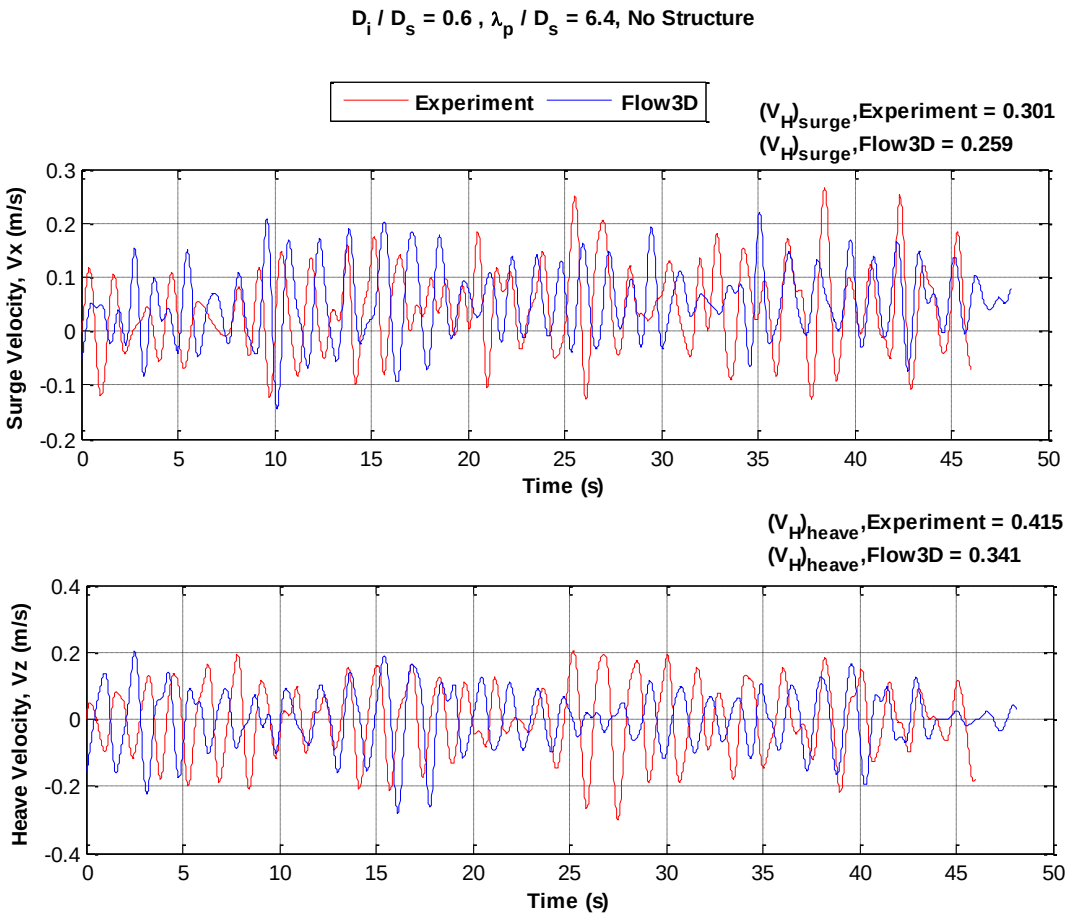

Figure 4.22: Comparison of surge and heave velocity between experiment and Flow3D for sphere $D_i/D_s = 0.6$ tested without structure in wave $\lambda_p/D_s = 6.4$

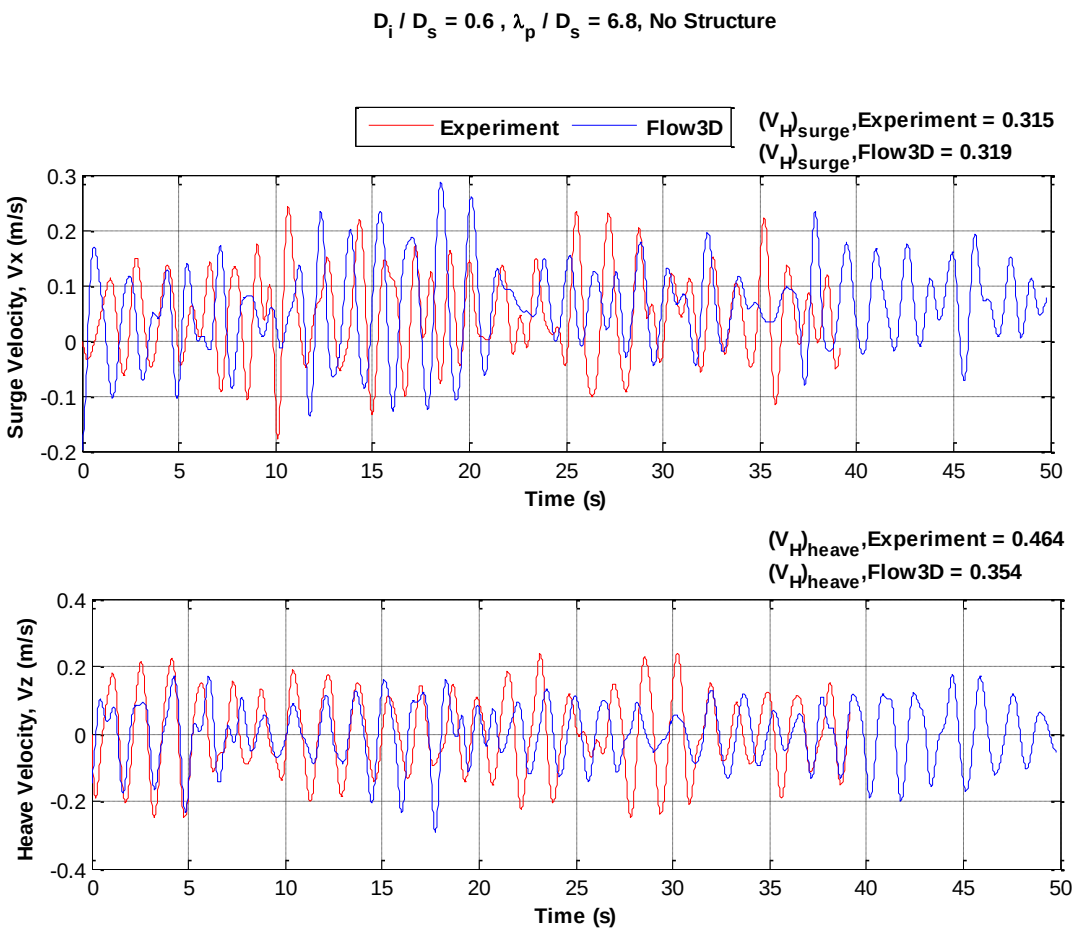

Figure 4.23: Comparison of surge and heave velocity between experiment and Flow3D for sphere $D_i/D_s = 0.6$ tested without structure in wave $\lambda_p/D_s = 6.8$

Figure 4.24 shows the time series comparison of surge displacement of the sphere tested with structure in waves $\lambda_p/D_s = 4.9, 6.4$ and 6.8. The results show reasonable agreement except for the wave $\lambda_p/D_s = 4.9$ for which the difference in average drift velocity between experiment and numerical simulation is high.

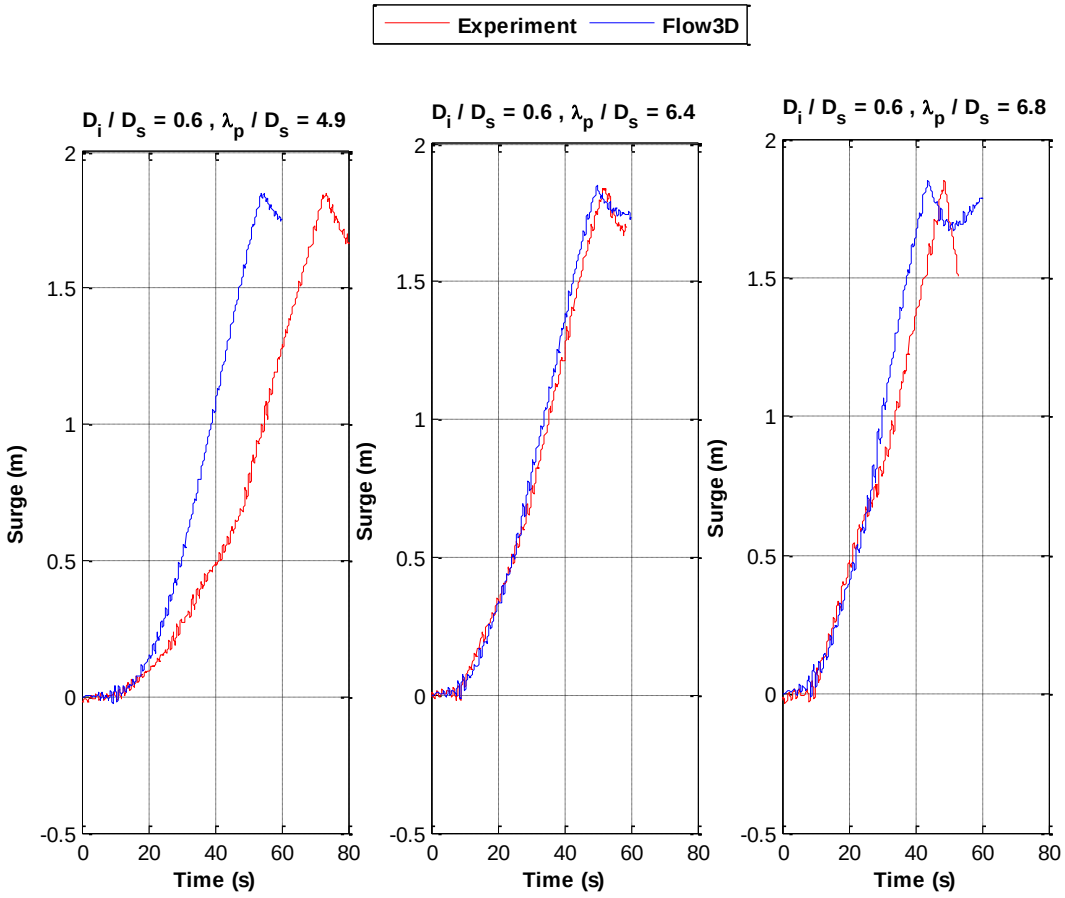

Figure 4.24: Time series comparison of surge displacement of the sphere tested with structure in waves $\lambda_p/D_s = 4.9, 6.4 \; and \; 6.8$

Figures 4.25 to 4.27 show the surge and heave velocities as a function of D/D_i between experiment and numerical simulation for the sphere tested with structure in waves $\lambda_p/D_s = 4.9, 6.4$ and 6.8 respectively. The corresponding surge and heave significant velocities are also given in the plots. The numerical results show some discrepancy with experiment which is more pronounced for heave velocities. Another reason for discrepancy is that the wave phases are not matched between experiment and numerical simulations.

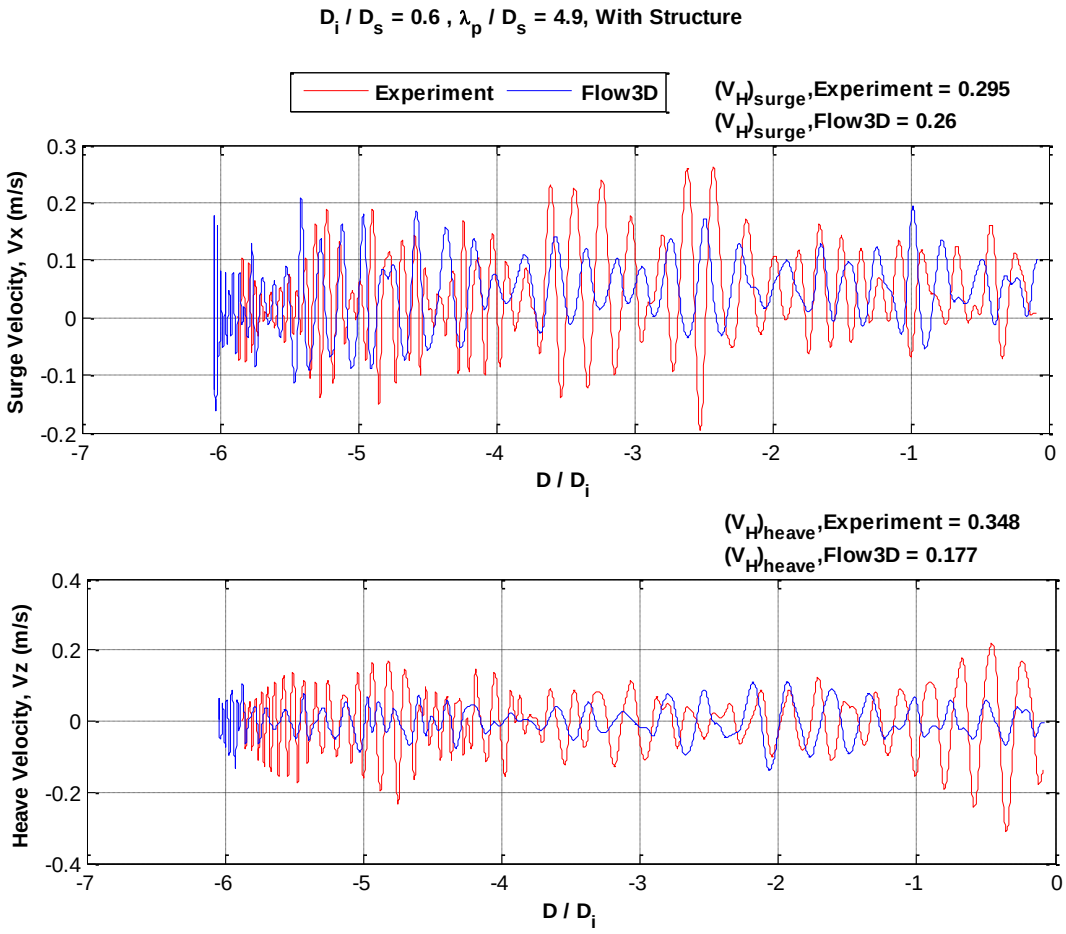

Figure 4.25: Comparison of surge and heave velocity between experiment and Flow3D for sphere $D_i/D_s = 0.6$ tested with structure and plotted against D/D_i in wave $\lambda_p/D_s = 4.9$

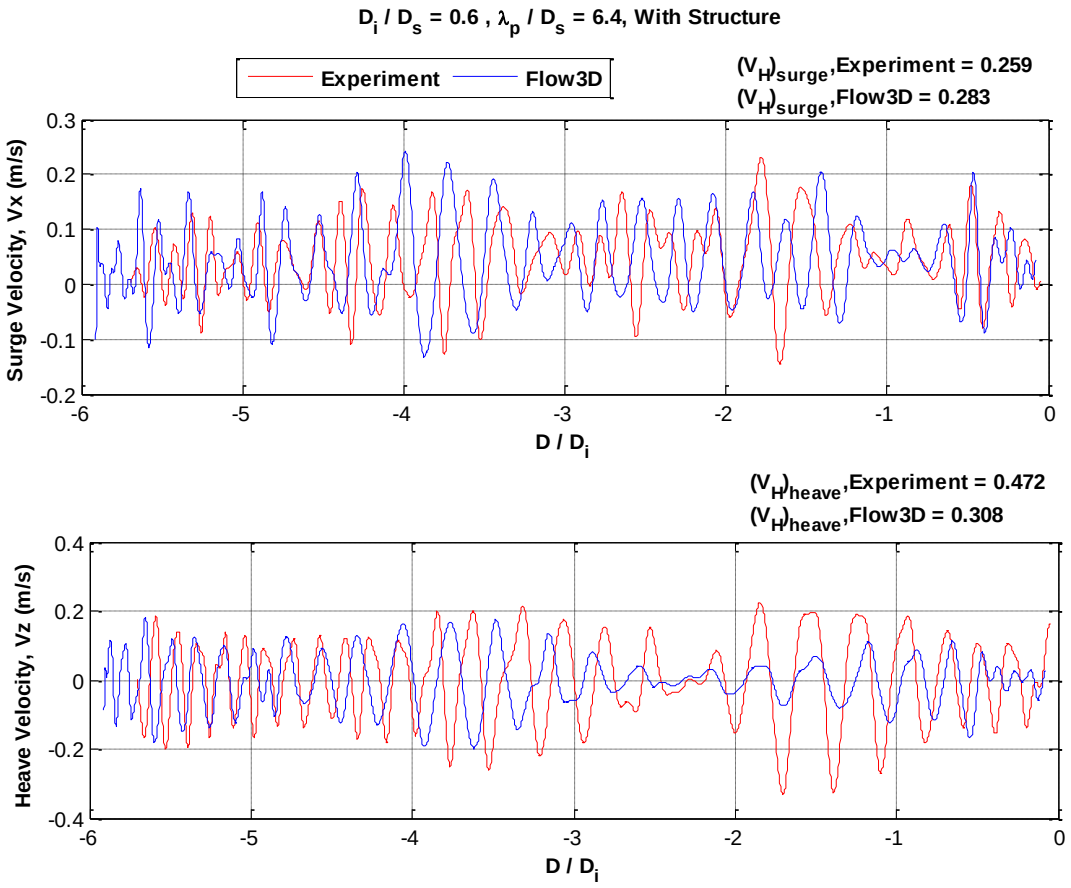

Figure 4.26: Comparison of surge and heave velocity between experiment and Flow3D for sphere $D_i/D_s = 0.6$ tested with structure and plotted against D/D_i in wave $\lambda_p/D_s = 6.4$

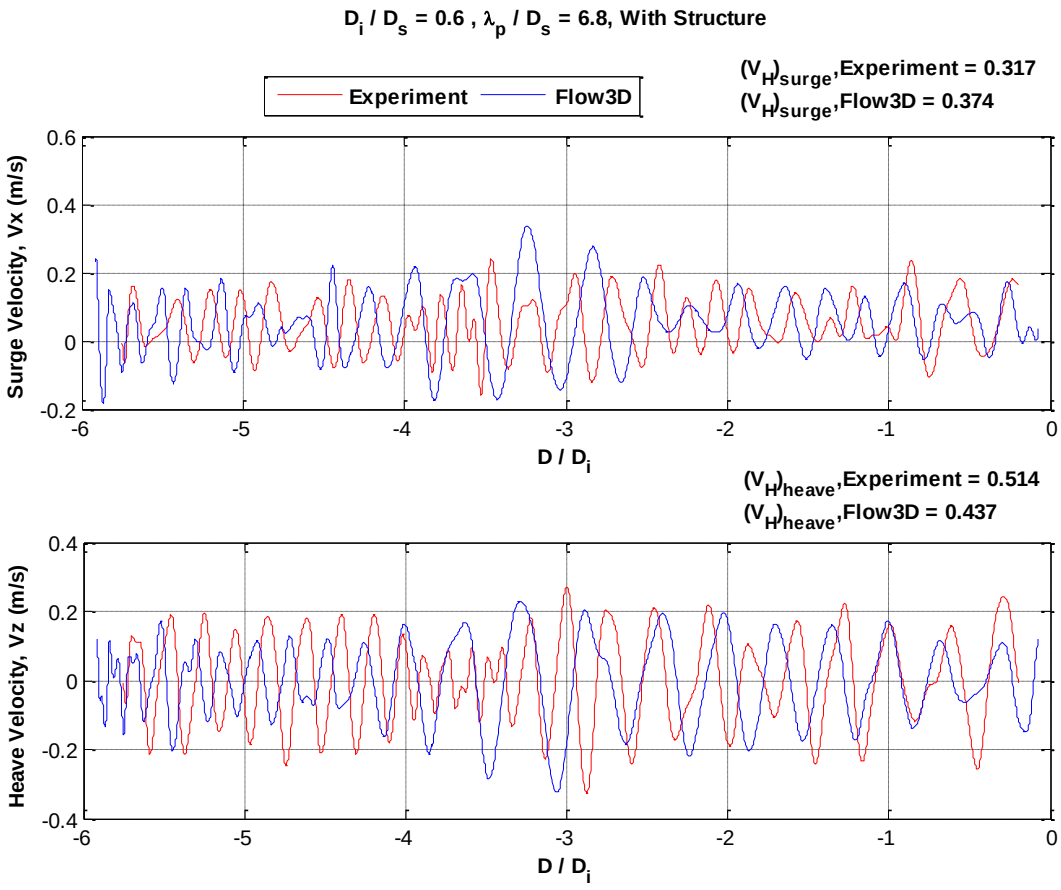

Figure 4.27: Comparison of surge and heave velocity between experiment and Flow3D for sphere $D_i/D_s = 0.6$ tested with structure and plotted against D/D_i in wave $\lambda_p/D_s = 6.8$

Chapter 5
Conclusions

5.1 Summary and Conclusions

The hydrodynamic interaction between an iceberg or a bergy bit and an offshore structure, when the two are in close proximity, is an important factor that governs the impact speed and consequently the input energy of potential collisions. In order to understand the phenomenon, a two phase, experimental and numerical, study has been conducted.

In the first phase, the objective was to investigate changes in wave load on the sphere at different separation distances from the structure. This has been a generalized study intended to identify trends that can be used to predict changes in impact velocity arising from changes in wave force for small ice masses approaching offshore structures.

The experimental results show that there is a significant change in the first and second order wave forces as a small body approaches a larger fixed structure. The mean drift forces in the horizontal direction are all positive (in the direction of wave propagation) when the structure is not present. These forces become negative for most of the cases when the body is close to the structure. The mean vertical forces are all positive for all waves and all separation distances, with or without the presence of the structure. Also as the body gets closer to the structure, the mean vertical force tends to increase.

The experimental results also show that the separation distance to wavelength ratio dictates the corresponding wave loads in both the horizontal and vertical directions. Also, as the body is positioned closer to the structure, the non-dimensional RMS forces in the horizontal direction decrease and the non-dimensional RMS forces in the vertical direction increase. This implies that the approaching body will be slowed down in surge but at the same time will experience

increased heave motion. This is consistent with the presence of a standing wave pattern arising from the combination of an incident wave field and the reflected wave field.

In the second phase, the objective was to determine the velocity profiles of approaching ice masses and how that changes prior to impact. The experimental results show that there is a significant change in the first and second order motions as a small body approaches a larger fixed structure. The motion results from the experimental data show excellent correlation with the force data gathered in the first phase experiments. The separation distance to wavelength ratio is found to dictate the corresponding wave induced motions in the same way as wave forces measured at different proximity to the fixed structure. The motions are amplified at nodes and antinodes of the standing wave in front of the structure. At nodes the surge motions are increased and heave motions are decreased and at antinodes the surge motions are decreased and heave motions are increased. As the body gets close to the structure, the surge motion slows and at the same time the heave motion is increased.

These changes in motions arising from changes in the wave forces indicate that velocity statistics for small ice masses should incorporate consideration of relative size and relative distance in considering potential impact scenarios with fixed structures. Reductions in surge drift and wave induced motions could lead to reduced impact forces while increases in heave motions may have implications for potential impacts with topsides and overhanging structures.

Some experiments have also been conducted to understand the effect of initial starting location on the resulting drift velocity. It was found that both initial starting conditions of location and wave phase have significant influence on the resulting direction of the drift velocity.

All the experimental data from both force and motion measurements are presented in a non-dimensional manner. The non-dimensional RMS surge and heave forces and motions for all the tested models are divided by D/λ and plotted against D/λ. This allows the derivation of a single equation that captures the results from all tests. These types of equations are particularly useful to provide guidelines for design codes.

In order to better quantify the real-life effects some experiments were conducted to investigate the motion behaviour in irregular waves. The objective is to know whether the observations found in regular waves will still hold in irregular seas. Wave data measured in front of structure showed that the significant wave heights follow a standing wave pattern generated by the superposition of incident and reflected peak frequency wave. Thus it may be inferred that the significant surge and heave forces and motions will be amplified at the node and antinode locations in front of the structure. Free floating motion data showed small differences in surge and heave velocity spectrum due to the structure presence. Further analysis of force spectrum generated from regular wave force data showed that beyond the nodal location at $D/\lambda_p \approx 0.25$, the significant surge force goes down and significant heave force goes up as the body gets closer to the structure. The effects of proximity in irregular seas are not as pronounced as those observed for regular waves, due to the multiple frequencies and wavelengths present in an irregular wave train. However the effects remain and are discernable with an approximate 10% decrease in surge force/motions and an approximate 60% increase in heave force/motions for proximities very close to the fixed structure.

Numerical investigations were conducted using RANS based commercial CFD code Flow3D. Selected test cases from both force and motion experiments are simulated and results are

compared. Flow3D is also used to simulate some force and motion studies in irregular waves generated from selected experimental spectrum.

For the force simulations, Flow3D show very good results when compared against three sets of experimental results. The results match quite well showing the highest and lowest forces at corresponding distance locations from the structure. For the motion simulations, Flow3D shows a good ability to capture the hydrodynamic interaction effect of a small moving body approaching a fixed structure. The velocity changes at node and antinode locations in front of the structure are also well captured by the numerical simulations. Significant differences were observed in some cases between experimental and simulated drift velocities. The challenges currently lie in the proper modeling of geometry and mass properties of the physical model considering the limitations of computational resources associated with large mesh requirements and the associated long computational times. The simulation results for irregular waves show the capability to simulate random waves and force and motion results in irregular waves are also reasonable showing the expected trends.

The fundamental conclusions of the study can be summarized as:

Reflected wave effects play a significant role in changing the hydrodynamic forces on a small body approaching a fixed structure. These effects are associated with the setup of wave nodes and antinodes in the wave field in front of the structure. Even for the case of irregular seas, the presence and effects of these nodes and antinodes are observed. For potential iceberg collisions, a reduction in forces and motions in surge of approximately 10% can be expected with many cases of greater reductions or complete deflection of the collision. Perhaps more significantly there is a larger increase in heave forces and motions with an expectation of an approximate 60%

increase in heave forces and the resulting motions. This has potential consequences in design of structures with deck or equipment overhangs.

A simple system of non-dimensionalizing the results from either fixed-position force measurements or free-floating motion measurements has been used to show good correlation between force and motion measurements. The system also demonstrates the importance of separation distance relative to wavelength in determining proximity effects and allows the results of experiments to be extended to different scales and sizes of structure and/or ice mass.

Finally it is evident that free surface flow solvers, that incorporate viscous flow modeling, are capable of simulating and capturing the effects of wave reflection and proximity in modeling the hydrodynamic forces and resulting motions for the case of a small ice mass approaching a fixed structure. There is still considerable computational cost associated with these models but the results agree very well with experimental results. This indicates that scenarios involving collisions between small ice masses and fixed structures can be modeled with good fidelity using modern and readily available software packages.

5.2 Recommendation and Future Work

This study focused on one aspect of the proximity problem which was thought to be the probable dominant mechanism influencing the near-field velocity. Based on the present work, additional questions were raised regarding other effects that might come in to play and the following future research works are recommended:

1. Some further investigation of irregular wave effects could be undertaken to better quantify the surge and heave effects in close proximity.
2. A broader range of structure sizes could be considered to expand the understanding of the relative size and size-wavelength effects.
3. This study focussed on wave effects as the probable dominant mechanism but additional work could focus on combined environments with wind and current effects. Starting position was shown to be important in determining the small body trajectory and other external influences may also play a role in determining the trajectory.
4. Expand the investigation to floating offshore structures where wave generation in addition to reflection might be expected to further influence the changes in surge and heave motions.

References

Ali, M. T., and Khalil, G. M. (2005). "On Hydrodynamic Interaction between Several Freely Floating Vertical Cylinders in Waves", *Proceedings of 24th International Conference on Offshore Mechanics and Arctic Engineering (OMAE)*, Halkidlki, Greece.

Arunachalam, V.M., Bobby, W., Muggeridge, D.B. and Stacey, R.A. (1985). A Review of the Interaction of Icebergs with Offshore Structures. *Proceedings of 4th Intl. Conf. on Behaviour of Offshore Structures, (BOSS)*, Delft, July. Elsevier, Amsterdam, pp. 693-704.

Arunachalam, V.M., Murray, J.J. and Muggeridge, D.B. (1987). "Short Term Motion Analysis of Icebergs in Linear Waves". *Cold Regions Science and Technology*, Vol. 13, No. 3, pp. 247-258.

Attwood, D. (1987). "Wave Induced Motion of Small Ice Masses", *Masters' thesis*, Memorial University of Newfoundland.

Bai, W., Zhang, T., and McGovern, D.J. (2017). "Response of Small Sea Ice Floes in Regular Waves: A Comparison of Numerical and Experimental Results", *Ocean Engineering*, Vol. 129, pp. 495-506.

Bass D, Gaskill, H, and Riggs, N, (1985). "Analysis of Iceberg Impact with Gravity Base Structures at Hibernia," *Proceedings of the 4th International Conference on Offshore Mechanics and Arctic Engineering*, Vol. 3, pp 255-259.

Bhinder, M. A., Mingham, C. G., Causon, D. M., Rahmati, M. T., Aggidis, G. A. and Chaplin, R. V. (2009). "A Joint Numerical and Experimental Study of a Surging Point Absorbing Wave Energy Converter (WRASPA)", *Proceedings of ASME 28th International Conference on Ocean, Offshore and Arctic Engineering (OMAE).*

Bøhlerengen, S. (2013). "Probabilistic Material Modeling of Iceberg for Analysis of Accidental Impacts with Ships and Offshore Structures", *Master's thesis*, Norwegian University of Science and Technology.

Bolen, Z. K. (1987). "Estimation of Loads Due to Simultaneous Occurrence of Waves and Iceberg Impacts",OTC-5599, *Offshore Technology Conference*, Houston, Texas.

Brown, R., and Daley, C. (1999). "Computer Simulation of Transverse Ship-Ice Collisions", *PERD/CHC Report* 9-79 for National Research Council of Canada.

Bruneau, S. E., Cammaert, A. B., and Croasdale, K. R. (1994). "Field Tests for Iceberg Impact Loading", *12th International Symposium on Ice, IAHR*, Vol.1, Pg. 187-197.

Bunnik, T., Pauw, W., and Voogt, A. (2009). "Hydrodynamic Analysis for Side-by-Side Offloading". *Proceedings of the 19th International Offshore and Polar Engineering Conference (ISOPE)*, Osaka, Japan.

Cammaert, A. B. and Tsinker, G. P. (1981). "Impact of Large Ice Floes and Icebergs on Marine Structures", *Proceedings. of the Sixth International Conference on Port and Ocean Engineering Under Arctic Conditions*, Quebec, Canada, Vol. II, pp. 653-667.

Cammaert, A. B. Wong, T. T., and Curtis, D. D. (1983). "Impact of Icebergs on Offshore Gravity and Floating Platforms", *Proceedings of the Seventh International Conference on Port and Ocean Engineering Under Arctic Conditions*, Helsinki, Finland.

Carrieres T., Sayed M, Savage S., and Crocker G. (2001). "Preliminary Verification of an Operational Iceberg Drift Model." *Proceedings of the International Conference on Port and Ocean Engineering under Arctic Conditions*, POAC- 01, pp 1107-1116.

Chen, X. B., (2005). "Hydrodynamic Analysis for Offshore LNG Terminals". *Proceedings of 2nd International Workshop on Applied Offshore Hydrodynamics*.

Chernetsov, V.A., Malyutin, A.A., and Karlinsky, S.L. (2008). "Floating Production Platform for Polar Seas Designed to Resist Iceberg Impact", *Proceedings of the Eighteenth International Offshore and Polar Engineering Conference*, pp. 679- 685.

Cheung, K. F. (1987). "Hydrodynamic Interactions between Ice Masses and Large Offshore Structures", *Masters' thesis*, University of British Columbia.

Chwang, A.T. (2003). "Interaction Hydrodynamics of Two Bodies". *Proceedings of the 13th International Offshore and Polar Engineering Conference (ISOPE)*, Honolulu, Hawaii, USA.

Colbourne, D. B., Smoes Re, A., Drodge, R., & Sullivan, M. (1998). "Terra Nova FPSO Iceberg Impact Tests". *IMD Report* TR-1998-18 (Protected) to SOFEC Inc.

Colbourne, D.B. (2000). "Scaling Pack Ice and Iceberg Loads on Moored Ship Shapes", *Oceanic Engineering International*, Vol. 4, No.1, pp. 39-45.

Crocker, G., Croasdale, K., McKenna, R., English, G., Guzzwell, J., Bruneau, S. (1997). "CCORE Iceberg Impact Experiment—Phase 2", *Final Report, C-CORE Publication* 96-C16, St. John's, NL, Canada.

Dean, R. G., Dalrymple, R. A. (1991). "Water Wave Mechanics for Engineers and Scientists", *World Scientific*, 1991.

Dmitriev, N.Ye., Nesterov, A.V. (2007). "Iceberg Drift in the Barents Sea According to the Observation Data and Simulation Results", *Proceedings of the Seventeenth International Offshore and Polar Engineering Conference*, pp. 633- 638.

Drover, E., and Kenny, S. (2012). "Finite Element Modeling of Iceberg Interaction with Subsea Protection Structures", OTC-23760, *Offshore Technology Conference,* Houston, Texas.

Duthinh, D. (1989). "Parametric Study of Iceberg Impact Loads." *Proceedings of the International Conference on Port and Ocean Engineering under Arctic Conditions*, POAC- 89, Luleaa, Sweden, pp 492-503.

Duthinh, D., Klein, K., Regrettier, J., Guichard, A., and Engler, M. (1990). "Full Scale Iceberg Impact: A Pilot Experiment in Antarctica." *Proceedings of the10th International Symposium on Ice*, IAHR 90, Espoo, Finland, pp 890-901.

Eik, K., Marchenko, A., and Løset, S. (2009). "Wave Drift Force on Icebergs – Tank Model Tests", *Proceedings of the twentieth International Conference on Port and Ocean Engineering under Arctic Conditions (POAC),* Luleå, Sweden.

Eik, K. (2009). "Iceberg Drift Modelling and Validation of Applied Metocean Hindcast Data", *Cold Regions Science and Technology*, Vol. 57, No. 2-3, pp. 67-90.

Falnes, J. (1983). "Added-Mass Matrix and Energy Stored in the Near-Field", *Internal Report*, Universiteteti Trondheim.

Foschi, R.O., Isaacson, M., Allyn, S., and Yee, S. (1996). "Combined Wave-Iceberg Loading on Offshore Structures." *Canadian J. Civil Engr.,* 23(5): 1099-1110.

Foschi, R.O., and Isaacson, M. (1996). "A Study of Wave-Iceberg Load Combination Factors" *Proceedings of the Sixth International Offshore and Polar Engineering Conference*, Los Angeles, USA.

Foschi, R.O., Isaacson, M., Allyn, S., and Yee, S. (1997). "Assessment of the Wave-Iceberg Load Combination Factor." *Proceedings of the Seventh International Offshore and Polar Engineering Conference*, v 2, p 434-441

Foschi, R.O., Isaacson, M., Allyn, N., and Yee, S. (1998). "Assessment of the Wave-Iceberg Load Combination Factor*." International Journal of Offshore and Polar Engineering.*, Vol.8, No.1, pp.1-8.

Foschi, R.O., Isaacson, M., and Allyn, N. (2004). "Reliability Calibration of a Waves-Icebergs Interaction Load Combination Factor" *Proceedings of 23rd International Conference on Offshore Mechanics and Arctic Engineering,* Vancouver, British Columbia, Canada.

Frederking, R., and Johnston, M. (2008). "Comparison of Local Ice Pressures on the CCGS Terry Fox with other Data", *Proceedings of the Eighteenth International Offshore and Polar Engineering Conference*, pp. 650- 654.

Fuglem, M., Muggeridge, K., Jordaan, I. (1999). "Design Load Calculations for Iceberg Impacts." *International Journal of Offshore and Polar Engineering.*, Vol. 9, No. 4, pp. 298-306.

Fuglem, M., Stuckey, P., and Suwan, S. (2015). "Estimating Iceberg-Wave Companion Loads using Probabilistic Methods" *Proceedings of 34th International Conference on Offshore Mechanics and Arctic Engineering (OMAE)*, St. John's, Newfoundland, Canada.

Gagnon, R. (2004a). "Analysis of Laboratory Growler Impact Tests", *Cold Regions Science and Technology*, Vol. 39, pp. 1-17.

Gagnon, R. E. (2004b). "Physical Model Experiments to Assess the Hydrodynamic Interaction between Floating Glacial Ice Masses and a Transiting Tanker". *Journal of Offshore Mechanics and Arctic Engineering*, Vol. 126, No. 4, pp. 297-309.

Gagnon, R.E., and Derradji-Aouat, A. (2006). "First Results of Numerical Simulations of Bergy Bit Collisions with the CCGS Terry Fox Icebreaker", *Proceedings of the 18th IAHR International Symposium on Ice*, Sapporo, Japan.

Gagnon, R. E. (2007). "Results of Numerical Simulations of Growler Impact Tests", *Cold Regions Science and Technology*, Vol. 49, pp. 206–214.

Gagnon, R., Cumming, D., Ritch, R., Browne, R., Johnston, M., Frederking, R., McKenna, R., Ralph, F. (2008a) "Overview Accompaniment for Papers on the Bergy Bit Impact Trials", *Cold Regions Science and Technology*, Vol. 52, Pg. 1-6.

Gagnon, R. (2008b) "Analysis of Data from Bergy Bit Impacts using a Novel Hull-Mounted External Impact Panel", *Cold Regions Science and Technology*, Vol. 52, Pg. 50-66.

Gagnon, R. E., and Wang, J. (2012). "Numerical Simulations of a Tanker Collision with a Bergy Bit Incorporating Hydrodynamics, a Validated Ice Model and Damage to the Vessel", *Cold Regions Science and Technology*, Vol. 81, pp. 26-35.

Gao, Y., Hu, Z., and Wang, J. (2014). "Sensitivity Analysis for Iceberg Geometry Shape in Ship-Iceberg Collision in View of Different Material Models", *Mathematical Problems in Engineering*, Hindawi Publishing Corporation, Article ID 414362.

Garrett, C. (1985), "Statistical Prediction of Iceberg Trajectories". *Cold Regions Science and Technology*, Vol. 11, pp. 255-266.

Gaskill, H.S., and Rochester, J. (1984), "A New Technique for Iceberg Drift Prediction". *Cold Regions Science and Technology*, Vol. 8, pp. 223-234.

Gershunov, E. M. (1986). "Collision of Large Floating Ice Feature with Massive Offshore Structure". *ASCE Journal of the Waterway, Port, Coastal and Ocean Engineering*, Vol. 112, No. 3, pp. 390-401.

Habib, K., Taylor, R., Jordaan, I., Bruneau, S. (2014) Experimental Investigation of Compressive Failure of Truncated Conical Ice Specimens. *Proceedings of 33rd International Conference on Ocean, Offshore and Arctic Engineering*, San Francisco, USA, 8–13 June, 2014 (OMAE2014-24184).

Hay and Company Consultants Inc. (1986). "Motion and Impact of Icebergs". *Environmental Studies Revolving Funds Report 044*. Ottawa. 136 p.

Hinchey, M., Muggeridge, D. B., Rzentkowski, G. and Lever, J. H. (1991). "Wave Induced Chaotic Motion of Bergy-bits." *Proceedings of the International Conference on Port and Ocean Engineering under Arctic Conditions*, POAC- 91, pp. 823-835.

Hong, D. C., Hong, S. Y., Nam, B. W., and Hong, S. W., (2013). "Comparative Numerical Study of Repulsive Drift Forces and Gap Resonances Between Two Vessels Floating Side-by-Side in Proximity in Head Seas using a Discontinuous HOBEM and a Constant BEM with Boundary Matching Formulation". *Ocean Engineering*, Vol. 72, pp. 331 – 343.

Holthe, K. (1989). "A Numerical Model for Predicting the Response of Concrete Gravity Platforms to Iceberg Impact." *Proceedings of the International Conference on Port and Ocean Engineering under Arctic Conditions*, POAC- 89, Luleaa, Sweden, pp 527-536.

Hsiung, C.C., and Aboul-Azm, A.F. (1982). "Iceberg Drift Affected by Wave Action". *Ocean Engineering*, Vol. 9, pp. 433-439.

Huang, G.,Wing-Keung, A.L., Huang, Z. (2011). "Wave-Induced Drift of Small Floating Objects in Regular Waves", Ocean Engineering, Vol. 38, pp. 712-718.

Huang, Z. J., Walker, K., M., Lee, S., Thanyamanta, W., and Spencer, D. (2014). "Transient Hydrodynamic Forces on a Disconnectable Turret Buoy", *Proceedings of 33rd International Conference on Offshore Mechanics and Arctic Engineering (OMAE)*, California, USA.

Huijsmans, R. H. M., Pinkster, J. A., and De Wilde, J. J. (2001). "Diffraction and Radiation of Waves Around Side-By-Side Moored Vessels". *Proceedings of 11th International Offshore and Polar Engineering Conference*, pp. 406-412.

Isaacson, M., and Dello Stritto, F.J. (1986). "Motion of an Ice Mass Near a Large Offshore Structure", OTC-5085, *Offshore Technology Conference*, Houston, Texas.

Isaacson, M. and McTaggart, K. (1990a). "Iceberg Drift Motions Near a Large Structure", *Proceedings of the First Pacific/Asia Offshore Mechanics Symposium*, Seoul, Korea.

Isaacson, M. and McTaggart, K. (1990b). "Modelling of Iceberg Drift Motions Near a Large Offshore Structure", *Cold Regions Science and Technology*, Vol. 19, pp. 47-58.

Isaacson, M. and Cheung, K. F. (1988a). "Hydrodynamics of Ice Mass Near Large Offshore Structure", *Journal of Waterway, Port, Coastal, and Ocean Engineering*, Vol. 114, No.4, pp. 487-502.

Isaacson, M. and Cheung, K. F. (1988b). "Influence of Added Mass on Ice Impacts", *Canadian Journal of Civil Engineering*, Vol. 15, No.4, pp. 698-708.

Isaacson, M. and McTaggart, K. (1990c). “Influence of Hydrodynamic Effects on Iceberg Collisions”, *Canadian Journal of Civil Engineering*, Vol. 17, No.3, pp. 329-337.

ISO 19906:2010. Petroleum and Natural Gas Industries – Arctic Offshore Structures.

Johnson, R. C., and Nevel, D.E. (1985). “Ice Impact Structural Design Loads”. *Proceedings of the Eighth International Conference on Port and Ocean Engineering Under Arctic Condition*, Narssarssuaq, Greenland, pp. 569-578.

Johnson, R. C., and Benoit, J. R. (1987). “Iceberg Impact Strength”, OTC-5599, *Offshore Technology Conference*, Houston, Texas.

Johnson, R. C., and Prodanovic, A. (1989). “Calculation of Iceberg Impact Forces”, *Proceedings of the International Conference on Port and Ocean Engineering under Arctic Conditions*, POAC-89, Luleaa, Sweden, pp 546-556.

Johnston, M., Ritch, R., and Gagnon, R. (2008). “Comparison of impact forces measured by different instrumentation systems on the CCGS Terry Fox during the Bergy Bit Trials”, *Cold Regions Science and Technology*, Vol. 52, Pg. 83-97.

Jones, S. J., Gagnon, R. E., Derradji, A. and Bugden, A. (2003). “Compressive Strength of Iceberg Ice”, *Canadian Journal of Physics*, Vol. 81, No. 1 / 2, pg. 191-200.

Jordaan, I., Stuckey, P., Liferov, P., and Ralph, F. (2014). “Global and Local Iceberg Loads for an Arctic Floater”, OTC-24628, *Offshore Technology Conference*, Houston, Texas.

Karlinsky, S.L., Chernetsov, V.A. (2010). “Floating Production Unit Resistance to Iceberg Impact”, *Proceedings of the Twentieth International Offshore and Polar Engineering Conference*, pp. 1202- 1206.

Kazi, I. H., Chwang, A.T., and Yates, G.T. (1998). "Hydrodynamic Interaction between a Fixed and a Floating Cylinder," *Inter Journal of Offshore and Polar Engineering (ISOPE),* Vol. 8, No. 1, pp. 46-50.

Kim, E. (2014). "Experimental and Numerical Studies Related to the Coupled Behavior of Ice Mass and Steel Structures During Accidental Collisions", *Doctoral thesis*, Norwegian University of Science and Technology.

Klopman, G. and van der Meer, J. W. (1999). "Random Wave Measurements in front of Reflective Structures", *Journal of Waterway, Port, Coastal, and Ocean Engineering*, Vol. 125, No.1, pp. 39-45.

Kristiansen, T., Faltinsen, O. M., (2009). "Studies on Resonant Water Motion between a Ship and a Fixed Terminal in Shallow Water", *Jounal of Offshore Mechanics and Arctic Engineering*, Vol. 131, No. 2.

Kristiansen, T., Faltinsen, O. M., (2012). "Gap Resonance Analyzed by a New Domain-Decomposition Method Combining Potential and Viscous Flow DRAFT", *Applied Ocean Research*, Vol. 34, pp. 198-208.

Kristiansen, T., Sauder, T., and Firoozkoohi, R. (2013). "Validation of a Hybrid Code Combining Potential and Viscous Flow with Application to 3D Moonpool", *Proceedings of the 32nd International Conference on Ocean, Offshore and Arctic Engineering (OMAE),* Nantes, France.

Kubat, I., Sayed, M., Savage, S.B., and Carrieres, T. (2005). "An Operational Model of Iceberg Drift." *International Journal of Offshore and Polar Engineering*., Vol.15, No.2, pp.125-131.

K.R. Croasdale & Associates Ltd. (2001). “Local Ice Load Data Relevant to Grand Banks Structures”, *PERD/CHC Report* 20-61 for National Research Council of Canada.

Lee, S.G., Lee, I.H., Baek, Y.H., Couty, N., Geoff, S.G., and Quenez, J.M. (2010). "Membrane-type LNG Carrier Side Collision with Iceberg - Effect of Impact Conditions on Structural Response through Sensitivity Analysis", *Presented at 6th Ann Arctic Shipping Summit*, Helsinki, Finland.

Lee, S.G., and Nguyen, H.A. (2011). “LNGC Collision Response Analysis with Iceberg Considering Surrounding Seawater”, *Proceedings of the Twenty-first International Offshore and Polar Engineering Conference*, pp. 1128- 1135.

Lever, J.H., and Sen, D. (1987). “A Method to Upgrade Iceberg Velocity Statistics to Include Wave-Induced Motion”. *Journal of Offshore Mechanics and Arctic Engineering*, Vol. 109, No. 2, pp. 278-286.

Lever, J.H., Attwood, D. and Sen, D. (1988a). “Factors Affecting the Prediction of Wave-Induced Iceberg Motion”. *Cold Regions Science and Technology*, Vol. 15, pp. 177-190.

Lever, J.H., Colbourne, B. and Mak, L. (1988b). “A Model Study of the Wave-Induced Motion of Small Icebergs and Bergy Bits”. *Journal of Offshore Mechanics and Arctic Engineering*, Vol. 110, No. 1, pp. 101-107.

Lever, J.H., Sen, D., Attwood, D., (1990a). “The Influence of Shape on Iceberg Wave-Induced Velocity Statistics”. *Journal of Offshore Mechanics and Arctic Engineering*, Vol. 112, No. 3, pp. 263-269.

Lever, J.H., Colbourne, B. and Mak, L. (1990b). "Model Study of Wave-Driven Impact of Bergy Bits with a Semi-Submersible Platform". *Journal of Offshore Mechanics and Arctic Engineering*, Vol. 112, No. 4, pp. 313-322.

Lever, J.H., Klein, K., Mitchell, D. and Diemand, D. (1991). "Wave- Induced Iceberg Motion". *Cold Regions Science and Technology*, Vol. 20, pp. 11-23.

Lewandowski, E. M. (2008). "Multi-Vessel Seakeeping Computations with Linear Potential Theory", *Ocean Engineering*, Vol. 35, pp. 1121-1131.

Liu, Z., and Amdahl, J. (2010). "A New Formulation of the Impact Mechanics of Ship Collisions and Its Application to a Ship-Iceberg Collision", *Marine Structures*, Vol. 23, pp. 360-384.

Liu Z, Amdahl J, Loset S. (2011a). "Plasticity Based Material Modelling of Ice and Its Application to Ship–Iceberg Impacts. *Cold Regions Science and Technology*, Vol. 65, pp. 326-334.

Liu, Z., Amdahl, J., and Løset, S. (2011b). "Integrated Numerical Analysis of an Iceberg Collision with a Foreship Structure", *Marine Structures*, Vol. 23, pp. 377-395.

Lu L., Cheng L., Teng B. and Zhao M. (2010). "Numerical Investigation of Fluid Resonance in Two Narrow Gaps of Three Identical Rectangular Structures", *Applied Ocean Research*, Vol. 32, No. 2, pp. 177-190.

Lu L., Teng B., Cheng L., Sun L. and Chen X. B. (2011). "Modelling of Multi Bodies in Close Proximity under Water Waves — Fluid Resonance in Narrow Gaps", *Science China Physics*, Vol. 54, No. 1, pp. 16-25.

Maguire, A. E. (2011). "Hydrodynamics, Control and Numerical Modelling of Absorbing Wavemakers", PhD thesis, University of Edinburg, UK.

Mak, L. M., Lever, J. H., Hinchey, M. J., and Duthinh, D. (1990). "Wave-Induced Bergy Bit Motion Near a Floating Oil Production Platform". *Proceedings of the 9th International Conference on Offshore Mechanics and Arctic Engineering*, Vol. IV, pp. 205-215.

Matskevitch, D. G. (1997a), "Eccentric Impact of an Ice Feature: Linearized Model". *Cold Regions Science and Technology*, Vol. 25, pp. 159-171.

Matskevitch, D. G. (1997b), "Eccentric Impact of an Ice Feature: Non- Linear Model". *Cold Regions Science and Technology*, Vol. 26, pp. 55-66.

McIver, P., and Evans, D. V. (1984). "The Occurrence of Negative Added Mass in Free-Surface Problems Involving Submerged Oscillating Bodies", *Journal of Engineering Mathematics*, Vol. 18, pp. 7-22.

McGovern, D.J., and Bai, W. (2014a). "Experimental Study on Kinematics of Sea Ice Floes in Regular Waves". *Cold Regions Science and Technology*, Vol. 103, pp. 15-30.

McGovern, D.J., and Bai, W. (2014b). "Experimental Study of Wave-Driven Impact of Sea Ice Floes on a Circular Cylinder". *Cold Regions Science and Technology*, Vol. 108, pp. 36-48.

McTaggart, K. A. (1989). "Hydrodynamics and Risk Analysis of Iceberg Impacts with Offshore Structures", *Ph.D. thesis*, University of British Columbia.

Mravak, Z., Rudan, S., Tryaskin, V., Coache, D., Lauzon, J. de, and Dudal, A. (2009). "Iceberg Collision with Offshore Unit", *Proceedings of the twentieth International Conference on Port and Ocean Engineering under Arctic Conditions* (POAC), Luleå, Sweden.

Mountain, D.G., (1980), "On Predicting Iceberg Drift". *Cold Regions Science and Technology*, Vol. 1, pp. 273-282.

Nallayarasu, S., Fatt, C. H., and Shankar, N. J. (1995). "Estimation of Incident and Reflected Waves in Regular Wave Experiments", *Technical Note, Ocean Engineering*, Vol. 22, No. 1. pp. 77-86.

Pauw, W. H., Huijsmans, R. H. M., and Voogt, A., (2007). "Advances in the Hydrodynamics of Side-by-Side Moored Vessels". *Proceedings of 26th International Conference on Offshore Mechanics and Arctic Engineering (OMAE)*, California, USA.

Pavec, M., and Coche, E. (2007). "A Stochastic Model of Iceberg Drift Including Wave Effect." *Proceedings of the International Conference on Port and Ocean Engineering under Arctic Conditions*, POAC- 07, pp 537-547.

Ralph, F., McKenna, R., Crocker, G., Croasdale, K. (2004). "Pressure/area Measurement from the Grappling Island Iceberg Impact Experiment", *Proceedings of IAHR Symposium on Ice*, 2, pp. 171–178. St. Petersburg, Russia.

Ritch, R., Frederking, R., Johnston, M., Browne, R., Ralph, F. (2008) "Local Ice Pressures Measured on a Strain Gauge Panel during the CCG Terry Fox Bergy Bit Impact Study", *Cold Regions Science and Technology*, Vol. 52, Pg. 29–49.

Salvalggio, M. A. and Rojansky, M. (1986). "The Importance of Wave-Driven Icebergs Impacting an Offshore Structure", OTC-5086, *Offshore Technology Conference*, Houston, Texas.

Sarpkaya, T. and Isaacson, M. (1981). "Mechanics of Wave Forces on Offshore Structures", Van Nostrand Reinhold Company.

Sen, D., (1983). "Prediction of Wave Loads and Motions of Floating Marine Structures by 3-Dimensional Flow Theory". *Masters' thesis*, Memorial University of Newfoundland.

Smith, S.D., (1993), "Hindcasting Iceberg Drift using Current Profile and Winds". *Cold Regions Science and Technology*, Vol. 22, pp. 33- 45.

Sodhi, D.S., and El-Tahan, M. (1980). "Prediction of an Iceberg Drift Trajectory During a Storm." *Annals of Glaciology*, Vol. 1, pp. 77-82.

Sodhi, D.S., and Haehnel, R. B. (2003). "Crushing Ice Forces on Structures", *Journal of Cold Regions Engineering*, Vol. 17, No. 4, pp. 153-170.

Song, M., Kim, E., and Amdahl, J. (2015). "Fluid-Structure-Interaction Analysis of an Ice Block-Structure Collision", *Proceedings of the 23rd International Conference on Port and Ocean Engineering under Arctic Conditions (POAC 15)*, Trondheim, Norway.

Subodh, C., Akinturk, A., and Colbourne, B. (2015). "Hydrodynamic Study of Submerged Ice Collisions", *Proceedings of 34th International Conference on Offshore Mechanics and Arctic Engineering (OMAE)*, St. John's, Newfoundland, Canada.

Swamidas, A. S. J., and Arockiasamy, M. (1984). "Iceberg Impact Forces on Gravity Platforms". *Proceedings of Cold Regions Engineering Specialty Conference*, Montreal, Canada.

Swamidas, A. S. J., El-Tahan, H., and Arockiasamy, M. (1986). "Structural Integrity of Semisubmersibles and Gravity Platforms to Bergy-Bit/Iceberg Impact", *OTC-5087, Offshore Technology Conference*, Houston, Texas.

Thanyamanta, W., Herrington, P. and Molyneux, D. (2011). "Wave Patterns, Wave Induced Forces and Moments for a Gravity Based Structure Predicted Using CFD", Proceedings of the

ASME 2011, 30th International Conference on Ocean, Offshore and Arctic Engineering, (OMAE), Rotterdam, The Netherlands, June 19-24.

Tsarau, A., Lubbad, R., and Loset, S. (2014). "A Numerical Model for Simulation of the Hydrodynamic Interactions between a Marine Floater and Fragmented Sea Ice". *Cold Regions Science and Technology*, Vol. 103, pp. 1-14.

Tsarau, A., Lubbad, R., and Loset, S. (2015). "Recent Advances in Modeling the Hydrodynamic Effects on Ice Motion and Ice-Structure Interactions Offshore". *Proceedings of the 23rd International Conference on Port and Ocean Engineering under Arctic Conditions (POAC 15)*, Trondheim, Norway.

Timco, G.W. (2011). "Isolated Ice Floe Impacts", *Cold Regions Science and Technology*, Vol. 68, pp. 35-48.

Turnbull, I.D., Fournier, N., Stolwijk, M., Fosnaes, T. and McGonigal, D. (2015). "Operational iceberg drift forecasting in Northwest Greenland", *Cold Regions Science and Technology*, Vol. 110, pp. 1-18.

Wang, C. Z., and Wu, G. X., (2010). "Interactions between Fully Nonlinear Water Waves and Cylinder Arrays in a Wave Tank". *Ocean Engineering*, Vol. 37, pp. 400–417.

Westmar Consultants Inc. (2001). "Load Estimates for Ship Damage Due to Impact with Icebergs", PERD/CHC Report 20-60 for National Research Council of Canada.

Wishahy, M., Pawlowski, J., Muggeridge, D. B. (1987). "The Nonlinear Heave Motion and Wave Forces on a Partially Submerged Sphere", pp. 42-48, OCEANS 1987, IEEE.

Zhou, Z. X., Edmond, Y. M. Lo, and Tan, S. K. (2005). "Effect of Shallow and Narrow Water on Added Mass of Cylinders with Various Cross-Sectional Shapes", *Ocean Engineering*, Vol. 32, pp. 1199-1215.

Zhou, Q., Liu, M., Peng, H., and Qiu, W. (2015). "Experimental Studies of Hydrodynamic Interaction of Two Bodies in Waves". *Proceedings of the 34th International Conference on Offshore Mechanics and Arctic Engineering*, St. John's, NL, Canada.

Zhu, R-C, Miao, G-P, and You, Y-X. (2005). "Influence of Gaps between 3-D Multiple Floating Structures on Wave Forces", *Journal of Hydrodynamics*, Vol. 17, No. 2, pp. 141-147.